Analysis of Small Volume Liquid Samples using Cavity Enhanced Absorption Spectroscopies



Cathy M. Rushworth

Worcester College

University of Oxford

A thesis submitted for the degree of

Doctor of Philosophy

Trinity 2012

For Cara

Acknowledgements

Firstly, I would like to thank my supervisor, Dr. Claire Vallance for her willing help and support throughout this project, as well as the Engineering and Physical Sciences Research Council for funding this project (EP/G027838/1). I would also like to thank the members of the Vallance group, particularly those on the cavity ringdown side of the laboratory:

- Jason Lee (D.Phil.) for all his LabVIEW programming, and for always being on hand for advice
- Yathukulan Yogarajah (Part II 2011/2012) for help with chip characterisation, nitrite analysis and pH determination
- Dean James (Part II 2010/2011) for help with initial chip characterisation and fibre notch fabrication
- Mathijs de Jong (M.Res. 2012) for constant enthusiasm and energy
- Bobby Oag (M.Phil.) for friendship during the first years of my project, and beyond

I am also grateful for the support from other members of the Vallance group, including Sara Gardiner, Laura Lipcuic, James Bull, Gabi de Wit, Cécilia Cauchy and Edward Wilman.

Within the Chemistry Department, I would also like to thank Simon Neil and Dr. Stuart Mackenzie for their collaboration on broadband cavity enhanced absorption spectroscopy, and Siti Aminah Setu and Dr. Dirk Aarts for providing access and training in the clean room facilities. Prof. Carol Robinson kindly allowed me to use the gold sputterer in her laboratory, and Dr. Robert Jacobs carried out metal evaporation deposition in the Surface Analysis Facility. The hard work of people in workshops, in particularly Charlie Jones, who manufactured the polishing wheel used in this thesis, as well as providing training in the student workshops, has also been invaluable.

Particular thanks to Phil Dolan and Dr. Jason Smith in the Department of Materials, who provided access to the focused-ion beam facility. Phil Dolan spent many hours on the weekend and evenings on this project, as well as providing coffee and company over the last years.

In addition, I would like to thank my examiners, Professor Gus Hancock and Professor Andrew Orr-Ewing, for their helpful comments and changes.

The majority of the microfluidic chips analysed in this thesis were fabricated by collaborators, and I would particularly like to thank Joanna Davies and Dr. João Cabral at Imperial College London; Yan Zhao and Prof. Hywel Morgan at the University of Southampton; and, Dr. Ruchi Gupta and Dr. Nick Goddard at the University of Manchester.

Finally, love and thanks to my family and friends who have always been supportive, in particular my parents and siblings, to whom I will be forever indebted. Kate and Conor have given me the most welcoming home from home, on the Ballymullan Road. Simon has been a loyal friend for many years, as well as providing technical advice, being an excellent teacher. My neighbours David and Mark have given me the happiest memories of Oxford, and their friendship over the last three years has been inestimable. My last six weeks in the lab have been brightened by Susannah, who is a joy to work with, and I wish her well in the remainder of her degree and beyond.

For Cara: “The whole world is divided for me into two parts: one is she, and there is all happiness, hope, light; the other is where she is not, and there is dejection and darkness...” (Tolstoy, War and Peace).

List of Publications

C. M. Rushworth, J. Davies, S. R. T. Neil, S. R. Mackenzie, J. T. Cabral, C. Vallance, Cavity enhanced optical methods for online microfluidic analysis, *Chem. Phys. Lett.*, in preparation.

C. M. Rushworth, Y. Yogarajah, Y. Zhao, H. Morgan, C. Vallance, Sensitive analysis of trace analytes using cavity ringdown spectroscopy, *Anal. Methods*, submitted.

D. James, B. Oag, C. M. Rushworth, J. W. L. Lee, J. Davies, J. T. Cabral, C. Vallance, High-sensitivity online detection for microfluidics via cavity ringdown spectroscopy, *RSC Advances*, 2, 5376, **2012**.

C. M. Rushworth, D. James, J. W. L. Lee, C. Vallance, Top notch design for fibre-loop cavity ringdown spectroscopy, *Anal. Chem.*, 83 (22), 8492, **2011**.

S. R. T. Neil, C. M. Rushworth, C. Vallance, S. R. Mackenzie, Broadband cavity-enhanced absorption spectroscopy for real time, in situ spectral analysis of microfluidic droplets, *Lab Chip*, 11 (23), 3953, **2011**.

C. M. Rushworth, D. James, C. J. V. Jones, C. Vallance, Fabrication of a reflective optical fiber coupler, *Opt. Lett.*, 36 (15), 2952, **2011**.

C. Rushworth, C. Vallance, Fibre-loop cavity ringdown spectroscopy for the sensitive and selective detection of minute sample volumes of liquid explosives, *Proc. SPIE*, 7838 (1), 78380Y, **2010**.

In addition, the work published in Optics Letters is subject to a British patent application from ISIS Innovation Ltd. (Application No. 1108557.8).

Analysis of Small Volume Liquid Samples using Cavity Enhanced Absorption Spectroscopies

Cathy M. Rushworth, Worcester College, University of Oxford

A thesis submitted for the degree of Doctor of Philosophy, Trinity 2012

Cavity enhanced absorption spectroscopies have earned themselves a place as one of the methods of choice for sensitive absorption measurements on gas-phase samples, but their application to liquid samples has so far been more limited. Sensitive short pathlength analysis of liquid samples is required for online analysis of microfluidic samples, which are processed in channels with dimensions of tens to hundreds of micrometres. Microfluidics is important for a range of applications including drug discovery and environmental sensing. This thesis explores the application of cavity enhanced absorption spectroscopies to short pathlength (0.010 mm to 2 mm) analysis of sub-microlitre volumes of liquids.

Three experimental set-ups have been been examined. Firstly, a single-wavelength cavity ringdown (CRD) spectrometer operating at 532 nm was assembled using two 99.8% reflectivity mirrors. High optical quality flow cells with short pathlengths ranging from 0.1 mm to 2 mm were inserted into this cavity at Brewster's angle. The detection limit of the set-up with each inserted flow cell was established using a concentration series of aqueous potassium permanganate ($KMnO_4$) solutions. For the 1 mm flow cell, a detection limit of 29 nM $KMnO_4$ or 1.4×10^{-4} cm^{-1} was established. Several different types of microfluidic devices were also inserted into the cavity, and it was found that the losses arising from the inserted chip were highly dependent on the method of chip manufacture. The CRD set-up with inserted 1 mm flow cell was applied to the detection of two important species, nitrite and iron(II), via analyte-specific colourimetric reactions. Detection limits of 1.9 nM nitrite and 3.8 nM iron(II) were established.

The second experimental set-up utilised broadband, supercontinuum light generated in a 20 m length of non-linear photonic crystal fibre. Broadband mirrors with around 99% reflectivity over the wavelength range from 400 to 800 nm were used to form the cavity, and a miniature spectrometer was used to wavelength-resolve the time-integrated cavity output. Flow cells and microfluidic chips were inserted into the cavity either at normal incidence or at Brewster's angle. This set-up was employed for reaction analysis of an iron complexation reaction with bathophenanthroline, and for a model organic reaction, the Diels-Alder reaction between anthracene and 4-phenyl-1,2,4-triazoline-3,5-dione. The same broadband set-up was also used for pH measurements using bromocresol green indicator solution. Using dual-wavelength CRD spectroscopy, the pH sensitivity was established to be around a few milli pH units.

Finally, an alternative type of cavity, formed from a loop of optical fibre has been investigated. A novel light-coupler was designed and fabricated in 365 μm core diameter multimode optical fibre. Sample designs employing both direct and evanescent wave absorption were investigated in small-core and large-core optical fibres, and the lowest detection limit of 0.11 cm^{-1} was determined in direct absorption measurements, with a pathlength of 180 μm, using our novel light coupler in 365 μm core diameter optical fibre.

Contents

1 Introduction **1**

1.1 Microfluidics . . . 1

1.2 Analysis . . . 3

1.3 Detection techniques . . . 5

1.3.1 UV/vis absorption spectroscopy . . . 5

1.3.2 Fourier Transform-Infrared spectroscopy . . . 6

1.3.3 Raman spectroscopy . . . 7

1.3.4 Laser-induced fluorescence . . . 8

1.3.5 Thermal lens microscopy . . . 9

1.3.6 Electrochemical detection . . . 9

1.4 Extended pathlength absorption detection . . . 10

1.4.1 Single-pass techniques . . . 11

1.4.2 Multi-reflection techniques . . . 13

1.4.3 Multi-pass absorption techniques . . . 17

1.5 Thesis outline . . . 17

2 Theory **19**

2.1 Absorption spectroscopy . . . 19

2.2 Cavity ringdown spectroscopy . . . 22

2.2.1 Detection sensitivity in CRDS . . . 25

2.3 Cavity enhanced absorption spectroscopy . . . 25

2.3.1 Detection sensitivity in CEAS . . . 28

2.4 Cavity stability . . . 28

2.5 Cavity mode properties . . . 31

2.6 Integration of liquid samples with CRDS . . . 35

3 Two-mirror cavity ringdown spectroscopy of liquids **37**

3.1 Introduction . . . 37

3.2 Cavity set-up . . . 40

3.2.1 Data analysis . . . 42

3.3 Characterisation of the cavity . . . 42

3.4 Introduction of a flow cell or microfluidic chip into the cavity . . . 42

3.4.1 Minimising reflection losses . . . 42

3.4.2 Pathlength calibration and determination of detection limit . . . 45

3.4.3 Commercial flow cells . . . 47

3.4.4 Etched glass chip . . . 51

3.5 Rapid prototyping of microfluidic chips . . . 52

3.5.1 Microscope slides and cover slides . . . 53

3.5.2 PDMS Chips . . . 54

3.5.3 Thiolene Chip . . . 57

3.6 On-chip measurements . . . 60

3.6.1 Permanganate calibration . . . 60

3.6.2 Reaction monitoring: Belousov-Zhabotinsky . . . 61

3.6.3 Droplet monitoring . . . 63

3.7 Conclusion . . . 65

4 Water Analysis **67**

4.1 Introduction . . . 67

4.1.1 Nitrite . . . 68

4.1.2 Iron . . . 70

4.2 Experimental . . . 71

4.2.1 Detection of nitrite via the Griess assay . . . 71

4.2.2 Detection of iron(II) via the bathophenanthroline assay . . . 73

4.3 Results . . . 74

4.4 Discussion . . . 76

4.4.1 Comparison of CRDS nitrite detection with other techniques . . . 78

4.4.2 Comparison of CRDS iron detection with other techniques . . . 81

4.4.3 Detection limit improvements . . . 84

4.4.4 Detection of other water analytes . . . 86

4.5 Conclusion . . . 87

5 Two-mirror cavity enhanced absorption spectroscopy of liquids **89**

5.1 Introduction . . . 89

5.1.1 Liquid-phase CEAS . . . 91

5.1.2 Supercontinuum light generation . . . 93

5.2 Experimental . . . 96

5.2.1 Light source . . . 96

5.2.2 Optical cavity . . . 98

5.2.3 Absorption cells . . . 98

5.2.4 Detector . . . 99

5.2.5 CEAS data analysis . . . 101

5.3 Characterisation of the cavity . . . 102

5.4 Characterisation of absorption cells . . . 104

5.4.1 Commercial flow cells . . . 104

5.4.2 Thiolene chips . . . 106

5.5 Single droplet analysis using CEAS . . . 110

5.6 Conclusion . . . 112

6 Reaction Analysis **113**

6.1 Introduction . . . 113

6.1.1 Reaction (i): Iron(II) Complexation . . . 116

6.1.2 Reaction (ii): Diels-Alder Reaction . . . 117

6.2 Experimental . . . 119

6.2.1 Syringe pump control . . . 120

6.3 Iron complexation reaction . . . 121

6.4 Diels-Alder reaction . . . 126

6.5 Determining cavity enhancement factors . . . 128

6.6 Conclusions and future work . . . 129

7 Spectrophotometric pH determination **131**

7.1 Introduction . . . 131

7.2 Theory . . . 134

7.3 Experimental . . . 137

7.3.1 Reagents . . . 137

7.3.2 Characterising the indicator dye: determining e_1 and e_2 . . . 137

7.3.3 Cavity set-ups . . . 139

7.4 Results and Discussion . . . 141

7.4.1 Finding CEF at 615 nm and 510 nm . . . 141

7.4.2 CEAS determination of pK_{a} . . . 142
7.4.3 CEAS pH measurements . . . 142
7.4.4 Dual-wavelength pH measurements using CRDS . . . 144
7.4.5 Sensitivity . . . 148
7.4.6 Increasing pH range . . . 151
7.4.7 Real water sample measurement . . . 152
7.5 Conclusion . . . 152

8 Fibre-loop cavity ringdown spectroscopy: Instrumentation 153
8.1 Introduction . . . 153
8.1.1 Optical fibres . . . 154
8.1.2 Linear fibre CRDS . . . 156
8.1.3 Fibre-loop CRDS . . . 157
8.1.4 Phase-shift CRDS . . . 158
8.1.5 Round-trip losses in fibre-loop CRDS . . . 159
8.1.6 Light coupling . . . 160
8.1.7 Chapter outline . . . 162
8.2 Instrumentation . . . 162
8.2.1 Light source and detector . . . 162
8.2.2 Data acquisition and analysis . . . 163
8.3 Light coupling . . . 163
8.3.1 Bend-coupled fibre-loop CRDS . . . 163
8.3.2 Design of a novel light-coupler . . . 165
8.3.3 Fabrication of a novel light-coupler . . . 167
8.3.4 Notch fabrication using focused ion-beam milling . . . 172
8.3.5 Alternative notch design . . . 174
8.3.6 Testing the FIB milled notches . . . 176
8.4 Sample region . . . 179
8.4.1 Direct absorption . . . 179
8.4.2 Lensing . . . 180
8.4.3 Evanescent field absorption . . . 182
8.5 Conclusion . . . 184

9 Fibre-loop cavity ringdown spectroscopy: Characterisation 185
9.1 Loss comparison . . . 185
9.2 Direct Absorption . . . 189
9.2.1 Light intensity . . . 190

9.2.2 Cavity mode structure . . . 190
9.2.3 Sensitivity analysis of direct absorption . . . 192
9.3 Evanescent wave absorption measurements . . . 193
9.4 Conclusions . . . 195

10 Concluding remarks **197**
10.1 Conclusions . . . 197
10.2 Future work . . . 198
10.2.1 Improving the sensitivity of iron detection . . . 199
10.2.2 Clinical applications . . . 200
10.2.3 Set-up miniaturization . . . 202
10.2.4 Sensor Deployment . . . 203

A Determination of $\Delta\mathbf{pH}_{\min}$ **207**

Bibliography **209**

Chapter 1

Introduction

Cavity enhanced absorption spectroscopies have earned themselves a place as one of the methods of choice for sensitive absorption measurements on gas-phase samples, but their application to liquid samples has so far been more limited [1]. We will explore the performance of cavity enhanced absorption spectroscopies for short pathlength measurements on liquids, focusing on applications in microfluidics and detection of trace compounds in water. We begin, therefore, with a description of the relatively new field of microfluidics, providing an outline of its advantages over macroscale systems and some of the special properties of fluid flow on the microscale. We then discuss the problems associated with detecting chemical species in such small volumes, and outline several of the key detection techniques that have been applied to microfluidic analysis. Of particular interest are the methods of improving the sensitivity of absorption spectroscopy by increasing the pathlength through the sample, and several single-pass methods that have attempted to achieve this will be outlined, before proposing our detection method, that of applying cavity enhanced absorption spectroscopies to small volume analysis. Finally, this Chapter concludes by providing an outline of the thesis.

1.1 Microfluidics

The field of microfluidics can be defined as "the science and technology of systems that process or manipulate small (10^{-9} to 10^{-18} L) amounts of fluids, using channels with dimensions of tens to hundreds of micrometres" [2]. The development of small-scale fabrication techniques led to the proposal by Manz in 1990 of the concept of a miniaturized total chemical analysis system (abbreviated as μTAS), capable of carrying out all the sample handling steps as well as detection within the same device [3]. Miniaturization has advantages over its macroscale companion: the reduction in size allows for analysis and reaction of scarce or expensive reagents, with the production of less waste, while also increasing the speed of

separations and reactions [4, 5]. One particular feature of microfluidic systems is the ability to create droplets and to use these as 'micro-reactors' [6–10], opening up opportunities for ultra-fast, facile reaction screening and optimisation [11].

The advantages of microfluidics can also be important in a wide range of applications, including drug discovery [12], the generation of combinatorial libraries [13, 14], bioanalysis [15, 16], DNA sequencing [17], protein crystallisation [18], nanoparticle synthesis [19], and environmental sensing [20–26]. Each application area comes with its own specific requirements. For example, environmental analysis *in situ* requires the development of a robust, portable and low power sensor system [26]. We are particularly interested in environmental sensing, which will be the subject of Chapters 4 and 7, and reaction analysis, which will be the subject of Chapter 6 in this thesis.

In addition to the small sample volumes, the miniaturization of fluid flow dramatically changes its properties [27–29]. The key dependence of fluid flow on size of channel is defined by the Reynolds' number R [27, 30, 31]:

$$R = \frac{\rho U_0 L_0}{\eta} \tag{1.1}$$

where ρ is the density, U_0 is the fluid velocity, L_0 is the typical length scale, defined by the channel width, and η is the shear viscosity of the fluid. The Reynolds' number thus provides a measurement of the ratio of the inertial to the viscous forces. Viscosity may be described as the resistance of a fluid to deformation under shear stress and encourages fluid to flow in parallel layers, with no interaction between the two layers (laminar flow), whereas inertia describes the tendency of the fluid to resist acceleration and counteract laminar flow [29]. In a macroscale environment, fluid flow is dominated by inertial forces (the Reynolds' number is large, typically $> 10^4$), and molecules in solution are typically brought together by fast turbulent flow. However, when the length scale is reduced to the dimensions found in microfluidic systems, the Reynolds' number becomes small (typically $< 10^2$), and flow is laminar. Under laminar flow conditions, there is no turbulence, and mixing of reagents can only occur by diffusion, which is slow compared with turbulence. Depending on the application, this slow mixing time can be a hindrance or a help. For example, if a chemical reaction is being investigated, different solutions need to be mixed rapidly together, in order to probe the kinetics of the reaction rather than the diffusion time of the molecules involved. However, if one is interested in sorting and analysing the products of the reaction, slower mixing can be useful [27].

The mixing time required under laminar flow conditions can be described as follows. If two fluids are injected to flow alongside each other, homogenisation can be assumed to occur once the molecules have diffused across the entire channel, which is described by a mixing time $\tau_D \sim w^2/D$, where w is the channel width and D is the diffusion coefficient [27]. During this mixing time, the molecules will have travelled a distance

$Z \sim U_0 w^2/D$ down the channel [27]. The number of channel widths required for complete mixing is then described by the Péclet number (P) [27]:

$$\frac{Z}{w} \sim \frac{U_0 w}{D} \equiv Pe \tag{1.2}$$

For example, a small solute ion flowing with the fluid through a 100 μm channel at 100 μm/s has $P \approx 5$, and therefore requires five channel widths (approximately 0.5 mm and 5 s) to mix completely. This mixing time is too long for kinetics measurements to be carried out on all but the slowest reactions. Efficient mixing, to enable rapid kinetics to be investigated, is therefore engineered through techniques designed to reduce the mixing path [32–34]. One example is flow-focusing; a technique in which three solution streams are introduced together. The sample solution flows in the centre of the two outer fluids, and the sample stream is thus reduced significantly in width compared to the size of the microchannel itself. As previously noted, the mixing time is directly proportional to the square of the diffusion pathlength (or channel width), so decreasing the stream width results in significantly faster mixing. Pabit and Hagan have demonstrated such a mixing device which can achieve microsecond mixing times and has a low sample consumption of only 6 nL s^{-1} with a sample stream width of < 1 μm [35].

Minute detection volumes and extremely short pathlengths severely limit the application of many traditional detection methods to microfluidic analysis, and the high flow rates also place a high demand on the time resolution of any detection method to be utilised. In the following Section, we discuss the different categories of analysis, and proceed to highlight some of the key detection techniques that have been applied to small volume detection.

1.2 Analysis

Liquid-phase analysis can be divided into several categories, depending on its location relative to the reaction. In 1987, Callis et al. defined the categories, which he named the "five eras of process analytical chemistry", as follows [36]:

1. **Offline analysis.** Sample is removed from the process line and sent to a separate, centralised facility. While this means that sophisticated instruments (such as GC-MS) can be used, with attendant expert staff to interpret the results, the time delay is a massive bottleneck for process optimisation, with concomitant high costs.

2. **Atline analysis.** Sample is removed from the process line and analysed using a dedicated instrument adjacent to the process line. While this represents a considerable time saving compared with offline

analysis, the lack of automation and requirement for large sample volumes (from multiple runs on-chip) makes this approach far from ideal for conventional analysis.

3. **Online analysis.** Automated sampling system is used to extract the sample, condition it properly, and send it to the analytical instrument for analysis, either in continuous (e.g. spectroscopic methods) or intermittent flow (e.g. GC).

4. **Inline analysis.** Chemical analysis is carried out *in situ* in the process line, using chemically sensitive probes, for example converting specific chemicals selectively into detectable products.

5. **Non-invasive analysis.** This is the ultimate analytical technique, as the analysis does not disturb the chemical reaction in any way. Most common methods rely on spectroscopy, in the UV, visible or near-IR spectral regions.

It should be emphasised that these subdivisions are meant as a framework only. However, these categories do provide a clear description of the different types of analytical techniques that may be applied to microfluidic analysis. As might be expected, offline or atline analysis tends to be used commonly for chip analysis, with conventional analytical techniques such as nuclear magnetic resonance (NMR) [37], mass spectrometry (MS) [38], high performance liquid chromatography (HPLC) [39, 40], gas chromatography (GC) [41] and coupled techniques such as GC-MS [42–44] often applied. Such techniques typically require the microfluidic chip to be operated for longer periods of time than necessary for the reaction or analysis to occur, in order for sufficient volume of sample to be generated for analysis. In addition, the integrity of the sample (which may require quenching before analysis) is not assured. Of course, such offline or atline analytical techniques do not take advantage of many of the key advantages of using a microfluidic device, including the small size and low costs of the device itself. It can be relatively straightforward to develop online versions of many of these techniques. For example, online HPLC was demonstrated by McMullen et al. for reaction optimisation [45,46], although quenching (in this case via cooling) of the reaction mixture was still required, as well as collection of a relatively large sample volume (20 mL in this case) before analysis. In recent years, there has been a shift towards the development of integrated analytical probes, which are of course preferred for microfluidic analysis, and fit closer within the ethos of μTAS, as first proposed by Manz [3].

Detection in microfluidic systems has been the subject of several recent reviews [26, 28, 47–56]. In the following Section, we concentrate on analysis that may be classed as either online, inline or non-invasive, with particular emphasis on non-invasive analysis. The majority of these techniques are either spectroscopic or electrochemical.

1.3 Detection techniques

1.3.1 UV/vis absorption spectroscopy

Absorption spectroscopy is a widely used analytical technique because it is universal: many analytes absorb light at a range of frequencies and, by selecting a frequency range at which the solvent is transparent, it is possible to perform label-free detection. Absorption spectroscopy is described by the well-known Beer-Lambert law, which will be derived in Chapter 2:

$$I = I_0 e^{-\alpha C l} \tag{1.3}$$

where I is the transmitted light intensity, I_0 is the initial light intensity, α is the absorption coefficient of the molecule, C is the concentration and l is the optical pathlength through the sample.

Conventional UV/vis analysis is carried out using spectrometers which commonly analyse a few mL of liquid sample, in a 1 cm pathlength cuvette, resulting in relatively sensitive measurements. For example, we have determined the detection limit of the Varian Cary 100 Bio UV/vis spectrometer (used for some of the work described in Chapter 4), defined as three times the standard deviation in the baseline measurement of I_0 at 532 nm, to be 3.8×10^{-3} cm^{-1}. Newer cuvette designs have also been developed, and these allow for detection of smaller volumes in similar or slightly shorter pathlengths, for example the Kratos Spectroflow 757 UV/vis absorption detector has an optical pathlength of 8 mm and a volume of only 12 μL. However, the exponential dependence of sensitivity on pathlength and concentration shown in Equation 1.3 illustrates the incompatibility of traditional single-pass absorption measurements with detection involving either very low concentrations and/or short pathlengths such as those found in the field of microfluidics.

Online absorption detection is additionally challenging because of the difficulty associated with transmitting light through a microfluidic channel, with low losses. Perhaps the most common method is to integrate optical fibres into the microfluidic chip, either in-the-plane (see, for example, [57]) or out-of-the-plane (see, for example, [58]) of the microchannel to be probed. The integration of optical fibres into microfluidic chips has been the subject of several papers [59, 60]. Typical concentration detection limits for on-chip absorption measurements are in the millimolar to micromolar range [29].

On-chip UV absorbance is particularly applied because many analytes have absorptions in the UV spectral region. For example, Lu et al. used online UV absorbance to monitor the pinacol formation reaction of benzophenone in isopropanol [61]. Jindal and Cramer applied UV absorbance detection at 240 nm to measure a detection limit of 0.167 mM thiourea across a channel with a physical pathlength of 43 μm [58]. A shorter effective channel depth of 23 μm was determined experimentally and theoretically, when divergence of light

between the two 600 μm core diameter optical fibre ends across the chip walls (formed from two pieces of quartz glass each roughly 1.6 mm thick) and the trapezoidal shaped channel was taken into account.

Although absorption spectroscopy can be a label-free technique, there is also a significant amount of interest in on-chip colourimetric analysis, in which specific analytes are chemically converted into a strongly coloured product [54]. The product, which is formed in a known ratio to the analyte, can thus be quantified using visible absorption spectroscopy, allowing the use of visible light sources [62, 63]. In addition, the absorption coefficient of the molecule is greatly enhanced, typically by several orders of magnitude, which allows the sensitivity to be significantly improved compared with measuring the analyte directly at its native absorption wavelength. Finally, such colour reactions can confer selectivity on an analyte, overcoming a particular problem associated with UV absorption in many real samples, where there can be hundreds of different species, many with overlapping absorption spectra.

For example, Wu et al. measured a detection limit of 0.45 mM lactate, by using an enzymatic colourimetric reaction to convert colourless lactate to a strongly coloured purple dye, with an absorption maximum at 540 nm [57]. A green light emitting diode (568 nm emission) was used in combination with a photodiode, with two 62.5 μm core diameter optical fibres inserted across a 250 μm pathlength channel for light delivery and collection in a compact and low-cost set-up. Pathlengths from 50 - 300 μm were investigated, but 250 μm was found to be the optimum in this case, as a compromise between detection sensitivity and interference from scattered light.

Methods to improve the sensitivity of absorption spectroscopy will be addressed later in this Chapter, after a discussion of several other spectroscopic and electrochemical detection techniques.

1.3.2 Fourier Transform-Infrared spectroscopy

Fourier-Transform Infrared spectroscopy (FT-IR) is a useful analytical tool, providing both structural information and a quantitative determination of species concentration, through measurement of the absorptions arising from vibrational excitation of the analyte molecules. FT-IR spectroscopy has been applied to on-chip reaction analysis [64–67]. Attention must be paid to the IR absorption of the chip material, for example borosilicate glass is only transparent below 2000 nm [64]. Silicon microdevices [68] and calcium fluoride devices [64] have been employed in order to improve IR transmission, but the use of non-standard materials usually entails more complicated device fabrication procedures. In addition, because of the strong IR absorption of many commonly used solvents, including water, it can be difficult to improve the sensitivity of IR analysis by extending the sample pathlength [68]. An alternative sampling strategy is, therefore, to take advantage of the evanescent wave between the solution and an attenuated total reflection (ATR, also known as multiple internal reflection) crystal embedded in the chip [65].

Unfortunately, FT-IR analysis can lack sensitivity, owing to the low absorption coefficients in the IR. For example, Herzig-Marx et al. estimated their ATR detection scheme to have a sensitivity in the 1 - 10 mM range for a wide range of reaction systems [65]. In this experiment, 500 scans were acquired, totalling an acquisition time of approximately 6.2 minutes [65]. For their set-up, which was used to monitor the relatively slow kinetics of ethyl acetate hydrolysis, this long acquisition time was not a problem. However, improving the temporal resolution is key for analysing systems with rapid kinetics.

Over recent years, several on-chip examples of FT-IR imaging have been demonstrated [69–72]. FT-IR imaging provides spatial resolution (typically 40 μm [72]), via the use of a focal plane array (FPA) IR detector, which in addition to the chemical information arising from the excitation of molecular vibrations, enables unlabelled monitoring of several analytes within continuous laminar flows [69]. Chan et al. have presented studies of the formation of HDO from D_2O and H_2O [70], as well as the mixing of polyethylene glycol (PEG) and water [71]. Unfortunately, conventional FT-IR imaging could not be applied to the analysis of flowing droplets because the data processing time was slow: typically, there was approximately 40 s between image acquisitions while the detector could not collect data [72]. In the last year, however, Chan et al. reduced the data processing time and were thus able to measure 4096 spectra in the range 1000 - 1974 cm^{-1} with a scanning time of 50 ms and a temporal resolution of 120 ms, exemplified by the monitoring of droplet flow within microfluidic channels [72].

1.3.3 Raman spectroscopy

In Raman spectroscopy, the weak inelastic scattering of monochromatic light from a laser is measured. The emitted photons exhibit characteristic frequencies for each functional group of a molecule, dependent on the rotational and vibrational energy states of the molecue. Unlike IR spectroscopy, which requires a change in dipole moment for a transition to be IR active, Raman spectroscopy requires the molecule to undergo a change in polarizability. On-chip reaction analysis using Raman spectroscopy has been demonstrated in both continuous [73–76] and droplet [77, 78] flow. High sensitivity has been demonstrated, for example Walker et al. reported a detection limit of 0.23 μM of the herbicides paraquat and diquat in a pathlength of only 75 μm and employing an integration time of 0.5 s [79]. Unfortunately, the inherently weak nature of the Raman scattering process means that relatively long integration times are often required, typically seconds to minutes. For example, Leung et al. used integration times ranging from 1 to 60 s, with 0.1 s rest time between acquisitions [74], while Barnes et al. used a 3 minute integration time [77]. Raman imaging techniques have also been developed for on-chip analysis [80].

For improving the sensitivity of Raman spectroscopy, surface-enhanced Raman spectroscopy (SERS) is a popular technique [81, 82]. The sensitivity enhancement of SERS compared to conventional Raman spectroscopy, which may be between 6 - 10 orders of magnitude, is thought to arise from a combination of

electromagnetic enhancement and chemical enhancement [82]. Electromagnetic enhancement arises from surface plasmon resonance (SPR) at the surface of the metallic nanoparticles typically used as SERS substrates. At the SPR frequency, conduction band electrons move easily and create a large oscillation in the local electric field intensity, which enhances the Raman signal. Chemical enhancement arises from bond formation between the interrogated molecule and the metal surface, which increases the polarizability of the molecule [82, 83]. Single molecule detection is possible with SERS [81], making SERS competitive with fluoresence detection, which will be discussed in Section 1.3.4.

SERS has been applied to both continuous flow [84] and droplet flow [83, 85, 86] on-chip analysis. While integration times of $\geq$ 1 s are most commonly used for spectrum acquisition, the most recent publication by Cecchini et al. should be highlighted. In this paper, Cecchini et al. developed an ultrafast version of SERS with submillisecond time resolution, by using a faster camera, which allowed for the acquisition of full Raman spectra multiple times within a single droplet for the first time [83].

A continued problem for quantitative analysis using SERS is the control of experimental conditions such as degree of metal particle aggregation, different sizes of metal particles and inhomogeneous distributions of molecules on the metal particles, all of which will affect the SERS signal [82]. In addition, SERS substrates may not be suitable for longer-term use, as the sensitivity enhancement at the metal surface decays as the metal surface becomes contaminated with use.

1.3.4 Laser-induced fluorescence

In laser-induced fluorescence, a molecule is excited from its ground electronic state (labelled S_0) into an electronically excited state (labelled S_1) by a laser. Fluorescence is the emission of the photon from the S_1 state. This fluorescence photon is typically at lower energy (higher wavelength) than the excitation photon, owing to the energy lost in rapid vibrational relaxation before the emission of a photon. This allows the fluorescence emission to be monitored at a wavelength with zero background, conferring great sensitivity on this detection technique [87]. Laser-induced fluorescence (LIF) is the most common detection method for microfluidic devices, because of its high sensitivity [29]. It is one of the few detection techniques that actually benefits from the reduction in size of the sample volume that occurs when moving to on-chip detection. This improvement in sensitivity with reduction in sample volume arises from the fact that the background signal (which generally arises from impurities in the sample and scattering) scales linearly with the size of the detection volume, while the fluorescence signal of a single molecule remains constant [88]. The main disadvantage of LIF is that most molecules require labelling with a fluorophore (a process known as 'tagging'), in order to exhibit a strong fluorescence signal. The first approaches to achieving single molecule detection via fluorescence were achieved by tagging a molecule with several fluorophores [89], but

the improvement in optical detectors since then has enabled single molecule detection to be achieved on-chip through fluorescence from a single fluorophore [90, 91].

Fluorescence has been used for monitoring millisecond reaction kinetics on-chip [6, 8, 92, 93], as well as for visualising microscale flow [94], to name just a few applications. More recently, a technique known as fluorescence lifetime imaging (FLIM) has been applied to droplet analysis [95, 96], which allows for flow mapping with 1 μs temporal resolution. A pulsed excitation laser is used and the fluorescence decay is recorded directly by using a time-correlated single-photon counting technique [87].

1.3.5 Thermal lens microscopy

Thermal lens microscopy (TLM) typically uses two laser beams, an excitation beam and a probe beam, which are both focused into a liquid sample [97]. If the energy of the excitation beam is absorbed by an analyte present in the solution, then a localised temperature increase is observed. The refractive index of the medium is, of course, temperature dependent, and thus the probe beam, which lies at a non-absorbing wavelength, is subjected to the 'thermal lens' effect. The resulting change in intensity of the probe beam can be measured directly, providing a very sensitive detection scheme, which has even been demonstrated down to sub-single molecule levels [98–100]. However, it typically lacks selectivity, because only the excitation beam, not the probe beam, is specific to the analyte's absorption. In addition, the bulky apparatus required has limited its application in the field to date, although Mawatari et al. have recently published a portable thermal lens spectrometer, which had a detection limit of 30 nM xylenecyanol solution, or 4.7×10^{-6} absorbance units, in an optical pathlength of only 52 μm [101].

1.3.6 Electrochemical detection

So far, we have only considered optical detection methods. Another important class of on-chip detection techniques employ electrochemical methods [102–104]. Electrochemical detection shows considerable promise for microfluidic systems, as it can offer excellent sensitivity, demonstrated even down to single molecule [105] levels off-chip, but more typically at nanomolar concentration levels on-chip [103]. In addition, the detection scheme is inherently capable of miniaturization and portability, with the attendant low cost and low power requirements [102]. While for optical measurements, the channel width determines the optical pathlength, and therefore sets a limit on the detection sensitivity, this is not the case for electrochemical measurements. Indeed, electrochemical detection may be favoured by the reduction in sample volume, as the increased surface to volume ratio can enhance the flux at the surface of an electrode, as well as reduce the background signal [102, 103].

Most commonly, electrochemical detection is performed by setting the potential of the working electrode to a fixed value (the optimum of which is determined for each target analyte), and then monitoring the current as a function of time. This technique is called amperometry [106]. The applied potential causes reduction or oxidation of the target analyte, and the current output exhibits spikes corresponding to electron transfer processes, which are directly related to the concentration of the analyte [102]. Such controlled-potential detectors are ideal for analytes that are easily oxidised or reduced, however some chemical derivitisation of the analyte may be required to convert less electroactive analytes into detectable compounds [102]. In addition, the kinetics of the charge transfer play a role, for example, the detection of nitrate, while thermodynamically feasible, is slow and not necessarily selective because of the need to apply large overpotentials [107]. A key problem with real sample analysis is also the deterioration of the electrode surface, which limits sensitivity over time [107].

1.4 Extended pathlength absorption detection

In this Section, we provide an overview of methods to improve the sensitivity of on-chip absorption detection. As we have already noted, absorption spectroscopy is attractive because it is a universal, label-free detection technique, which does not require a complex experimental set-up. However, it suffers from poor sensitivity in short pathlength systems such as those found in microfluidic devices.

We distinguish between three cases of extended pathlength strategies for absorption measurements: single-pass techniques (Section 1.4.1); multi-reflection techniques (Section 1.4.2); and, multi-pass techniques (Section 1.4.3). These approaches are outlined in Figure 1.1. In the first case, single-pass techniques improve absorption sensitivity by increasing the physical length of the sample. In the second case, multi-reflection absorption techniques improve absorption sensitivity by reflecting the light through a sample several times, usually in a 'zig-zag' path. Multi-pass absorption techniques form a subset of multi-reflection techniques, in which light retraces the same path through the sample many times. Such methods are very promising for microfluidic detection systems as the sample pathlength is increased without requiring the sample volume to be increased.

A comparison of the various strategies will be made, focusing on the physical pathlength, required volume of sample and detection limit. Detection limits are most commonly reported in the literature either in g mL^{-1} or mol L^{-1}. In order to make comparison of the detection limits for different absorption techniques more straightforward, and independent of the identity of the absorbing sample, we also convert reported detection limits, where possible, into absorption per unit pathlength, $\kappa_{\min}$, where $\kappa_{\min} = C_{\min} \times \alpha$. When the absorption coefficient α_λ was reported in the cited paper, this value was used to perform the conversion, otherwise a value was sourced from other literature, care being taken to use the natural logarithm form of the Beer-Lambert law to define α_λ.

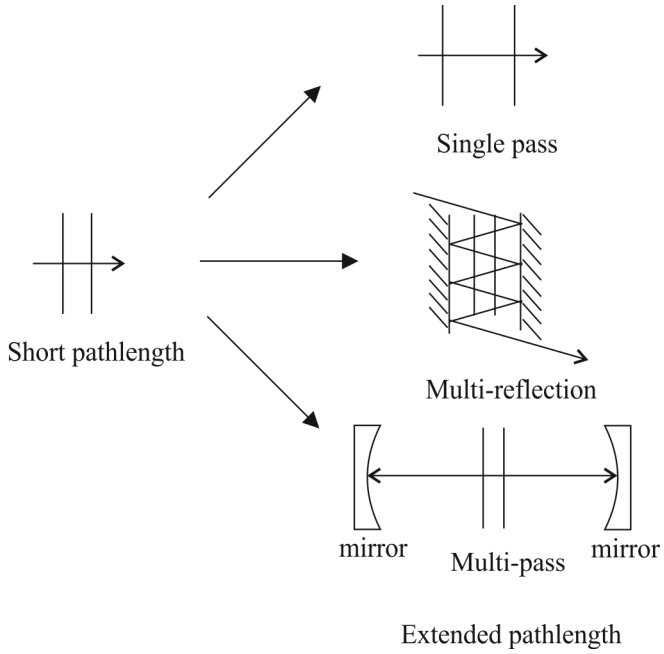


Figure 1.1: Methods of extending short pathlength analysis, including single-pass, multi-reflection and multi-pass techniques.

1.4.1 Single-pass techniques

The most straightforward way to improve absorption sensitivity in small volume analysis is to increase the pathlength of light through the sample, while attempting to keep the sample volume small. Generally, this means directing light across a sample along the direction of fluid flow, thereby increasing the interaction length between light and the sample without needing to increase the sample volume significantly. This approach was originally applied in capillary electrophoresis (CE) detection. For a description of CE see [108], and for a general review of detection methods used most commonly in CE see [47, 109]. In terms of absorption detection, U-shaped cells (Figure 1.2(a)), Z-shaped cells (Figure 1.2(b)), upside-down T-shaped cells (Figure 1.2(c)), and bubble cells (Figure 1.2(d)) have all been integrated for on-column detection.

The key experimental parameters associated with each approach are summarised in Table 1.1. Typically, single-pass absorption pathlengths are between 0.5 and 5 mm. It is important to minimise divergence of the light beam across the sample in order to ensure that as much light as possible is detected. In most cases this can be achieved simply by incorporating a lens into the beam path before the sample. For example, Moring et al. found that by extending the pathlength they improved their detection sensitivity by a factor of eight, which rose to a factor of 13 when a ball lens was used to focus the light onto the detector [110]. In their Z-shaped cell, Ro et al. added a microlens to the delivery optical fibre end to improve light collimation, and also reduced stray light by a factor of 10 by using a 50 μm by 27 μm slit in front of the detector [111].

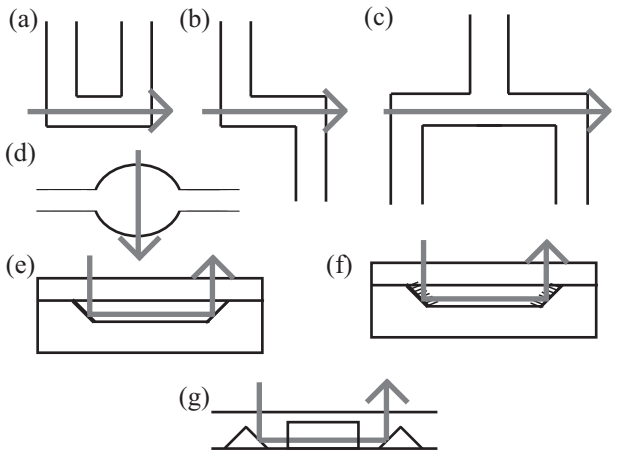


Figure 1.2: Methods of increasing the pathlength in single-pass absorption techniques. (a) U-shaped cell [112]. (b) Z-shaped cell [113]. (c) Upside-down T-shaped cell [114]. (d) Bubble cell [115]. (e) Reflection at uncoated 110 plane mirrors in silicon (45°) [116]. (f) Reflection at mirrored 45° plane in metal-coated silicon [116]. (g) Total internal reflection v-groove [117].

Sieben et al. achieved an impressive detection limit of 5.6×10^{-4} cm^{-1} by manufacturing a 25 mm long Z-shaped absorption cell in a microfluidic chip made from tinted polymethylmethacrylate (PMMA) [22]. The tinted PMMA was used to block stray light, which had not passed through the sample region, from reaching the detector and was found to improve the detection limits significantly compared with an absorption cell fabricated using untinted PMMA. This set-up was successfully applied to *in situ* nitrite analysis at Southampton Dockhead by Beaton et al. [24]. Floquet et al. also applied a similar set-up to the determination of iron(II) concentration and pH [23]. The detection limit for iron(II) was reported as 226 nM in clear PMMA, 33 nM in light grey PMMA and 21 nM in dark grey PMMA, with the absorption pathlengh fixed at 25 mm, demonstrating the improvement in sensitivity achievable by the rejection of stray light travelling in the channel walls [23]. Using an 80 mm pathlength absorption cell, an excellent absorption detection limit of 6.3×10^{-5} cm^{-1} was found at 435 nm, using 10 s signal averaging [23], demonstrated using a pH assay with thymol blue as an indicator (after [118]).

An alternative strategy is to direct light perpendicularly across the microfluidic channel. Xue et al. first suggested the bubble cell (Figure 1.2(d)), an expanded channel region, as a strategy for improving the sensitivity of on-column detection [115]. In a more recent publication, Alves-Segundo et al. used a bubble cell to improve the sensitivity of chromate (VI) detection via a colourimetric reaction [119].

Figures 1.2(e)-(g) show an alternative approach to extending the single-pass pathlength, which relies on reflecting light into and out of the sample region. Tiggelaar et al. investigated reflection at two uncoated silicon planes, and also two mirrored silicon planes, and found, as expected, that the improved signal levels in Figure 1.2(f) compared with Figure 1.2(e) led to a significant improvement in sensitivity, to a detection limit of only 2 nM indophenol blue (around 4×10^{-4} cm^{-1}) [116]. Steigert et al. took advantage of total internal reflection at two 45° grooves fabricated in a CD and used this "lab-on-a-disk" for centrifugal analysis

and point-of-care diagnostics, demonstrating the improvement in detection limit achievable using the long pathlength cell relative to perpendicular analysis through the 1 mm channel [120].

1.4.2 Multi-reflection techniques

Multi-reflection techniques increase the pathlength of the light through the sample by forcing the light to pass through the sample several times. In multi-reflection techniques, the light passes through a different region of the sample on each pass. This is in contrast to multi-pass techniques (Section 1.4.3), where light passes through exactly the same sample region on each pass.

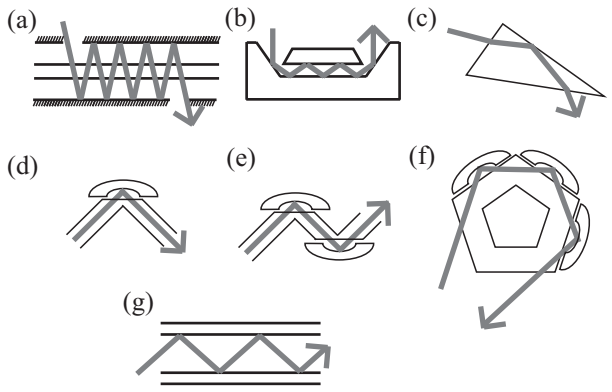


Figure 1.3: Methods of increasing the pathlength in single-pass, multi-reflection absorption techniques. (a) Mirror-coated capillary [124]. (b) Uncoated silicon flow cell [125]. (c) Single reflection at solution/chip wall [126]. (d) Single reflection at wall/air pocket [127]. (e) Dual reflection sites at wall/air pockets [127]. (f) Three reflection sites at cyclic array of wall/air pockets [127]. (g) Total internal reflection where solution has higher refractive index than wall (liquid waveguide) [128].

The first multi-reflection cell designed for small volume analysis is depicted in Figure 1.3(a). In this case, Wang et al. coated the outside of a glass capillary with a silver mirror, leaving gaps for light to be coupled into and out of the cell [124]. Salimi-Moosavi et al. used a similar design in a later publication, patterning aluminium mirrors above and below a flow channel with 30 μm in and out gaps positioned 200 μm apart.

Verpoorte et al. proposed a different design, shown in Figure 1.3(b), in which a multi-reflection flow cell was built in silicon [125]. Two 54.7° silicon faces allowed for light to be directed into the sample. Between these two faces, light reflects at 70.6° at the water/silicon boundary a maximum of five times. In principle, increasing the number of reflections increases the sample pathlength, and hence the sensitivity, but in reality this is offset by the increased losses leading to lower signal levels. The problem with both multi-reflection cells shown in Figure 1.3(a) and (b) is that the number of reflections is severely limited by the low reflectivity of the mirrors used, which causes the light intensity to decrease rapidly as the number of reflections is increased. For example, because of the low reflectivity of the water/silicon boundary, Verpoorte et al. only collected 0.15% of the light from the end of the uncoated cell after five

Table 1.1: A comparison of single-pass extended pathlength techniques, as shown in Figure 1.2. Where several analytes were measured, the stated detection limit corresponds to detection of the first listed analyte. λ is the wavelength of analysis in nm, l is the optical pathlength in mm, Vol. is the probed volume in nL, $C_{\min}$ is the minimum detectable concentration, which is also converted into κ, the absorption per unit pathlength, in cm^{-1} where α, the absorption coefficient of the analyte, is known. Where possible, concentration detection limits have been calculated from three standard deviations (3σ) of the reported baseline noise, but limits marked with * have been estimated using other reported data.
^{T} These analytes are not detected directly, but rather through a colourimetric reaction to form a strongly coloured product whose concentration is proportional to the concentration of the original analyte. Details of each reaction can be found in the respective references.

Reference	Fig.	Analyte	λ / nm	l / mm	Vol. / nL	$C_{\min}$ / μM	$\kappa_{\min}$ / cm^{-1}
Petersen et al. [112]	1.2(a)	Caffeine, Paracetamol, Ketaprofen, L-ascorbic acid	254	0.75	0.27	300*	4.5 [121]
Liang et al.	1.2(a)	Fluorescein	488	0.140	0.099	5.6	0.83
Chervet et al. [113]	1.2(b)	Nucleosides, Nucleotides, Peptides	254, 210	3.0	5.9	0.89*	-
Moring et al. [110]	1.2(b)	DMSO, Fluorescein, Uracil	200	3.0	13	0.030*	-
Mainka et al. [122]	1.2(b)	Formaldehyde,^{T} & other aldehydes	UV	3.0	5.9	0.17	-
Ro et al. [111]	1.2(b)	Fluorescein, New coccine	488	0.50	0.68	1.2*	4.6×10^{-2}
Sieben et al. [22]	1.2(b)	Nitrite,^{T} Scarlet food dye	525	25	2,250	0.014	5.6×10^{-4}
Kim et al. [114]	1.2(c)	Fluorescein isothiocyanate, Dansyl-amino acids	488	3.0	13	0.32	-
Xue et al. [115]	1.2(d)	Malachite green, Potassium permanganate	633	0.57	0.72	0.004*	-
Alves-Segundo et al. [119]	1.2(d)	Chromate (VI)^T	565	0.6	26,680	0.170	-
Tiggelaar et al. [116]	1.2(e)	Indigo carmine	592	6.0	700	-	-
Noda et al. [123]	1.2(e)	Amaranth, Haemoglobin	555	5.0	5000	3.3*	1.4×10^{-1}
Tiggelaar et al. [116]	1.2(f)	Indophenol blue	592	6.0	700	0.002*	-
Grumann et al. [117]	1.2(g)	Glucose^T	650	10	10,000	120*	1.1×10^{-2}
Steigert et al. [120]	1.2(g)	Haemoglobin^T	532	5.0	5000	45*	8.1×10^{-2}

Table 1.2: A comparison of multi-reflection techniques, as shown in Figure 1.3. Where several analytes were measured, the stated detection limit corresponds to detection of the first listed analyte. λ is the wavelength of analysis in nm, l is the optical pathlength in mm, Vol. is the probed volume in nL, $C_{\min}$ is the minimum detectable concentration, which is also converted into κ, the absorption per unit pathlength, in cm^{-1} where α, the absorption coefficient of the analyte, is known. Where possible, concentration detection limits have been calculated from three standard deviations (3σ) of the reported baseline noise, but limits marked with * have been estimated using other reported data.
^{T} These analytes are not detected directly, but rather through a colourimetric reaction to form a strongly coloured product whose concentration is proportional to the concentration of the original analyte. Details of each reaction can be found in the respective references.

Reference	Fig.	Analyte	λ / nm	l / mm	Vol. / nL	$C_{\min}$ / μM	$\kappa_{\min}$ / cm^{-1}
Wang et al. [124]	1.3(a)	Brilliant green	633	0.70	6.6	0.065*	5.3×10^{-3}
Salimi -Moosavi et al. [129]	1.3(a)	Bromothymol blue	633	0.20	0.14	3.4	2.5×10^{-1}
Ellis et al. [130]	1.3(a)	Reactive phosphorus	652	10	5,000	0.097*	-
Mishra et al. [131]	1.3(a)	Bromothymol blue	613	20	510	0.0044*	3.8×10^{-4}
Verpoorte et al. [125]	1.3(b)	Cibacron blue 3G	633	10	15	-	-
Llobera et al. [132]	1.3(c)	Fluorescein Methyl orange	460	3.58	1,777	2.3*	-
Llobera et al. [127]	1.3(d)	Fluorescein	460	2.77	790	1.8*	
Llobera et al. [127]	1.3(e)	Fluorescein	460	6.36	1,430	0.11*	5.4×10^{-3}
Llobera et al. et al. [127]	1.3(f)	Fluorescein	460	14.26	5,340	0.041*	1.4×10^{-3}
Duggan et al. [128]	1.3(g)	Crystal violet	590	5.0	350	0.54*	6.5×10^{-2}
Patey et al. [133]	1.3(g)	Nitrate^T, nitrite,^{T} Phosphate^T	540 710	20,000	4 mL	0.0015 0.8 nM	-
Pan et al. [134]	1.3(g)	Cholesterol, DNA	497 260/280	15	100	260	-

reflections [125]. The optimum number of passes is therefore a compromise between these the increased pathlength and the decreased signal levels. Tiggelaar et al. found that signal levels and hence sensitivity were actually improved by reducing the number of internal reflections through the sample, and thus Figure 1.2(f), in which light is reflected into the sample path, but does not undergo repeated reflection within the sample, was a preferable cell design to Figure 1.3(b) [116].

In 2005, Llobera et al. first presented a hollow Abbe prism structure, with light reflecting at the solution/ poly(dimethylsiloxane) (PDMS) wall in order to increase absorption pathlength, as shown in Figure 1.2(c) [126, 132]. This strategy had two problems: firstly, the reflection coefficient at the solution/PDMS wall was low (< 0.062), meaning that only a single reflection structure could be included, and that long integration

times were required in order to obtain a sufficient signal to noise ratio; and secondly, light diverges across the long pathlength between the input and output optical fibres, meaning that above a certain optical pathlength, a significant proportion of the transmitted light was not collected by the detector, further decreasing the sensitivity. Llobera et al. addressed both these concerns in their follow-up paper, where reflection was instead designed to occur at a boundary between PDMS and an air pocket or "air mirror", where total internal reflection occurs between the high refractive index PDMS ($n \approx 1.4$) and the air mirror ($n \approx 1.0$)) [127]. The air mirrors were curved, in order to direct the light beam through the fluid flow. Several different structures were designed, three of which are shown in Figure 1.2(d) - (f). The details of each structure are highlighted in Table 1.2. A summary of the work from this group can be found in [135]. While detection limits are good, the volume probed is still rather large, often microlitres or greater, and the structures themselves are relatively complicated.

A somewhat simpler approach to achieving long pathlength absorption sensing via total internal reflection of light along the liquid path is to use liquid core waveguides (LCWs). Liquid core waveguides have been the subject of several recent articles (see, for example [136–140]), and will be covered only briefly here, where they are applied to the problem of on-chip detection. A conventional glass capillary can act as a LCW if it is filled with a liquid which has an index of refraction above that of glass ($n \approx 1.5$). This is of course not the case for most common solvents, such as water ($n \approx 1.33$) and ethanol ($n \approx 1.36$). In this case, a capillary must either be fabricated from, or coated with, a low refractive index polymer, such as Teflon ($n \approx 1.3$). LCWs have the advantage that, in theory, the optical pathlength can be increased dramatically compared to single pass techniques, without decreasing the signal-to-noise ratio. In reality, there are a few problems associated with LCWs. The first is the somewhat problematic coupling of light and liquid into and out of the LCW. One of the common methods to achieve this is to use commercially available T-connectors, in which the fibre and flow channel are connected in line with each other, and the liquid is introduced at 90° through the third arm of the 'T'. T-connectors, however, can have a significant amount of dead volume at the join between the optical fibre, fluid inlet and LCW, which can reduce the sensitivity of the system significantly. Pan et al. have recently designed a coupler that allows light to be coupled in and out of a LCW without the need for a T-connector [134]. In their work, the LCW is bent at the start and end of a short length of capillary, in a similar manner to that shown in Figure 1.2(a). Light is coupled into the LCW at the first bend, propagates along the fluid-filled channel, and is coupled out at the second bend, where it can be detected. By separating liquid and fluid inlets, Pan et al. significantly simplified the set-up, and achieved a detection limit of 0.1 μg mL^{-1} DNA in a sample volume of only 0.1 μL.

The second problem of LCWs is that the presence of any bubbles or contaminants in the LCW will scatter the light travelling down the LCW, and prevent absorbance measurement. In order to circumvent these problems, LCWs can require periodic cleaning to maintain long-term performance [141]. In addition, as the micro-bubbles often stick to the LCW walls, in order to maintain reliability, there is a limit to the length of LCWs

that can be sensibly used.

For environmental analysis, LCWs several metres in length have been used to achieve nanomolar detection limits for several analytes (see for example [133]). However, the achieveable pathlength is often limited by the absorption of the solvent at the wavelength of interest. For example, Patey et al. note that wavelengths above 750 nm cannot be used for analysis of water samples in long-pathlength LCWs [133]. Nevertheless, LCWs remain an attractive and straightforward way to increase the pathlength of on-chip absorption measurements, and have even been used in *in situ* measurements (see for example [142]) owing to the simplicity of their set-up.

1.4.3 Multi-pass absorption techniques

The problem with all of the extended pathlength techniques discussed up to this point is that, while the interaction between the excitation light and the sample is increased, the sample volume itself is also increased, sometimes beyond dimensions commensurate with microfluidic systems. A more desirable solution is to increase the extent of the interaction between the light and the sample, without increasing the sample volume probed. This is possible by reflecting the light across the same region of sample many times, by trapping the light within an optical cavity. In this way, sensitivity can be improved without increasing the actual sample volume probed. These multi-pass absorption techniques are known as cavity enhanced absorption spectroscopies, and while they have so far been applied mainly to gas phase analysis [1], there is a growing body of researchers looking at applying these techniques to the problem of small volume liquid analysis [143]. The interrogation of small volume liquid samples, ranging from microlitres to nanolitres, with cavity enhanced absorption spectroscopies is the subject of this thesis.

1.5 Thesis outline

In Chapter 2, we provide a derivation of the key equations to be used throughout this thesis, as well as covering the theory of cavity enhanced absorption spectroscopies in detail. In Chapter 3, we characterise various flow cells and microfluidic chips in a two-mirror CRDS set-up. The optimised set-up is then applied to the sensing of trace analytes in water samples in Chapter 4. Chapter 5 presents a broadband set-up, which is applied to reaction analysis in Chapter 6 and pH analysis in Chapter 7. A new type of cavity, based on a loop of optical fibre, is presented in Chapter 8 and Chapter 9. Finally, we finish with some concluding remarks in Chapter 10, with a discussion of future work arising from this thesis.

Chapter 2

Theory

In this Chapter, we describe the theoretical basis of two key cavity enhanced absorption spectroscopy experiments, beginning with the cornerstone of absorption spectroscopy, the Beer-Lambert law. The equations derived in this Chapter underpin the experimental work carried out in the remainder of this thesis, and key equations will be reproduced at the appropriate point later in the thesis, where helpful.

2.1 Absorption spectroscopy

Absorption spectroscopy is a standard analytical technique. It relies on the interaction of light (electromagnetic radiation) with a sample (atoms or molecules), which causes the light to be either scattered or absorbed. Absorption only occurs when the photon energy matches that of an atomic or a molecular transition. The type of energy levels involved in these transitions depends on the wavelength (λ) of light being absorbed: electronic transitions can be induced by ultraviolet and visible light sources ($\lambda < 700$ nm), vibrational transitions can be induced by infrared light ($\lambda < 0.1$ mm), and rotational transitions can be induced by microwave radiation ($\lambda < 1$ cm) [144].

The frequency ν of the transition is defined by Planck's law [145]:

$$\nu_{10} = \frac{E_1 - E_0}{h} \tag{2.1}$$

where E_1 and E_0 are the energies of the upper and lower levels respectively, and $h = 6.626 \times 10^{-34}$ J s is Planck's constant. The frequency is related to the wavelength by $c = \nu\lambda$, where c is the speed of light.

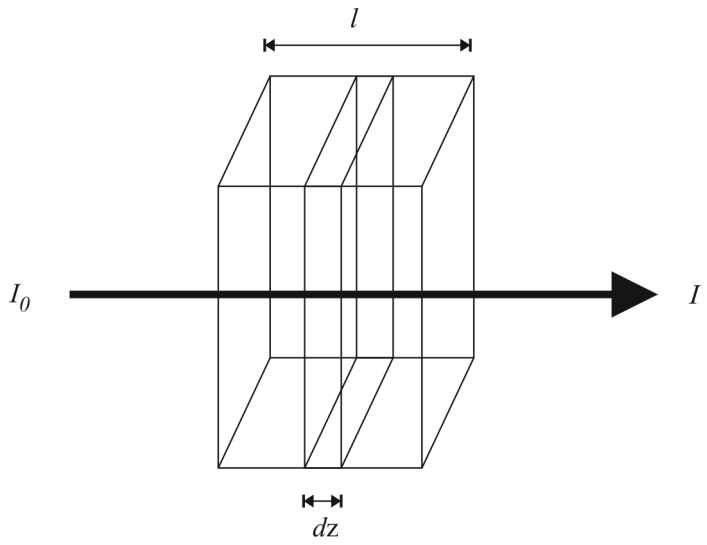


Figure 2.1: Schematic of single-pass absorption spectroscopy. I_0 is the intial light intensity, I is the transmitted light intensity, dz is a layer of infinitesimal thickness and l is the total sample pathlength.

The Beer-Lambert law describes the attenuation in intensity of radiation propagating through a sample (Figure 2.1). It was first described by Bouguer in 1729 [146] and was later revised by Lambert and Beer [147, 148].

In a conventional UV/vis spectrometer, a light beam with intensity I_0 passes through a cuvette with an optical pathlength l, and the transmitted light intensity I is measured. The decrease in intensity arises from absorption, reflection and scattering losses through the cuvette and the sample. In order to eliminate the reflection and scattering losses associated with the sample, as well as the cuvette losses, thereby allowing the sample absorption losses to be isolated, most spectrometers use a dual-beam configuration. I_0 and I are measured simultaneously by passing the reference beam I_0 through a cuvette filled with the sample solvent, without the absorbing sample, while passing the sample beam I through an identical cuvette filled with the sample solution. The ratio of the two beam intensities can then be measured, and the difference in intensity dI can be assumed to arise solely from sample absorption losses. In single-beam configurations, I_0 and I can be measured by alternating a measurement of the solvent absorption (also referred to as the 'blank') with an absorption measurement of the solution of interest.

First let us consider the absorption through a infinitesimally thin layer dz. This absorption arises from the number of molecules present in the beam area n, which can be calculated from the number density of sample molecules N (molecules cm^{-3}), the beam cross-sectional area S (cm^2) and the thickness dz (cm) as $n = NSdz$.

If the absorption cross-section of each molecule is σ, then the fraction of light absorbed by one molecule is $\frac{\sigma}{S}$. The total fraction of light absorbed by all molecules in the illuminated area is simply the product of the number of illuminated molecules and the fraction of light absorbed per molecule $(NSdz) \times (\frac{\sigma}{S}) = \sigma \mathrm{N dz}$.

The transmitted light intensity through the slab is $I_z - dI$, where I_z is the light intensity entering the slab. Thus, the fraction absorbed can be written as

$$\frac{dI}{I_z} = -\sigma N dz. \tag{2.2}$$

For a layer of thickness l, the total decrease in light intensity is obtained by integrating Equation 2.2 over z between the limits $z = 0$ and $z = l$ which leads to

$$\ln \frac{I}{I_0} = -\sigma N l. \tag{2.3}$$

where we have applied the boundary condition that at $l = 0$, $I = I_0$.

For liquid samples, σN is usually rewritten as αC, where α is the absorption coefficient, in units of dm^3 mol^{-1} cm^{-1}, and C is the molar concentration. Thus, the Beer-Lambert law can be rearranged and expressed in its common form for liquid analysis:

$$I = I_0 e^{-\alpha C l} \tag{2.4}$$

The Beer-Lambert law is also often expressed using the decadic logarithm $\log_{10}$ rather than the natural logarithm $\ln$. In this case, the absorption coefficient is replaced by $\epsilon = \frac{\alpha}{2.303}$ and the Beer-Lambert law is written:

$$I = I_0 10^{-\epsilon C l} = I_0 10^{(-\alpha/2.303) C l} \tag{2.5}$$

Throughout this thesis, we use α values rather than ϵ values, and care is taken to convert literature values of ϵ into α where necessary, for comparison with our data. In addition, conventional UV/vis spectrometers usually output dimensionless values of absorbance, defined as $A = -\log \frac{I}{I_0} = \epsilon C l$, and special care must be taken to convert these A values into their natural log equivalent, $A = -\ln \frac{I}{I_0} = \alpha C l$. The Beer-Lambert law can also be expressed in terms of absorption per unit pathlength, $\kappa = \frac{A}{l} = \alpha C$, usually in units of cm^{-1}.

Close to the detection limit, where the absorption loss is small, $-\ln \frac{I}{I_0} \approx 1 - \frac{I}{I_0}$, and the minimum detectable absorption per unit pathlength, $\kappa_{\min}$, can therefore be defined as:

$$\kappa_{\min} = \frac{1}{l}\left(1 - \frac{I_{\min}}{I_0}\right) = \frac{1}{l}\left(\frac{\Delta I_{\min}}{I_0}\right) \tag{2.6}$$

where $I_{\min}$ is the minimum detectable intensity smaller than I_0 and $\Delta I_{\min}$ is the minimum change in I that can be detected, typically defined as three times the standard deviation 3σ in repeated measurements of I_0.

In this thesis, we are concerned solely with visible absorption spectroscopy. Transitions in the visible part of the spectrum (from 400 to 750 nm) typically arise from electronic excitations, involving the outer electrons of an atom or molecule. In organic molecules, visible absorption arises in functional groups containing valence electrons with relatively low excitation energy. These electronic transitions can have $n\pi*$ character, if the molecule contains atoms with lone pairs of electrons (for example, oxygen or nitrogen atoms) or $\pi\pi*$ character, if the molecule contains unsaturated groups (for example, a benzene ring). Typically, $\pi\pi*$ transitions are more intense than $n\pi*$ transitions. In inorganic molecules, visible absorption often arises from charge transfer transitions [149].

It should be noted that as we are concerned with liquid-phase absorptions, the absorption bands tend to be broad (ca. 100 nm). When a molecule is dissolved in a liquid, the disorder inherent in the structure of the liquid provides numerous different solvent environments for the solute, each of which perturbs the molecular energy levels in a slightly different way. Each molecule therefore exhibits a slightly different absorption spectrum, and the measured absorption spectrum is composed of all the different spectra for each molecular environment. The lineshape is described as being inhomogeneously broadened [150].

2.2 Cavity ringdown spectroscopy

Cavity ringdown spectroscopy (CRDS) was initially developed by Anderson et al. [151] as a method for characterising the reflectivity of highly reflective mirrors [1]. Light trapped between two highly reflective mirrors decays in an exponential manner, as a constant fraction is lost on each pass through the cavity. This exponential decay is characterised by the decay time constant for the cavity (its 'ringdown time'), which is dependent on the cavity length and the mirror reflectivity. O'Keefe and Deacon were the first to realise that if an absorbing species is introduced into a cavity, this introduces an additional loss. The resulting reduction in ringdown time allows the loss to be measured very accurately, allowing highly sensitive spectroscopic absorption measurements to be made [152]. A gaseous sample can be introduced to fill the entire space between two highly reflective mirrors. With mirrors 99.9% reflective, and a 1 m cavity, ringdown times of > 3 μs can be achieved, corresponding to absorption pathlengths of around 1 km from a physical pathlength of 1 m. This vast increase in pathlength, without an increase of the sample volume probed, is one reason why CRDS is such a sensitive multi-pass technique.

The two methods employed for the work presented in this thesis are: cavity ringdown spectroscopy (CRDS) [152] and cavity enhanced absorption spectroscopy (CEAS) [153]. CRDS and CEAS techniques have been the subject of several excellent reviews, and we highlight a few for further interest [1, 143, 154–159].

The principle underlying both techniques is the trapping of light in an optical cavity, as depicted in Figure 2.2. The difference lies primarily in the method of output detection: while the intensity coupled out from the cavity is time-resolved in CRDS measurements, the intensity measurements in CEAS are time-integrated. CRDS will be discussed first, as the chronological precursor to CEAS, although it should be emphasised that both CRDS and CEAS are currently in widespread use.

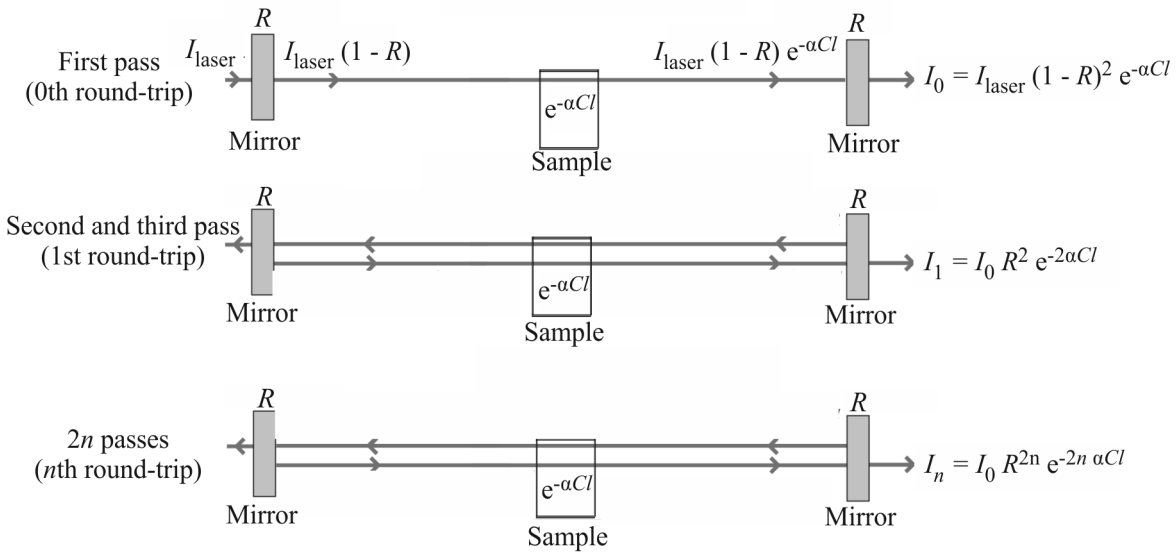


Figure 2.2: A schematic diagram showing the decrease in intensity as a light pulse travels in a cavity.

If the laser pulse duration is shorter than the round-trip time of the cavity then the cavity output signal will consist of a pulse train with decaying intensity, as a result of the imperfect reflections at each mirror. If we define the reflectivity of the mirrors as R then the transmission through the mirrors on each reflection is $T = 1 - R$.[1] If a cavity of length d is excited by a laser pulse with intensity I_{laser}, then the light will decay as it encounters the mirrors and is absorbed by any sample present. Light is reduced in intensity by a factor R on each reflection from a mirror, $1 - R$ on transmission through a mirror, and a factor $e^{-\alpha Cl}$ on each pass through the sample. Thus, after the first pass through the cavity the light emerging from the second mirror will have an intensity I_0 given by [157]:

$$I_0 = I_{\text{laser}} (1 - R)^2 e^{-\alpha Cl} \tag{2.7}$$

After the second pass (the first round-trip) through the cavity, the intensity will be decreased further by reflection at each mirror, and any absorption in the cavity medium:

[1] Since different mirrors are never of exactly equal reflectivity, R is actually the geometric average, $R = \sqrt{R_1 R_2}$, of the reflectivities of the two mirrors.

$$I_1 = I_0 R^2 e^{-2\alpha C l} \tag{2.8}$$

Thus, after n round-trips in the cavity, the intensity of the measured pulse peak will be:

$$I_n = I_0 R^{2n} e^{-2n\alpha C l} \tag{2.9}$$

Using the fact that $R^{2n} = e^{2n \ln R}$, this can be rewritten

$$I_n = I_0 e^{-2n(-\ln R + \alpha C l)} \tag{2.10}$$

As will be seen, in many of our experiments, we record a series of discrete pulses with intensities I_n as above. It is worth, however, also continuing this analysis in the case when the discrete round-trip number n is replaced with the continuous variable of time, $t = \frac{2dn}{c}$, where c is the speed of light in the cavity medium. Substituting for n in Equation 2.10 leads to

$$I(t) = I_0 e^{-\frac{tc}{d}(-\ln R + \alpha C l)} \tag{2.11}$$

The $1/e$ decay time, known as the ringdown time τ, is defined as the time taken for the light to decay to $1/e$ of its initial intensity. In other words,

$$I(t) = I_0 e^{-\frac{t}{\tau}} \tag{2.12}$$

Comparing Equation 2.11 and Equation 2.12 we can see that the exponential decay constant, or 'ringdown time', for the cavity is given by

$$\tau = \frac{d}{c(-\ln R + \alpha C l)} \tag{2.13}$$

In low loss systems $\ln R \approx -(1 - R)$ and thus Equation 2.12 can be further simplified into the form

$$\tau = \frac{d}{c(1 - R + \alpha C l)} \tag{2.14}$$

Recording ringdown traces in the absence (τ_0) and presence of an absorber (τ) allows $\kappa = \alpha C$, the absorption per unit pathlength, to be determined:

$$\kappa = \frac{d}{cl}(\frac{1}{\tau} - \frac{1}{\tau_0}) \tag{2.15}$$

2.2.1 Detection sensitivity in CRDS

To estimate the detection limit based on the signal-to-noise ratio of the baseline ringdown signal, we rewrite Equation 2.15 as

$$\kappa = \frac{d}{cl}(\frac{\tau_0 - \tau}{\tau\tau_0}) \tag{2.16}$$

At the detection limit, corresponding to the minimum detectable change in ringdown, we have $\tau_0 - \tau = \Delta\tau_{\min}$ and $\tau\tau_0 \approx \tau_0^2$, giving

$$\kappa_{\min} = \frac{d\Delta\tau_{\min}}{cl\tau_0^2} \tag{2.17}$$

In the present work, we define $\Delta\tau_{\min}$ to be three times the standard deviation in repeated measurements of the baseline ringdown time τ_0.

For comparison with single-pass experiments, it can also be helpful to define the number of passes of light through the sample in one unit ringdown time, N_τ given by:

$$N_\tau = \frac{\tau_0 c}{d} \tag{2.18}$$

From N_τ, the absorption pathlength traversed in one ringdown time, $l_\tau = N_\tau \times l$, can also be calculated. In reality, it is common to acquire signal over three to five ringdown times and thus the total number of passes recorded will be several times larger than N_τ. N_τ is related to the cavity finesse, which provides a description of the quality of the cavity. N_τ is inversely proportional to $1 - R$, and the cavity finesse is given by $F = \frac{\pi\sqrt{R}}{1-R}$ [157].

2.3 Cavity enhanced absorption spectroscopy

A related technique, with a simpler experimental set-up, is cavity enhanced absorption spectroscopy (CEAS), also known as integrated cavity output spectroscopy (ICOS). In CEAS, the cavity is excited continously, and the total, time-integrated light intensity (output) transmitted through the cavity is measured [157]. For an incident light intensity I_{laser}, the total output intensity is a superposition of all intensities coupled out of

the cavity after an odd number of passes [160]. This is depicted in Figure 2.2. The output intensity can be calculated as the exact sum of the following geometric series [157]:

$$I_{\text{out}} = I_{\text{laser}}(1-R)^2 e^{-\alpha C l} \sum_{n=0}^{\infty} R^{2n} e^{-2n\alpha C l} \tag{2.19}$$

This summation can be rewritten as $\sum \left(R^2 e^{-2\alpha C l}\right)^n$, and since $R^2 e^{-2\alpha C l} < 1$, this converges to $1/(1-R^2 e^{-2\alpha C l})$. Substituting this result back into Equation 2.19 gives:

$$I_{\text{out}} = I_{\text{laser}} \frac{(1-R)^2 e^{-\alpha C l}}{(1-R^2 e^{-2\alpha C l})} \tag{2.20}$$

If I_{out} is measured in the absence of an absorber (yielding intensity I^0_{out}) then Equation 2.20 can be simplified:

$$\begin{aligned} I^0_{\text{out}} &= I_{\text{laser}} \frac{(1-R)^2}{(1-R^2)} \\ &= I_{\text{laser}} \frac{(1-R)}{(1+R)} \end{aligned} \tag{2.21}$$

Thus, measuring the intensity without (I^0_{out}) and with an absorber (I_{out}) present allows for the measurement of αC:

$$\begin{aligned} \frac{I^0_{\text{out}}}{I_{\text{out}}} &= \frac{I_{\text{laser}}(1-R)(1-R^2 e^{-2\alpha C l})}{I_{\text{laser}}(1+R)(1-R)^2(e^{-\alpha C l})} \\ &= \frac{(1-R^2 e^{-2\alpha C l})}{(1-R^2)e^{-\alpha C l}} \end{aligned} \tag{2.22}$$

To find the Beer-Lambert law absorption term $A = \alpha C l$, Equation 2.22 can be rearranged to give:

$$R^2 (e^{-\alpha C l})^2 + (1-R^2)\frac{I^0_{\text{out}}}{I_{\text{out}}} e^{-\alpha C l} - 1 = 0 \tag{2.23}$$

which can be solved for $e^{-\alpha C l}$ using the quadratic formula:

$$e^{-\alpha C l} = \frac{1}{2R^2} \left(\frac{I^0_{\text{out}}}{I_{\text{out}}}(R^2-1) \pm \sqrt{(\frac{I^0_{\text{out}}}{I_{\text{out}}}(R^2-1))^2 + 4R^2} \right) \tag{2.24}$$

The absorption per unit pathlength κ can then be written:

$$\kappa = -\frac{1}{l}\ln\left[\frac{1}{2R^2}\left(\frac{I^0_{\text{out}}}{I_{\text{out}}}(R^2-1)+\sqrt{(\frac{I^0_{\text{out}}}{I_{\text{out}}}(R^2-1))^2+4R^2}\right)\right] \tag{2.25}$$

Equation 2.25 allows for the measurement of both weak and strong absorptions, as no assumptions have been made in its derivation. More commonly, when the absorption losses are small ($e^{-\alpha Cl} \rightarrow 1$), and the reflectivity of the cavity mirrors is high ($R \rightarrow 1$), Equation 2.25 can be approximated as [160]:

$$\kappa \approx \frac{1}{l}(\frac{I^0_{\text{out}}}{I_{\text{out}}}-1)(1-R) \tag{2.26}$$

Equation 2.26 is commonly used to analyse CEAS data. If we plot κ versus I_0/I as predicted by Equation 2.25 and Equation 2.26, then we can assess the conditions under which use of the approximate form is valid. These plots are shown in Figure 2.3 for $R = 99\%$ and $l = 0.1$ cm. Using the Beer-Lambert law (Equation 2.4), κ can also be used to determine the percentage loss per pass. The dotted line marked on Figure 2.3 indicates 25% loss per pass, which corresponds to the point at which the two plots start to diverge. In other words, we can use Equation 2.26 as a good approximation for Equation 2.24, provided the losses do not exceed $\sim 25\%$ per pass. At these significant losses per pass, the experiment could most likely be conducted in a single-pass set-up anyway, so Equation 2.26 can safely be used for the majority of cavity experiments.

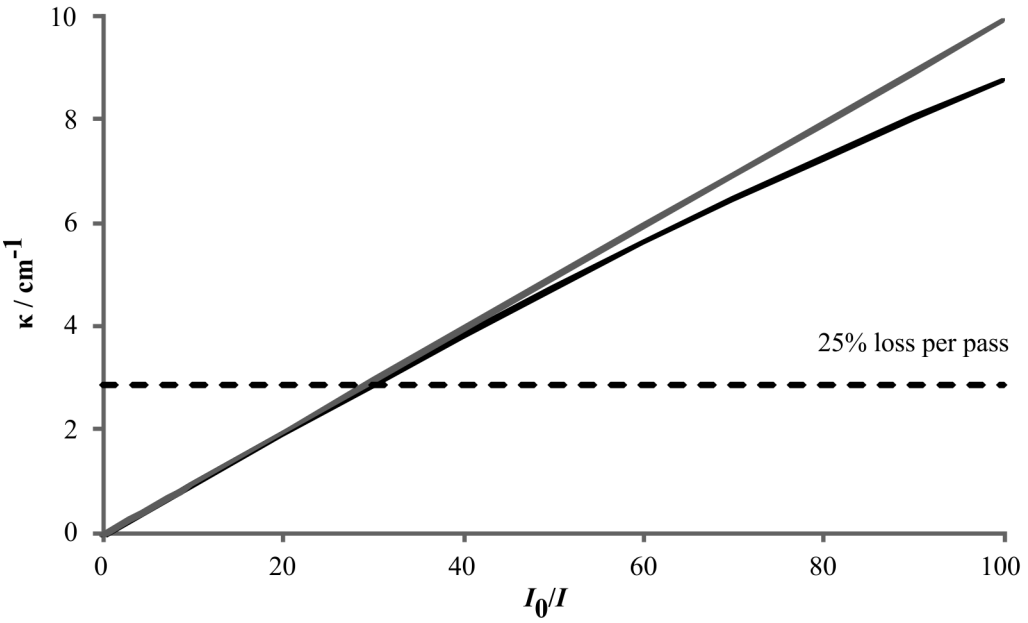


Figure 2.3: Plot of absorption per unit pathlength κ as a function of I_0/I for an optical cavity composed of two 99% reflectivity mirrors, with a sample pathlength of 0.1 cm. The grey line is a plot of Equation 2.26, while the black line is a plot of Equation 2.25. The dotted line marks the point at which the two plots start to diverge noticeably, at around 25% loss per pass.

2.3.1 Detection sensitivity in CEAS

Given Equation 2.26, the sensitivity of CEAS can be defined, approximating $\frac{I^0_{\text{out}}-I_{\text{min}}}{I_{\text{min}}} \approx \frac{I^0_{\text{out}}-I_{\text{min}}}{I^0_{\text{out}}}$:

$$\kappa_{\text{min}} = \frac{1}{l}\left(\frac{\Delta I_{\text{min}}}{I^0_{\text{out}}}\right)(1-R) \tag{2.27}$$

where I_{min} is the minimum detectable intensity smaller than I^0_{out}, and $I^0_{\text{out}} - I_{\text{min}} = \Delta I_{\text{min}}$ is the minimum change in I that can be detected, typically defined as three times the standard deviation 3σ in repeated measurements of I_0. Equation 2.27 can be compared to Equation 2.6, which defines κ_{min} for a single-pass absorption measurement, revealing that CEAS is a factor of $(1-R)^{-1}$ more sensitive than a conventional single-pass measurement. This factor $(1-R)^{-1}$ is referred to the cavity enhancement factor (CEF), and corresponds to the ratio of the measured absorbance to that for a single pass. For example, if 99% mirrors are used, then the sensitivity will be 100 times enhanced compared to a single-pass experiment.

Unlike CRDS (Equation 2.15), the absorption measured in CEAS is dependent on the initial light intensity (Equation 2.26). This has several important consequences. Firstly, in order to determine absolute absorption values, either a calibration must be carried out, or the mirror reflectivities must be known over the entire wavelength range of the cavity output. Secondly, a bright light source is required in order to achieve a large signal-to-noise ratio at the detector. This means that at some point, increasing the mirror reflectivity will not improve the sensitivity, once the signal levels become the limiting factor. Finally, CEAS measurements are dependent on the fluctuations in the light source used, and thus if there are significant fluctuations in the light source intensity, this will manifest as a lower sensitivity for CEAS measurements relative to CRDS. Nevertheless, CEAS has been shown to be at least as sensitive as CRDS in many cases [1]. In addition, CEAS has advantages over CRDS, including a simpler experimental set-up and simpler data analysis. Thus, the major disadvantage of CEAS tends to be the requirement for calibration of the mirror reflectivity at each wavelength. The analysis of CEAS results, including cavity calibration, will be discussed in more detail in Chapter 5.

2.4 Cavity stability

An additional constraint on the cavity is its optical stability, which must be maintained over the course of a cavity enhanced absorption experiment, typically over several microseconds. When designing a cavity, there are requirements regarding its length and the curvature of the concave mirrors used to form the cavity.

A stable cavity is formed when a beam of light reflecting backwards and forwards in a cavity reproduces itself on each round-trip. The beam can be described at some point z in the propagation direction in terms of its

width and the curvature of its wavefronts. Both properties are usually written in terms of a complex quantity ζ, the complex beam parameter [161]:

$$\frac{1}{\zeta(z)} = \frac{1}{R(z)} - \frac{i\lambda}{\pi\omega^2} \tag{2.28}$$

where R is the radius of curvature of the wavefront, ω is the beam width and λ is the wavelength of light.

A beam propagating through an optical system is described using ray transfer matrix analysis [161]. This means that the change in ζ during propagation through the optical system is described by a transformation matrix, which is written as:

$$\begin{pmatrix} \zeta_2 \\ 1 \end{pmatrix} = \begin{pmatrix} A & B \\ C & B \end{pmatrix} \begin{pmatrix} \zeta_1 \\ 1 \end{pmatrix} \tag{2.29}$$

where ζ_1 is the complex beam parameter entering the optical system and ζ_2 is the complex beam parameter after the transformation applied by the optical system. The ray transfer matrices for many optical elements, and combinations of optical elements, are well-established and available in the literature [161]. For example, the ray matrix for travelling through empty space (i.e. the cavity) of length d is given by [161]:

$$\begin{pmatrix} 1 & d \\ 0 & 1 \end{pmatrix} \tag{2.30}$$

and the matrix for for light travelling through a thin lens of focal length f, or undergoing reflection at a mirror with radius of curvature R (which is positive for a concave mirror), is [161]:

$$\begin{pmatrix} 1 & 0 \\ -\frac{1}{f} & 1 \end{pmatrix} = \begin{pmatrix} 1 & 0 \\ -\frac{2}{R} & 1 \end{pmatrix} \tag{2.31}$$

It will be seen that it is convenient to rewrite R in terms of the stability parameter of the mirror g, where $g = 1 - \frac{d}{R}$. Thus, the matrix for reflection at a concave mirror becomes:

$$\begin{pmatrix} 1 & 0 \\ \frac{2g-2}{d} & 1 \end{pmatrix} \tag{2.32}$$

Light travelling in a cavity can be described using ray transfer matrices as follows. An optical cavity will support a wave when the wave is superimposed on every round-trip through the cavity (in terms of wavefront,

curvature, beam size and phase). In other words, a standing wave is formed within the cavity. If the ABCD matrix represents the transformation from one position in the cavity to the same position after a round-trip, it must be true that $\zeta_2 = \zeta_1$. In this case, the ABCD matrix describes the reflection of the beam at one mirror (with radius of curvature R_1), propagation through the cavity of length d to the second mirror, reflection at the second mirror (radius of curvature R_2) and propagation back through the cavity of length d to reach the first mirror again.

The resulting matrix after one round trip in the cavity is found by multiplying the matrices of the constituent mirrors with the stability parameters g_1 and g_2 and the matrices of propagation in space:

$$\begin{aligned}\begin{pmatrix} A & B \\ C & D \end{pmatrix} &= \begin{pmatrix} 1 & d \\ 0 & 1 \end{pmatrix} \begin{pmatrix} 1 & 0 \\ \frac{2g_2-2}{d} & 1 \end{pmatrix} \begin{pmatrix} 1 & d \\ 0 & 1 \end{pmatrix} \begin{pmatrix} 1 & 0 \\ \frac{2g_1-2}{d} & 1 \end{pmatrix} \\ &= \begin{pmatrix} 4g_2g_1 - 2g_2 - 1 & 2g_2d \\ \frac{4g_1g_2-2g_2-2g_1}{d} & 2g_2 - 1 \end{pmatrix}\end{aligned} \tag{2.33}$$

We can rearrange Matrix 2.29, given that $\zeta_1 = \zeta_2 = \zeta$, to:

$$\frac{1}{\zeta} = \frac{C + D\frac{1}{\zeta}}{A + B\frac{1}{\zeta}} \tag{2.34}$$

and substitute Matrix 2.33 into Equation 2.34, to obtain

$$\frac{1}{\zeta} = \frac{\frac{4g_1g_2-2g_2-2g_1}{d} + (2g_2 - 1)\frac{1}{\zeta}}{4g_2g_1 - 2g_2 - 1 + (2g_2d)\frac{1}{\zeta}} \tag{2.35}$$

If we solve for $\frac{1}{\zeta}$ using the quadratic formula, we know that the discriminant must be negative for ζ to be a complex number, which is required in order for the beam width ω to have a finite value (see Equation 2.28). Thus, given

$$B\left(\frac{1}{\zeta}\right)^2 + (A - D)\frac{1}{\zeta} - C = 0 \tag{2.36}$$

the discriminant can be written as

$$(A - D)^2 + 4BC < 0 \tag{2.37}$$

which simplifies to

$$g_1^2 g_2^2 - g_1 g_2 < 0 \tag{2.38}$$

This leads to the requisite condition that

$$0 < g_1 g_2 < 1 \tag{2.39}$$

In other words, for a stable cavity, the product of the stability parameters of the two constituent mirrors of the cavity should be between 0 and 1. For a symmetrical cavity, as used throughout this thesis, with two concave mirrors with equal radius of curvature R, this means that

$$0 < \left(1 - \frac{d}{R}\right)^2 < 1 \tag{2.40}$$

and thus

$$0 < d < R \quad \text{or} \quad \mathrm{R < d < 2R} \tag{2.41}$$

For a stable cavity, the inequality 2.41 means that the cavity length can either be between 0 and R or between R and $2R$.

2.5 Cavity mode properties

Our description of CRDS and CEAS so far has treated the light travelling in the cavity as a 'photon bullet' [155]. While this is generally a good enough approximation for cavities using pulsed laser sources (as we shall see), we now extend our consideration to include the more rigorous treatment of light in terms of cavity modes. More detail can be found in Siegman's textbook on Lasers [145]. A cavity mode exists when the amplitude of an electromagnetic wave reproduces itself exactly on each round-trip of the cavity, and when the electromagnetic wave experiences a phase shift which is an integer multiple of 2π. This can only occur for certain optical frequencies. Cavity modes are described by three indices, the transverse mode indices n and m, and an axial (or longitudinal) mode number q, typically written TEM_{nmq}. Modes with $n = m = 0$ are called axial or longitudinal modes, and all other modes are called higher-order transverse modes. Thus, the longitudinal modes differ only in frequency (or wavelength) whereas the transverse modes can differ in both frequency and spatial profile.

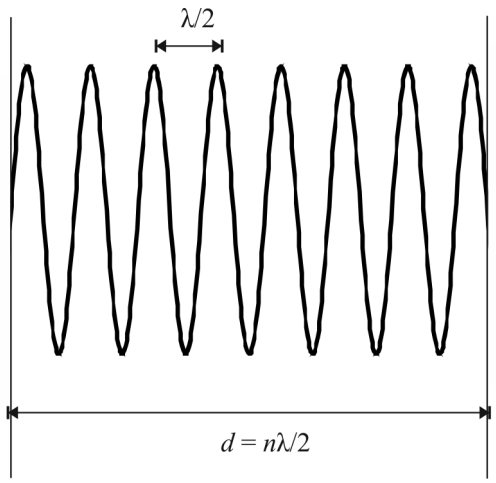


Figure 2.4: Schematic of the axial-mode resonance condition required to produce a standing-wave between two mirrors. Sine wave plotted as amplitude along the cavity length.

Figure 2.4 demonstrates pictorially the requirement for forming a standing-wave in a cavity. For a linear cavity, the phase condition is met at a set of discrete and equally-spaced axial-mode frequencies given by:

$$\nu = q \times \frac{c}{2d} \tag{2.42}$$

where q is an integer, the axial mode number defined previously, c is the speed of light and d is the cavity length, as before. The axial modes therefore occur at the resonant frequencies where there are exactly q half-wavelengths along the cavity axis between the laser mirrors (Figure 2.4): $q = \frac{2d}{\lambda}$. A typical cavity length ranges from a few tens of centimetres to a few metres, $d >> \lambda$, and thus q is typically large. For example, for light with a wavelength of 500 nm travelling in a 1 m long cavity, $q = 4 \times 10^6$.

The axial cavity modes are therefore equally spaced in frequency, with an axial mode separation, $\Delta\nu$, also defined as the free spectral range (FSR) of the cavity, given by:

$$\Delta\nu = \frac{c}{2d} \tag{2.43}$$

A 1-m long cavity has a FSR of 150 MHz, which is much smaller than the bandwidths of most pulsed lasers, such as those used in our experiments. This is shown in Figure 2.5. As our laser source has a bandwidth that may overlap many cavity modes, mode-matching the light to the cavity is not a requirement. In contrast, we note that for single-mode diode lasers, tuning the laser into resonance with a cavity mode is a key consideration [157].

In order to describe the transverse modes, it is necessary to take the wave nature of light into account. The following description is abbreviated from that provided by Kogelnik and Li [161].

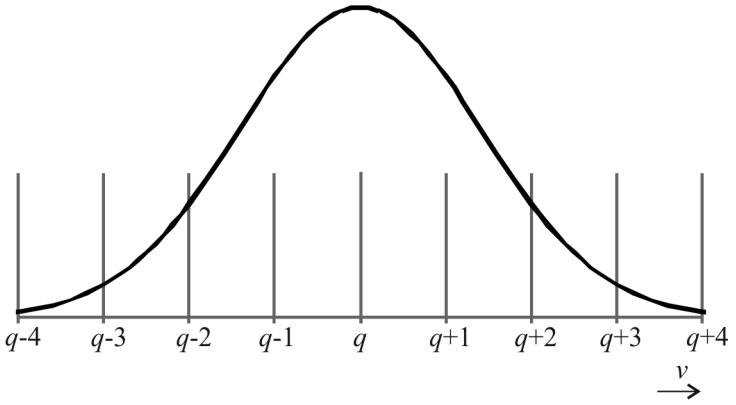


Figure 2.5: Excitation of multiple axial-mode frequencies using a pulsed laser

A field component u is described by the Helmholtz equation:

$$\nabla^2 u + k^2 u = 0 \tag{2.44}$$

where $k = \frac{2\pi}{\lambda}$ is the propagation constant or wave vector. For light travelling in the z-direction,

$$u = \Psi(x, y, z) \exp(-ikz) \tag{2.45}$$

where Ψ is a complex function which represents the differences between the laser beam and a plane wave, including a nonuniform intensity distribution, beam expansion over distance z and curvature of the phase front. If we insert Equation 2.45 into Equation 2.44, neglecting the second derivative with respect to z (which is assumed to be slow enough that $\partial^2\Psi/\partial z^2 \approx 0$), then

$$\frac{\partial^2 \Psi}{\partial x^2} + \frac{\partial^2 \Psi}{\partial y^2} - 2ik\frac{\partial \Psi}{\partial z} = 0 \tag{2.46}$$

A solution of Equation 2.46 is

$$\Psi = \exp\left\{-i\left(P(z) + \frac{k}{2\zeta(z)}(x^2 + y^2)\right)\right\} \tag{2.47}$$

where $P(z)$ represents a complex phase shift and $\zeta(z)$ is the complex beam parameter (defined previously in Equation 2.28), which describes both the Gaussian variation in beam intensity perpendicular to the optical axis and the curvature of the phase front. If this expression for Ψ is inserted into Equation 2.46, then we find that $\frac{d\zeta(z)}{dz} = 1$ and $\frac{dP(z)}{dz} = -\frac{i}{\zeta(z)}$. Integrating the first of these two differential equation results in:

$$\zeta_2 = \zeta_1 + z \tag{2.48}$$

where ζ_1 is the complex beam parameter entering the optical system and ζ_2 is the complex beam parameter exiting the optical system, where ζ was defined previously in Equation 2.28. It can be shown by inserting Equation 2.28 into Equation 2.47 that the parameters $R(z)$ and $\omega(z)$ are the radius of curvature at the z-axis and the beam radius respectively. The beam radius is defined as the radial distance from the beam axis at which the intensity has decreased by $1/e$ relative to that on the optical axis.

For a Gaussian beam, Equation 2.45 can be written as:

$$u(x, y, z) = \frac{\omega_0}{\omega} \exp\left\{-i\left(kz - \Phi\right) - \left(x^2 + y^2\right)\left(\frac{1}{\omega^2} + \frac{ik}{2R}\right)\right\} \tag{2.49}$$

where $\Phi = \arctan\left(\lambda z/\pi\omega_0^2\right)$ and ω_0 is the minimum beam waist.

Equation 2.46 has additional solutions, which form a complete and orthogonal set of functions. Equation 2.49 is modified to describe a higher-order mode by multiplying the Gaussian beam by the function appropriate for the system symmetry. For modes with cylindrical symmetry, the solutions arise from Laguerre polynomials [161]. General notation follows TEM_{nm} convention, where n is the number of radial nodes and m is the number of angular nodes. Figure 2.6 presents the mode patterns in cylindrical symmetry for different n and m.

The frequencies of the resonant modes are given by [145, 161]:

$$\nu_{qnm} = \frac{c}{2d}\left(q + \frac{n + m + 1}{\pi}\arccos\sqrt{\left(1 - \frac{d}{R_1}\right)\left(1 - \frac{d}{R_2}\right)}\right) \tag{2.50}$$

Each longitudinal mode has an associated set of transverse modes, which are much more closely spaced in frequency than the longitudinal modes. Multiple longitudinal and transverse mode excitation results in multi-exponential decays, because each mode has a different ringdown time. In addition, interference between cavity modes can decrease the accuracy of a ringdown fit. For this reason, single-mode laser sources are preferred for highest sensitivity measurements. While we cannot control the number of longitudinal modes excited using our pulsed laser sources, the number of transverse modes can be reduced by careful alignment of the cavity mirrors, as well as by inserting a pinhole into the cavity that ensures only the TEM_{00} mode can propagate in the cavity. Typically, the transverse modes can also be visualised at the cavity output mirror, particularly when using visible lasers with modest reflectivity mirrors, which helps alignment.

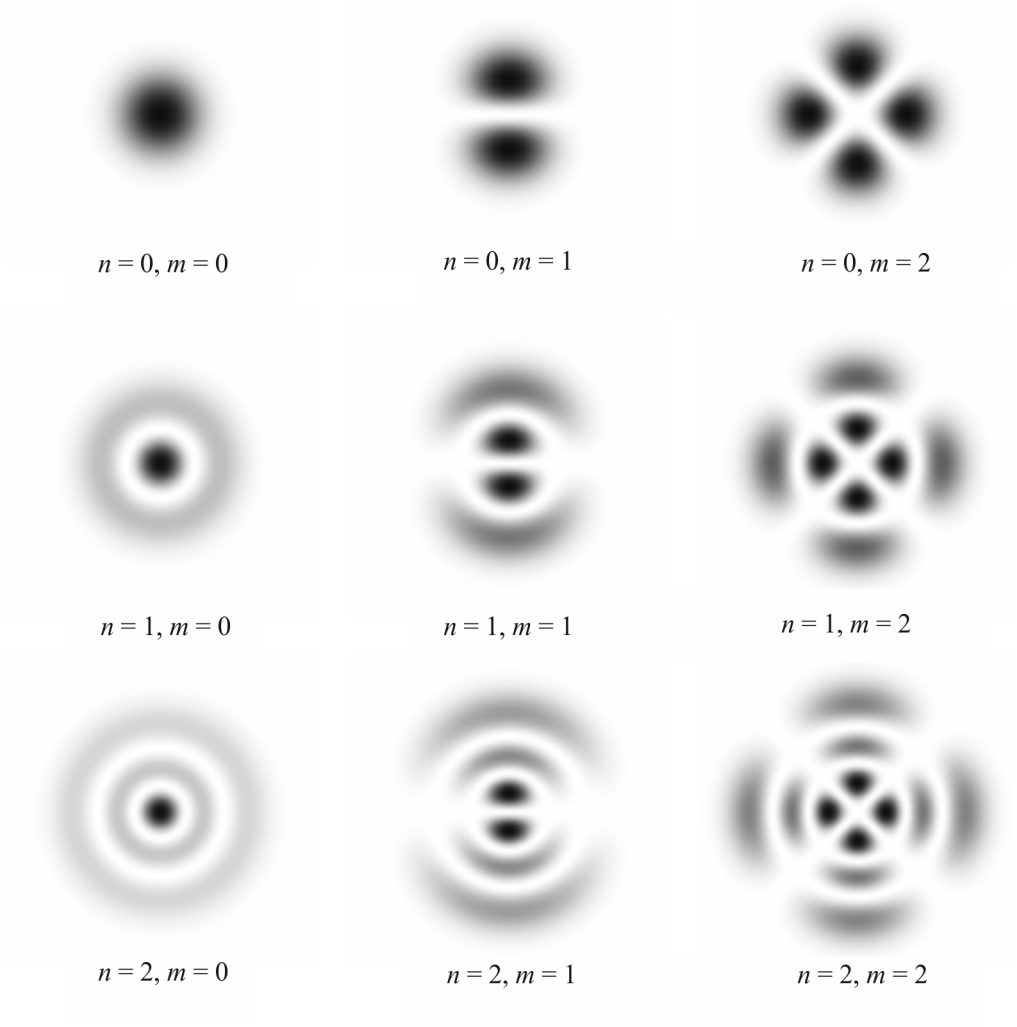


Figure 2.6: Mode patterns in cylindrical symmetry.

2.6 Integration of liquid samples with CRDS

Gas-phase analysis using two-mirror CRDS has now reached maturity, allowing detection limits in the range 10^{-6} to 10^{-10} cm^{-1} to be achieved [162]. Liquid-phase CRDS is more challenging, because it is diffcult to introduce liquid sample into a high-finesse cavity formed from two highly reflective mirrors without compromising the cavity finesse, and hence lowering the sensitivity of the technique. Thus, lower detection limits in the range 10^{-2} to 10^{-7} cm^{-1} have been reported for liquid samples [143].

There have been several strategies employed to incorporate liquid analytes into a two-mirror CRDS experiment: (a) fill the entire cavity with liquid [163], (b) insert a single optically-transparent cell at normal incidence [164], (c) insert a single optically-transparent cell at Brewster's angle [165], (d) insert two optically-transparent cells at Brewster's angle [165] and (e) direct a flowing sheet jet through the cavity at Brewster's angle [166] (Figure 2.7). Each set-up has its advantages and disadvantages, which will be

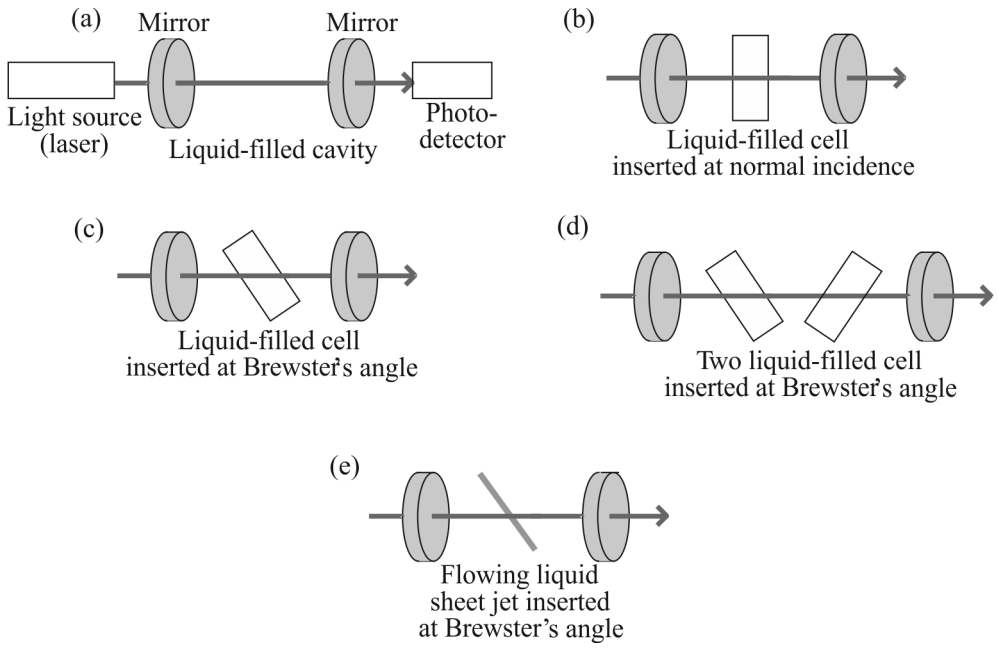


Figure 2.7: Introduction of liquid sample into a two-mirror cavity. (a) Fill entire cavity with liquid [163]. (b) Insert absorption cell at 90° [164]. (c) Insert absorption cell at θ_B [165]. (d) Insert two absorption cells at θ_B [165]. (e) Flowing liquid sheet jet [166]. The references provided within this caption and in the text correspond to the first time this set-up was demonstrated.

discussed at the start of Chapter 3 and 5, along with a full literature review of each approach. For now, we merely present the different approaches in Figure 2.7 for reference later in the thesis.

In this Chapter, we have derived the key equations necessary for both CRDS and CEAS analysis, as well as investigated the behaviour of light within an optical cavity. This theory underpins the remainder of this thesis, and will be referred to within each Chapter.

Chapter 3

Two-mirror cavity ringdown spectroscopy of liquids

"It is very difficult ('impossible') to place a cell inside a cavity since the reflection and absorption losses of the cell windows are too large for observing a CRD transient"
G. Berden, R. Peeters, G. Meijer, Int. Rev. Phys. Chem., Vol. 19, No. 4, 2000 [162].

3.1 Introduction

Cavity ringdown spectroscopy (CRDS) is a highly sensitive spectroscopic technique, used most commonly for the analysis of weak optical absorptions of trace gas species [152]. The experimental set-up is straightforward: a pulse of light (usually from a laser) is injected into an optical cavity formed from two highly reflective mirrors, and the exponential decay of the light intensity within the cavity is recorded, usually by monitoring the small amount of light that 'leaks out' through one of the mirrors. The exponential decay time constant, or 'ringdown time' of the cavity provides a sensitive measure of the cavity losses, in particular any optical absorption by a sample placed within the cavity. The high sensitivity of cavity ringdown techniques has two sources. Firstly, light trapped within the cavity undergoes multiple passes through the sample, vastly increasing the effective absorption pathlength relative to single-pass methods; for gas-phase species, path lengths of several kilometres are typically achieved in an experimental footprint of a few tens of centimetres. Secondly, since the rate of decay of the light intensity within the cavity is measured, rather than the light intensity itself, the signal is decoupled from the initial light intensity injected into the cavity, and is virtually immune to shot-to-shot variations in the laser intensity.

Over the past decade, there has been considerable interest in exploring the potential scope of CRDS for liquid-phase measurements [143, 159]. There have been several strategies employed to allow the incorporation of liquid analytes in to a two-mirror CRDS experiment: (a) fill the entire cavity with liquid, (b) insert a single optically transparent cell at normal incidence, (c) insert a single optically-transparent cell at Brewster's angle, (d) insert two optically-transparent cells at Brewster's angle and (e) direct a flowing sheet jet through the cavity at Brewster's angle. These approaches were highlighted in Figure 2.7 at the end of Chapter 2. A chronological summary of two-mirror liquid-phase CRDS measurements performed to date is presented in Table 3.1.

Table 3.1: Chronological summary of two-mirror liquid-phase cavity ringdown spectroscopy. λ is the wavelength in nm, l is the optical pathlength in mm, V_{sample} is the total volume of sample required for the measurement, and V_{illum} is the total volume illuminated by the light beam during the measurement. C_{min} is the lowest detectable concentration, which corresponds to the minimum concentration of the first listed analyte, if several analytes were measured. Where possible, concentration detection limits have been calculated from three standard deviations (3σ) of the reported baseline noise, but limits marked with * have been estimated using other reported data. C_{min} is converted into the minimum detectable absorption per unit pathlength, κ_{min}, in cm^{-1} using the literature absorption coefficient value for the respective analyte at the appropriate wavelength. N_τ is the number of passes through the sample recorded during 1 unit ringdown time.
**Nitro-PAHs is an abbreviation of nitro-polyaromatic hydrocarbons.
$^{+}$ calculated from the stated cavity finesse as τ_0 was not stated in this case.

Ref.	Fig.	Analyte	λ / nm	l / mm	V_{sample} (V_{illum}) / nL	C_{min} / nM	κ_{min} / cm^{-1}	N_τ
Xu et al. [165]	2.7(c)	Benzene	590 - 620	10	Few mL	-	2×10^{-7}*	750
Xu et al. [165]	2.7(d)	Benzene	590 - 620	20	Few mL	-	5×10^{-7}*	428
Hallock et al. [163]	2.7(a)	Laser dyes Inorganics	620 - 670	210	50 mL	0.001	10^{-6} - 0.01	423
Hallock et al. [167]	2.7(a)	Methylene blue	655	230	60 mL	-	1×10^{-6}	-
Snyder et al. [168]	2.7(c)	Quinalizarin, Anthraquinones	470	0.30	10,000 (500)	30	6.2×10^{-4}	750
Bahnev et al. [169]	2.7(a)	Crystal violet	532	2.0	12,000 (4,000)	3.75	4.7×10^{-4}	2765
Bechtel et al. [170]	2.7(c)	Anthraquinones	488	0.30	10,000 (500)	-	7.8×10^{-6}	1739
Sneppen et al. [171]	2.7(a)	Azo dyes	532	2.0	12,000	15*	4.8×10^{-4}	9369^{+}
Sneppen et al. [172]	2.7(a)	Direct red 10, Azo dyes	457	2.0	12,000	17*	5.9×10^{-4}	8487
Sneppen et al. [172]	2.7(a)	2-nitrofluorene, Nitro-PAHs**	355	2.0	12,000	75*	1.8×10^{-3}	2425
Alexander [166]	2.7(e)	Malachite green	628	0.023	-	71	1.6×10^{-2}	848
Sneppen et al. [173]	2.7(b)	2-nitrofluorene, Nitro-PAHs**	355	10	80,000	40*	9.4×10^{-4}	487
Sneppen et al. [173]	2.7(b)	Benzopurpurine, Nitro-PAHs**	273	10	80,000	500*	3.7×10^{-2}	142

The lowest loss experimental set-up (which should correspond to the highest sensitivity) is usually arrangement (a), in which the analyte solution fills the entire space between the mirrors. However, there is often difficulty in implementing strategy (a), for several reasons. Firstly, in order to probe only a small volume, the cavity length must be very short (few millimetres compared with metres), meaning that it becomes difficult to measure the ringdown time accurately, as precision of sub-nanoseconds may be required. Even with a short cavity, filling the entire space with solvent will greatly increase the scattering losses through the liquid. In addition, placing the liquid sample directly into contact with the mirrors usually lowers the reflectivity owing to the change in refractive index at the mirror surface. Finally, placing liquid directly into contact with the mirror surface can lead to chemical degradation, especially for harsh chemicals. Nevertheless, arrangement (a) has been successfully applied in several studies [163, 167, 169, 171, 172]. In the first two studies, which were carried out by Hallock et al. [163, 167], a relatively long cavity length was used ($>$ 20 cm), and thus large volumes (ca. 50 mL) were required. However, the minimimum absorption per unit pathlength was favourable (10^{-6}). In later experiments, Bahnev et al. [169] and van der Sneppen et al. [171, 172] developed a miniaturized cavity, with a pathlength of only 2 mm, in order to reduce the total filled cavity volume from millilitres to microlitres. In this case, the 'blank' ringdown time was only 65 - 75 ns.

As an alternative, confining the liquid sample within a high optical quality cell allows for longer cavity lengths without increasing the sample volume, as well as keeping any potentially damaging substances away from the mirror surfaces. Absorption cells have been inserted into a cavity either at normal incidence (arrangement (b)) or at Brewster's angle (arrangement (c)). For an interface between two media with refractive indices n_1 and n_2, Brewster's angle (θ_B) may be defined as $\theta_B = \tan^{-1} \frac{n_2}{n_1}$. For a typical air/glass boundary, where $n_1 = 1.00$ and $n_2 = 1.52$, $\theta_B = 56.7°$. [1] At this angle, there is theoretically no reflection loss for light plane-polarized parallel to the plane of incidence [168]. Thus, when linearly polarised light is used to excite the cavity, losses in the cavity caused by inserting an optical element can be minimised, hence maximising the sensitivity of the ringdown experiment. Of course, when an absorption cell is inserted into the cavity, there are four interfaces that must be considered, as refraction occurs at air/glass, glass/liquid, liquid/glass and glass/air interfaces as light passes through the cell, and it is difficult to match Brewter's condition for each interface. Nevertheless, impressive detection limits (10^{-7} cm^{-1}) were reported by Xu et al. in the first application of CRDS to the liquid-phase, recording spectra of the C-H stretching fifth vibrational overtones of benzene using both a single and double Brewster's angle cell configuration [165]. Snyder et al. designed a special liquid flow cell which ensured light struck each boundary at the correct θ_B for each interface [168].

Many liquid-phase CRDS experiments have been targeted towards improving the sensitivity of UV/vis detection for high performance liquid chromatography (HPLC). In this case, the refractive index dependence of Brewster's angle must be stressed: generally the cell is aligned in the cavity at Brewster's angle for one

[1] The quoted refractive indices in this Chapter are all given for each material at 532 nm, our laser wavelength.

analyte/solvent, and thus when the refractive index changes (for example during column elution), the ringdown time will drop as the Brewster angle condition is no longer met for the new refractive index medium. Without calibration, this drop caused by a refractive index change is indistinguishable from any change arising from absorption.

For this reason, normal incidence flow cells may sometimes be preferred. In particular, van der Sneppen et al. inserted a cuvette into a cavity only 4 cm long, so that the majority of surface reflections from the cuvette could be trapped within the cavity [173]. Van der Sneppen et al. also investigated liquid-phase CRDS in the ultraviolet (UV) region, finding that the poorer mirror reflectivity as the wavelength decreases limited the application of liquid-phase CRDS in UV absorption measurements, despite this being a very important part of the spectrum for a wide variety of analytical applications. As light sources and mirror coating technology continues to improve, UV applications of liquid-phase CRDS are expected in the future.

In terms of shorter pathlength analysis, the work of Snyder et al. [168], Bechtel et al. [170] and Alexander [166] must be highlighted. Snyder et al. and Bechtel et al. both used the same custom-designed Brewster's angle flow cell, with the latter achieving an improvement in sensitivity by changing from a pulsed to a more stable continuous wave light source. Alexander's demonstration of a flowing liquid-sheet jet combined with CRDS achieved the shortest pathlength (only 23 μm), even though a large reservoir volume was used.

In the present work, we apply CRDS to small volume (sub-microlitre) analysis of liquid samples contained either within flow cells or microfluidic chips. In this Chapter, we explore the losses associated with the insertion of either a flow cell or a microfluidic chip, and work to minimise these losses, in order to optimise the detection sensitivity. We apply CRDS to monitoring chemical reaction kinetics on a microfluidic chip, tracking the oscillation period of the well-known Belousov-Zhabotinsky reaction. We also demonstrate single-droplet detection. In Chapter 4, we apply the highest sensitivity set-up to the analysis of trace analytes in water.

3.2 Cavity set-up

The light source employed in all of the cavity ringdown measurements is a microchip Nd:YAG laser (NP-10620-100, Teem Photonics), which produces 0.9 ns, 6 μJ pulses at 1064 nm with a repetition rate of 7.4 kHz. It should be noted that as the passively Q-switched pulses are not strictly periodic, laser pulses cannot be externally-triggered. For our experiments, this is not a problem, as we use a signal from a photodiode that detects a fraction of the laser pulse to trigger the rest of the experiment from the initial laser pulse.

The laser beam is frequency-doubled to produce 532 nm light, which is separated from the fundamental using a cold mirror, before being injected into the cavity. The fundamental beam transmitted by the cold mirror

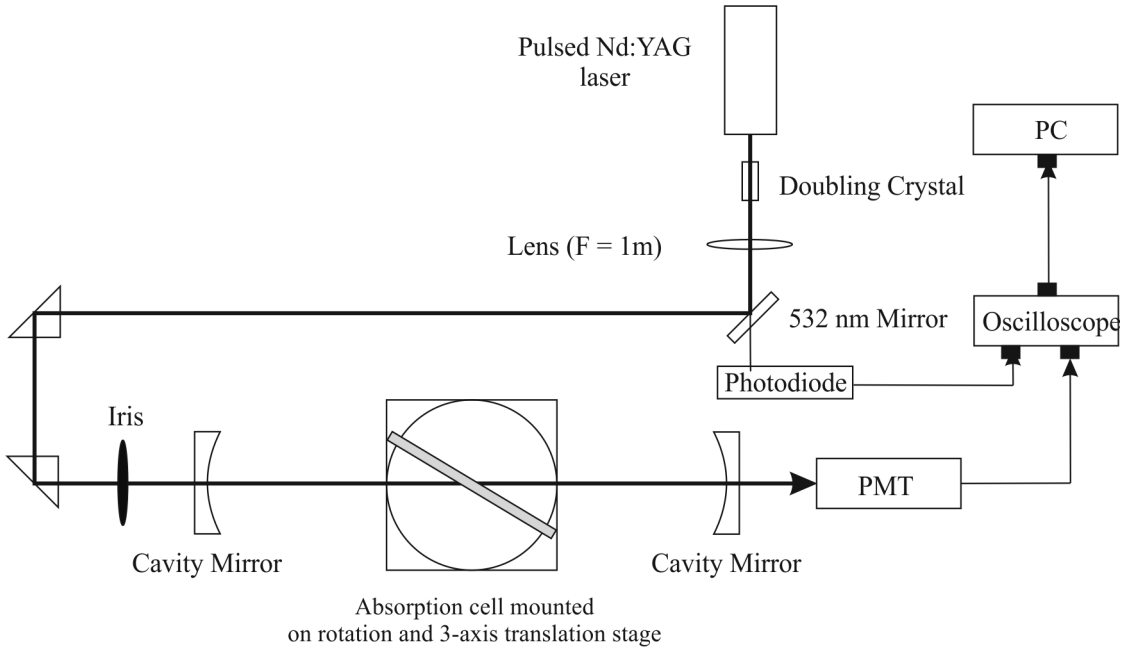


Figure 3.1: Schematic of CRDS set-up consisting of a Nd:YAG laser, beam focusing and steering optics, two-mirror cavity (R $>$ 99.8%) containing the absorption cell, and a photomultiplier tube (PMT) detector.

is collected by a photodiode (DET10A/M, Thorlabs) and used to trigger the oscilloscope. Two right-angled prisms are used for beam-steering into the optical cavity.

The optical cavity is formed from two concave 25 mm dielectric mirrors (CVI Melles Griot, radius of curvature 1 m, reflectivity ca. 99.8% at 532 nm) positioned at a separation of 58.5 cm.

On each experimental cycle, a light pulse is coupled into the cavity through the back face of the first mirror, and undergoes repeated reflections within the cavity. A small amount of light is coupled out of the cavity through the mirrors on each reflection. Behind the second mirror, the cavity output is collected by a 3 mm diameter liquid lightguide (NT53-428, Edmund Optics), which directs the light to a photomultiplier tube (PMT, Hamamatsu, H6780-20). The signal from the PMT is displayed on a digital oscilloscope (Tektronix, TDS 3044B), which has a vertical (y-axis) resolution of 9 bits and a horizontal (x-axis) resolution of 0.2 ns. The oscilloscope is interfaced to a personal computer via a GPIB-USB interface (National Instruments, 778927-01). Ringdown traces (averaged up to 512 times on the oscilloscope) are acquired and analyzed continuously using a home-written LabVIEW program (National Instruments, LabVIEW 10). As the laser pulse duration is shorter than the cavity round-trip time, the signal consists of a train of pulses with exponentially decaying intensities, $I(t)$. An example ringdown trace is shown in Figure 3.2.

3.2.1 Data analysis

Determination of the ringdown time τ is carried out automatically by the same LabVIEW interface that acquires the data. The signal is baseline-subtracted and thresholded before a peak-finding algorithm determines the amplitude of each peak in the exponentially decaying pulse train. The ringdown time, τ, is then determined from the slope of a log plot of peak intensity vs time i.e. $\ln I(t) = \ln I(0) - t/\tau$.

κ is determined using Equations 2.13 and 2.15 from Section 2.2.

3.3 Characterisation of the cavity

Before insertion of an absorption cell into the cavity, the ringdown time of a 532 nm light pulse was measured to be 952 ns. This corresponds to a mirror reflectivity of 99.795% at this wavelength, close to the manufacturer's specification of 99.8%. This ringdown signal is presented in Figure 3.2(a). A small time section is also shown in Figure 3.2(b) to demonstrate the resolution of each light pulse passing the detector.

3.4 Introduction of a flow cell or microfluidic chip into the cavity

As shown in Figure 3.1, for the small volume liquid measurements, a flow cell or microfluidic chip was positioned vertically in the centre of the cavity on a double-rotation (Thorlabs, RP01) and three-axis translation stage (Newport Corporation, 443), equipped with micrometer resolution actuators (Newport Corporation, SM-25). This allowed the angle of the cell with respect to the laser beam polarization to be optimised in order to maximise the ringdown time, and hence the sensitivity of the absorption measurement. Liquid was delivered to the cells using syringe pumps (Fusion 400, Chemyx).

We have investigated the insertion of commercial flow cells, with short pathlengths from 0.1 mm to 2 mm, before moving on to the characterisation of lab-fabricated microfluidic chips in a two-mirror cavity ringdown set-up.

3.4.1 Minimising reflection losses

Integration of microfluidic samples into an optical cavity requires careful optimisation in order to minimise the scattering and absorption losses caused by both the condensed phase sample and its container. As noted previously, incorporating an absorption cell into the cavity introduces four additional surfaces (as illustrated in Figure 3.3) at which scattering, refraction and reflection occur. To minimise these losses, there are two key factors to be considered. Firstly, any optical imperfections in the region probed by the laser, for example dust,

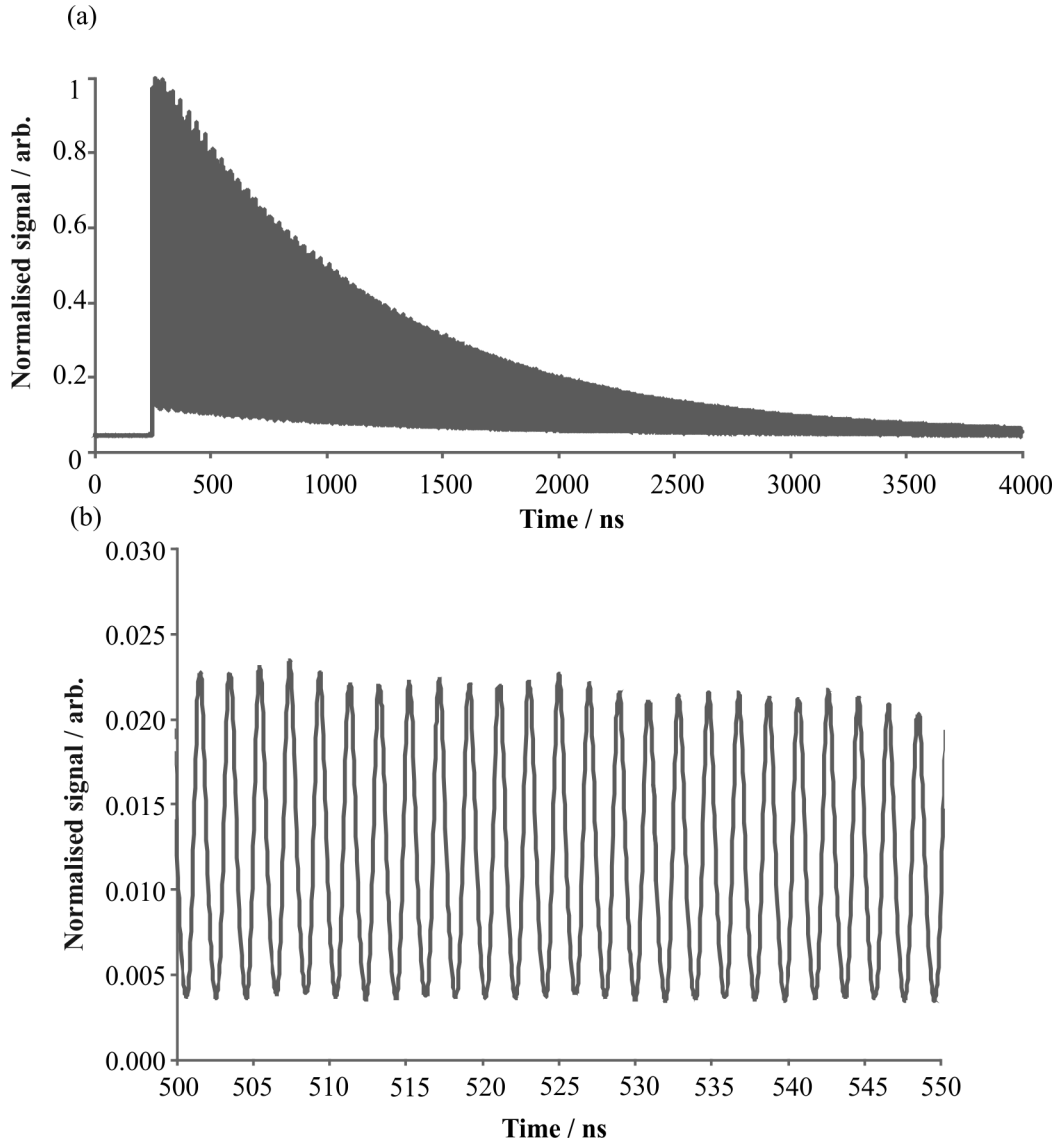


Figure 3.2: (a) Ringdown signal for empty cavity. (b) Enlarged time section, shown to demonstrate the peak-resolved output.

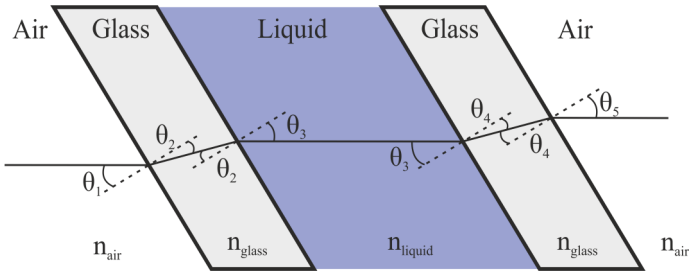


Figure 3.3: The interfaces encountered by the light beam as it passes through the absorption cell inside the cavity.

adhesive residue or solvent smears, will increase scattering losses and adversely affect the performance of the cavity. These losses can be minimised by using high-optical-quality flow cells, or in the case of microfluidic chips, by carefully controlling the quality of both the external and internal surfaces during chip fabrication. Before placing any absorption container into the cavity, the external surfaces are throughly cleaned. The internal surfaces are harder to clean. Typically, we flow solvent through the cell for several minutes before taking any measurements, in order to ensure the internal surfaces are free from contamination.

As noted in Section 3.1, reflection losses can be minimised by placing the chip at Brewster's angle to the laser beam axis inside the cavity. The situation is in our case somewhat complicated because we have four interfaces to consider (Figure 3.3). In this case, where there are several parallel interfaces, a true θ_B will not occur, and there will always be some reflection loss. However, this reflection loss can still be minimised by finding an optimum angle that minimises losses as light traverses the four interfaces. This theoretical reflection minimum is calculated by propagating Snell's law (Equation 3.1) at each interface, in the following form:

$$\sin\theta_2 = \frac{n_1}{n_2}\sin\theta_1 \tag{3.1}$$

The reflection loss at each interface can then be modelled using the Fresnel equation (Equation 3.2), where R_p is the proportion of p-polarised light reflected.

$$R_p = \left[\frac{n_1\sqrt{1-(\frac{n_1}{n_2}\sin\theta_1)^2} - n_2\cos\theta_1}{n_1\sqrt{1-(\frac{n_1}{n_2}\sin\theta_1)^2} + n_2\cos\theta_1}\right]^2 \tag{3.2}$$

The optimum angle for inserting an absorption cell into the cavity can then be calculated by combining the results of Equations 3.1 and 3.2. The overall transmission ($T = 1 - R$) through all four interfaces is simply a product of the transmission at each interface, for a certain θ_1. An example plot of transmission versus θ_1 is shown in Figure 3.4, for $n_{\mathrm{air}} = 1.00$, $n_{\mathrm{glass}} = 1.52$ and $n_{\mathrm{liquid}} = 1.33$. In this case, the optimum angle is 56.9°, which yields a reflection loss of only 0.19%. This angle is slightly higher than θ_B calculated previously for a single borosilicate glass interface. The predicted ringdown time resulting from this model can be calculated from Equation 2.13 given the calculated losses associated with the cell and the cavity mirrors. The ringdown times predicted from this simple model will be compared with those measured experimentally in Sections 3.4.3 to 3.5.3. It should be noted that the reflection loss calculated at 0° is an overestimation of the real cavity loss at this incidence angle, as the light reflected at normal incidence can be retained within the cavity if all the interfaces are aligned to be perfectly parallel, such that these reflections do not necessarily add a loss to the round-trip transmission of the cavity. We record two maxima experimentally, one at 0° and one at θ_B. The maximum at 0° only occurs when all surfaces are aligned perfectly normal to the laser

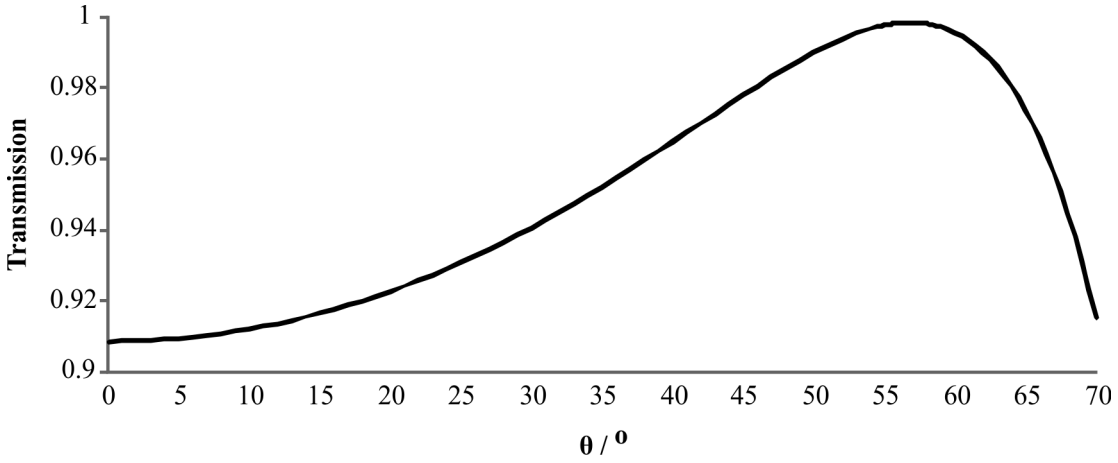


Figure 3.4: Calculated transmission versus angle of incidence ($\theta/^\circ$), for a water-filled ($n_{\mathrm{liquid}} = 1.33$) borosilicate glass ($n_{\mathrm{glass}} = 1.52$) cell in air ($n_{\mathrm{air}} = 1.00$).

beam, whereas the Brewster's angle maximum manifests as a broad peak spanning a range of angles, making alignment much easier.

3.4.2 Pathlength calibration and determination of detection limit

As noted in Section 3.4.1, the flow cell or microfluidic chip is generally positioned between the cavity mirrors at an angle to the cavity axis so as to maximise the measured ringdown time. This increases the optical pathlength slightly relative to the manufacturer's specifications for light incident normal to the flow cell surface. To obtain an accurate determination of the optical pathlength through each flow cell when positioned at the optimum angle within the ringdown cavity, a calibration was carried out based on the known absorption of a series of dilute aqueous solutions of potassium permanganate, $KMnO_4$. The absorption coefficient, α, for $KMnO_4$ at 532 nm was determined to be (4805 $\pm$ 10) M^{-1} cm^{-1} in a conventional single-pass absorption measurement carried out on a commercial UV-vis spectrometer (Varian Cary-100 Bio UV-vis spectrometer) employing a 1 cm cuvette. The full recorded spectrum is shown in Figure 3.5. As well as allowing an accurate determination of the pathlength, the measurements on the permanganate concentration series also allow the detection limit κ_{min} to be determined.

We have determined the detection limit in two different ways, firstly from the signal to noise ratio of the baseline ringdown measurement, and secondly from the uncertainty in the y-intercept of a plot of measured optical absorption κ vs analyte concentration. To estimate the detection limit based on the signal-to-noise ratio of the baseline ringdown signal, we use the following Equation, which was derived in Chapter 2:

$$\kappa_{\mathrm{min}} = \frac{d\Delta\tau_{\mathrm{min}}}{cl\tau_0^2} \tag{3.3}$$

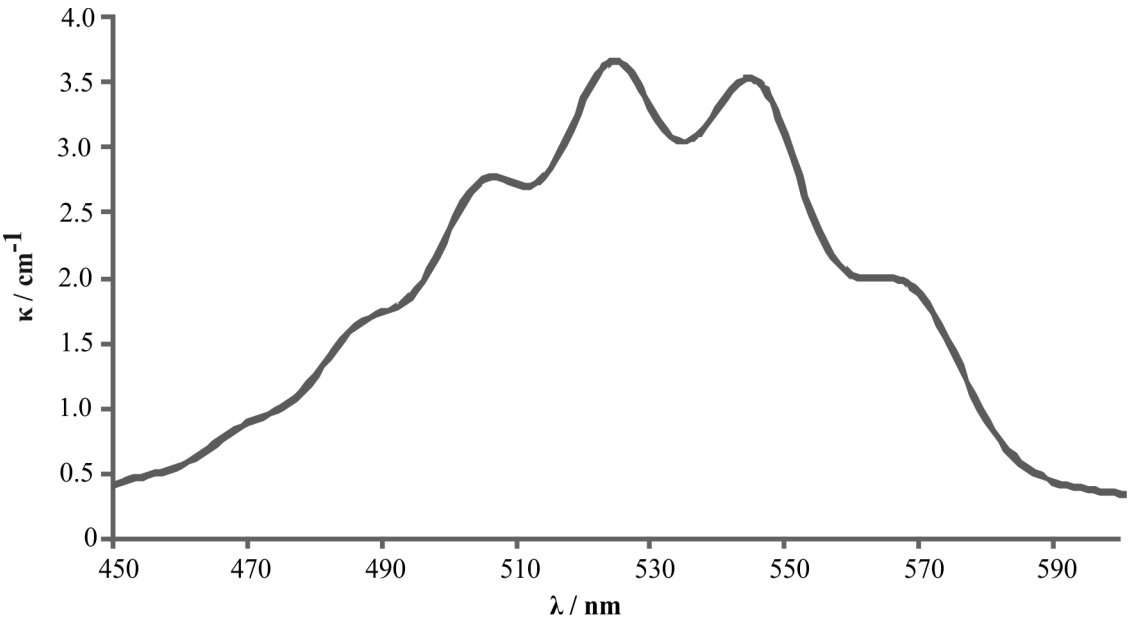


Figure 3.5: Visible absorption spectrum of aqueous potassium permanganate, 0.65 mM concentration.

In the present work, we define $\Delta\tau_{\mathrm{min}}$ to be three times the standard deviation 3σ in repeated measurements of the baseline ringdown time τ_0. Determination of the detection limit using this method accounts for limitations on the detection sensitivity imposed by the intrinsic noise associated with the measurement, and represents the potential detection limit of the CRDS measurements using the current experimental set-up. However, it does not account for any other sources of experimental uncertainty e.g. impurities in the reagents used, or drifts in alignment during the complete experiment time. To determine the detection limit when all sources of error are taken into account, we have measured the absorption per unit pathlength, κ, as a function of concentration, C, for each of the analytes studied. When κ is plotted as a function of C, the uncertainty in the κ intercept gives a good measure of the limit of uncertainty in the measurement of κ, which is equivalent to the detection limit.

The former detection limit, determined using Equation 3.3, is labelled $\kappa_{\mathrm{min,s}}$, where the subscript s indicates that the detection limit in this case is determined by the 'spectral' method [174]. The latter detection limit, determined from a plot of absorption as a function of concentration, is labelled $\kappa_{\mathrm{min,r}}$, where the subscript r indicates that the detection limit is determined by the 'regression' method [174]. Unsurprisingly, $\kappa_{\mathrm{min,r}}$ is typically larger than $\kappa_{\mathrm{min,s}}$, as $\kappa_{\mathrm{min,r}}$ encompasses all the errors associated with the measurement, while $\kappa_{\mathrm{min,s}}$ only includes the intrinsic noise associated with the measurement. We believe that $\kappa_{\mathrm{min,s}}$ therefore provides a fairer indication of the detection limit of the technique.

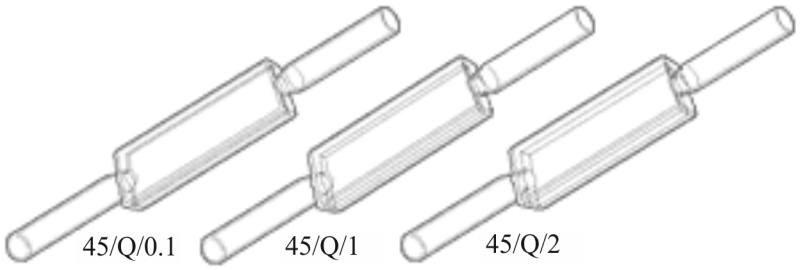


Figure 3.6: Schematic of the three Starna flow cells employed for the CRDS measurements reported in this Chapter. Image reproduced from www.starna.co.uk.

3.4.3 Commercial flow cells

As a first study for small volume analysis, we use commercial flow cells with short pathlengths from 0.1 mm - 2 mm, but wide flow channel widths, which facilitates alignment within our cavity. The characteristics of the three different flow cells employed in this work are listed below.

1. Starna Scientific Ltd 45/Q/2 rectangular flow cell, optical pathlength 2 mm, internal width 10 mm, nominal volume 0.90 mL.
2. Starna Scientific Ltd 45/Q/1 rectangular flow cell, optical pathlength 1 mm, internal width 10 mm, nominal volume 0.45 mL.
3. Starna Scientific Ltd 45/Q/0.1 rectangular flow cell, optical pathlength 0.1 mm, internal width 10 mm, nominal volume 0.045 mL.

All three flow cells had the same total wall thickness, of 2.5 mm. Intially, the optimum angle of insertion for each water-filled flow cell was found, by measuring the ringdown time versus angle of incidence. A plot of the theoretical curve predicted by the model outlined in Section 3.4.1, and the experimental curve measured using the 1 mm flow cell, are shown in Figure 3.7. The flow cell walls are fabricated from fused silica ($n_{\mathrm{silica}} = 1.46$). The theoretical optimum angle is therefore $55.8°$, where the reflection loss is only 0.09%. Experimentally, the optimum ringdown time was found to occur at a slightly higher angle of 57° to the cavity axis, and experiments were carried out in this configuration. Once the angle of incidence has been optimised, the flow cell is typically translated left and right relative to the cavity axis, in order to find the optimum point of incidence on the cell. The variation in ringdown time across the flow cell arises from small imperfections at any of the interfaces, and the lowest loss (maximum ringdown) point is used for experiments.

The ringdown times (averaged over 12,800 ringdown traces) for a cavity with a flow cell filled with MilliQ deionised water were determined to be 415 ns, 458 ns, and 584 ns for the 2 mm, 1 mm, and 0.1 mm cells, respectively. By measuring the cavity transmission T in the presence and absence of the flow cell, the losses associated with the cell can be quantified, and are found to be around 0.25%. Table 3.2 lists the ringdown

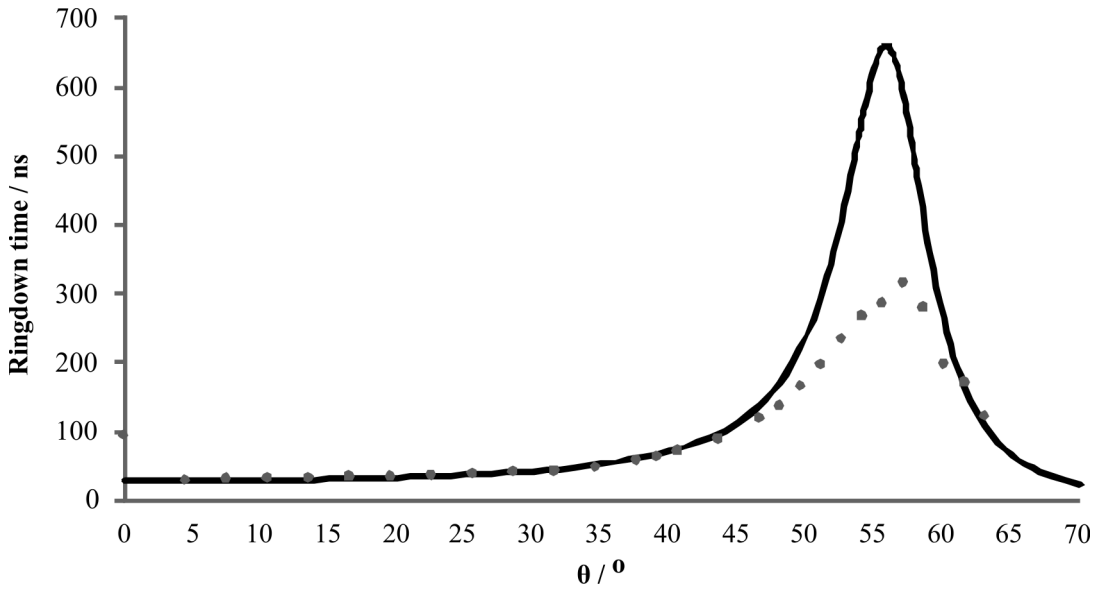


Figure 3.7: Plot of ringdown time / ns versus angle of incidence ($\theta/^\circ$) for 1 mm flow cell. The black line is the theoretical ringdown time, and the grey data points are the experimentally measured values.

time, total cavity loss, the loss associated with the flow cell, the number of passes through the sample during one ringdown time τ, and the associated effective pathlength per unit ringdown time, l_τ, for each flow cell arrangement. We see that the 1 mm and 2 mm cells yield effective pathlengths of several tens of centimetres, while even the 0.1 mm cell has an effective pathlength of 3.5 cm. We typically record the ringdown time over three to five ringdown times, yielding total pathlengths of around 2 m, 1 m, and 15 cm for the 2 mm, 1 mm, and 0.1 mm cells.

We can break down T_{cell} further, into a product of the transmission arising from Fresnel transmission, and from absorption and scatter both in the walls of the flow cell and in the solvent. In other words

$$T_{\mathrm{cell}} = T_{\mathrm{Fresnel}} T_{\mathrm{walls}} T_{\mathrm{solvent}} \tag{3.4}$$

It is possible to separate out the three contributions as follows. The Fresnel transmission (calculated to be 99.91%) should be the same for each flow cell, as this is defined by the refractive indices of each interface, which are identical in each case. Additionally, the transmission arising from absorption and scatter in the cell walls T_{walls} should be the same, given that the total wall thickness l_{walls} is the same (2.5 mm) in all three flow cells. Absorption and scatter in the solvent increases with optical pathlength l_{solvent}, and is therefore the cause of the observed reduction in ringdown time as the pathlength through the flow cell increases. This is quantified by the transmission factor T_{solvent}.

We can make the approximation that $T_{\mathrm{walls}} T_{\mathrm{solvent}} \approx T_{\mathrm{solvent}}$ in all three flow cells, as the visible absorption through 2.5 mm of fused silica is negligible (10^{-6} cm^{-1}) [175]. Converting T_{solvent} into absorbance, and

Table 3.2: Total cavity loss L_{tot}, loss associated with the flow cell L_{cell}, number of passes through the sample per unit ringdown time N_τ, and effective pathlength per unit ringdown time l_τ, for each of the three flow cells employed.

Flow cell	L_{tot} /%	L_{cell} /%	N_τ	l_τ
2.0 mm	0.469	0.265	213	440
1.0 mm	0.425	0.221	235	289
0.1 mm	0.333	0.129	299	35

plotting this as a function of pathlength (not shown) allows the absorption coefficient of water at 532 nm to be roughly estimated at 7×10^{-3} cm^{-1}. This estimated value is nearly an order of magnitude larger than the value of 9×10^{-4} cm^{-1} reported in the literature [176].

An accurate measurement of the pathlength and determination of the limit of detection for each flow cell when used for absorption measurements within our CRDS set-up was carried out as described in Section 3.4.2. For each flow cell, a series of measurements was made for $KMnO_4$ solutions spanning the dynamic range of the cell, with the minimum concentration corresponding to the minimum detectable change in ringdown, and the maximum to the onset of signal saturation. These ranges spanned 10 nM to 25 μM for the 2 mm cell, 13 nM to 130 μM for the 1 mm cell, and 200 nM to 500 μM for the 0.1 mm cell. Ringdown times for the $KMnO_4$ solutions were measured in alternation with distilled water 'blanks', in order to ensure that complete flushing of the flow cell with the solution of interest had been achieved, confirmed by τ returning to its original value. Each measurement was repeated three times to ensure reproducibility. Flushing of the cells for between one and two minutes at flow rates of 0.5 - 2.0 mL min^{-1} was required to ensure complete flushing. Measurement of the ringdown time was performed under stopped flow conditions, although no noticeable difference was observed when recording under flow conditions.

The calibration data for each flow cell, together with sample ringdown traces, are shown in Figure 3.8. The pathlengths for the 2 mm, 1 mm, and 0.1 mm flow cells when placed at Brewster's angle within the cavity were determined to be 2.07 mm, 1.23 mm, and 0.117 mm, respectively.

As explained in Section 3.4.2, the detection limit for each of the three analytes studied was determined using two different methods, the spectral method, based on the 3σ uncertainty in the baseline τ_0 measurement (around 0.4% in our current experimental set-up), and the regression method, based on the uncertainty in the intercept of a plot of κ, the absorption per unit pathlength, vs analyte concentration C. Table 3.3 lists the results of this analysis for the potassium permanganate measurements, which were used both to calibrate the absorption pathlength per pass and to quantify the minimum detectable absorption per unit pass using each of the three flow cells. The table summarises the geometrical properties of each flow cell (optical pathlength when inserted into the cavity at the appropriate angle to optimise the ringdown time, and total probed volume of liquid), the baseline ringdown time and its 3σ uncertainty for a flow cell filled with MilliQ deionised water, as well as the detection limit expressed both in terms of minimum detectable absorbance per unit pass and

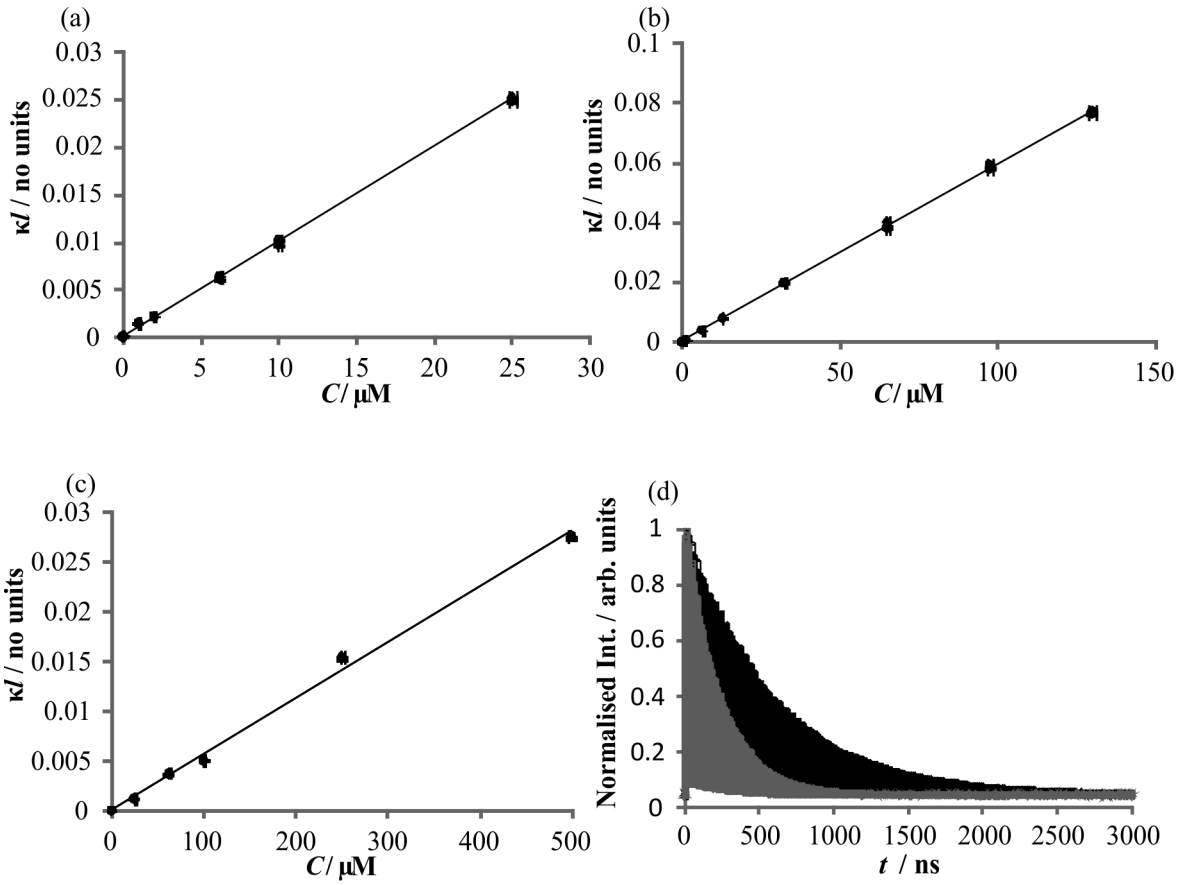


Figure 3.8: (a) κl versus permanganate concentration C / μM, determined in 2 mm flow cell (absorption pathlength $l = 2.07$ mm). (b) κl versus permanganate concentration C / μM, determined in 1 mm flow cell (absorption pathlength $l = 1.23$ mm). (c) κl versus permanganate concentration C / μM, determined in 0.1 mm flow cell (absorption pathlength $l = 0.117$ mm). (d) Example ringdown traces recorded in the 0.1 mm flow cell. The black trace corresponds to the ringdown time when the flow cell is water-filled, $\tau_0 = 588$ ns, and the overlain grey trace corresponds to the ringdown time when the flow cell is filled with 100 μM permanganate, $\tau = 232$ ns.

Table 3.3: A summary of the results determined using the permanganate calibration for each flow cell. Ill. is an abbreviation for the illuminated volume, which is estimated as a maximum beam spot diameter of 0.5 mm.

Flow cell	l / mm	Illuminated volume / nL	τ_0 / ns	$\kappa_{\mathrm{min,s}}$ / cm^{-1}	C_{min} / nM
2.0 mm	2.07	393	415 ± 1.6	9.1×10^{-5}	19
1.0 mm	1.23	196	458 ± 1.8	1.4×10^{-4}	29
0.1 mm	0.117	20	584 ± 2.3	1.1×10^{-3}	240

minimum detectable permanganate concentration, as determined from the uncertainty in the τ_0 measurement using Equation 2.17.

The minimum detectable absorbances determined from the baseline τ_0 measurement are 9.1×10^{-5} cm^{-1}, 1.4×10^{-4} cm^{-1}, and 1.1×10^{-3} cm^{-1} for the 2.0 mm, 1.0 mm, and 0.1 mm cells, respectively. If we instead estimate the detection limits based on the 3σ uncertainty in the y intercept of a κ vs concentration plot, we obtain values of 8.1×10^{-4}, 2.5×10^{-3}, and 5.8×10^{-2} cm^{-1} for the three cells. As noted previously, the fact that the former values are higher the latter is unsurprising, since they include all sources of experimental uncertainty, including variations in analyte concentrations when preparing the standard solutions.

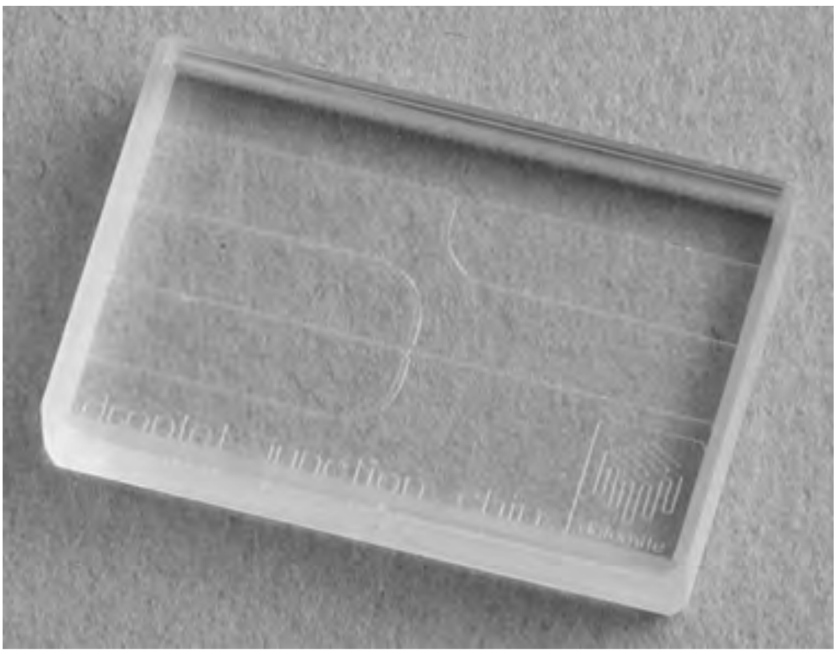
3.4.4 Etched glass chip

The high-optical quality flow cells outlined in the previous Section represent an idealised sample container for CRDS measurements on small volume liquid samples. However, the flow cells have a wide channel, and the total volume required for making a measurement is greater than the desired sub-microlitre range we would like to investigate. There are a variety of benefits to coupling a microfluidic channel with CRDS, including control of the liquid flow conditions (Section 1.1) and reducing the volume required for flushing, as well as enabling more rapid reaction kinetics to be analysed because of the reduction in time required to fill the sample container.

The first microfluidic chip we characterised was a commercial fused silica chip. Figure 3.9 shows a photo of a standard chip purchased from Dolomite (3200132 Quartz Droplet Junction Chip 190 μm etch depth) together with a diagram of the channel cross-section. The chip walls are fabricated from high quality fused silica, and the channels are fabricated using controlled hydrofluoric acid etching on the surface of two pieces of glass, followed by thermal bonding the two pieces of glass together to form the enclosed channel. The chip has a total wall thickness of 4 mm, with a channel height of 190 μm. The surface roughness of the channels is 5 nm.

We have recorded an optimum ringdown of 707 ns through the fused silica channel walls, which corresponds to an absorption and reflection loss through the 4 mm fused silica glass of 0.071%. However, we were not successful in measuring a ringdown through the channel. According to the manufacturer's specification, the channel is 390 μm wide, with a 95 μm radius on each side and a 200 μm flatter section in the centre. Even

(a)



(b)

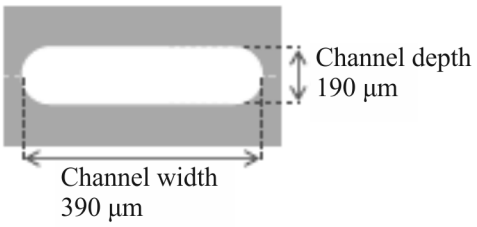


Figure 3.9: (a) Photograph of commercial etched glass chip (b) Side-view of etched channel, demonstrating rounding of channel corners. Images reproduced from www.dolomite-microfluidics.com.

when an iris was used to reduce the beam diameter, to well below 200 μm, we could not measure a ringdown signal when the laser beam was directed through the channel. Given that the surface roughness of the channel is known to be good, we attribute this poor signal to slight curvature across the whole microfluidic channel, with the resulting lensing effect destroying the stability of the cavity. This is a common feature of hydrofluoric acid-etched channels, as the etch process is radial [177].

3.5 Rapid prototyping of microfluidic chips

Given the restricted availability and high costs of commercial microfluidic chips, we were interested to ascertain the suitability of lab-fabricated microfluidic chips for insertion into a two-mirror cavity. Often, lab-fabricated microfluidic chips are fabricated using two pieces of either microscope slide or cover slip

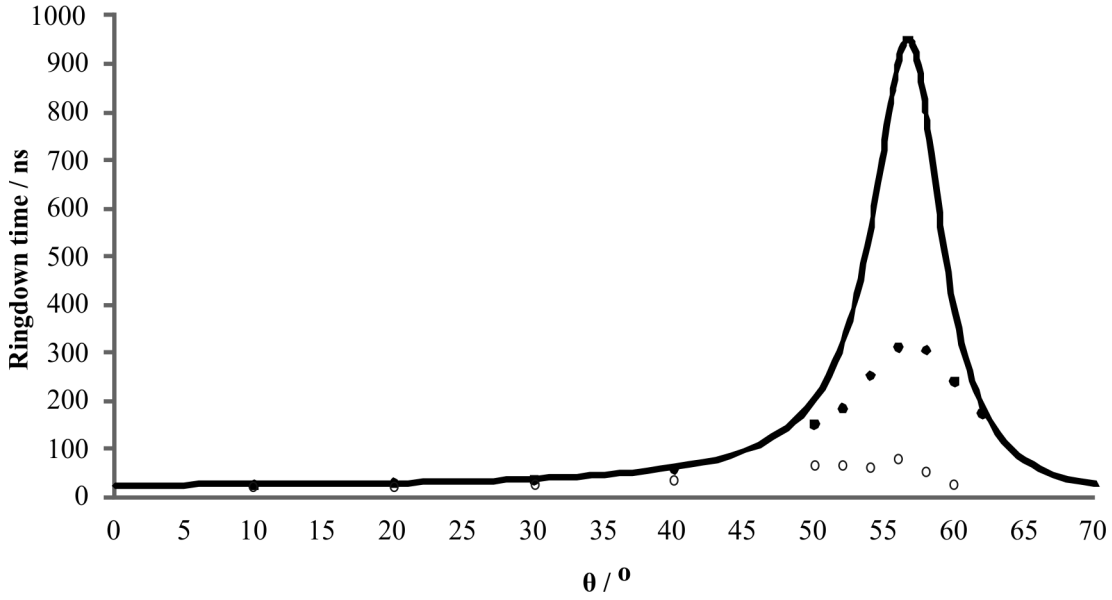


Figure 3.10: Plot of ringdown time / ns versus angle of incidence ($\theta/^\circ$) for a borosilicate glass microscope slide. The black line corresponds to the theoretical plot (see Section 3.4.1), while the black filled-in circles correspond to the experimental values determined through a cleaned microscope slide and the empty circles correspond to the experimental values determined through a microscope slide before cleaning.

borosilicate glass, with some channel structure between the two pieces of glass. We first characterise the typical losses through what will become the channel walls, the microscope slide and cover slide, before charactering the microfluidic chips themselves.

3.5.1 Microscope slides and cover slides

The transmission through three different standard microscope slides and cover slides (VWR International) was tested in the two-mirror cavity. Firstly, the ringdown time was measured as a function of incidence angle for a microscope slide inserted into the cavity. This plot is shown in Figure 3.10. Experimental points were measured for a microscope slide before and after cleaning, and the large improvement in ringdown time can be seen by comparison of the empty circles and the black circles in Figure 3.10. Cleaning was required to remove residual dust and grease from the microscope slides. The theoretical optimum angle of 57 $^\circ$ based on the model described in Section 3.4.1 is close to that determined experimentally (56 $^\circ$).

Having found the optimum angle of incidence, three different microscope slides, labelled (a), (b) and (c) in the following, were tested in the cavity. The thicknesses of the microscope slides were measured using a micrometer and found to be (a) 0.913 mm, (b) 0.936 mm and (c) 0.930 mm respectively. The maximum ringdown times through the microscope slides at Brewster's angle were determined to be (a) 338 ns, (b) 302 ns and (c) 311 ns. Within each microscope slide, the ringdown time at 10 random points was measured, and the average and standard deviation of these measurements was found to be (a) (314 ± 23) ns, (b) (290 ± 7) ns and

(c) (294 ± 13) ns. These values are significantly lower than those measured through the fused silica flow cell and Dolomite chip wall. The increased losses arise from a combination of poorer surface quality and higher intrinsic absorption losses associated with borosilicate glass compared to fused silica.

In order to ascertain the relative contributions to the loss from absorption and from poor surface quality, we also tested three cover slides, labelled (d), (e) and (f), at Brewster's angle. The thicknesses of the cover slides were measured using a micrometer and found to be (d) 0.119 mm, (e) 0.119 mm and (f) 0.115 mm respectively. The maximum ringdown times through each cover slide at Brewster's angle were determined to be (d) 497 ns, (e) 492 ns and (f) 536 ns. Within each cover slide, the ringdown time at 10 random points was measured, and the average and standard deviation of these measurements was found to be (d) (462 ± 19) ns, (e) (454 ± 18) ns and (f) (500 ± 23) ns. These ringdown times are significantly higher than those recorded using the microscope slides. The surface roughness is expected to be similar in each case, and thus we attribute the increase in ringdown time to lower absorption losses in the thinner cover slides compared to the microscope slides.

We can convert the average ringdown time determined for the three microscope slides and cover slides, 299 ns and 472 ns respectively, into the transmission through the inserted piece of glass, given that $T_{\mathrm{Tot}} = T_{\mathrm{Mirrors}} T_{\mathrm{Glass}}$. It is found that the transmission through a cover slide is comparable to the mirror reflectivity (99.792% compared to 99.795%), while the transmission through a microscope slide is higher than the mirror reflectivity (99.555% compared to 99.795%).

This comparison indicates that microfluidic chips fabricated using cover slides rather than microscope slides will be preferred in terms of their transmission. Generally, microfluidic chips are fabricated from microscope slides because the increased thickness of microscope slides compared to cover slides gives the fabricated chips greater strength, which can be particularly important when using high pumping speeds. In addition, liquid inlet and outlet holes are typically drilled into one wall of the microfluidic chip, and drilling cover slides is harder than drilling a microscope slide, because the thin cover slide is much more likely to crack during drilling than the thicker microscope slide. In this Chapter, we use microfluidic chips solely fabricated from two pieces of borosilicate cover glass, as we are working with high reflectivity mirrors, and thus it makes sense to maximise the chip transmission, even at the expense of more complicated chip fabrication. In later Chapters, when using mirrors with a lower reflectivity of 99%, chips fabricated using microscope slides can be used because the transmission in this case is dominated by the higher mirror losses rather than the chip losses.

3.5.2 PDMS Chips

The first lab-fabricated microfluidic chips tested were fabricated using polydimethylsiloxane (PDMS), a soft, transparent polymer. PDMS is commonly used for rapid-prototyping of microfluidic chips [73].

Two different types of PDMS chips were fabricated. In the first instance, chips were fabricated in a clean room according to the protocols described by Campo et al. [178], with advice from Siti Aminah Setu, a D.Phil. student in the Dirk Aarts group. An embossed silica wafer (which can be reused many times) was produced, which acts as a template for the PDMS chip. A 65 μm thick SU-8 (SU-8 2025) photoresist layer was spun onto a silica wafer with a spin speed of 500 revolutions per minute (rpm) for 25 seconds, followed by a spin coating speed of 1500 rpm for 30 seconds. The substrate was then soft baked on a hot plate at 65°C for 3 minutes, and at 95°C for a further 5 minutes to remove the photoresist solvent. After the substrate cooled to room temperature, a UV mask with a negative of the chip design (see Figure 3.11) was placed over the coated wafer, and the system was cured using a collimated UV source. A post-exposure bake was then performed at 65°C for 1 minute, and 95°C for 5 minutes. The photoresist was then developed in the SU-8 developer for 10 minutes to dissolve the unexposed SU-8, and the system was rinsed with isopropyl alcohol to remove any developer residue. The embossed silicon wafer can then be used to imprint the 1 mm wide, 65 μm deep channels into a layer of PDMS as it is cured.

PDMS prepolymer (DOW Corning) was thoroughly mixed with curing agent at a weight ratio of 10:1 and degassed by spinning in a centrifuge for 10 minutes at 1500 rpm. 3 mL of this mixture was then poured onto the embossed silicon wafer and cured for over an hour at 80°C. After curing, the PDMS layer (thickness of 500 μm) was peeled from the silicon wafer and cut to a size of 2.5 cm by 5 cm. Three holes with $<$1 mm diameter were punched through the PDMS layer with a syringe needle at the positions marked on Figure 3.11, to act as inlets/outlets. The PDMS layer and a 140 μm thick glass cover slip were then treated with oxygen plasma in a plasma cleaner (PPC-32G, Harrick). This process activates the silica bonds at the surface of both the glass and PDMS, producing -Si-OH end groups on both surfaces. The PDMS layer and glass cover slip are then brought into contact, bonding together via a condensation reaction to enclose the microfluidic channel and complete the chip.

PDMS blocks (5 mm in height), with holes bored through with a syringe needle, were then attached at the inlet/outlet holes by treatment with oxygen plasma. A mixture of PDMS prepolymer and curing agent was then applied at the edges of the blocks and cured for 1 hour at 80°C to provide increased mechanical strength. These blocks allow 1 mm capillary tubing to be connected to the PDMS microfluidic chip, such that liquid samples can be pumped through with a syringe pump. The completed microfluidic chip is then mounted on a 1 mm thick glass microscope slide to provide a rigid point at which the chip can be clamped in place inside the ringdown cavity.

Intially, the optimum angle of insertion for a water-filled PDMS/glass chip was found, by measuring the ringdown time as a function of angle of incidence. A plot of the theoretical and experimental curves is shown in Figure 3.12. In this case, the cavity length was 87.5 cm rather than the 58.5 cm used for the majority of the measurements carried out in this Chapter, so the ringdown values discussed here should not be compared directly with those measured with a shorter cavity. Of course, the measured transmission values can still be

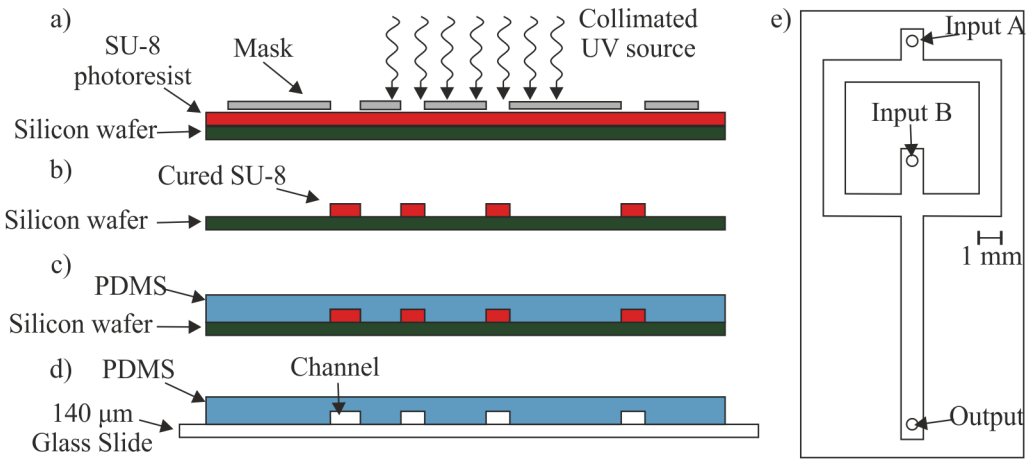


Figure 3.11: (a) Curing SU-8 photoresist. (b) Embossed silicon wafer template. (c) Imprinting channels into PDMS layer prior to curing. (d) Completed PDMS chip.(e) Channel design, with labelled inlet and outlet holes.

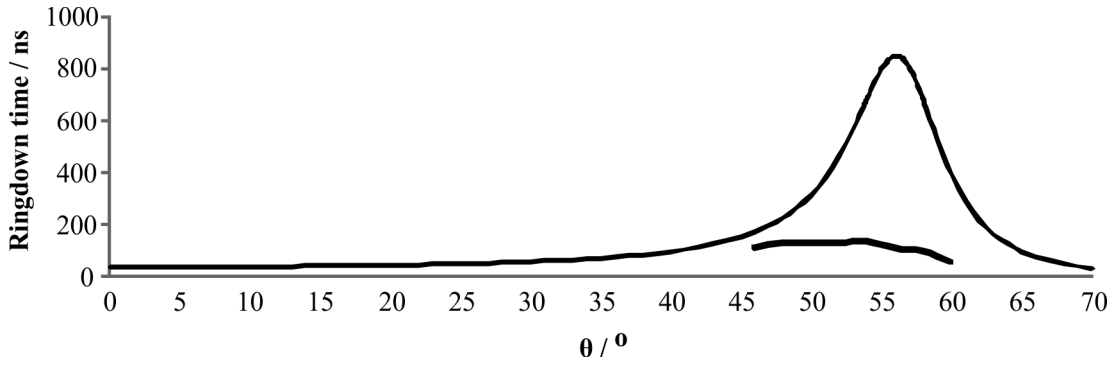


Figure 3.12: Theoretical and experimental ringdown time / ns versus incidence angle ($\theta/^\circ$) for water-filled glass/PDMS chip, in 87.5 cm length cavity.

compared directly. The PDMS chip walls are fabricated from borosilicate glass on one side ($n_{\text{glass}} = 1.52$) and PDMS on the other side ($n_{\text{PDMS}} = 1.42$ [179]). The theoretical optimum angle is therefore 56.1°, where the reflection loss is 0.14%. Experimentally, no real optimum angle was found, as can be seen in Figure 3.12. Indeed, the maximum ringdown time recorded was only 135 ns, compared with the predicted maximum value of 848 ns. This corresponds to a experimentally determined chip loss of 2.0%, far too high for cavity experiments. This is most probably a result of increased scattering losses caused by particulates adhering to the soft elastomeric surface of the PDMS chip, which remains somewhat 'tacky' after fabrication. In non-clean room environments, this makes bare PDMS a difficult substrate to handle in a cavity.

In addition, large variations in ringdown time were observed upon change in flow rate, or movement of the capillary tubing connected to the PDMS chip. This was attributed to deformation of the chip. PDMS is a soft elastomer capable of expansion under pressure [180], especially when such a thin layer is used. Deformation is particularly undesirable during absorption measurements, as it leads to increased scattering losses and lensing effects, as well as altering the absorption pathlength.

For these reasons, the second PDMS chip fabricated had two glass walls, with the PDMS layer only acting as an internal pattern for the channels, but not coming into contact with the laser beam path. This chip is shown in Figure 3.13, and was fabricated by Yan Zhao, a Ph.D. student in Professor Hywel Morgan's research group at the University of Southampton. In this case, a cavity length of 58.5 cm was used. The incidence angle was optimised, and a ringdown value of 101 ns was recorded when the chip was filled with water, corresponding to a chip loss of 1.7%. The loss is too high for this chip to be used in a cavity experiment, although it is slightly lower than that determined using the first PDMS chip.

3.5.3 Thiolene Chip

The thiolene-glass chips were designed and manufactured by Joanna Davies, a Ph.D student in the group of Dr. João Cabral in the Department of Chemical Engineering at Imperial College, London. Thiolene glue (a photopolymerising adhesive) is sandwiched between two pieces of glass (either 141 μm thick glass cover slips or 1 mm thick glass microscope slides), held a fixed distance of 320 μm apart by two spacers, as illustrated in Figure 3.14(a). An acetate film printed with a negative of the chip design (shown in Figure 3.14(b)) is then placed over the top layer to act as a mask, and the system is cured under a collimated UV source in a process known as frontal photopolymerisation [181]. A fixed dose of UV light is delivered to ensure that the thiolene in the unmasked regions is completely cured, whilst the masked regions remain uncured. The uncured thiolene is then flushed out of the chip with air and acetone at elevated temperatures to form the microfluidic channels. Finally, the channels are inspected using an inverted microscope (IX71, Olympus) to ensure that no defects or contaminants are present (Figure 3.15). Nanoports (Upchurch Scientific) were fitted to holes drilled through one of the glass walls, forming three inlets and one outlet capable of connection to a syringe pump. The completed microfluidic chip is then mounted on a 1 mm thick glass microscope slide to provide a rigid point at which the chip can be clamped in place inside the ringdown cavity.

A significant difference in chip quality was noticed when using fresh thiolene, compared with aged thiolene (which has been stored for over six months). Figure 3.15 compares images of a chip fabricated using fresh thiolene (a) - (c) and aged thiolene (d) - (f). It is known that the polymerisation of thiolene under ambient conditions is slow, but significant over a timescale of several months. Once polymerisation has begun to occur, it becomes difficult to flush the thiolene out of the channels without leaving behind significant residues. These residues significantly impact the ringdown measurements, as any residues cause light to scatter significantly. Indeed, in these cases, typically no ringdown signal will be observed.

It is found that the ringdown times recorded for the thiolene chips vary significantly both between chips, and across the same chip. One factor is the flushing out of thiolene. We typically record the best ringdown signals from a chip when the laser beam impinges the chip in a region that was cleared of unpolymerised thiolene near the beginning of the flushing process. As the channel length increases, the pressure builds up

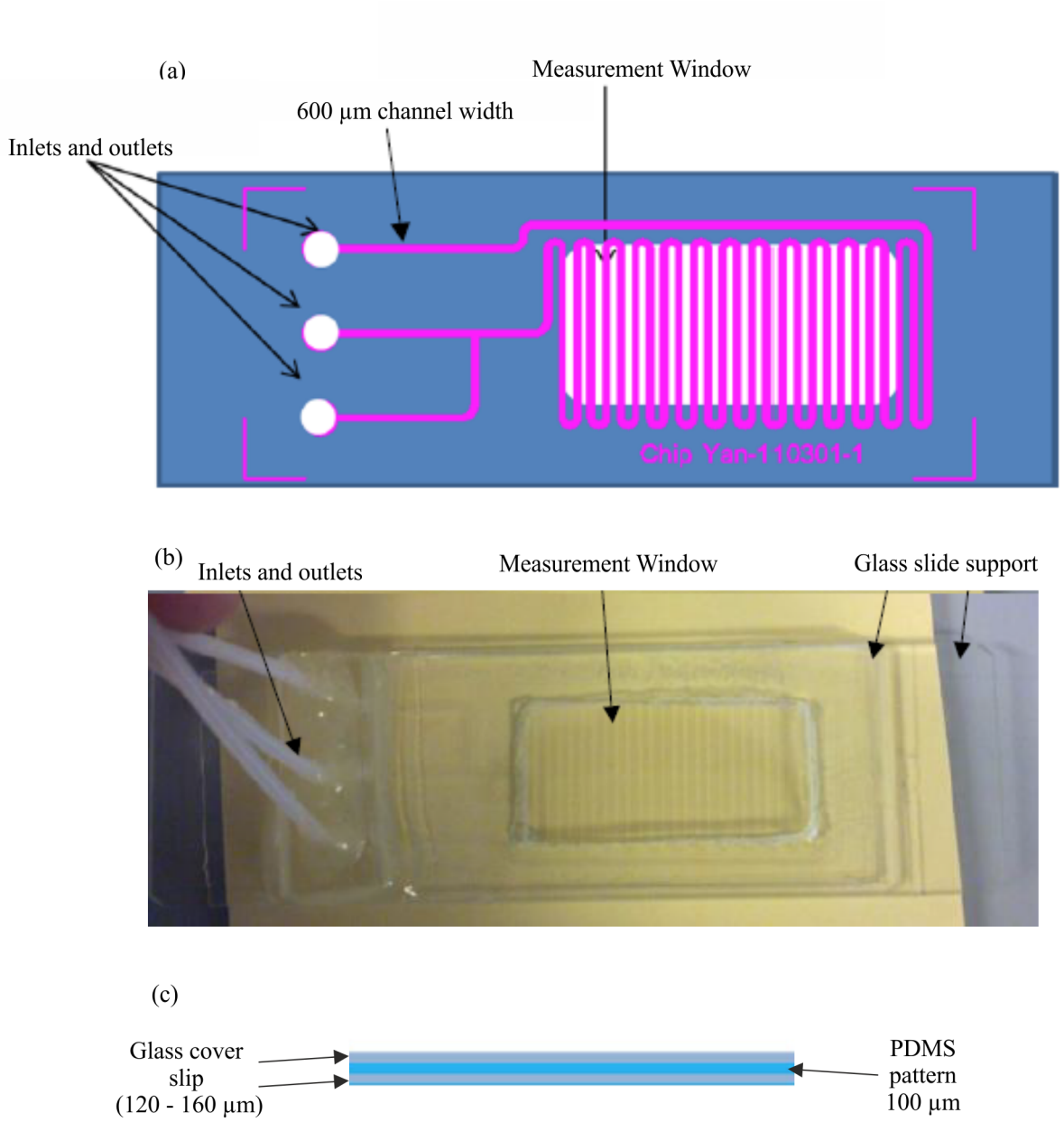


Figure 3.13: (a) PDMS design for second chip, provided by Yan Zhao from the University of Southampton. (b) Photograph of glass/PDMS device. (c) Schematic of side-view, illustrating thickness of walls and PDMS layer in measuring window.

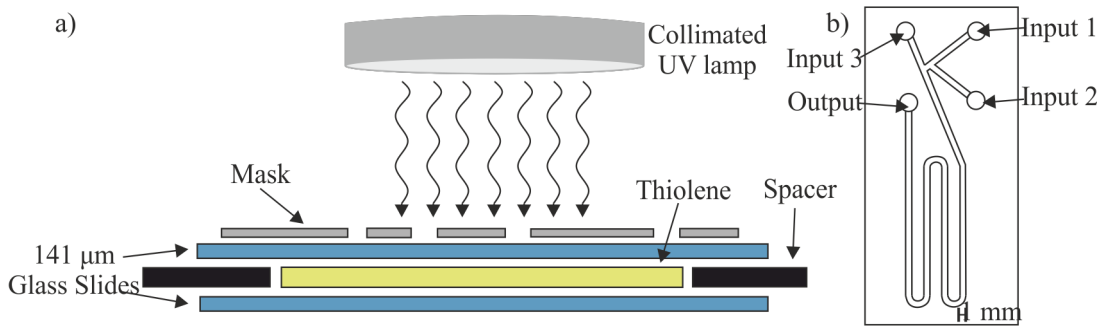


Figure 3.14: (a) Schematic of process used to manufacture thiolene-glass microfluidic chips. (b) Mask design.

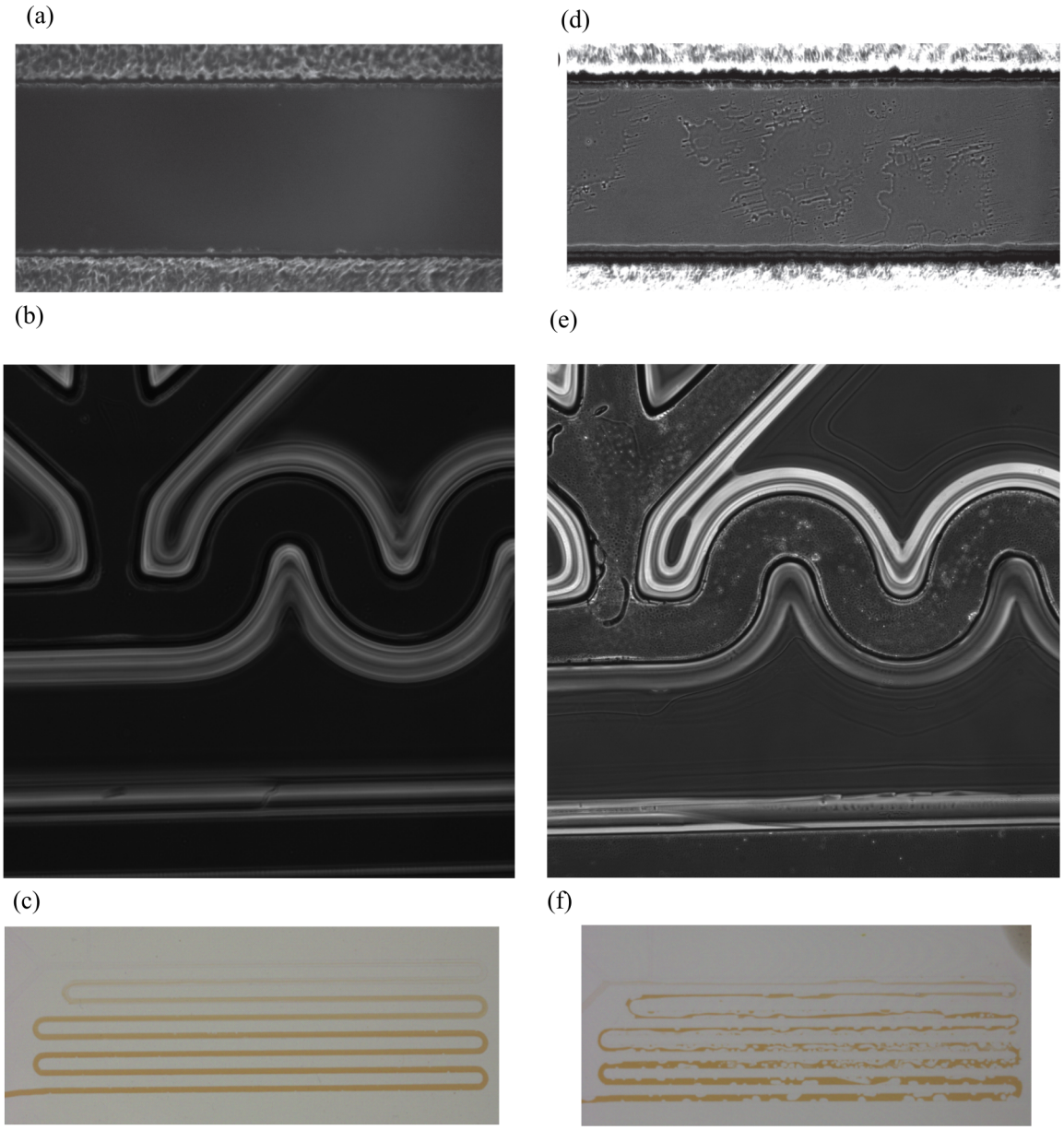


Figure 3.15: Microscope images of chip fabricated using fresh thiolene (a) - (c). Images of chip fabricated using old thiolene (d) - (f). The problem of thiolene residue remaining in the channels can clearly be seen.

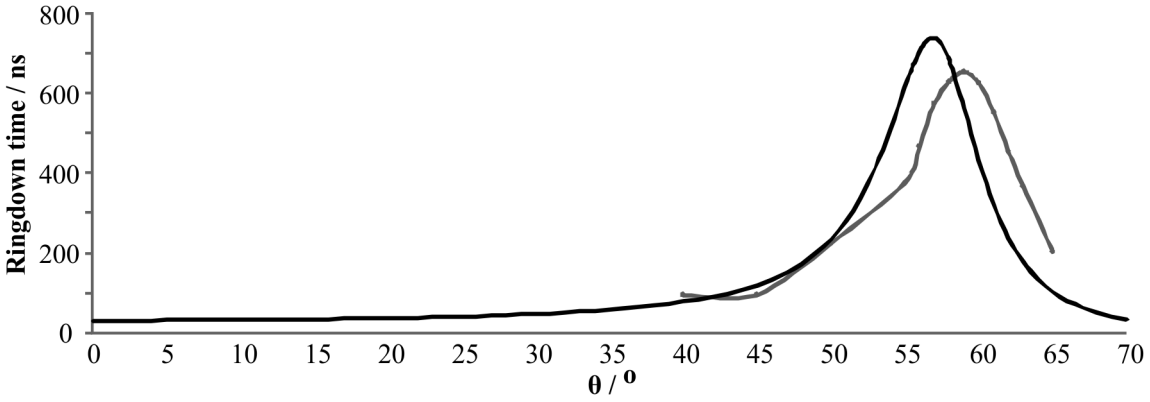


Figure 3.16: Theoretical and experimental ringdown time versus incidence angle ($\theta/^\circ$) for water-filled glass/thiolene chip, in 87.5 cm length cavity.

and it becomes harder to flush thiolene out of the channels, thus the ringdown tends to drop as the laser beam impinges the chip further along the channel. In addition to this general trend there are significant fluctuations arising from defects in the channel or poorly cleaned regions.

The dependence of the ringdown time on chip angle for a cavity with an inserted thiolene chip was measured in a cavity of length 87.5 cm, and is presented in Figure 3.16. The chip walls are fabricated from borosilicate glass on both sides ($n_{\mathrm{glass}} = 1.52$). The theoretical optimum angle is therefore 56.9°, where the reflection loss is only 0.19%. Experimentally, the optimum angle is slightly higher (59°), as can be seen in Figure 3.16. In this case, the maximum ringdown time recorded was 654 ns, corresponding to a chip loss of 0.242%. This is an excellent result, as the chip loss in this case is comparable to that obtained using a commercial flow cell. This chip had a channel height of 1 mm, and a total wall thickness (comprising two cover slips) of only 282 μm. Unfortunately, this was not necessarily a reproducible result, as the quality of the thiolene chips varied significantly.

3.6 On-chip measurements

3.6.1 Permanganate calibration

A $KMnO_4$ pathlength and detection sensitivity calibration was carried out on a thiolene chip with a channel height of 600 μm inserted into a 58.5 cm cavity. The measured ringdown time for a chip filled with pure water was 271 ns, with a standard deviation of 0.6 ns. Determining the detection limit from the uncertainty in the τ_0 measurement, as described in Section 3.4.2, we have $\Delta\tau = 3\sigma = 1.8$ ns, which when substituted into Equation 2.17 yields an absorbance detection limit of $\kappa_{\mathrm{min,s}} = 1.0 \times 10^{-3}$ cm^{-1}. This corresponds to a concentration detection limit for $KMnO_4$ of approximately 214 nM in an illuminated volume of (132 $\pm$ 3) nL,

which is in qualitative agreement with the concentration at which a change in ringdown time can be discerned relative to the reference measurement.

The sensitivity of absorption measurements on this chip was established using aqueous permanganate solutions, in a similar manner to that described for the flow cells (Section 3.4.3). A concentration series of permanganate from 10^{-4} to 10^{-7} M was investigated. Solutions were flowed at 0.2 mL/min for 5 minutes, and τ was acquired under static conditions, although it should be noted that there was no observed difference between the stability of the ringdown time acquired under static or flowing conditions.

The pathlength across the chip, measured using a micrometer, was found to vary by several tens of micrometres, as the two chip faces were not fixed perfectly parallel to each other. In order to ensure accurate determination of the pathlength at the intersection point of the laser beam, we use the known α for permanganate at 532 nm, which was measured using a UV-vis spectrometer (Figure 3.5). The pathlength is determined from the gradient of a plot of κl versus concentration, shown in Figure 3.17, and was found to be 466 ± 10 μm.

The detection limit can also be estimated using the regression method, as described in Section 3.4.2. The value of $\kappa_{\mathrm{min,r}} = 5.2 \times 10^{-3}$ cm^{-1} obtained in this way is somewhat higher than $\kappa_{\mathrm{min,s}} = 1.0 \times 10^{-3}$ cm^{-1}, as expected.

For permanganate concentrations less than 25 μM, no chip degradation was observed. However, after higher concentrations (> 25 μM), were flowed onto the chip, τ_0 could not be recovered to its previous value. We believe that this is caused by damage to the thiolene layer of the chip at higher permanganate concentrations. However, even with this degradation in absorption signal, absorption measurements could still be made at these high concentrations, since by alternating τ_0 and τ measurements the overall decrease in τ_0 was accounted for.

The drop in ringdown time while using the chip may be a significant problem. Many microfluidic chips are designed to be single-use, disposable items, as they are cheap and rapid to fabricate. In our case, it can take a significant amount of time to find a region of the chip which can be probed with relatively high sensitivity in a ringdown experiment, and thus any rapid decay of the ringdown time with use is problematic. For our potassium permanganate experiments, a drop in ringdown time is recorded at the highest concentrations, and the original ringdown time cannot be recovered with washing. In later experiments (Chapter 6), we will see that the use of toluene with thiolene channels is also problematic.

3.6.2 Reaction monitoring: Belousov-Zhabotinsky

The Belousov-Zhabotinsky (BZ) reaction forms part of a class of reactions known as 'oscillating reactions' [182]. Ce(IV)/Ce(III) is used to catalyse the oxidation and bromination of malonic acid by BrO_3 in H_2SO_4

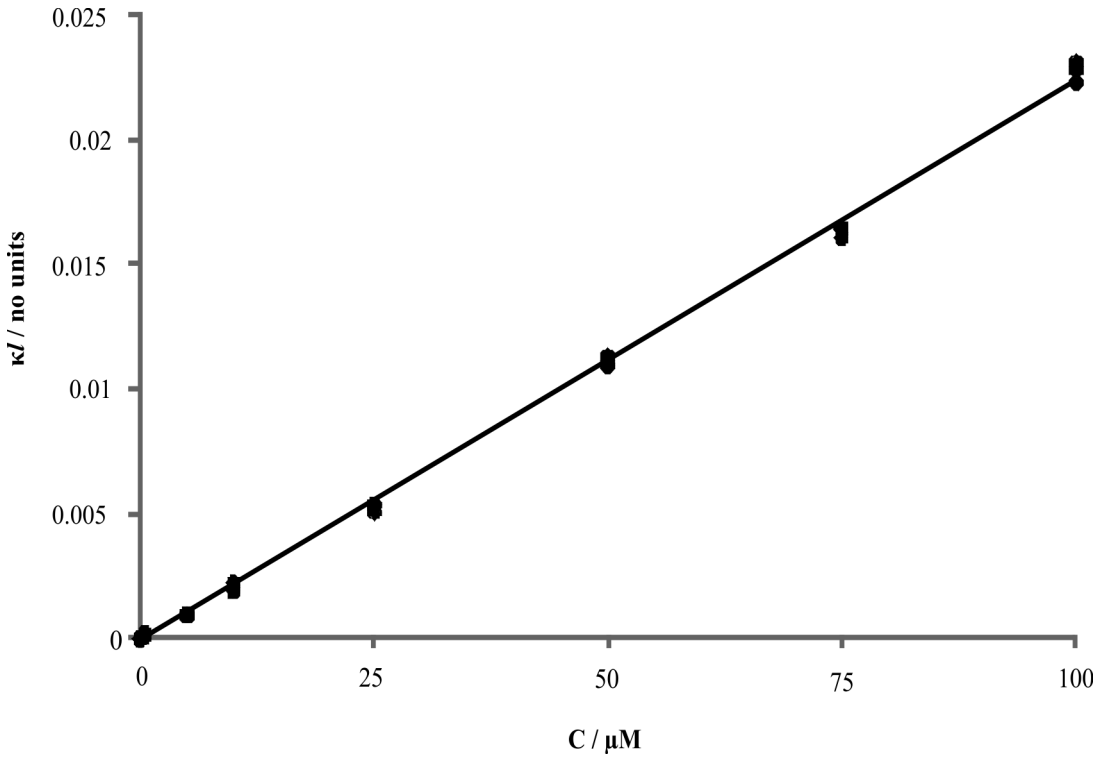


Figure 3.17: Plot of measured absorbance κl versus permanganate concentration determined in a thiolene chip. The pathlength through the chip, determined from the gradient, is 0.0466 cm.

in a periodic cycle accompanied by colour changes between red and blue when performed in the presence of Ferroin indicator. When red, the solution absorbs at our operating wavelength of 532 nm, which allows the progress of the reaction to be monitored. As a first proof-of-concept of the ability of the system to follow a dynamic reaction system, the BZ reaction was performed on a thiolene chip inside the cavity, and the frequency of the reaction's oscillations measured. The results were then compared with similar measurements on the bulk reaction.

For simplicity, the reagents (5 ml of 0.23 M $NaBrO_3$ aqueous solution, 5 ml of a 0.31 M malonic acid and 0.059 M NaBr aqueous solution, 5 ml of a 0.019 M $Ce(NH_4)_2(NO_3)_3$ and 2.7 M H_2SO_4 solution, with 0.1 ml of 0.0125 M ferroin indicator) [182] were mixed in bulk prior to being injected into the chip at a constant flow rate of 0.1 mL min^{-1}. Once the continuous flow had passed the laser beam position, the flow was stopped and the oscillations were recorded under static conditions. Ringdown traces were averaged 32 times on the oscilloscope, and the resulting traces were transferred to the data acquisition computer once per second. The oscillations were then followed by monitoring the change in τ over time. To obtain a set of reference data for comparison, the experiment was repeated at the same concentration in a 1 cm cuvette and monitored as a function of time, using a standard single-pass 532 nm absorption measurement using a photodiode (DET10A/M, Thorlabs).

A series of different concentrations of the indicator (Ferroin) were used to discover the optimum concentration

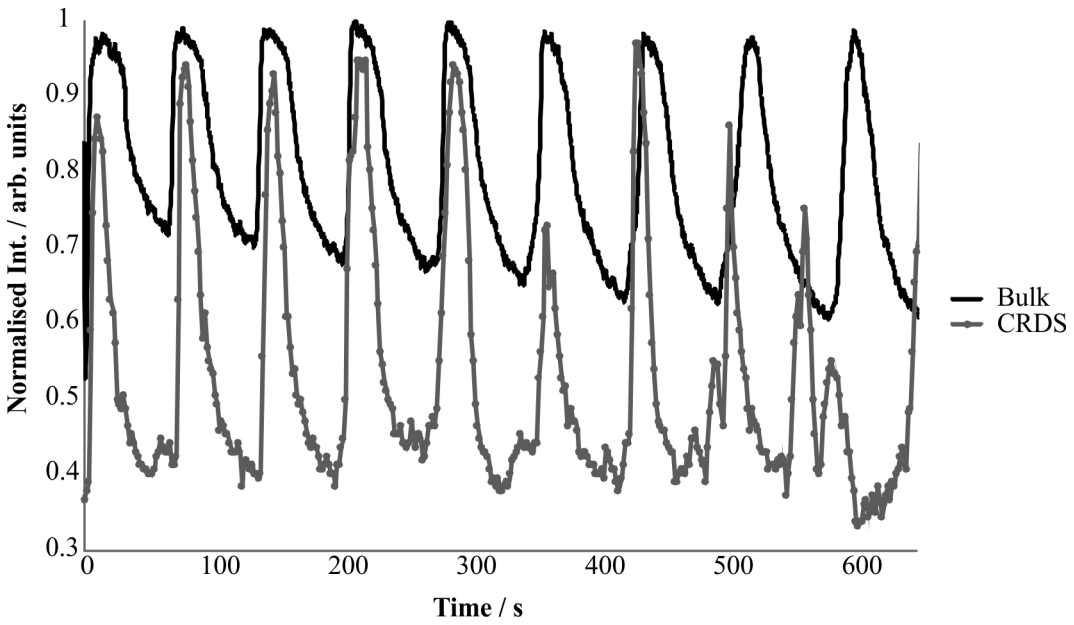


Figure 3.18: Belousov-Zhabotinsky oscillations monitored on a microfluidic chip and in bulk.

at which the reaction can be monitored both on a microfluidic chip via CRDS and in a larger volume via traditional single-pass absorption measurements. Figure 3.18 is an example data set recorded with a 2.5×10^{-4} M concentration of ferroin. Under our reaction conditions, the oscillation period of around 70 seconds is similar on-chip and in bulk solution. After several oscillations, bubbles of CO_2 begin forming in the microfluidic chip, leading to poorly resolved oscillations; however these do not appear to affect the period of oscillation. These results demonstrate the ability of the system to monitor the changing concentration of a reagent that absorbs at 532 nm. Obviously, the formation of bubbles observed is particularly undesirable in a microfluidic chip, as the pressure build-up can cause the chip to crack. There are a number of variations on the BZ reaction that use slightly different chemicals, and thus the production of carbon dioxide during the reaction can be avoided [183].

3.6.3 Droplet monitoring

In the final demonstration of this Chapter, the CRDS set-up was used to follow the flow of droplets or 'slugs' of an aqueous phase seeded in a toluene carrier phase, within a microfluidic channel. A diagram of the chip is shown in Figure 3.19(c). Figures 3.19(a) and 3.19(b) clearly show the change in ringdown time for two different sets of flow conditions as slugs of aqueous Rhodamine solution pass through the laser beam. To acquire these data, the toluene carrier phase was injected into the chip shown in Figure 3.19(a) through input 2 at a flow rate rate of 0.003 mL min^{-1} (Figure 3.19(a)) or 0.05 ml/min (Figure 3.19(b)), and a 10^{-5}M aqueous solution of Rhodamine 6G was flowed through input 1 at 0.005 mL min^{-1} (Figure 3.19(a)) or 0.025 mL min^{-1} (Figure 3.19(b)).

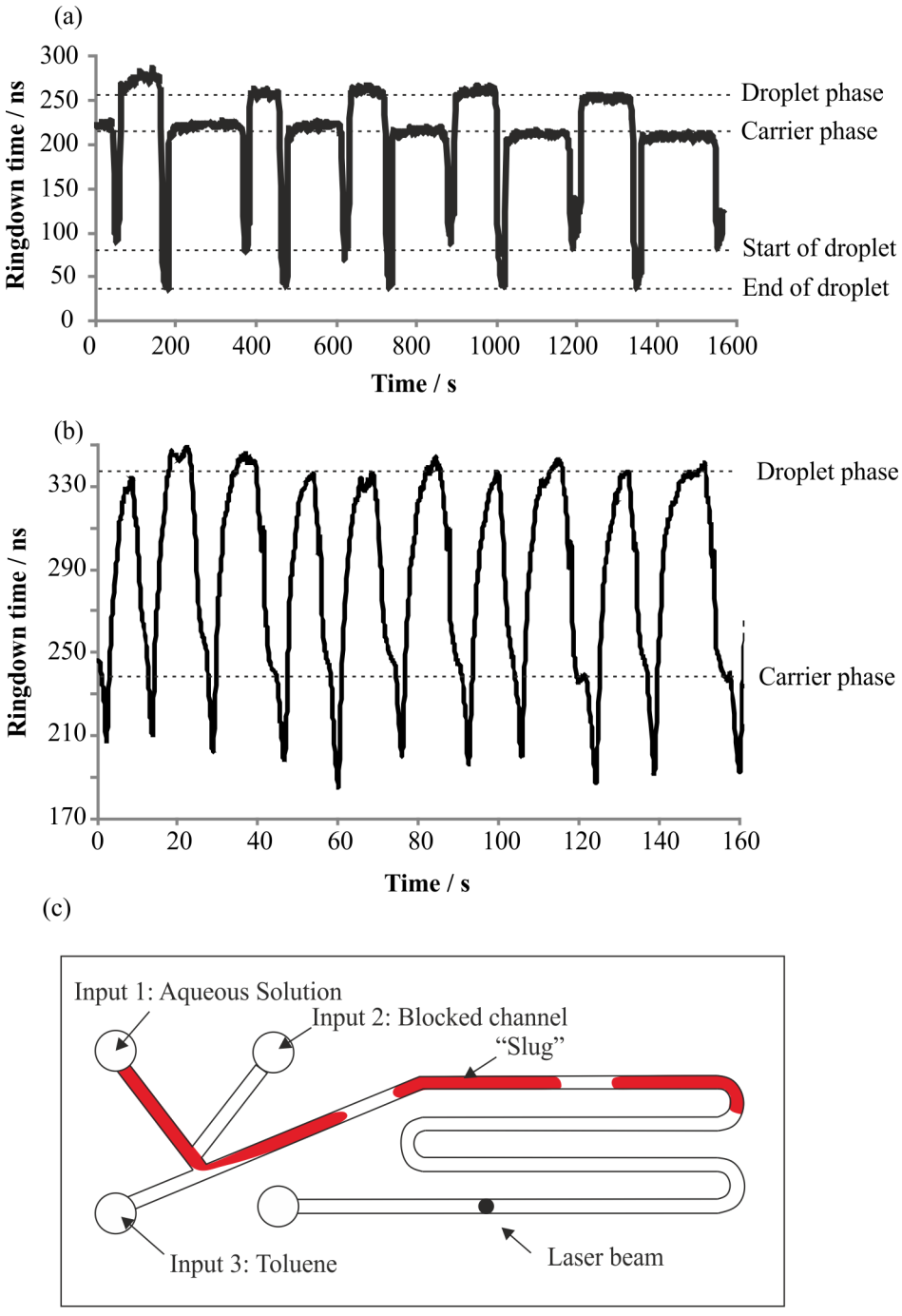


Figure 3.19: Droplet flow analysis using CRDS on a microfluidic chip. The ringdown time is tracked as droplets of 1×10^{-6} M Rhodamine 6G solution in a toluene carrier phase are flowed through a thiolene-glass chip at a total flow rate of (a) 0.008 mL min^{-1} and (b) 0.075 mL min^{-1}. (c) Schematic of chip employed for these single droplet measurements.

The behaviour of τ has several notable features. A clear change in ringdown time is seen as the aqueous (droplet) and toluene (carrier) phases pass through the laser beam. For the data shown in Figure 3.19(a), for example, the ringdown time switches from ~ 220 ns for the toluene phase to ~ 260 ns for the aqueous phase. As described earlier, the mounting angle of the chip within the cavity has been optimised for measurements on aqueous phases. The refractive indices of water (n = 1.333) and toluene (n = 1.496) differ sufficiently that the ringdown time is longer for the aqueous phase than for the toluene phase, even though Rhodamine absorbs light at the wavelength of the laser. For experiments in which quantitative absorption analysis of droplets is the goal, the chip mounting angle should be optimised to achieve the greatest difference in ringdown time between the droplet and carrier phases. This was the case for the data shown in Figure 3.19(b), in which the ringdown times are ~ 240 ns for the toluene phase and ~ 340 ns for the aqueous phase.

At low flow rates, a sharp reduction in τ is observed as the boundaries of each droplet pass through the laser beam. This is caused by the meniscus at the droplet/carrier phase boundary forming a lens that scatters the incident laser light out of the cavity, dramatically reducing the ringdown time. The consistent form of these scattering signals suggests that the topology of the interface between the two immiscible solutions is identical for each droplet, and a quantitative analysis of the signals could even be used to study droplet morphology. This structure is much less visible in Figure 3.19(b), mostly due to the fact that the droplet flow rate in this experiment was close to the limiting time resolution imposed by our current fairly slow data acquisition system.

These results demonstrate the ability of the two-mirror CRDS system to interrogate and distinguish between individual droplets. The acquisition time of the ringdown is of the order of hundreds to thousands of nanoseconds. With an improved data transfer system (currently limited at 4Hz), measurements at kHz or even MHz data rates should become possible, allowing the spatio-temporal resolution of fast moving droplets, commensurate with kHz microfluidic label-free droplet production systems.

3.7 Conclusion

In this Chapter, we have investigated the application of CRDS to small volume analysis. We have found that the highest sensitivity is achieved using commercial fused silica flow cells at Brewster's angle incidence. We have also tested a variety of microfluidic chips and found that the chip manufacture process plays a major role in determining the measured ringdown time. For example, hydrofluoric acid-etched channels have been shown to be incompatible with CRDS interrogation. Chips with open PDMS faces cannot be used because of the 'tackiness' of the PDMS, which causes the surface quality to deteriote rapidly in use outside a cleanroom environment. Successful results have been obtained using a thiolene chip with two cover slides for chip walls. Additionally, we have demonstrated the application of on-chip analysis to following reaction kinetics

and droplets. In the following Chapter, we apply the highest sensitivity set-up, using flow cells, to sensitive analysis of trace water analytes.

Chapter 4

Water Analysis

4.1 Introduction

Sensitive and selective chemical analysis of trace analytes in water remains a challenge. A plethora of colour reactions have been developed in order to convert colourless or weakly absorbing species into strongly absorbing, visible derivatives [62, 63]. Yet, even with such strong signal amplification, the detection of extremely low concentrations of even these strongly absorbing products remains a challenge. This is especially true when employing microfluidic sensing platforms. Sensors based on microfluidic platforms are attractive, consuming less power and fewer reagents than their larger-scale counterparts, and opening the way to remote sensors able to operate for long periods of time without human intervention. However, the tiny sample volumes and short optical pathlengths inherent in microfluidic sensors necessiates the development of highly sensitive detection techniques.

In this Chapter, we demonstrate the application of the single-wavelength CRDS set-up outlined in Chapter 3 to the sensitive detection of two key chemicals present in aquatic environments: nitrite and iron(II). The importance and detection of both analytes will be outlined first.

Table 4.1: Typical concentrations of nitrite and iron in different aquatic and marine environments. Where single values are provided, these represent maximum concentrations set by the WHO.

Water sample	[Nitrite] / nM	[Iron] / nM
Tap water	62,500	3,600
Rivers	220	300 - 25,000
Coastal waters	100 - 50,000	0.1 - 10
Open ocean	100 - 50,000	0.02 - 2

4.1.1 Nitrite

Nitrite is a reactive chemical species which plays an important part in the global carbon and nitrogen cycles, as well as being a key marine nutrient required for phytoplankton growth [184, 185]. In seawater, nitrite levels range from 0.1 to 50 μM, but are most commonly below 0.2 μM [186]. In river water, European Union guidelines set a maximum of 0.01 mg L^{-1} (0.22 μM) for rivers supporting salmon fisheries [187], but significantly higher river values have been been reported across Europe [188]. At excess levels, nitrite is harmful to both humans and aquatic life. Indeed, the World Health Organization (WHO) lists nitrite as one of the chemicals presenting the greatest health concern in some natural waters [189]. Nitrates and nitrites are most commonly introduced into household water supplies via contamination of the source water from either sewage or agricultural runoff, and can be difficult to remove [189]. Nitrite is the more reactive (and hence more toxic) form, and excess nitrite is implicated in methaemoglobinaemia ('blue baby' syndrome), as well as possibly in the production of several known carcinogens [190]. The current guidelines for short-term exposure of nitrates and nitrites provided by WHO are 3 mg/L (62.5 μM) for nitrite, and 50 mg/L (807 μM) for nitrate [189].

Nitrite (and nitrate) detection has recently been the subject of three excellent reviews [107, 133, 191]. Spectroscopic methods, including direct UV absorption [192], indirect visible absorption [22], and fluorescence [193, 194] are the most commonly used, owing to their superior limits of detection and relative experimental simplicity [107]. Of the spectroscopic methods, determination of nitrite with the Griess Assay, first published in 1879 [195], is by far the most common detection technique [107]. In the Griess Assay, nitrite is acidified and undergoes diazotisation with a primary amine (such as sulphanilamide), followed by coupling to an aromatic molecule to produce an intensely coloured azo dye, which has an absorption maximum in water of around 80,000 M^{-1} cm^{-1} at 520 nm [22, 63]. The dye is formed in a 1:1 ratio from nitrite in the sample. Thus, by monitoring the reaction using spectrophotometry at a wavelength at or close to the absorption maximum for the azo dye, measurement of nitrite concentrations in water samples can be made. The Griess Assay owes its popularity to the high sensitivity that can be achieved owing to the dye's high peak absorbance, and to the high selectivity of the reaction, owing to the nitrite-specificity of diazotisation. Both of these factors mean that sample pre-treatment is not usually required.

An outline of the Griess reaction mechanism is shown in Figure 4.1. The mechanism was examined in detail by Fox in 1979 [196]. Nitrite is first acidified to produce the electrophilic nitrosyl cation, which then undergoes diazotisation with the electron-donating primary amine group of sulphanilamide, via addition and then internal rearrangement, to produce the diazonium cation. Nitration occurs in preference with the primary amine over the aromatic ring because the primary amine group is a better nucleophile than the benzene ring. Internal rearrangement to form the diazonium ion has been previously shown to be the rate-limiting step [196]. The diazonium cation then rapidly couples to N-(1-Naphthyl)ethylenediamine dihydrochloride (NED), to produce the intensely coloured azo dye. When using the Griess reaction for nitrite analysis, both

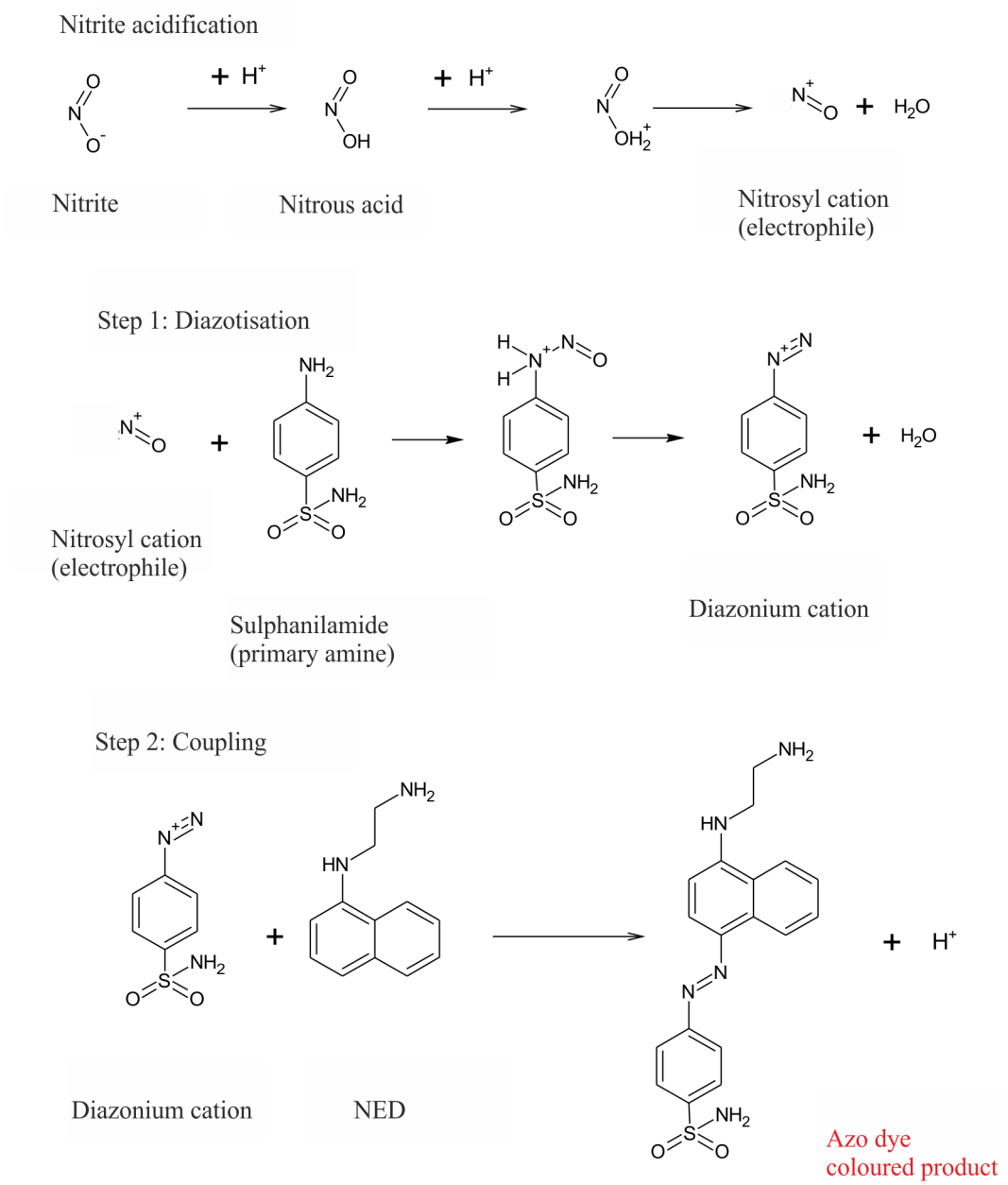


Figure 4.1: An outline of the Griess reaction mechanism, highlighting the need for nitrite acidification, followed by the two key steps: diazotisation and coupling, which lead to the formation of the coloured azo dye. NED stands for N-(1-Naphthyl)ethylenediamine dihydrochloride.

sulphanilamide and NED are present in excess over the unknown nitrite concentration to be measured. We wait for the reaction to complete before carrying out the analysis. Under these experimental conditions, the amount of nitrite present is directly related to the azo dye production.

In addition, it should be noted that the chemical detection of nitrate usually occurs via the detection of nitrite, owing to nitrite's higher chemical reactivity. Commonly, the nitrite concentration of a sample is determined, and then the sample is reduced on a reducing column (using, for example copperised cadmium [197]) in order to convert any nitrate present to nitrite. The nitrite concentration of the sample is then reassessed, and the difference between the measurements before and after sample reduction enable the determination of the nitrate concentration. In our experiments, we focus on the detection of nitrite, for simplicity, and note only that extrapolation of the experimental set-up to include detection of nitrate is a relatively trivial extension, and should result in a similar (if not identical) dynamic range and detection limit to that established here for nitrite.

4.1.2 Iron

Iron is an essential element for all known living organisms [198]. The concentration of dissolved iron in marine and aquatic environments varies widely, depending to a large extent on the dissolved oxygen concentration. The median iron concentration in rivers has been reported to be 12.5 μM [189], with a range of 3 - 25 μM [198]. In contrast, in the open ocean, iron is present at such low concentrations (0.02 - 2 nM) that it is thought to be one of the limiting factors for phytoplankton production [198]. The development of methods for quantifying iron in surface sea water is therefore of growing importance. In drinking water, iron levels are considered primarily in terms of their consequences for taste and appearance, rather than in the context of any health issues [189]. In the UK, the maximum level of iron permitted in tap water is 3.6 μM [189].

Iron concentrations can be determined colourimetrically using any one of several reactions [62, 199, 200], including complexation with thiocyanate for Fe^{3+} [201], complexation with 4,7-diphenyl-1,10-phenanthroline (known as bathophenanthroline), for Fe^{2+}, [202] and complexation with 3-(2-pyridyl)-5,6-bis(4-phenylsulfonic acid)-1,2,4-triazine (known as ferrozine) for Fe^{2+} [203]. The maximum optical absorption coefficient achieveable using the thiocyanate method is reported to occur at 480 nm [201]. However, in order to minimise absorption from Fe^{3+}, which occurs at short wavelengths, detection is often carried out at 500 nm where the absorption coefficient is reported to be 18,150 M^{-1} cm^{-1} [204]. The maximum absorption coefficient when using the ferrozine method is reported to be 64,300 M^{-1} cm^{-1} at 562 nm [203], falling to an estimated 40,200 M^{-1} cm^{-1} around 532 nm. Finally, the maximum absorption coefficient of the bathophenanthroline method is reported to be 51,600 M^{-1} cm^{-1} at 533 nm [202]. We chose to use the bathophenanthroline method as this method had the highest absorption

coefficient at the wavelength of our laser (532 nm). The reaction scheme is shown in Figure 4.2. It should be noted that Fe^{3+} can also be detected using Fe^{2+}-specific reagents after reduction to Fe^{2+} (see, for example, [205]).

The concentrations of both nitrite and iron in tap water, river water and oceans are summarised in Table 4.1

4.2 Experimental

The experimental set-up used was that outlined in Section 3.4.3. The detection limit of the set-up at 532 nm was previously established (Section 3.4.3) through calibration with solutions of potassium permanganate in a 1 mm flow cell, and was determined to be 29 nM, or 1.4×10^{-4} cm^{-1}.

4.2.1 Detection of nitrite via the Griess assay

Nitrite was quantified using the well-known Griess assay, described in Section 4.1.1. The assay was first published in 1879 [195], and several versions of this reaction now exist. The method we chose to use was that described by Sieben et al. [22] and Tovar et al. [186]. Reagents were purchased from Sigma Aldrich and used without further purification. The "Griess reagent" was created by dissolving 0.5 g of sulphanilamide (Sigma Aldrich, S9251) in 50 mL of MilliQ water and 5 mL of concentrated hydrochloric acid (analytical reagent grade) in a 500 mL volumetric flask. To this was added 0.05 g of N-(1-Naphthyl)ethylenediamine dihydrochloride (Sigma Aldrich, 33461), and the resulting solution was made up to 500 mL with MilliQ deionised water. Standard nitrite solutions were created by serial dilution in MilliQ water from a standard 1 M sodium nitrite solution (Sigma Aldrich, 35271).

To perform a nitrite determination measurement, the Griess reagent and nitrite solution were mixed in a beaker and left to stand for at least 10 minutes to ensure that the Griess reaction had reached completion before the azo dye absorption was measured.

Conventional UV/vis analysis was first carried out using a commercial spectrometer (Varian Cary 100 Bio UV/vis), analysing a few mL of sample in a 1 cm cuvette. Eleven different nitrite concentrations were investigated, in the range 0.1 - 75 μM.

The Griess reaction was then analysed in a 1 mm flow cell using our CRDS set-up. In this case, rather than using MilliQ water to determine the 'blank' τ_0 value for our ringdown measurements, a 1:1 mixture of MilliQ water and the Griess reagent was employed. This was found to be essential in order to eliminate contributions to the signal from trace quantities of nitrite present in the MilliQ water and/or the reagents used to formulate the Griess reagent. Absorption measurements were made using the 1 mm flow cell. For each measurement, a series of ringdown traces were acquired at time intervals of 2 s while the flow cell was flushed firstly with

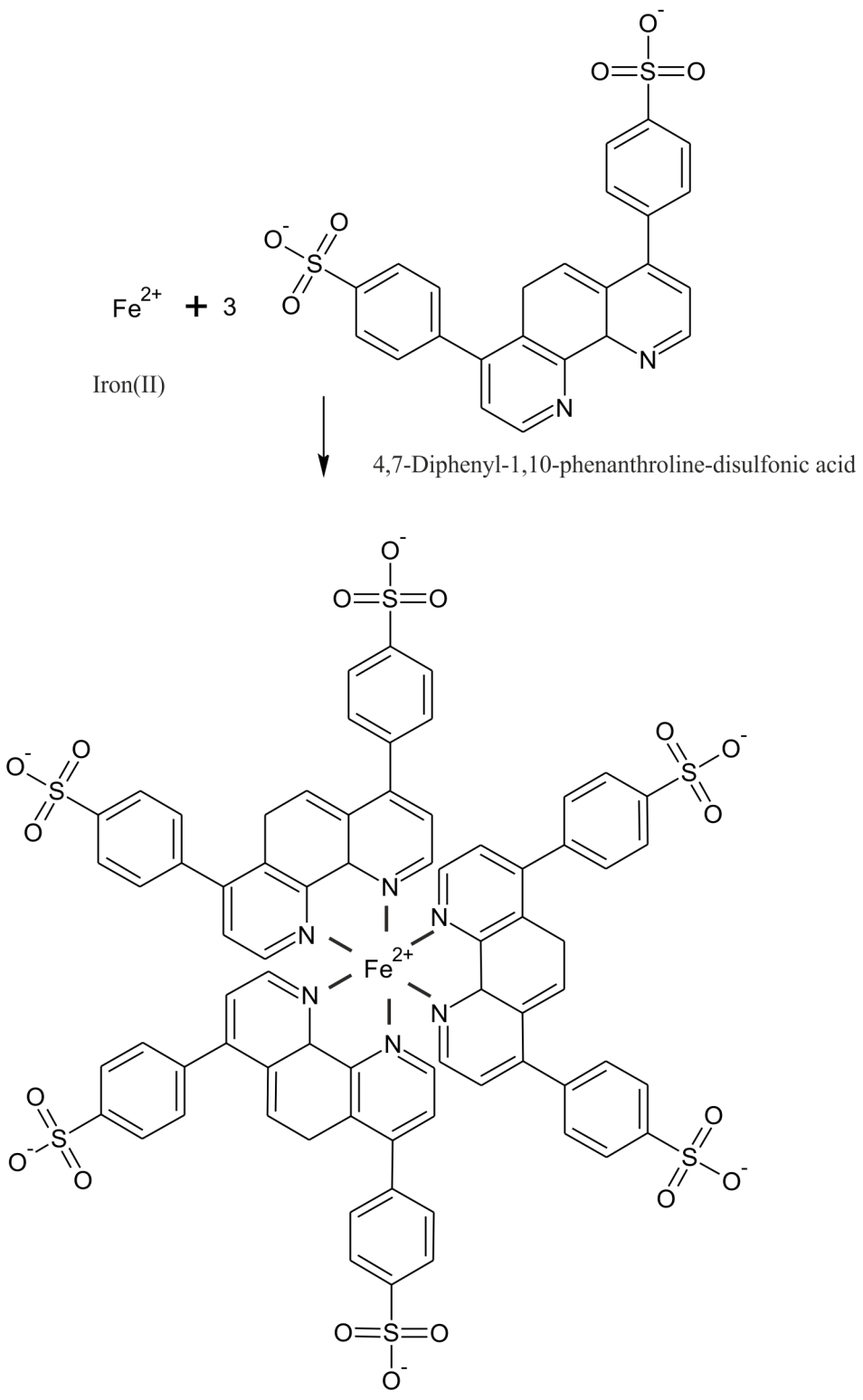


Figure 4.2: Schematic of the iron complexation reaction between Fe(II) (colourless) and 4,7-diphenyl-1,10-phenanthroline-disulfonic acid (colourless) to form an intensely red-coloured complex.

MilliQ water, then a 1:1 mixture of Griess reagent and water (constituting the τ_0 measurement), and finally a 1:1 mixture of Griess reagent and the nitrite solution of interest. A sample data set showing the variation in ringdown time during this procedure is shown in Figure 4.4. Seven different nitrite concentrations were investigated, in the range 25 nM - 10 μM.

The selectivity of the Griess reaction should be emphasised: it suffers from no known interferences in oxygenated seawater [133].

4.2.2 Detection of iron(II) via the bathophenanthroline assay

Colourimetric determination of iron(II) was achieved using sulphonated bathophenanthroline (Sigma Aldrich, 11890), which reacts with Fe(II) in a 3:1 ratio to produce a strongly absorbing product with peak absorption at 533 nm. The reagent is readily soluble in aqueous solutions [206], and thus avoids the time-consuming organic steps traditionally required for the use of non-sulphonated bathophenanthroline. Iron(II) standard solutions were prepared by dissolving iron(II) chloride (Sigma Aldrich, 372870) in deionised water, followed by serial dilution to produce a range of iron(II) concentrations in the millimolar to nanomolar range. The reaction is usually carried out at low pH. However, acidifying the samples using 1 mM hydrochloric acid (analytical reagent grade) to produce a final solution of pH $\sim$3 led to a very poor blank ringdown measurement ($<$100 ns), presumably owing to significant levels of iron present in the hydrochloric acid. Instead, iron (II) and bathophenanthroline were prepared in MilliQ water, without attempting to control the pH. Blair and Diehl [207] investigated the pH dependence of the formation of iron(II) tribathophenanthroline disulphonic acid, and found that the complex was stable within the pH range 3 - 11. Although acidic reaction conditions are thus not required for complex formation, Bruland and Rue note in Chapter 6 of [198] that the oxidation kinetics of Fe(II) to Fe(III) can be markedly slowed by acidifiying the sample to a pH near 3. To prevent decrease in iron(II) concentrations through oxidation to iron(III), we prepared fresh iron(II) solutions twice daily: during this time, under our experimental conditions, oxidation was not noticeable.

A 3 mM stock solution of bathophenanthroline was used in all cases, in a large excess compared to the iron concentrations. The characteristic red colour of the product formed instantly, and did not fade, as has been previously reported [62], thus the solutions were flowed onto the flow cell immediately after thorough mixing. In analogy to the nitrite measurements, a 1:1 mixture of water and bathophenanthroline solution was used to record the blank τ_0 value, with the data acquisition sequence following that outlined above for the nitrite measurements. Measurements were made using all three flow cells over a range of Fe(II) concentrations.

Data analysis was carried out as outlined in Section 3.2.1.

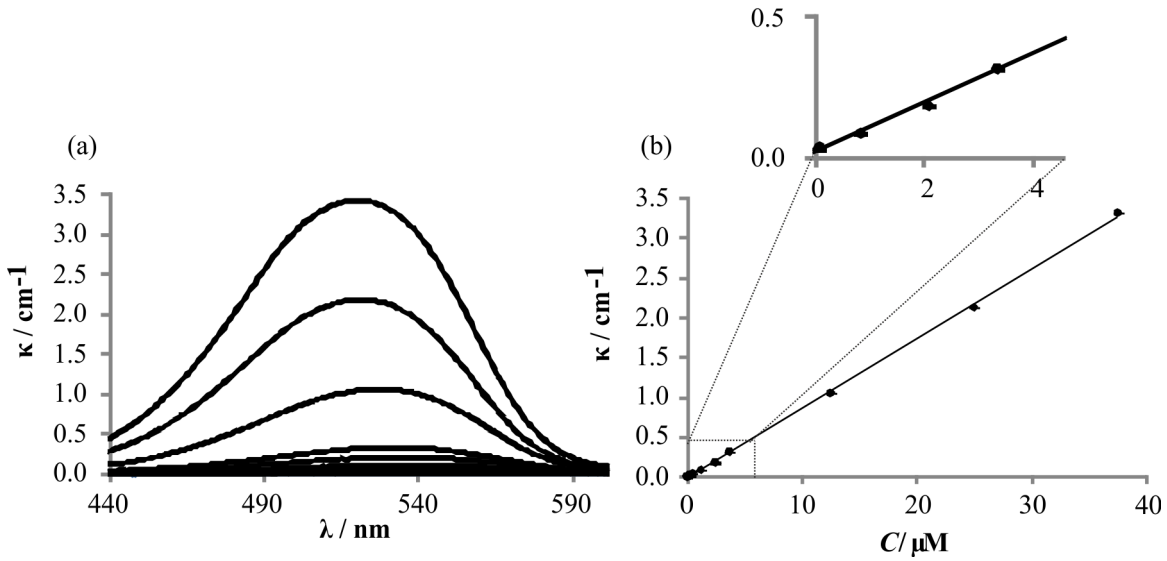


Figure 4.3: (a) κ / cm^{-1} versus wavelength for different nitrite concentrations 0.1 - 75 μM, determined in commercial UV/vis spectrometer. (b) Plot of κ / cm^{-1} versus nitrite concentration C / μM, determined at 532 nm. The gradient of the graph is $(87,600 \pm 1,990)$ M^{-1} cm^{-1}.

4.3 Results

Single-pass Griess reaction data collected using a commercial UV/vis spectrometer are presented in Figure 4.3, as: (a) absorption spectra recorded for different nitrite concentrations; and (b) a plot of absorption at 532 nm versus nitrite concentration. The slope of the plot yields a (natural) absorption coefficient for the azo dye product of the Griess assay of $(87,600 \pm 1,990)$ M^{-1} cm^{-1} at 532 nm. Given the 3σ error in repeated measurements of the 'blank' light intensity (I_0) determined at 532 nm, the detection limit for the commercial UV/vis spectrometer was established to be $\kappa_{\mathrm{min,s}} = 3.8 \times 10^{-3}$ cm^{-1}, which given the determined α, corresponds to a concentration detection limit of nitrite of 43 nM in a 1 cm pathlength cuvette. As described in Section 3.4.2, an alternative estimation of the detection limit, based on the 3σ uncertainty in the y-intercept of the plot in Figure 4.3(b), yields a value of $\kappa_{\mathrm{min,r}} = 2.8 \times 10^{-2}$ cm^{-1}, or 320 nM nitrite. Unsurprisingly, this error estimate is nearly an order of magnitude higher than that determined through the 3σ error in a repeated measurements of I_0, as this second error estimate includes the total errors for this data run, which we believe to be dominated by concentration and washing errors, rather than the signal-to-noise achievable in the instrumental measurements.

Figure 4.4(a) shows a typical data set for a CRDS-based nitrite determination measurement, illustrating the different ringdown times recorded for MilliQ water, a 1:1 mixture of MilliQ water and Griess reagent, and finally a 1:1 mixture of a nitrite solution and Griess reagent. Figure 4.4(b) shows the κ vs concentration plot obtained after carrying out a series of such measurements for nitrite solutions spanning a range of concentrations in the nanomolar to millimolar range. Given the known absorption pathlength for the 1 mm

flow cell, the slope of the plot yields an absorption coefficient for the azo dye product of the Griess assay of $(96,400 \pm 1,620)$ M^{-1} cm^{-1}. This, together with our previously determined minimum detectable absorption per unit pathlength for this cell of $\kappa_{\min,s} = 1.4 \times 10^{-4}$ cm^{-1}, would predict a nitrite detection limit of 1.4 nM, based solely on the signal-to-noise ratio in our measurement of τ. Determination of the detection limit using the regression method (Section 3.4.2), based on the 3σ uncertainty in the y-intercept of the plot in Figure 4.4(b), yields a value of $\kappa_{\min,r} = 3.9 \times 10^{-3}$, or 39 nM nitrite. Unfortunately, these concentrations are significantly exceeded by the concentration of nitrite present in the MilliQ deionised water and/or the reagents, complicating the verification of the detection limit through measurements on standard solutions. Based on the difference in ringdown times measured for pure MilliQ water and a 1:1 mixture of MilliQ water and Griess reagent (see Figure 4.4(a)), we estimate the total nitrite concentration in the deionised water and/or reagents to be 170±70 nM. It should be noted that this large high blank value has been reported in some previous studies. For example, Yao and coworkers noted in 1998 that sample blanks left directly exposed to air in two laboratories overnight acquired nitrite concentrations between 73 and 170 nM [208]. To reduce the effects of variations such as these on our nitrite measurements, within each three-stage measurements of the type shown in Figure 4.4(a), the same batch of deionised water was used. This seems to be a valid approach, since a redetermination of $\kappa_{\min,s}$ based on the 3σ uncertainty in the Griess:MilliQ mixture yields a value of 1.8×10^{-4} cm^{-1}, or 1.9 nM nitrite, only slightly higher than the value obtained using pure MilliQ water as the blank. We have verified detection of nitrite down to a concentration of 12.5 nM. At these levels, a clear difference could be seen in the ringdown time of the Griess:nitrite solution (357 ns) relative to the Griess:MilliQ solution (367 ns). It is likely that the actual detection limit is close to the predicted 1.4 nM (with the higher value determined from the plot being an artefact of the purity of the deionised water available to us), but we are hampered in accessing lower concentrations by the high blank concentration of nitrite. Even so, this detection limit is significantly below the ambient nitrite concentration in marine and aquatic environments, such that CRDS represents a promising approach for detecting low levels of nitrite in such environments.

Iron is present at considerably lower levels than nitrite in marine environments, and is consequently much more difficult to detect. For this reason, detection limits were determined using all three flow cells in order to determine the optimum pathlength for such measurements. Plots of κ vs Fe(II) concentration for each flow cell are shown in Figure 4.5. Based on the signal-to-noise in the baseline τ_0 measurement recorded for a 1:1 mixture of bathophenanthroline and deionised water, the minimum detectable absorptions per pass, $\kappa_{\min,s}$, for the 2.0 mm, 1.0 mm, and 0.1 mm flow cells were determined to be 5.2×10^{-4} cm^{-1}, 1.9×10^{-4} cm^{-1} and 8.1×10^{-4} cm^{-1}, respectively. Given the absorption coefficient for the absorbing species, determined from the gradient of the κ vs C plot to be (51,200±2,600) M^{-1} cm^{-1}, this corresponds to the detection of 10 nM, 3.8 nM and 16 nM iron in each case. When the illuminated volume is taken into account, we find that this corresponds to the detection of around 1 billion molecules. Using the regression method (Section 3.4.2), the detection limits are 5.2×10^{-3} cm^{-1} for the 2 mm flow cell, 1.5×10^{-3} cm^{-1} for the 1 mm flow cell

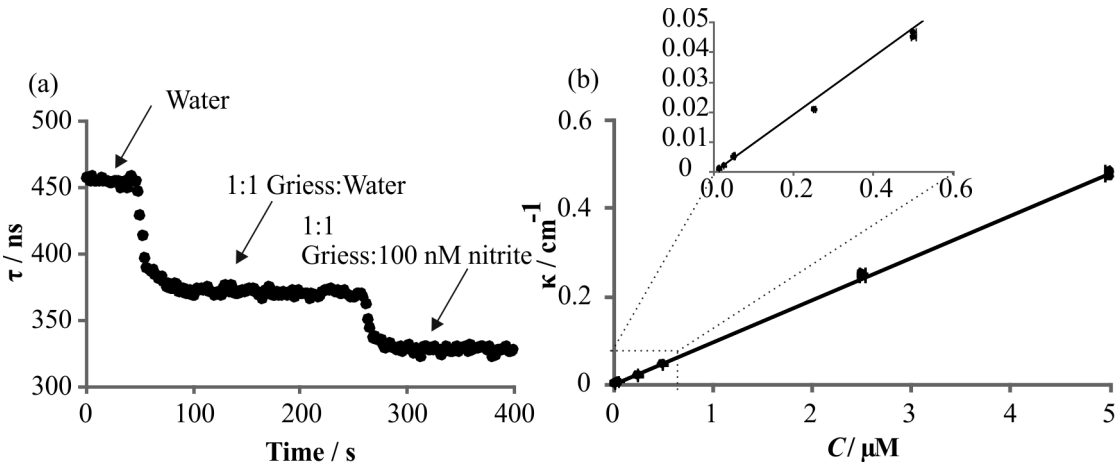


Figure 4.4: (a) Example graph of ringdown time versus time, as water, then 1:1 Griess:water, then 1:1 Griess:100 nM Nitrite is flowed through the 1 mm cell. (b) Plot of κ / cm^{-1} versus nitrite concentration C / μM, determined in 1 mm flow cell. The gradient of the graph is $(96,354 \pm 1,623)$ M^{-1} cm^{-1}.

and 8.0×10^{-3} cm^{-1} for the 0.1 mm flow cell. Qualitatively, we detected a reproducible ca. 2 ns change in ringdown time using the 1 mm flow cell when measuring 5 nM iron (the lowest concentration measured in this data set), and a reproducible ca. 3 ns change in ringdown time using the 0.1 mm flow cell when measuring 50 nM iron. In contrast, using the 2 mm flow cell, 50 nM (the lowest concentration measured) was not detectable, owing to the higher variation in the blank signal, which arises from the longer pathlength, and caused the minimum detectable change in ringdown time to be higher than measured with the 1 mm and 0.1 mm flow cells. Thus, we can see that the 1 mm flow cell has the most favourable limit of detection under our current experimental conditions.

4.4 Discussion

The results described above demonstrate that CRDS has sufficient sensitivity to detect nitrite and iron at concentrations in the nanomolar range, for optical pathlengths of 2 mm to 0.1 mm, making CRDS compatible with microfluidic sensors. At this stage, we should compare the detection sensitivities achieved using CRDS with those obtained using existing techniques.

King et al. state that using a standard spectrophotometer with 10 cm cells, the practical detection limit for Fe(II) using the ferrozine assay is 20 nM [209]. By placing a flow cell in a cavity, we have improved on this detection limit by an order of magnitude, while also reducing the optical pathlength by two orders of magnitude. Similarly, for nitrite, Raimbault et al. achieved a detection limit of 1.2 nM nitrite using a 5 cm cell [210]. An alternative method of achieving greatly increased absorption pathlengths is to employ a liquid core waveguide (LCW) [140]. LCWs have been applied to both nitrite [211] and iron detection [212,213], and detection limits in the 0.1 nM concentration range have been demonstrated when using LCWs

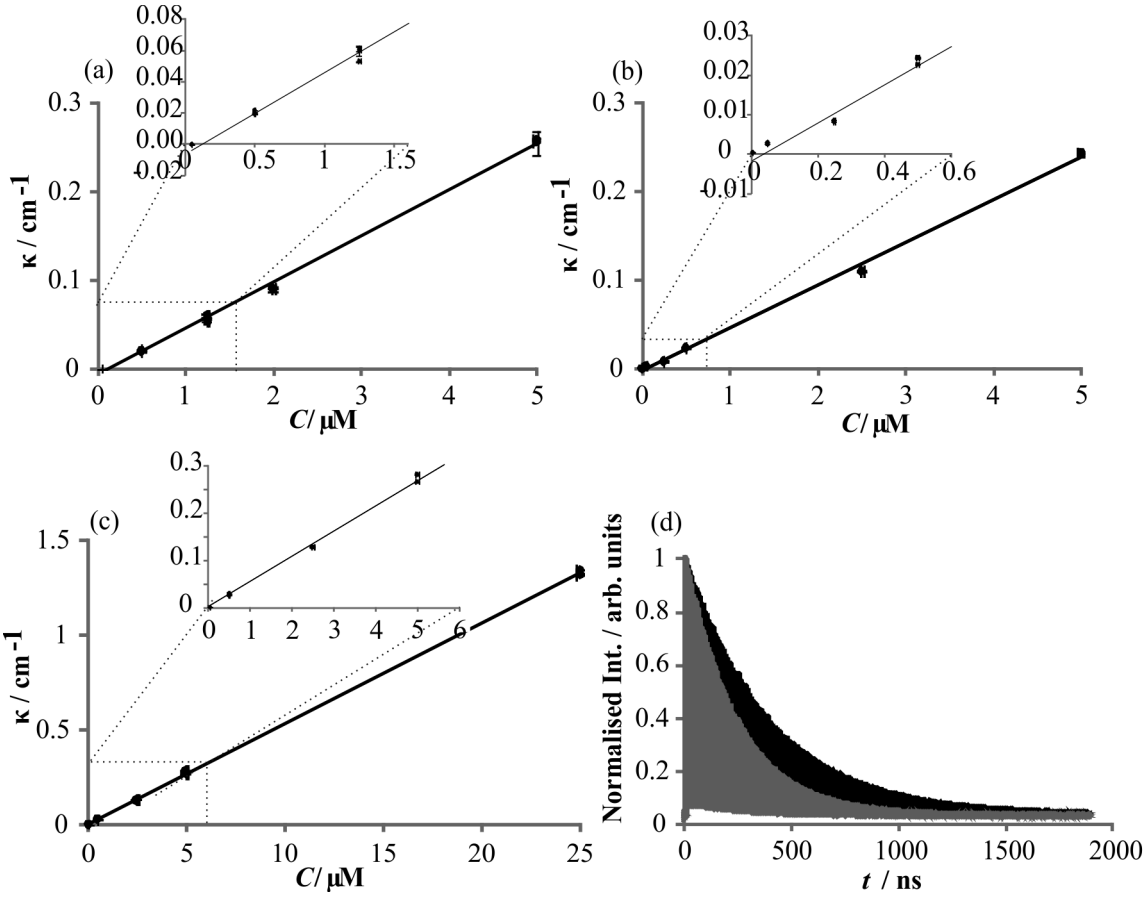


Figure 4.5: (a) Plot of κ / cm^{-1} versus iron concentration C / μM, determined in 2 mm flow cell. The gradient of the graph is (52,400 $\pm 2,100$) M^{-1} cm^{-1}. (b) Plot of κ / cm^{-1} versus iron concentration C / μM, determined in 1 mm flow cell. The gradient of the graph is (48,200 $\pm 1,800$) M^{-1} cm^{-1}. (c) Plot of κ / cm^{-1} versus iron concentration C / μM, determined in 0.1 mm flow cell. The gradient of the graph is (53,000 $\pm$699) M^{-1} cm^{-1}. (d) Example ringdown traces recorded using the 1 mm flow cell. The black trace is the ringdown time for the water-filled cell, $\tau_0 = 383$ ns, and the overlain grey trace is the ringdown time for 0.5 μM iron, $\tau = 241$ ns.

Table 4.2: Chronological examples of nitrite detection using the Griess reaction. LCW is an abbreviation of liquid core waveguide. Vol_T is the total sample volume required for analysis. Vol_P is the actual sample volume probed during analysis. C_{min} is the minimum concentration detection limit of nitrite reported. C_{max} is the maximum detectable concentration of nitrite. N.R. is an abbreviation of not reported.

Reference	Notes	Location	λ / nm	Optical l / cm	Vol_T (Vol_P) / mL	C_{min} / nM	C_{max} / μM
Raimbault et al. [210]	-	Shipboard	540	5	5	1.24	10
Yao et al. [208]	LCW	Lab.	540	450	2 (1.1)	0.5	0.03
Greenway et al. [215]	On-chip (glass)	Lab.	526	N. R.	N. R.	200	100
Zhang et al. [214]	LCW	Shipboard	540	200	0.5	0.1	0.05
Manzoori et al. [216]	Preconcentration (factor 70)	Lab.	553	1	500	3.8	0.52
Steimle et al. [211]	LCW	*In situ* (500 m depth)	540	100	N.R. (0.52)	2.5	N. R.
Adornato et al. [141]	LCW	*In situ* (200 m depth)	541	97	N.R. (0.5)	1	0.5
Patey et al. [133]	LCW	Shipboard	540	200	N. R.	1.5	0.6
Sieben et al. [22]	On-chip (tinted PMMA)	Lab.	525	2.5	0.08	14	10
Beaton et al. [24]	On-chip (tinted PMMA)	*In situ* (1 m depth)	525	2.5	0.25	15	N. R.
This work	Cavity enhanced	Lab.	532	0.123	1 (196 nL)	1.9	10

several metres in length [213, 214]. LCWs provide an attractive approach, using relatively small volumes of reagents, and achieving high sensitivity in a relatively small experimental footprint which is easily interfaced with flow systems, and gains sensitivity without additional complexity. However, LCWs suffer from high blank signals, significant dead volume at the liquid/light interface, and the measurements are also prone to contamination from micro-air bubbles, which have a tendency to attach to internal surfaces of the LCW and cause erroneously high and fluctuating absorbance values to be measured [133]. Though we have not yet demonstrated detection limits on the sub-nanomolar level, for measurements in which a slightly poorer detection limit is tolerable, cavity ringdown measurements provide a long effective absorption pathlength while maintaining a short physical pathlength that avoids most of the problems associated with LCWs.

4.4.1 Comparison of CRDS nitrite detection with other techniques

Table 4.2 provides a chronological summary of applications of the Griess reaction to nitrite detection. In general, detection limits in the nanomolar concentration range can be achieved with optical pathlengths of a few centimetres. Subnanomolar concentrations can be achieved with the use of longer pathlength LCWs. Preconcentration techniques have been less widely applied to nitrite detection, when compared with iron

detection. Large sample volumes are required for preconcentration, and when detecting nitrate and nitrite, nitrate reduction in addition to sample preconcentration can significantly add to system complexity.

Table 4.2 also highlights the location of operation, and includes laboratory-based experiments, shipboard-based experiments, and finally *in situ* experiments. The necessity to miniaturize, improve system stability and reduce power consumption increases as experiments are moved out of a laboratory environment, onto a ship, and finally packaged into a system that can be submersed at depth.

While the Griess reaction is the most commonly used technique for nitrite detection, alternative methods, have also been investigated and will be briefly covered here. For futher details, the reader is directed to a particularly excellent overview of nanomolar nitrite detection in seawater [133]. Detection methods applied to nitrite include UV absorbance, fluorescence, chemiluminescence, thermal lensing and electrochemical methods. These methods are discussed below.

UV absorbance (at 210 nm and 220 nm), in combination with ion exchange chromatography, has been used to detect nitrate directly, without requiring chemical conversion [217, 218]. However, the measurements are significantly slower than colourimetric analysis (40 minutes analytical cycle time), and the detection limit was not found to be lower than that achieved using long pathlength colorimetry. Maruo et al. reported a detection limit of 40 nM nitrate [218], while Hu et al. reported a detection limit of 8 nM nitrate [217]. One advantage is that nitrate is detected separately from nitrite. However, there are some problems with selectivity in seawater analysis, in which bromide tends to elute along with nitrate.

UV absorbance (at 307 nm), in combination with high performance liquid chromatography, has also been applied to sub-nanomolar nitrite detection, based on the reaction of nitrite with 2,4-dinitrophenylhydrazine to form an azide, which is chromatographically separated from interfering compounds, and measured at concentrations down to 0.1 nM nitrite [219]. Although highly sensitive, the method is more complex than colourimetric analysis and has not yet been applied in shipboard analysis.

An alternative detection strategy is to use fluorescence, although chemical conversion is still required. The chemistry is similar to that of the Griess reaction, as nitrite (and nitrate if reduced to nitrite) is detected after acidification and coupling with aniline to form the diazonium ion, which fluoresces. Using this method, Masserini and Fanning measured a detection limit of 4.6 nM nitrite and 6.9 nM nitrate employing an excitation wavelength of 220 nm and an emission wavelength of 295 nm [220]. At these wavelengths, interference from dissolved organic matter can be significant, and thus is corrected for as part of the analysis. Alternatively, Zhan and coworkers demonstrated fluorescence quenching of tetra-substituted amino aluminium phthalocyanine by nitrite, and measured a detection limit of 7 nM [221]. In this case, a red-region fluorescent dye was used, with an excitation wavelength of 610 nm and an emission wavelength of 678 nm, and thus selectivity was enhanced compared to Masserini and Fanning's work.

Gas-phase chemiluminescence has also been applied to nitrite detection. Nitrite is first converted to nitric oxide, and the nitric oxide is then determined via the chemiluminescence reaction between nitric oxide and ozone. Typically, detection limits range from 1 nM to 10 nM nitrite using liquid sample volumes of 1 - 20 mL [222–224]. The main drawbacks of this approach include its experimental complexity and the high temperatures (600 ^{o}C) required.

A highly sensitive absorption technique, known as thermal lens spectroscopy (Section 1.3.5), has also been applied to nitrite detection [225]. For nitrite detection, an Ar^{+} laser operated at 514.5 nm has been used to detect the azo dye product from the Griess reaction [225]. In a pathlength of 1 cm, a detection limit of 0.2 nM was measured, more than 200 times smaller than the detection limit of ordinary spectrometers. The complexity and cost of this technique have somewhat limited its application to date.

Electrochemical techniques have been applied to nitrite detection, but tend to suffer from poorer sensitivity compared to the spectroscopic techniques discussed above, often limited to 4 μM nitrite [191]. In particular, there are also problems arising from electrode fouling in real samples, which limit performance over longer periods of time. One area of electrochemical research that does show great promise is that of biosensors. Biosensors are attractive for nitrite detection because they can be operated in modes that are remote, reagentless, sensitive and selective. For example, Ferretti and coworkers demonstrated a detection limit of 75 nM nitrite by monitoring the decrease in intensity of the 460 nm absorption band associated with the d_1 haem (the nitrite binding site) in cytochrome cd_1 [226].

In summary, a wide variety of methodologies have been applied to nitrate/nitrite detection. The Griess reaction is preferred to other methods for its high sensitivity and high selectivity. Sensitivity is achieved by carrying out long pathlength absorption spectroscopy, commonly using liquid core waveguides. We have achieved a cavity enhanced pathlength of nearly 1 m from a single-pass pathlength of only 1 mm, by applying CRDS to nitrite detection using the Griess reaction, in a laboratory set-up.

The next challenge is to package this set-up into a sensor that is automated and can be operated firstly shipboard, and secondly, *in situ*. When quantifying nitrite, it is often sample integrity rather than sensitivity that is the issue. By carrying out analysis *in situ*, sample integrity can be most closely maintained. For example, analysers can be attached to submersible probes, such as those used in the worldwide Argo float program [227]. When taking seawater measurements, the sampling rate must be enhanced, as submersible probes can descend and rise rapidly. For example, Adornato et al. used a 2 s sampling period, in continuous flow, combined with a descent rate of 11 cm/s, in order to profile the nitrite concentration at 22 cm resolution [141]. In our experiments, it should be noted that we waited for at least 10 minutes in order for maximum colour development to occur. For more rapid measurements, the colour development within only the first few minutes could be utilised. For example, Adornato et al. state that significant colour development must occur within several minutes for sufficiently rapid analysis [141]. Of course, this would compromise sensitivity (as α would effectively decrease) while at the same time improving the time resolution.

4.4.2 Comparison of CRDS iron detection with other techniques

Iron detection in real samples is more challenging than nitrite detection for two reasons: firstly, the ultralow ambient iron levels, which lie in the picomolar range in many seawater regions, and secondly, the complex speciation of iron between different redox states (Fe^{2+}/Fe^{3+}) and physical states (particulate, dissolved, complexed). Most detection techniques will detect a particular redox and physical state. In oxygenated seawater, Fe^{3+} is the dominant form of iron, with Fe^{2+} being rapidly oxidised to the Fe^{3+} oxidation state [199]. However, in surface seawater, Fe^{2+} may be responsible for up to 50% of the total dissolved iron, partially as a result of photoreduction of Fe^{3+} [228]. Fe^{3+} is highly insoluble as it forms oxyhydroxides. To combat this low iron solubility, phytoplankton and bacteria are known to produce natural organic chelators to complex iron (in both redox states) and maintain a higher solubility in seawater [229,230]. The determination of the redox states of iron in natural waters is the subject of its own review [200]. To quote directly from Achterberg et al.: "An essential development will be a method capable of measuring dissolved iron(II) in surface open ocean waters at picomolar concentrations and ambient pH. These measurements are important because photochemical cycling of dissolved iron(II) in surface waters significantly increases the solubility of iron(III) colloids and hence the pool of bioavailable iron." [199].

In the laboratory, iron can be detected with high sensitivity using graphite atomic absorption spectrometers (GFAAS) [231] or inductively coupled plasma mass spectrometers (ICP-MS) [198]. However, the storage of low iron concentration samples without contamination or disturbing the natural redox and physical speciation states is challenging.

Table 4.3 provides a chronological summary of applications of colourimetric reactions to iron detection. Over the last few decades, ferrozine has been used for the majority of analyses, as it has the highest peak absorption coefficient in the visible spectral region, roughly 20% higher than the peak absorption coefficient of sulphonated bathophenanthroline. The first example, from 1980, demonstrates the application of intracavity laser absorption spectroscopy to iron detection, improving the detection limit by a factor of 2 - 10 [232, 233]. Intracavity laser absorption can be considered as one of the precursor techniques to CRDS, and it is interesting that it was applied to trace iron analysis so early on, but then not revisited in the literature.

The lowest detection limit reported using colourimetric analysis was found by Blain and Trégeur, who reported a detection limit of 0.1 nM using the ferrozine method combined with a preconcentration step [234].

The most recent paper by Floquet et al. should be highlighted. In their work, long pathlength absorption cells were manufactured in dark grey tinted polymethylmethacrylate (PMMA) [23]. This effectively creates a pinhole along the channel, ensuring that only light that has passed through the sample but not the channel walls reaches the detector. Two optical pathlengths were investigated: 25 mm and 80 mm, but no significant

Table 4.3: Chronological examples of iron detection using colourimetric reactions. LCW is an abbreviation of liquid core waveguide. Vol_T is the total sample volume required for analysis. Vol_P is the actual sample volume probed during analysis. C_{min} is the minimum concentration detection limit of iron(II) reported. C_{max} is the maximum detectable concentration of iron(II) reported. N.R. is an abbreviation of not reported.

Reference	Notes	Location	λ / nm	Optical l / cm	Vol_T (Vol_P) / mL	C_{min} / nM	C_{max} / μM
Harris et al. [233]	Ferrozine, laser intracavity	Lab.	584	1	Few mL	9	54
King et al. [209]	Ferrozine, preconcentration factor 40	Lab.	562	10	50 - 400	0.6	185
O'Sullivan et al. [235]	Ferrozine, preconcentration factor 40	Shipboard (100 m depth)	562	10	400	0.12	N.R.
Blain et al. [234]	Ferrozine, preconcentration	Lab.	560	3	40 (0.015)	0.1	N. R.
Waterbury et al. [212]	Ferrozine, LCW	Lab.	562	447	N.R. (0.3)	0.2	10
Zhang et al. [213]	Ferrozine, LCW	Lab.	562	200	2 (0.5)	0.1	50
Floquet et al. [23]	Ferrozine, on-chip (tinted PMMA)	Lab.	562	2.5	N.R. (0.007)	21	N. R.
Floquet et al. [23]	Ferrozine, on-chip (tinted PMMA)	Lab.	562	8	N.R. (0.0224)	20	N. R.
This work	Cavity enhanced	Lab.	532	0.123	1 (196 nL)	4	10

improvement was found at 80 mm owing to traces of iron in the blank sample. With a 25 mm optical pathlength, the limit of detection was improved from 226 nM in clear PMMA to 21 nM in dark grey tinted PMMA.

Alternative methods that have also been demonstrated for iron detection include catalytic spectrophotometry [236], chemiluminescence [237], thermal lens spectroscopy [97] and stripping voltammetry [238].

Catalytic spectrophotometry has been widely applied to sub-nanomolar iron detection, although it should be noted that it does not permit redox speciation measurements. In this method, the ability of iron to catalyse reactions that can be monitored spectrophotometrically is exploited. Hirayama and Unohara first reported a batch method for the catalytic spectrophotometric of iron(III) based on the catalytic action of iron(III) on the oxidation of N,N-dimethyl-p-phenylenediamine by hydrogen peroxide in weakly acidic media [236]. The catalyzed reaction can be monitored at 514 nm in a 10 mm cell, with the absorbance increasing over 10 minutes. Hirayama and Unohara chose a reaction time of 5 minutes as a compromise between enhanced sensitivity and longer analytical cycle time. Measures et al. reoptimised Hirayama and Unohara's reaction conditions to enable a shorter reaction time of 1 minute, compatible with flow injection analysis [239]. An inline preconcentration step was incorporated, using a column of resin-immobilised 8-hydroxyquinoline, and the detection limit of the method was reduced to 0.025 nM. This method was applied to shipboard measurements of iron in open ocean water samples from the equatorial Pacific and the North Atlantic. Weeks

and Bruland [240] further reduced the detection limit to 0.016 nM iron by carrying out the reaction at a slightly elevated temperature of 30^{o}C, rather than at room temperature as used previously by Measures et al. Shipboard catalytic spectrophotometry has also been carried out by Sedwick et al. [241] in sub-Antarctic waters.

There has been a significant amount of interest in the detection of iron using chemiluminescence. Reaction with luminol offers the lowest detection limits for iron in seawater. Obata et al. reported the lowest detection limit of 0.01 nM for iron using the luminol/hydrogen peroxide method combined with preconcentration [237]. de Jong et al. [242] and Sohrin et al. [243] applied Obata's method to iron detection in the Southern Ocean. De Jong et al reported dissolved iron concentrations ranging from 0.05 - 0.3 nM [242], while Sohrin et al. reported dissolved iron concentrations ranging from 0.14 - 1.2 nM [243]. Chemiluminescence, combined with flow injection analysis, provides a robust, portable, low-cost instrument, capable of rapid and sensitive analysis, with the ability to distinguish different redox states of iron.

Interestingly, Bowie and coworkers carried out a lab- and ship-based analytical intercomparison of flow injection with catalytic spectrophotometric with N,N-dimethyl-p-phenylenediamine dihydrochloride, and flow injection with luminol chemiluminescence detection, incorporating a preconcentration step for both methods [244]. The detection limits for catalyic spectrophotometry were found to range from 18 - 34 pM, and the detection limits for chemiluminescence were found to range from 19 - 49 pM. Slight variations in measurements of iron in surface seawater samples were accounted for by the different sensitivity of each method to different iron species.

In the early 1980s, Imasaka and coworkers demonstrated a dual-beam thermal lens set-up [97], using a 100 mW Ar^+ laser, whose 514.5 nm line lies close to the maximum of the iron(II)-bathophenanthroline disulfonate complex [245], along with a second probe beam from a He-Ne laser. The detection limit of 700 nM in 1 cm was reported to be 7 times better than that achieved using spectrophotometry in the same pathlength. Chernysh et al. improved the thermal lens set-up and achieved a detection limit of 1 nM iron in 1 cm, detecting the phenanthroline complex [246].

The last method that we shall discuss is a technique known as adsorptive cathodic stripping voltammetry (abbreviated AdCSV) [199]. In this method, a preconcentration step allows for iron to be selectively complexed by a ligand, which is then adsorbed onto a hanging mercury drop electrode at a specific potential. The complex is then reduced back into solution during a cathodic scan, the stripping step, while the reduction current is recorded. Gledhill and van der Berg have used AdCSV with 1-nitroso-2-naphthol as the complexing ligand, and measured a detection limit of 0.08 nM iron [238]. Iron in both redox states and several physical states can be determined by sequential control of the complexing conditions, including uniquely organic/inorganic iron speciation via measurements with a competitive ligand [247]. However, scan speeds are slow, and thus stability of analysis may be an issue.

A brief mention should also be made of the poorer selectivity of metal complexation reactions compared to, for example, the Griess reaction. For example, Cu(I) is known to form a coloured complex with ferrozine, as are Co(II) and Ni(II) to a lesser extent [209]. Blair and Diehl tested several ions to see whether they interfered with the detection of iron using sulphonated bathophenanthroline: their findings are presented in Table 1 of [207]. Clark also tested the interference of ions on the bathophenanthroline method [248]. Some metal ions such as Co(II) and Cu(I) interfere via the formation of their own complex with bathophenanthroline, although the developed colour is in these cases, yellow, and thus absorbance measured at 533 nm will not change, unless the concentration of bathophenanthroline is limiting. Other ions, including Co(II), have been shown to reduce iron(III) to iron(II), and thus cause an increase in the absorbance signal [248]. V^{5+} nearly completely eliminated iron(II) absorbance, owing to oxidation of Fe^{2+} to Fe^{3+} [248]. Cr(III), Mn(II), Ni(II) and Zn(II) were found not to interfere with the signal [248].

4.4.3 Detection limit improvements

As we do not currently have the required sensitivity to be able to detect iron in the sub-nanomolar concentrations present in the open ocean, we conclude with a brief discussion of possible improvements to the set-up which may lower the detection limit further. In a cavity ringdown measurement, the detection limit can be improved either by increasing the ringdown time (i.e. reducing the cavity loses), by increasing the pathlength per pass, or by minimising the shot-to-shot variation in τ. We will consider each of these factors in turn.

Increasing the ringdown time can be achieved either by increasing the reflectivity of the mirrors or by minimising the flow cell losses. Since our cavity losses are currently dominated by losses associated with the flow cell, increasing the mirror reflectivity will have a limited effect. For example, based on the current losses associated with our 1.0 mm flow cell, increasing the mirror reflectivity from the current relatively modest value of 99.8% to the 'best available' value of 99.999%, assuming we could still measure the ringdown time to an accuracy of $\sim$0.4% as at present, would only improve our detection sensitivity by around a factor of two. This improvement would come at the cost of greatly reduced signal levels, since a much smaller amount of light can be coupled into and out of the cavity on each pass. Losses associated with the flow cell could be reduced by the use of custom-designed Brewster's angle flow cells. Such an approach was demonstrated in 2003 by Snyder and Zare, who used a specially designed Brewster's angle flow cell which allowed for light to strike each surface at the correct Brewster's angle for each interface [168]. The loss through this 300 μm pathlength flow cell (0.06%) is roughly half the loss we determined through our 100 μm flow cell, despite the three times longer pathlength, demonstrating the improvement possible through the use of a better designed flow cell. In our case, if we inserted Snyder and Zare's flow cell into our present cavity, we would potentially achieve $\kappa_{\min} = 3.6 \times 10^{-4}$ cm^{-1}, corresponding to a detection limit of 7.0 nM iron in a 300 μm pathlength. If we combined Snyder and Zare's flow cell with 99.99% mirrors, we

could potentially achieve $\kappa_{\min} = 1.9 \times 10^{-5}$ cm^{-1}, corresponding to a detection limit of 0.37 nM iron over a 300 μm pathlength.

Though Equation 2.13 implies that an increased pathlength should improve the detection sensitivity in a cavity ringdown measurement, this is unfortunately not always the case. We have already shown that increasing the pathlength will not necessarily increase the sensitivity if the blank concentration is high. Additionally, increasing the pathlength increases the scattering and absorption losses through the solvent significantly, and thus lowers the ringdown time. The relatively high blank signal could certainly be improved by the use of higher purity reagents/solvents; in the present work we used all reagents as purchased without further purification. It is worth noting that in the first application of CRDS to liquid-phase analysis, Xu et al inserted single 1 cm or double 1 cm quartz cells into a ringdown cavity formed from two 99.97% reflectivity mirrors, and $\kappa_{\min} = 5 \times 10^{-5}$ cm^{-1} was achieved through measurement of benzene in the pure liquid and in hexane [165]. This is comparable with the values obtained in the present work in the 2 mm flow cell.

The detection limit can also be improved by reducing the variation in the measured ringdown time, τ. This would most readily be achieved by moving from a pulsed laser source to a CW source. For example, Zare and coworkers improved on their minimum detectable absorbance measured in 2005 [170], by replacing the pulsed light source with a single-mode, continuous-wave light source which allowed excitation of only a single cavity mode. This reduced the shot-to-shot variation in τ from 1% [168] to 0.05%, allowing determination of $\kappa_{\min} = 7.8 \times 10^{-6}$ cm^{-1} [170]. In our case, the variation in τ is already only 0.4%, and we believe that our measurements are more significantly affected by the degree of flushing of the flow cell, and volume errors in making up the stock solutions.

The detection limit could be improved by using a light source operating at 562 nm, and using the ferrozine method. Unfortunately, we are somewhat limited in the availability of appropriate laser sources at this wavelength. One solution for lab-based measurement is to use a supercontinuum laser source, which produces light across the entire visible spectrum, and thus can be filtered for single-wavelength CRDS measurements at 562 nm. However, this would make the experimental set-up considerably less compact and more expensive.

An alternative would be to move to the UV spectral region, although in this case it is likely that additional separation techniques such as capillary electrophoresis would be required, as the selectivity in this region is poorer. Xu et al. employed a detection wavelength of 270 nm instead of the usual 508 nm for monitoring the phenanthroline-iron complex [202], thereby increasing the molar absorbance by about 8 times [249].

We are also interested in applying the catalytic spectrophotometric method to iron detection (Section 4.4.2). Absorbance measured at 532 nm, close to the stated absorption maximum of 514 nm for this method [236], can be monitored, using our current CRDS set-up. It is likely that this rate method is more sensitive than the

Table 4.4: Examples of colourimetric detection applied to other seawater analytes. C_{typ} is the typical seawater concentration value, or range, taken from [184]. C_{min} is the concentration we can detect given our $\kappa_{\text{min}} = 1.4 \times 10^{-4}$ cm^{-1} in our 1 mm pathlength flow cell, assuming that our set-up is applied with the current sensitivity to the appropriate wavelength for each colour reaction.

Analyte	C_{typ}	Reagent	λ / nm	α / M^{-1} cm^{-1}	C_{min} / nM	References
Major	/ mM					
Magnesium	54	Methylthymol blue	610	3.5×10^4	✓4.0	[250]
Calcium	11	O-cresolphthalein	575	1.1×10^4	✓13	[251]
Boron	0.42	Curcumin	555	4.2×10^5	✓0.33	[252, 253]
Fluoride	0.072	Alizarin	610	2.9×10^4	✓4.8	[254]
Nutrients	/ μM					
Phosphate	1.9, 0 - 3.2	Molybdenum blue	882	4.1×10^4	✓3.4	[133, 255]
Silicate	71, 0 - 180	Molybdenum blue	810	6.0×10^4	✓2.3	[256]
Minor	/ nM					
Vanadium	23 - 36	Diantipyryl derivative	450	1.1×10^7	✓0.013	[257]
Nickel	2 - 12	Benzothiaxolyldiazo -aminoazobenzene	550	4.5×10^5	✓0.31	[258]
Chromium	3 - 5	1,5-Diphenylcarbazide	540	2.1×10^5	✓0.67	[259]
Copper	0.5 - 6	Bathocuproine	483	2.8×10^4	✗5.0	[207]
Manganese	0.08 - 3	Diantipyryl derivative	480	3.0×10^6	✓0.047	[260]
Cobalt	0.02 - 0.4	Nitroso-R-salt	500	6.5×10^3	✗22	[261]

bathophenanthroline method used in this Chapter, and we plan to investigate this in the near future (Chapter 10).

Finally, as for any analytical technique, the detection limit can be improved by incorporating a preconcentration step into the analysis. For example, King et al. found a 40-fold improvement in the detection limit for iron when using a ferrozine-coated C_{18} column [209]. Blain and Treuger achieved a detection limit of 0.1 nM Fe(II) and 0.3 nM Fe(III), by carrying out analysis in a 3 cm optical pathlength cell, after preconcentration using a similar column [234]. Manzoori et al. found a detection limit of 3.8 nM nitrite in a 1 cm cuvette, gaining a 70-fold improvement through preconcentration using a sodium-dodecyl-sulphate-coated alumina column [216]. These preconcentration factors would allow us to determine iron at close to the lowest ambient seawater levels in our 1 mm flow cell. However, preconcentration will greatly increase the sample volume (and hence sensor size) required for analysis, and will also complicate the chemical steps necessary for analysis.

4.4.4 Detection of other water analytes

Colourimetric reactions abound in the literature, and have been applied to the detection of many other cations and anions, beyond the detection of nitrite and iron we have carried out in this Chapter. It is therefore of value to list other colour reactions, along with an indication of the sensitivity required. This will enable us to place our detection technique into context. We will focus our analysis on the detection of analytes in

seawater, as this is the most dilute, and hence most challenging matrix for analysis. In seawater, analytes are divided into major and minor constituents. The major constituents are those which make up $> 99\%$ of the soluble ionic species of seawater, that is sodium, potassium, magnesium, calcium, strontium, chloride, sulphate, bromide, hydrogen carbonate, borate and fluoride [184]. Analysis of the major seawater constituents is greatly simplified by the concept known as conservatism, whereby it is assumed that the ratios of the major constituents remain unchanged, while the concentrations change due to addition or removal of water only. Thus, in order to fully characterise the major constituents of seawater, it is sufficient to measure only one constituent, which is simple to detect and conservative with respect to the other major constituents. Of the major constituents, colourimetric analysis is most commonly used to detect magnesium, calcium, boron and fluoride. These analytes are listed first in Table 4.4. The traditional nutrients are listed next, followed by a selection of the minor constituents of seawater.

The millimolar concentrations of major constituents are sufficiently high that cavity enhanced methods do not need to be used, unless very short optical pathlength analysis is needed. The concentrations of marine nutrients, generally around the nanomolar to micromolar level, lie in the range where cavity enhanced methods can provide good sensitivity for short optical pathlengths. Detection of minor constituents is more challenging. At nanomolar levels and above, our CRDS set-up can be applied. For some minor constituents with particularly strongly absorbing colour products, for example, vanadium, nickel, chromium and manganese, even sub-nanomolar levels may be achieved.

4.5 Conclusion

In summary, we have demonstrated the application of CRDS to the detection of both nitrite and iron in pathlengths similar to those encountered in microfludic systems, and have shown that the method could potentially be useful for developing ship-based or remote sensors for monitoring trace species in marine and aquatic environments. The detection sensitivity for nitrite is already sufficient to monitor ambient levels in nearly all such environments. The detection sensitivity for Fe(II) is sufficient for monitoring levels in river or drinking water, but not yet sufficiently low to monitor Fe(II) in marine environments. Potential approaches for improving the detection limit into the range required for such measurements have been discussed.

The potential for miniaturization of our laboratory set-up will be discussed in detail in the last Chapter of this thesis. For now, we note that it remains to be seen whether the impressive detection limits achieved in such short optical pathlengths can be replicated on-ship or *in situ*.

Chapter 5

Two-mirror cavity enhanced absorption spectroscopy of liquids

"In escaping from the confines of conventional fibre optics, photonic crytal fibres have created a renaissance of new possibilities in a large number of diverse areas of research and technology, in the process irrevocably breaking many of the tenets of received wisdom in fibre optics."
P. Russell, Science, Vol. 299, 2003 [262].

5.1 Introduction

In the previous Chapters, we have demonstrated high sensitivity, single-wavelength CRDS, and its application to the analysis of small volume liquid samples. It is desirable to extend single-wavelength analysis to cover a wide range of wavelengths, particularly in the case of liquid-phase absorption studies, for which the absorption bands are generally broad (often spanning a wavelength region on the order of 100 nm). In addition, multi-wavelength detection can allow for the detection of more than one analyte simultaneously, providing that the absorption spectra of the two species do not overlap significantly, or at least are different enough that spectra can be fitted to extract the relative contribution from each absorber [263, 264]. CEAS has many advantages over CRDS for broadband measurements [1].

In order to carry out out a broadband cavity enhanced absorption measurement, the experimental set-up described previously (Chapter 3) must be altered. A light source capable of producing a wide span of wavelengths is required, as well as a cavity that supports such a wide range of wavelengths, and a detector capable of resolving intensity as a function of wavelength.

There are a variety of broadband light sources available, many of which have been applied in cavity experiments. It is worth noting that the definition of 'broadband' in the literature is not well-defined, and depends on the desired application: it can be used to describe anything from the output of a free electron laser (spanning the range from 5.380 - 5.382 μm) [265] to that of a Xe arc lamp (spanning 390 - 620 nm) [266]. Conventional incoherent light sources have been used for CEAS, including lamps [160] and light emitting diodes (LEDs) [267]. While lamps offer extremely wide spectral coverage, ranging from the UV to the near-IR, as well as having a good intensity stability (1 - 2%), the light beam is non-directional and hence difficult to focus into a cavity. LEDs have obvious advantages in their robustness, compactness and low cost, but, compared with lamps, typically have lower power output and higher divergence, as well as being available only at certain wavelengths, with a much narrower spectral range (typically 10 nm around the centre wavelength only). So-called 'white-light' LEDs do exist but are in fact a combination of blue, green and red LEDs, and hence only have high emission output at these centre wavelengths.

While it would appear more straightforward to use continuous wave sources such as lamps and LEDs for a continuous wave CEAS experiment, there is in fact a great deal of interest in applying broadband pulsed laser sources, such as supercontinuum sources [268] for CEAS experiments, as a directional, high power beam can be more easily used in a cavity experiment. Supercontinuum sources are a relatively new spectroscopic tool, which have spatial coherence and a broad bandwidth, typically spanning a few hundred nanometres. We use a supercontinuum source in our CEAS experiments and will discuss supercontinuum generation in detail in the Section 5.1.2. For now, we simply note that the generation of a supercontinuum occurs when a high light intensity passes through a highly non-linear optical medium. A comparison of the output of several different broadband light sources is provided in Figure 5.1.

A broadband CEAS experiment also requires a broadband cavity to be used in combination with the light source. Typical high reflectivity dielectric mirrors, such as those used in CRDS experiments, tend to have a relatively narrow reflectivity range of around 10% of the centre wavelength. There is generally a trade-off between wider bandwidth and higher reflectivity, although more recently thin film coating technology has improved. For example, Layertec provide mirrors with reflectivities $> 99.85\%$ over a wavelength range of 400 - 800 nm. Alternatively, broadband cavities can be designed which rely on total internal reflection in Brewster's angle prisms [269, 270] or optical fibres (Chapter 8) [271–273]. The sensitivity of such prism and optical fibre cavities is determined by the absorption loss in the substrate material.

For cavity output detection, CEAS typically uses a grating to disperse the wavelengths and a CCD array to image the resulting spectrum (see, for example [164]). The cavity output is time-integrated, typically over milliseconds to seconds, although even shorter integration times (10 μs) can be used depending on the sensitivity of the camera [274]. Alternative broadband detection strategies were reviewed by Ball and Jones in 2003 [275].

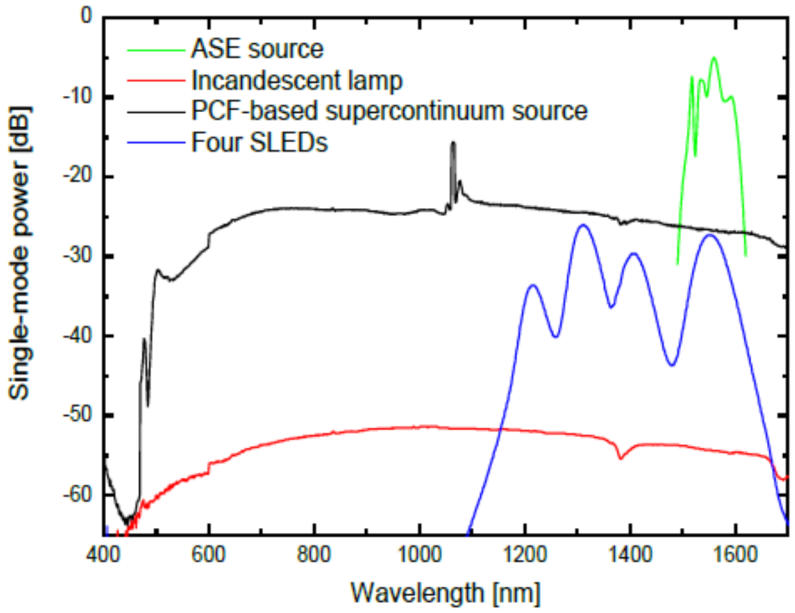


Figure 5.1: Comparison of the power spectral density delivered into a single-mode fibre for several different broadband sources. Reproduced from www.NKTPhotonics.com.

5.1.1 Liquid-phase CEAS

The first application of CEAS to liquid-phase analysis was presented by Fiedler et al. in 2005 [164], and since then optical pathlengths up to 20 cm have been investigated. Table 5.1 presents a summary of these studies.

A key difference between CEAS and CRDS studies on liquid samples is that, to date, all experiments have been performed either by filling the cavity entirely with liquid sample, or by inserting absorption cells into the cavity at normal incidence. There are a number of reasons why experiments using Brewster's angle cells have been avoided for the most part. Firstly, for the unpolarised light sources used in these measurements, inserting a cell at Brewster's angle would reduce the initial light intensity significantly. The reduction in light intensity will be discussed in Section 5.2.3. In addition, Fiedler et al. have previously noted that for incoherent broadband light sources, such as the Xe lamp used in their experiments, the light rays coupling into the cavity have a certain angular distribution, which can cause the Brewster's angle to be poorly defined, and hence cause cuvette insertion to occasion higher losses at Brewster's angle than at normal incidence [164]. Finally, Brewster's angle incidence precludes the use of standard cuvettes, which may not have sufficient width to allow for rays at Brewster's angle incidence to pass through the cuvette front faces without encountering one of the cuvette side walls.

In the first example of the application of CEAS to liquid-phase analysis, Fiedler et al. simply modified a commercial double-beam UV/vis absorption spectrometer, placing two 99% reflective mirrors around three different sample cuvettes, with optical pathlengths ranging from 0.1 mm - 100 mm. A cavity enhancement

Table 5.1: Chronological summary of two-mirror liquid-phase cavity enhanced absorption spectroscopy. Where several analytes were measured, the stated detection limit corresponds to detection of the first listed analyte. λ is the wavelength in nm, l is the optical pathlength in mm, Vol. is the total probed volume of sample, $C_{\min}$ is the lowest detectable concentration, which corresponds to the minimum concentration of the first listed analyte, if several analytes were measured. Where possible, concentration detection limits have been calculated from three standard deviations (3σ) of the reported baseline noise, but limits marked with * have been estimated using other reported data. $C_{\min}$ is converted into the minimum detectable absorption per unit pathlength, $\kappa_{\min}$, in cm^{-1} using the literature absorption coefficient value for the respective analyte at the appropriate wavelength. CEF is the cavity enhancement factor, the number of passes measured compared to a single-pass experiment

Ref.	Fig.	Analyte	λ / nm	l / mm	Vol. / mL	$C_{\min}$ / nm	$\kappa_{\min}$ / cm^{-1}	CEF
Fiedler et al. [164]	2.7(b)	Benzene	607, 450 - 650	100 1,10	$>$ mL	-	9×10^{-6}	10
McGarvey et al. [276]	2.7(a)	Bacterio-chlorophyll a	783	1.75	0.01	0.2	3×10^{-6}	23,000
Islam et al. [277]	2.7(b)	Brilliant blue-R, dyes, Ho^{3+}	630, 420 - 670	2.0	0.9	0.62	5.1×10^{-5}	51
Seetohul et al. [263]	2.7(b)	Rhodamine B, Rhodamine 6G	450 - 600	10	0.07	0.27	1.9×10^{-5}	45
Seetohul et al. [174]	2.7(a)	Sudan black	584, 400 - 700	200	98	0.018	1.0×10^{-6}	82
Seetohul et al. [174]	2.7(a)	Methylene blue	655	200	98	0.0046	2.8×10^{-7}	429
Kiwanuka et al. [264]	2.7(b)	Rhodamine 6G	400 - 700	54	2.7	0.2	9.1×10^{-6}	-

factor (CEF) of 10 was achieved [164]. We noted earlier in Chapter 2 that a CEF of 100 would be predicted for mirrors with 99% reflectivity. The poorer CEF achieved by Fiedler et al. arises from the additional losses occasioned by the insertion of a solvent-filled cuvette into the cavity, which can be estimated to contribute a high loss of around 9%, given that CEF $= \frac{1}{1-R}$.

Following this study, Islam's group have placed both a 2 mm cuvette [277] and a 10 mm HPLC flow cell [263] at normal incidence into a cavity. In their first paper, a variety of analytes were investigated, using mirrors ranging from 99% - 99.9% reflectivity [277], and $\kappa_{\min}$ values ranging from 5.1×10^{-5} to 3.1×10^{-3} cm^{-1} were achieved. The values shown for this reference [277] in Table 5.1 correspond to values acquired with a set of 99% reflective mirrors. Somewhat counter-intuitively, Islam et al. found that the detection limit improved with decreasing mirror reflectivity from 99.9% to 99%. This was attributed to the decrease in the intensity of light reaching the detector as the reflectivity of the mirrors increases, which required the integration time on the CCD array to be increased to enhance the signal. However, Islam et al. found that increasing the integration time above 100 ms caused the dark noise to increase in a non-linear fashion, owing to the lack of thermoelectric cooling of the CCD array [277]. Thus, the increased noise associated with the absorption measurement made with higher reflectivity mirrors actually caused the limit of detection to decrease despite the improvement in CEF within the cavity itself. Islam's second study presented the first demonstration of CEAS to HPLC detection [263], using a similar set-up to that presented in [277].

Fiedler et al. initially noted that filling the entire cavity directly with liquid was not necessarily a good strategy for CEAS measurements, because the mirror reflectivity, which will vary for liquid-filled cavities, must be accurately known in a CEAS measurement in order to determine absolute absorption coefficients [164]. The reflectivity of the mirror is of course dependent on the difference in refractive index between the boundary layer of the dielectric coating and the surrounding medium, which is usually air. When a liquid sample is placed directly in contact with the mirror surface, the reflectivity is typically reduced, as we have already noted in Chapter 3 for CRDS measurements carried out in direct contact with liquid samples. For example, Bahnev et al. noted that placing liquid directly in contact with the mirrors typically reduced the ringdown time of the cavity by 25% [169]. Nevertheless, Islam demonstrated one of the most sensitive absorption measurements in the literature to date, by filling a 20 cm long cavity composed of 99.9% mirrors directly with sample solutions, enabling the detection of 4.6 pM methylene blue [174]. The reported CEF of 419 is approximately one half lower than that predicted for 99.9% reflectivity mirrors (CEF = 1000), which indicates that the mirror reflectivity was reduced by contact with the liquid sample to approximately 99.8%.

The most impressive cavity enhancement factor was achieved by McGarvey et al., who filled a cavity only 1.75 mm in length directly with solutions of bacteriochlorophyll a in acetone [276]. The impressive reported sensitivity gain of 23,000 arises from two key factors. Firstly, and most importantly, the high reflectivity mirrors which were used in this work (99.998%); and, secondly, the short pathlength which means that the scattering and absorption losses from the solvent are minimal. We note that the CEF is approximately half that which would be predicted from the mirror reflectivity alone, indicating that the mirror reflectivity is reduced by contact with the liquid sample, as expected. Nevertheless, McGarvey et al. discuss the possibility of single bacteriochlorophyll a molecule detection if a very short cavity (around 10 μm in length) was designed, which would be compatible with microfluidic systems. It should be emphasised that one of the key advantages of CEAS compared to CRDS is that such short cavities can be used, because there is no longer a requirement to achieve nanosecond timescale detection, as the intensity is time-integrated.

CEAS studies to date have often probed sample volumes significantly larger than those typical for microfluidic analysis (i.e. millilitre rather than sub-microlitre volumes). In this Chapter, we explore the application of CEAS to small volume analysis.

5.1.2 Supercontinuum light generation

Supercontinuum light sources are a relatively new tool for spectroscopy [278]. They have a wavelength range that can span several hundreds of nanometres and have an intensity many orders of magnitude greater than the conventional broadband light sources outlined in the earlier part of this chapter.

When a light wave propagates through a medium, the oscillating electromagnetic field exerts a polarising force on the electrons in the medium [279]. This polarisation mostly affects the more weakly bound outer

electrons. For conventional light sources, the linear pertubation is small, as the field from the light is much weaker than the field binding the electrons to the atoms. However, when the radiation field becomes comparable to the atomic fields, then the relationship between electric field and polarisation is no longer linear, and we enter the regime known as non-linear optics.

Supercontinuum light is produced by aligning a high intensity, monochromatic light beam through a non-linear medium. A series of non-linear processes broaden the frequency of the incident beam equally to the high and low frequency side of the source wavelength. Initial experiments were conducted by Alfano and Shapiro in the 1970s [278]. By illuminating a crystal of borosilicate (BK-7) glass with a focused laser beam (530 nm, 5 mJ), a supercontinuum spanning spanning 400 to 700 nm was created. Since then a variety of non-linear media have been used to generate supercontinuua, including carbon tetrachloride solution [280] and optical fibre tapers [281].

We use a 20 m length of non-linear photonic crystal fibre (PCF) to generate a supercontinuum. PCF, also known as 'holey' or 'microstructured' fibre, first became commercially available in the 1990s [262]. Figure 5.2 shows some images of the PCF. The fibre has an outer diameter of 125 μm, a core diameter of 5 μm and is protected by a single layer acrylate coating. Our PCF consists of a solid core, surrounded by a 'holey' cladding. The air-holes in the cladding lower the refractive index of the cladding so that light will undergo total internal reflection in the solid core, without the usual need for chemically-doping the cladding in order to lower the refractive index of a conventional solid-state optical fibre. Compared to conventional optical fibres, PCFs can be engineered to have a range of special properties. For example, the arrangement of holes or the shape of the core can be used to alter the non-linearity of the fibre.

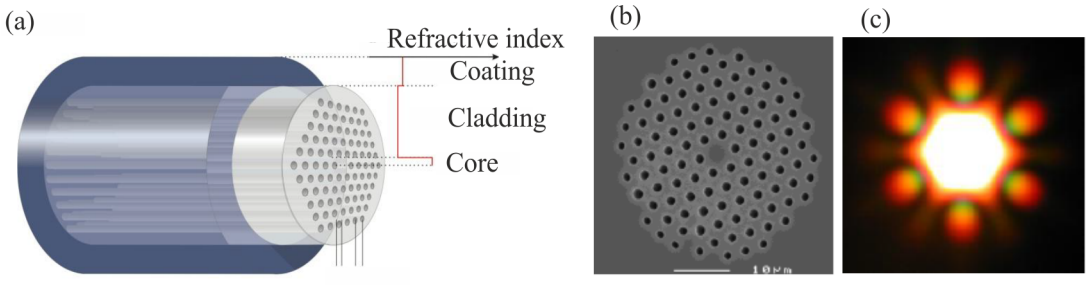


Figure 5.2: (a) Schematic of the photonic crystal fibre (PCF), where the solid core is embedded in a cladding comprising a triangular lattice of air holes. (b) Scanning electron microscope image of the end of the PCF. (c) Far field output of the PCF. Images reproduced from www.NKTPhotonics.com

Solid-core PCFs are fabricated by stacking silica capillary tubes around a rod of glass in a close-packed array, which is then inserted into a plastic jacket [282]. The preform is then heated and pulled in a fibre draw tower, to a length of a few kilometres. The fine structure of the fibre remains intact during the drawing process, leaving a solid core surrounded by an ordered array of air holes that run along the fibre axis for its entire length, as shown in Figure 5.2. The layout and size of the air holes can be varied to fine-tune properties including the zero dispersion wavelength and non-linear index. At the zero dispersion wavelength,

the effect of chromatic dispersion, caused by the variation of refractive index with wavelength, and waveguide dispersion, resulting from the wavelength dependence of the fibre propagation constant, cancel one another. By coupling a high intensity light pulse, with wavelength close to the zero dispersion wavelength, into a length of PCF, a supercontinuum can be generated. The small core of PCF (typically only a few microns in diameter) ensures that focused laser light travelling in the fibre core reaches high light intensities, causing the light to undergo non-linear optical processes.

A variety of non-linear optical processes contribute to supercontinuum generation in PCFs, namely stimulated Raman scattering, self-phase modulation and four-wave mixing [283]. These processes will be briefly discussed in turn. Most readers will be familiar with Raman scattering in the gas phase, which involves a transition between vibrational (ν) or rotational energy levels of the sample via a virtual energy state. These transitions can take two forms: either the sample absorbs energy, known as Stokes scattering ($\Delta\nu = +1$); or it emits energy, anti-Stokes scattering ($\Delta\nu = -1$). Raman processes can also occur in the solid state. In the solid state, as in single molecules, vibrational modes are quantised. These modes are called phonons and represent a collective vibrational motion of the crystal lattice. When an intense laser source is used to excite transitions, a population inversion is created between the virtual and final states leading to stimulated emission at a variety of wavelengths. These new frequency components broaden the laser pulse and can themselves act as exciting wavelengths for further Raman scattering processes, and so on.

The Kerr effect is the change in refractive index of a medium induced by an intense electric field. The changing phase of the propagating pulse causes a change in the frequency of the light as follows [284]:

$$\Delta\omega(t) = -n_2 \frac{dI(t)}{dt} \frac{\omega d}{c} \tag{5.1}$$

where ω is the frequency, n_2 is the non-linear refractive index of the medium, I is the intensity, t is time, d is the length of the optical medium and c is the speed of light. The sign of the frequency change depends on the slope of the intensity profile, which produces new frequency components that are redder and bluer at short and long times respectively. This process is called self-phase modulation and leads to significant spectral broadening.

Finally, four-wave mixing occurs when a fourth wavelength is generated from three photons of different frequencies, as follows [285]:

$$\omega_{ijk} = \omega_i + \omega_j - \omega_k \tag{5.2}$$

The efficiency of four-wave mixing depends strongly on phase-matching conditions, chromatic dispersion of the fibre and fibre length.

In our non-linear PCF, the combination of the various non-linear processes described transforms the monochromatic (1064 nm) input pulse into a broadband pulse spanning a wavelength range of around 1.5 μm, from 400 - 1900 nm.

Supercontinuum sources are beginning to be more widely applied in broadband cavity-based experiments [264,268,269,286,287]. Sneppen et al. recently published a comparative paper on the use of supercontinuum sources and white LEDs for use in evanescent wave broadband cavity enhanced absorption spectroscopy, and found that the higher power of the supercontinuum source was superior in allowing for broadband tracking of fast kinetics (integration time 10 μs) [274]. Kiwanuka et al. used a supercontinuum source in their liquid-phase CEAS measurements, in combination with 99% reflectivity mirrors, determining a detection limit of 9.1×10^{-6} cm^{-1} in a cuvette with an optical pathlength of 5.4 cm [264].

5.2 Experimental

In order to ascertain the performance of CEAS for small volume analysis, we have carried out several experiments. Firstly, the empty cavity was characterised (Section 5.3), in terms of reflectivity versus wavelength and also noise versus wavelength. Secondly, we inserted two commercial flow cells into a 13.5 cm long cavity at normal incidence and carried out CEAS measurements on a concentration series of potassium permanganate (Section 5.4.1). Thirdly, we inserted thiolene microfluidic chips, the fabrication of which was described in Chapter 3, into a 49.5 cm long cavity at both normal and Brewster's angle incidence, in order to determine the optimum angle of incidence for CEAS measurements (Section 5.4.2). These results were compared with simultaneously acquired CRDS measurements, in order to compare the sensitivity of the two techniques directly (Section 5.4.2). Finally, we demonstrate the detection of the full visible broadband spectrum of single droplets using CEAS (Section 5.5).

The various components of the experimental set-up will first be described in detail.

5.2.1 Light source

Our supercontinuum light source consists of a 20 m length of non-linear PCF (purchased from NKT Photonics, SC-5.0-1040), which is pumped by two different lasers. Firstly, a Nd:YAG laser (Ekspla, NL-202, 1064 nm) was used. The 2 mJ pulse energy (repetition rate programmable from 1 - 1000 Hz, 2 mm beam diameter) of the Nd:YAG laser is well above the experimentally determined damage threshold of the photonic crystal fibre, so a suitable pump beam is generated by taking a primary surface reflection from a glass slide placed at 45° to the beam axis, yielding a pump energy of 30 - 60 μJ/pulse. The remainder of the Nd:YAG beam passes through the slide and is dumped. An iris is placed along the pump beam path in order to remove the second reflection from the window's rear surface. This reduces the likelihood of the incident

laser pulse damaging the fibre end and hampering supercontinuum generation. Unfortunately, a malfunction of the laser diode pumping the Ekspla laser took this laser out of service for several months, and the remainder of the experiments were instead carried out using a microchip Nd:YAG laser (NP-10620-100, Teem Photonics) for pumping the supercontinuum fibre. This laser produces 0.9 ns, 6 μJ pulses at 1064 nm with a repetition rate of 7.4 kHz, and is well-matched to the damage threshold of the PCF. In addition, the higher repetition rate of this laser is advantageous for these experiments in which the cavity output is time-integrated.

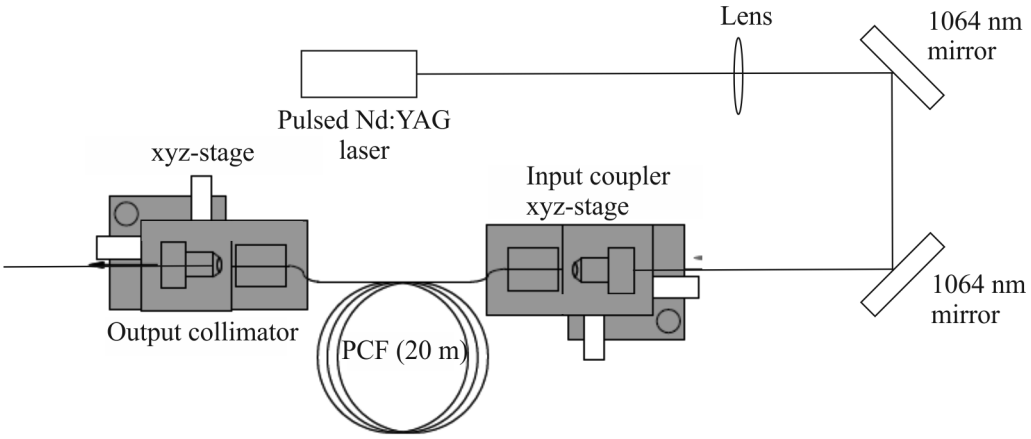


Figure 5.3: Schematic of supercontinuum set-up.

In both cases, the pump laser beam is coupled into the supercontinuum fibre using a microscope objective lens (COMAR, singlet, 6.3 mm focal length), to ensure high efficiency coupling into the small fibre core. A schematic of the experimental set-up for supercontinuum generation is shown in Figure 5.3. Input coupling is a critical stage of the supercontinuum generation process. The laser beam is aligned through a series of pinholes to ensure that it couples into the fibre along the optical axis. Non-linear optical processes are very sensitive to variations in the input power, which occurs on even slight misalignments owing to the small size of PCF core. Generally, it is sufficient to realign the fibre at the start of each day. At the output, a second microscope objective is used to collimate the SC output into a beam, which is then passed through an optical filter to remove light above 720 nm, preventing the intense near-IR light, which is produced with high efficiency and transmitted through the mirrors, from reaching the detector.

PCF can be treated in a similar way to conventional optical fibre, although there are a few additional considerations. The bare fibre ends are very susceptible to dust and solvent contamination, and should never be cleaned in liquid, as the liquid enters the holes via capillary forces, damaging the fibre's performance. Bare fibre ends can be periodically recleaved, although as the PCF is very expensive, persistent recleaving is not recommended. We have found the most stable supercontinuum generation to occur when at least the input fibre end is connectorised and heat-treated, in order to collapse the air-holes at the end of the fibre, and thus facilitate light-coupling into the fibre core.

5.2.2 Optical cavity

The optical cavity is formed from two concave 25 mm dielectric mirrors (Layertec, radius of curvature 1 m, reflectivity ca. 99% from 400 - 800 nm). In the first experiments, where only CEAS data were recorded, mirrors were positioned at a separation of 13.5 cm. In later experiments, this cavity length was increased to 49.5 cm to allow for facile switching between CEAS (which does not require a long cavity) and CRDS measurements (which does require a longer cavity). Combined CEAS and CRDS enabled mirror calibration to be carried out, as well as providing a direct measure of the loss arising from insertion of various absorption cells.

5.2.3 Absorption cells

As before (Chapter 3), absorption cells were positioned in the centre of the cavity on a double-rotation (Thorlabs, RP01) and three-axis translation stage (Newport Corporation, 443), with micrometer resolution actuators (Newport Corporation, SM-25). Liquid was delivered to the cells using syringe pumps (Fusion 400, Chemyx).

We have investigated the performance of two commercial flow cells, with pathlengths of 0.1 mm and 2 mm, as well as thiolene microfluidic chips, all of which which were described in detail in Chapter 3. Their suitability for CEAS measurements is evaluated in Section 5.4.

Flow cell measurements were only carried at normal incidence, but microfluidic chip measurements were carried out at both normal incidence and Brewster's angle incidence. A key difference between the single-wavelength light source used in Chapter 3 and the supercontinuum light source used in this Chapter is the polarisation. The single-wavelength laser source is polarised, and thus reflection losses can be minimised, without reducing the light intensity, by inserting the absorption cell at Brewster's angle. In contrast, the supercontinuum light source is unpolarised and thus placing an absorption cell at Brewster's angle will reduce the cavity output light intensity by approximately 50% relative to normal incidence interrogation. This approximation of 50% reduction in light intensity can be explained by the use of the Fresnel equations for p- and s-polarised light [279]. At Brewster's angle, the transmission of p-polarised light (T_p) through an interface is maximised, while the transmission of s-polarised light (T_s) is significantly reduced. For example, the Fresnel transmission for each polarisation for a microscope slide inserted at Brewster's angle incidence can be calculated to be $T_p = 1.00$ and $T_s = 0.71$. The Fresnel transmission for each polarisation can be converted into a predicted ringdown time for a particular cavity set-up, by taking into account the mirror reflectivity, and using Equation 2.13. Given a mirror reflectivity of 0.9898 (which will be determined in Section 5.2.5), the resulting ringdown values for each polarisation can be calculated to be $\tau_p = 161$ ns and $\tau_s = 5$ ns (given to the nearest nanosecond). Given that $I_{\mathrm{CEAS}} = \int_0^\infty I_0 e^{-\frac{t}{\tau}} dt = I_0 \tau$, this shows that the majority of s-polarisation does not contribute to the intensity measured at Brewster's

angle, and the light intensity is reduced by $\sim$ 50% compared with unpolarised light at normal incidence, where the ringdown time arises from equal contributions from both s- and p-polarisation.

5.2.4 Detector

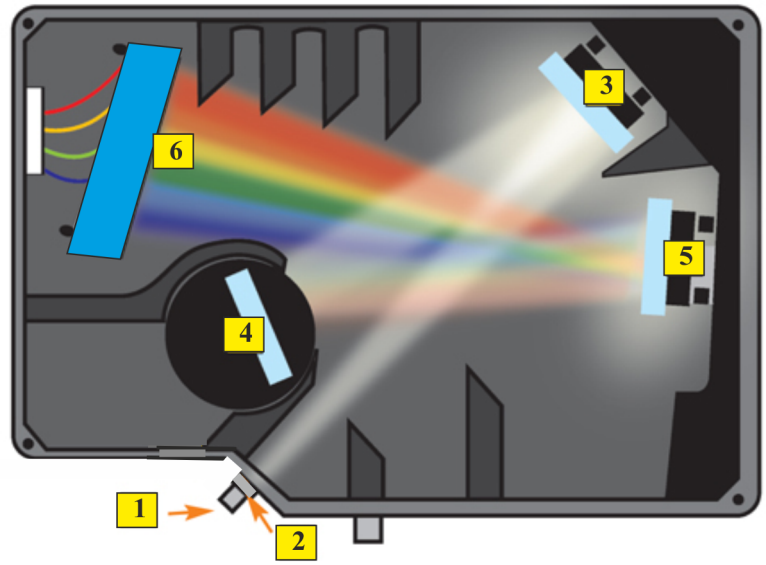


Figure 5.4: Schematic of the optical bench used in Ocean Optics HR4000 spectrometer. The labels correspond to elements detailed in the text. Image adapted from an image downloaded from www.oceanoptics.com.

For recording broadband CEAS data, the cavity output is collected using a 105 μm core multimode fibre, which couples the cavity output light into the spectrometer. We use a USB spectrometer (Ocean Optics, HR4000) to wavelength-resolve the output. The spectrometer consists of a number of key elements, which are shown in Figure 5.4.

1. Fibre input. A precision SMA 905 Connector allows a connectorised optical fibre to be screwed into the spectrometer's entrance aperture with optimum alignment.

2. Entrance slit. Rectangular aperture, 1 mm tall and with a fixed width of 50 μm, defining the amount of light entering the spectrometer.

3. Collimating mirror. The collimating mirror is matched to the 0.22 numerical aperture of the optical fiber cable. Light reflects from this mirror, as a collimated beam, toward the grating. The mirrors are aluminum-coated with more than 95% reflectivity across the visible and near-IR region.

4. Grating. We use a broadband grating (Ocean Optics, HC-1) which provides the spectrometer with its wide wavelength range. Its blaze wavelength is around 400 nm. The grating is installed on a rotating

platform and then permanently fixed in place to eliminate mechanical shifts or drift, removing the need for frequent wavelength recalibration.

5. Focusing Mirror. The focusing mirror focuses light onto the detector plane.
6. Linear silicon CCD array detector (Toshiba TCD1304AP). Effective wavelength range of 200 – 1100 nm.

The spectrometer interfaces to a computer via USB 2.0, and we use a modified LabVIEW program downloaded from National Instruments to connect to the instrument. Spectra can be collected either in single-shot or continuous-mode. The readout rate of the spectrometer is 20 Hz and the integration time can be set from 3.8 ms to 10 s.

The spectrometer can be triggered externally via a breakout box (Ocean Optics, HR4-Breakout) but we choose to run it in free running mode. At its shortest integration time of 3.8 ms, the spectrometer averages over 28 laser shots when using the 7.4 kHz repetition rate Nd:YAG laser to pump the supercontinuum source. By acquiring several spectra recorded with this integration time, or by increasing the integration time, depending on the light levels on the detector, we can average over a greater number of laser shots. We typically acquire 50 spectra for CEAS measurements, which at the spectrometer's shortest integration time of 3.8 ms, corresponds to averaging over a total of 1400 laser shots.

Simultaneous CEAS and CRDS measurements were carried out for three reasons. Firstly, the single-pass optical pathlength through microfluidic chips requires accurate calibration in order to interpret the CEAS measurements correctly, and thus we use CRDS measurements on a concentration series of permanganate to establish the pathlength accurately before determining the CEF of CEAS measurements. Secondly, the loss through the microfluidic chips was found to increase with use, as the chip contents often degrade the optical quality of the channel walls over time, and thus CRDS measurements provided an accurate calibration of the chip loss during the day. Finally, the CEF is of course highly alignment sensitive, especially when directing the laser beam withing the cavity through small microfluidic (< 1 mm) channels, and thus recording simultaneous CRDS measurements enabled the alignment to be optimised whenever an unexplained drop in ringdown time was observed.

In order to acquire simultaneous CEAS and CRDS measurements, we place a 50:50 beamsplitter behind the cavity output. One half of the beam is then focused into the spectrometer for broadband CEAS detection, while the other half of the beam passes through a narrow bandpass filter and is detected at a single-wavelength (570 nm) using a PMT. The CRDS analysis was carried out as described in detail in Chapter 3.

5.2.5 CEAS data analysis

One advantage of CEAS over CRDS is that no data fitting procedure is required in order to extract information from the experiment: raw intensity values can be converted into absorption values given the previously derived Equation [160]:

$$\kappa \approx \frac{1}{l}(\frac{I_{\mathrm{out}}^{0}}{I_{\mathrm{out}}} - 1)(1 - R) \tag{5.3}$$

Equation 5.3 is valid when the loss per pass is less than $\sim 25\%$. Care must be taken to ensure that the intensity values are correctly baseline-subtracted before insertion into Equation 5.3. The baseline is determined by measuring the spectra at various integration times when the light source is off. This procedure also enabled us to determine the noise inherent in the detector and the light source independently.

Typically, we plot CEAS data as $(\frac{I_{\mathrm{out}}^{0}}{I_{\mathrm{out}}} - 1)$ as a function of concentration. $(1 - R)^{-1}$ is defined as the cavity enhancement factor (CEF), which is the ratio of the measured absorbance to that for a single pass. The gradient m of this linear plot corresponds to $\alpha l\mathrm{CEF}$ where α is the absorption coefficient and l is the optical pathlength, and thus we can calculate that the $\mathrm{CEF} = \frac{m}{\alpha l}$.

Two points must be emphasised from Equation 5.3. Firstly, the optical pathlength must be precisely known in order to quantify the CEF, which must be determined before quantitative absorption measurements can be carried out. Typically, we determine the CEF for each experimental set-up before using the set-up for unknown analytical measurements. In effect, this calibration determines the cavity transmission, which accounts for losses associated both with the mirrors, and with the flow cell or microfluidic chip used to contain the liquid sample.

The calibration requirement for CEAS is well-known. For our purposes, as we are dealing with broad absorption bands, a high resolution calibration of R versus λ is not necessarily required. However, compared to gas-phase measurements, we have the added difficulty that any absorption measurement carried out in our absorption cell will combine the cell and mirror losses. Given that we are working with modest reflectivity mirrors (99%), it was possible to use the manufacturer's reflectivity data. This plot is shown as the red line in Figure 5.5(a), plotted on the right-hand y-axis. Clearly, there is significant variation in the reflectivity of the multilayer dielectric coating across the broad wavelength range plotted. This variation arises from the multistack design needed for large bandwidth, and can be problematic for CCD detection because the variation of intensity as a function of wavelength can result in saturation at certain pixels and low counts at others.

In addition to using the manufacturer's reflectivity data, we have also determined the ringdown time of the empty cavity at three different wavelengths, by using three different bandpass filters (bandwidth 10 nm) for wavelength-selection. Unfortunately, we cannot correlate this measured reflectivity at one wavelength

with an unknown reflectivity at a different wavelength because of the significant variation in intensity of the supercontinuum source across the visible spectrum. However, the results provide an indication of how the mirror reflectivity measured in the cavity matches up to the manufacturer's specification. The ringdown time for a empty cavity of length 49.5 cm was determined to be 155 ns at 510 nm, 161 ns at 570 nm, and 133 ns at 610 nm. This corresponds to a mirror reflectivity of 98.94% at 510 nm, 98.98% at 570 nm, and 98.77% at 610 nm. These mirror reflectivity values determined from the ringdown times (presented as green dots on Figure 5.5(a)) correspond well to the mirror reflectivity determined from Figure 5.5(a) at the two lower wavelengths, although there is a discrepancy between the values determined at 610 nm. This indicates that Figure 5.5(a) should only be used for mirror calibration with caution.

As shown previously in Chapter 2, the detection limit of a CEAS measurement can be determined from the minimum detectable change in transmitted intensity $\Delta I_{\min}$ as [160] (Chapter 2):

$$\kappa_{\min} = \frac{1}{l}\left(\frac{\Delta I_{\min}}{I^0_{\text{out}}}\right)(1-R) \tag{5.4}$$

We also compare this sensitivity to the 3σ uncertainty in the x-intercept of a plot of $(\frac{I^0_{\text{out}}}{I_{\text{out}}} - 1)$ versus concentration, determined through a concentration series of permanganate solutions, similarly to the CRDS calibration carried out in Chapter 3.

5.3 Characterisation of the cavity

Before insertion of an absorption cell into the cavity, we have characterised the cavity output in terms of both transmission versus wavelength (the black line in Figure 5.5(a)) and noise versus wavelength (the red line in Figure 5.5(b)). There are two key features apparent in Figure 5.5(a). Firstly, the significant variation in mirror reflectivity versus wavelength (the red line in Figure 5.5(a)) maps directly onto the plot of intensity transmitted through the cavity (the black line in Figure 5.5(a)). The peaks in mirror reflectivity correspond to peaks in intensity. This seems counter-intuitive, as increasing the mirror reflectivity of course reduces the light intensity entering the cavity. However, this reduction can be partly offset by the increase in ringdown time of the cavity with increasing mirror reflectivity, which therefore increases the time-integrated cavity output. The resulting intensity of the cavity output is a trade-off between these two factors.

On top of this significant variation in mirror reflectivity, there is a more gradual decrease in light intensity output from the supercontinuum itself as the wavelength decreases. As the supercontinuum is pumped at 1064 nm, its output efficiency is greatest in the red region of the visible spectrum. As we move towards the blue region of the visible spectrum, the light intensity falls off, becoming undetectable with the spectrometer below 480 nm. As a result, the signal becomes much noisier at these lower visible wavelengths, as is evident

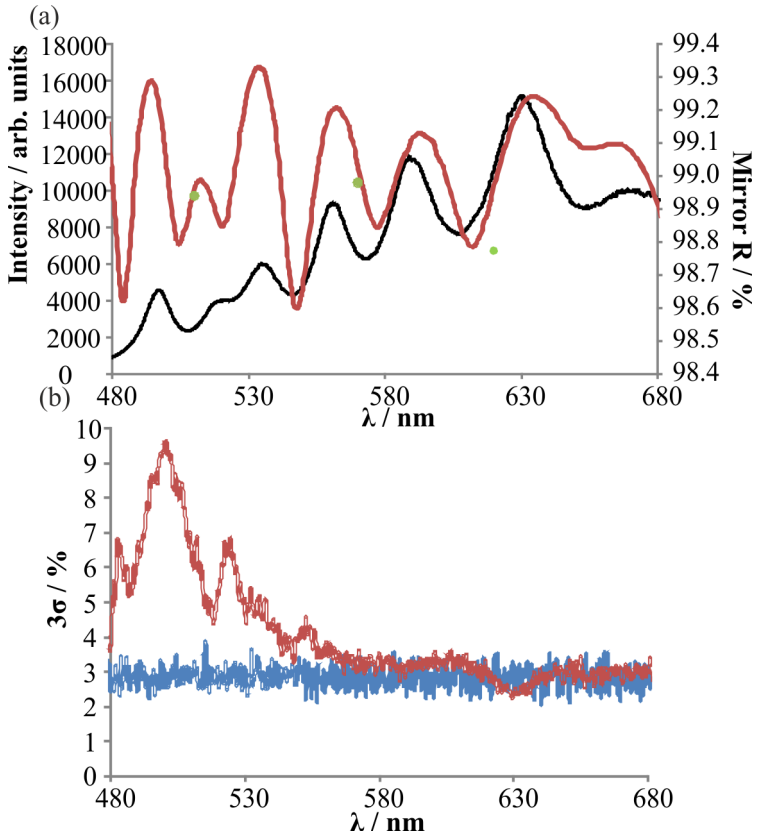


Figure 5.5: (a) Comparison of the intensity of the cavity output (black line), plotted as intensity on the left-hand y-axis versus wavelength, and the manufacturer's mirror reflectivity data (red line) measured for this coating run, plotted as reflectivity on the right-hand y-axis versus wavelength. The three green dots correspond to the mirror reflectivity measured using CRDS at these three wavelengths, and indicate the relatively good agreement between the ringdown data and the mirror reflectivity data. (b) Three times the standard deviation (3σ) uncertainty (in %) for the cavity output, determined from 50 consecutive spectra recorded at 10 ms integration time. The blue line corresponds to the noise when the supercontinuum source is off, and the red line corresponds to the noise when the supercontinuum source is on. Note that the slight dip in the red line around 630 nm is an artefact resulting from the onset of saturation around this wavelength, rather than a real reduction in noise at this wavelength.

from the red line in Figure 5.5(b). The red line can be compared to the blue line, which is the noise when the light source is off, and thus corresponds to the detector noise. Both plots represent the 3σ variation in intensity over 50 recorded spectra. Figure 5.5(b) indicates that above approximately 560 nm, it is the detector noise that is limiting rather than the light source noise. In contrast, below 560 nm, the light source shot noise is limiting the sensitivity. Of course, the shot noise in the light source below 560 nm can be improved by increasing the integration time, but this comes at the risk of saturating the signal at longer wavelengths, where the light intensity is higher. We have plotted the noise at 510 nm versus integration time (not shown) and found that the light source shot noise drops below the 3% noise observed in the detector at around 50 ms.

Taking both plots in Figure 5.5 together, we would therefore expect that absorption measurements should be most sensitive at wavelengths above 560 nm, where the noise level is determined by the detector rather than

the light source, and at intensity peaks, which correspond to small improvements in mirror reflectivity.

5.4 Characterisation of absorption cells

5.4.1 Commercial flow cells

The commercial flow cells were characterised in Chapter 3 at Brewster's angle incidence for use in single-wavelength CRDS measurements. As explained in Section 5.2, for CEAS measurements the cells were first inserted into the cavity normal to the beam axis. We have carried out various measurements to characterise the performance of the flow cells in this configuration. First, we evaluated the dynamic range of the 2 mm and 0.1 mm flow cells at normal incidence through measurements using a concentration series of potassium permanganate. Figure 5.6 shows plots of $\frac{I_{\mathrm{out}}^0}{I_{\mathrm{out}}} - 1$ versus permanganate concentration, at a wavelength of 570 nm, for (a) the 2 mm flow cell and (b) the 0.1 mm flow cell. As discussed in Section 3.2.1, this plot allows us to establish the CEF of each set-up. There are several important differences between these two plots. Firstly, a different laser was used for generating the supercontinuum used to analyse each flow cell. The Ekspla Nd:YAG laser had a maximum repetition rate of 1000 Hz, and a 25 ms integration time was used when calibrating the 2 mm flow cell. The Teem Photonics Nd:YAG laser used subsequently for the 0.1 mm flow cell and the remainder of the experiments in this Chapter had a higher repetition rate of 7.4 kHz, and thus a lower integration time could be used for the 0.1 mm flow cell (8 ms in this case). It is not, therefore, intended that the reader directly compare these two plots in terms of CEF for each flow cell, as they were carried out under different experimental conditions. The plots instead can be used to demonstrate some important points relating to CEAS. Notably, no breakdown in the assumptions leading to Equation 5.3 is observed for either cell, as the highest concentration analysed corresponds to a loss per pass of 5.6% in the case of the 2 mm cell, and 3.0% for the 0.1 mm cell, well within the limits of Equation 5.3, which is expected to be a good approximation up to a loss per pass of around 25%. This demonstrates that Equation 5.3 is particularly well suited for short pathlength analysis.

The gradient of each plot can be used to establish the CEF (see Section 3.2.1). It was found that the CEF when using the 2 mm flow cell was 93, and the CEF for the 0.1 mm flow cell was 134. This is in agreement with the higher losses associated with the longer pathlength flow cell established in Chapter 3 using CRDS.

The detection limit established using the spectral method (Section 3.4.2), $\kappa_{\mathrm{min,s}}$, is established using Equation 5.4. ΔI_{min} is established through the 3σ variation in I_{out}^0, which was determined to be 10.1% for the 2 mm cell and 2.5% for the 0.1 mm cell. I_{out}^0 was approximately 64% lower for the 2 mm cell, compared to the 0.1 mm flow cell, which is a consequence of the different laser used for pumping the supercontinuum in each case. Given these parameters, $\kappa_{\mathrm{min}} = 4.8 \times 10^{-3}$ cm^{-1} for the 2 mm flow cell and 1.9×10^{-2} cm^{-1} for the 0.1 mm flow cell.

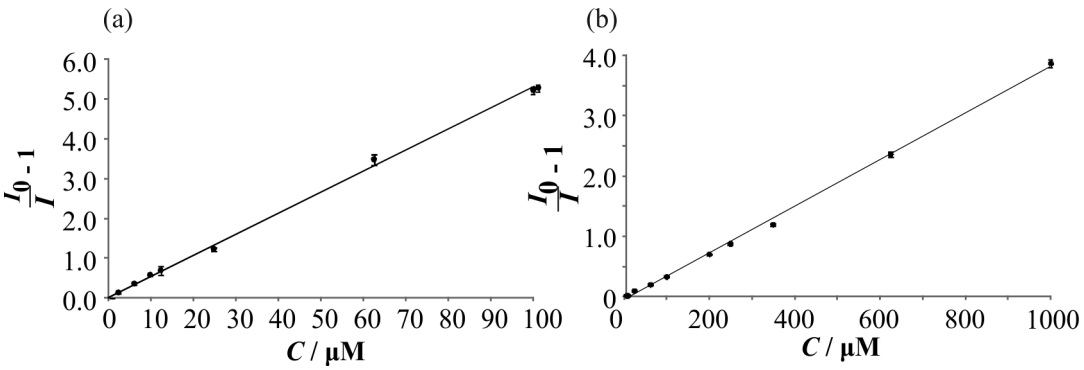


Figure 5.6: $\frac{I^0_{\text{out}}}{I_{\text{out}}} - 1$ versus permanganate concentration C/μM, at a wavelength of 570 nm for (a) 2 mm flow cell and (b) 0.1 mm flow cell, both inserted at normal incidence.

We can also determine the detection limit from the uncertainty in the x-intercept of the plots shown in Figure 5.6, given that the concentration can be converted into κ by multiplying C by the known absorption coefficient at 570 nm, $\alpha_{570} = 2875.6$ M^{-1} cm^{-1}. In this manner, the detection limit calculated using the regression method (Section 3.4.2) was determined to be 4.2×10^{-3} cm^{-1} for the 2 mm flow cell and 2.5×10^{-2} cm^{-1} for the 0.1 mm flow cell. These values are similar to the detection limits calculated using Equation 5.4, indicating the validity of both approaches.

Thus far in our analysis of the CEAS data, we have focused on measurements made at one wavelength. Given that $\frac{I^0_{\text{out}}}{I_{\text{out}}} - 1 \propto A$, a plot of $\frac{I^0_{\text{out}}}{I_{\text{out}}} - 1$ versus wavelength yields the absorbance at each wavelength. This plot is presented in Figure 5.7(a). However, as we have already shown, the mirror reflectivity varies with wavelength, and thus this absorbance value needs correcting in order to account for the changing CEF at each wavelength. Figure 5.7(b) presents a plot of CEF versus wavelength, which is then converted into the total effective 'reflectivity' of both the mirrors and the flow cell (Figure 5.7(c)). Given the previously established mirror reflectivity (Figure 5.5(a)), this allows the transmission through the flow cell to be determined at each wavelength (Figure 5.7(d)). The transmission through the flow cell decreases with decreasing wavelength, as expected. This decrease in transmission with wavelength is expected to be reasonably smooth, and the 'ripples' on the transmission curve are most likely an artefact resulting from uncertainties in the mirror reflectivities determined earlier in the single pass measurements. As noted previously, for maximum accuracy of determination of mirror reflectivity versus wavelength, a ringdown measurement should be carried out at every wavelength for each different cavity set-up, as the effective mirror reflectivity depends on the mirror alignment. As we are working with moderate reflectivity mirrors here, and do not have access to a monochromator, our 10 nm bandwidth filters would not provide sufficient wavelength resolution across the visible spectrum. We have found a solution in the form of carrying out simultaneous CRDS and CEAS measurements, as described in the following Section.

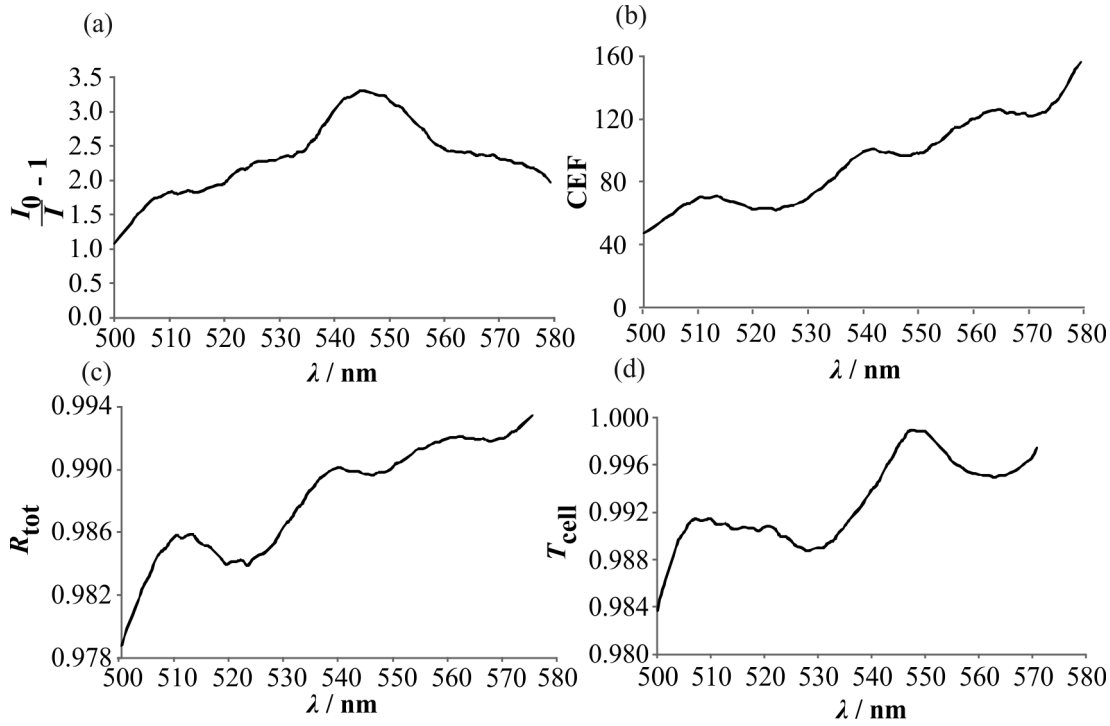


Figure 5.7: Example plots, in this case for 625 μM permanganate, determined in the 0.1 mm flow cell. (a) $\frac{I^0_{\rm out}}{I_{\rm out}} - 1$ versus wavelength. (b) CEF versus wavelength. (c) Total reflectivity versus wavelength. (d) Transmission of flow cell versus wavelength.

5.4.2 Thiolene chips

Several thiolene-based microfluidic chips (the fabrication of which was described in detail in Chapter 3), with chip walls composed of 1 mm thick microscope slides, were also tested in the cavity. Typically, the CEF through a thiolene chip with a channel height of 600 - 700 μm and a channel depth of 100 - 400 μm was found to be around 50 at 570 nm. This compares well with the previously determined values for the flow cells, as in these set-ups it is the mirror reflectivity not the loss through the absorption container that is limiting the CEF. In order to ascertain the sensitivity of CEAS versus CRDS, for chips inserted into the cavity at both normal incidence and Brewster's angle incidence, a series of permanganate solutions were flowed onto a thiolene chip which consisted of a 700 μm channel height and 140 μm channel depth (optical pathlength at normal incidence). Simultaneous CEAS and CRDS measurements were carried out by placing a 50:50 beamsplitter behind the cavity output, and then filtering one beam component before detecting this wavelength (570 nm) using a PMT, while sending the other beam component into the spectrometer as before. This type of set-up is also used in Chapter 7, for dual wavelength CRDS, and diagrams of the experimental set-up are provided in that Chapter. CRDS measurements were caried out at 570 nm, in order to compare the results directly with those obtained when characterising the flow cells, as described in Section 5.4.1.

As we have discussed previously in Chapter 3, the pathlength through the thiolene-chip must be established

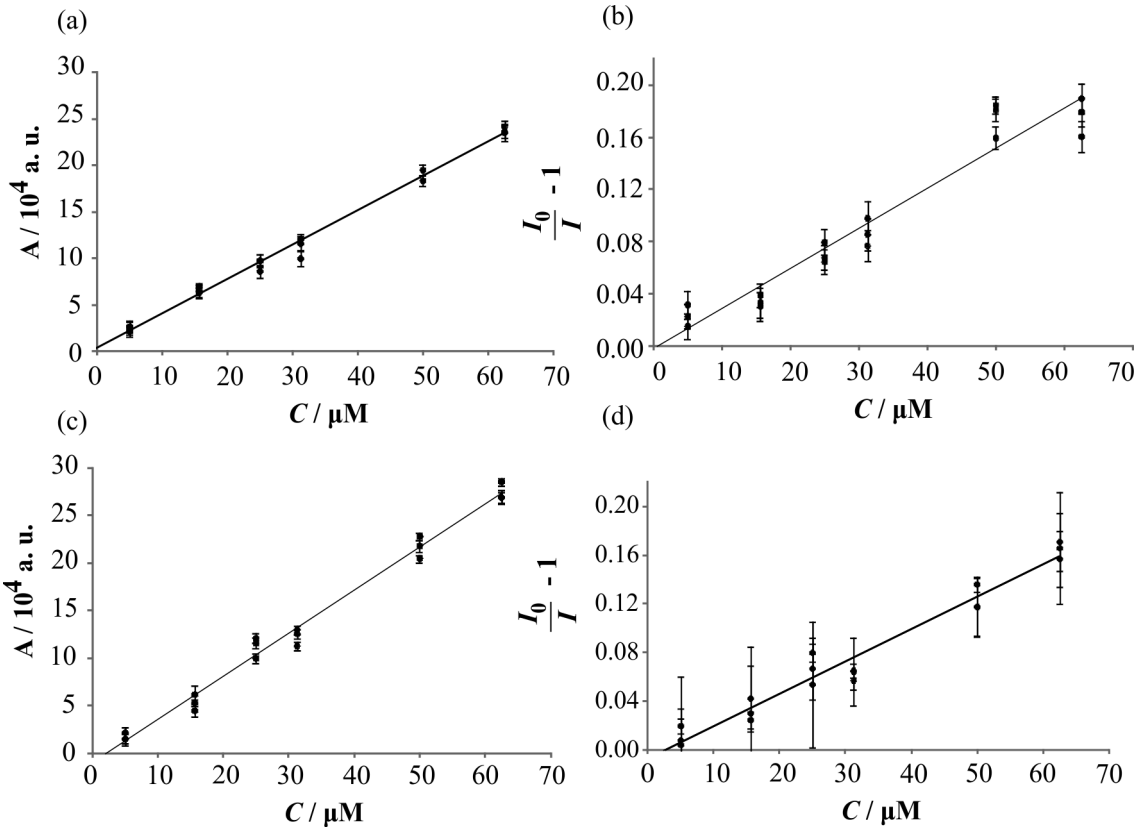


Figure 5.8: Example data from a thiolene chip, with data acquired at 570 nm. (a) CRDS data, plotted as A / μ a. u. (absorbance units) versus permanganate concentration C / μM, at normal incidence. (b) CEAS data, plotted as $\frac{I_{\rm out}^0}{I_{\rm out}} - 1$ versus permanganate concentration C / μM, at normal incidence. (c) CRDS data, plotted as A / μ a. u. (absorbance units) versus permanganate concentration C / μM, at Brewster's angle incidence. (d) CEAS data, plotted as $\frac{I_{\rm out}^0}{I_{\rm out}} - 1$ versus permanganate concentration C / μM, at Brewster's angle incidence. 1σ error bars are shown for each pair of blank/sample values recorded, where σ was established through repeated measurements of τ or I, respectively.

before using the chip for quantitative absorption measurements. A plot of $A = \alpha C l$, as determined from the CRDS data, versus concentration allows the pathlength l to be determined given a known α. A concentration series of aqueous permanganate solutions was used, ranging from 5 μM to 62.5 μM. Higher permanganate concentrations were not used because of the noticeable deterioration in ringdown time arising from degradation of the microfludic chip at high permanganate concentrations. Solutions were flowed onto the chip at a flow rate of 0.4 mL min^{-1}, and data were acquired under flow conditions. Simultaneous CRDS and CEAS data were acquired first at normal incidence and then at Brewster's angle incidence. The data are presented in Figure 5.8, where (a) and (b) are acquired at normal incidence and (c) and (d) are acquired at Brewster's angle incidence.

The ringdown time at 570 nm for an empty cavity was found to be 161 ns. Once the thiolene chip was inserted at normal incidence, a ringdown time of 121 ns was established through the channel walls (glass/thiolene/glass) and a ringdown time of 100 ns was established at normal incidence through the

water-filled channel. This corresponds to a loss of 1.02% at the mirrors, 0.34% through the channel walls and 0.62% through the channel. At Brewster's angle, the ringdown time was found to be similar to that at normal incidence, although as the Brewster's angle measurements were made after a concentration series of permanganate had been analysed at normal incidence, the ringdown time through the channel at normal incidence had already dropped to 93 ns due to chip degradation, corresponding to a loss of 0.75%. In addition, the Brewster's angle measurements were made at a slightly different point along the chip channel than the normal incidence measurements, and the ringdown values may not necessarily be directly comparable as the ringdown time is known to vary along the channel. We would expect the loss at Brewster's angle to be slightly higher than that at normal incidence because the absorption through the chip walls and the scattering and absorption losses through the solvent will be increased owing to the slightly longer pathlength at Brewster's angle incidence compared to normal incidence.

The pathlength through the chip was determined from the gradient of Figure 5.8(a) to be 128 μm at normal incidence, and from the gradient of Figure 5.8(c) to be 157 μm at Brewster's angle incidence. Given that Brewster's angle is expected to occur at approximately 56.9°, when taking into account reflection and refraction at all four interfaces, as discussed in Chapter 3, we would predict the pathlength to be increased by roughly 1.3 times at Brewster's angle compared to normal incidence. Given a normal incidence pathlength of 128 μm, we would therefore predict the pathlength at Brewster's angle to be 165 μm. This is a little longer than actually determined at Brewster's angle incidence (157 μm), which can be attributed to the fact that we may not be probing at precisely Brewster's angle incidence. In addition, we are probing a different point along the channel in both measurements, and the chip was measured to have a height variation of 11 μm from one end of the channel to another, which could also explain the discrepancy.

The ringdown time is determined to be 100 ns at normal incidence and 93 ns at Brewster's angle incidence. This value corresponds to the first determined ringdown value through the chip channel in each case, before permanganate solutions had begun to damage the channel and hence cause the ringdown time to drop. The 3σ uncertainty in τ_0 is determined to be 0.8% in both cases. This is higher than the uncertainty in ringdown time determined in Chapter 3, because the ringdown times are significantly shorter in this chapter. Using these values in Equation 2.17, together with the determined pathlength at normal incidence (128 μm) and Brewster's angle incidence (157 μm) allows us to determine $\kappa_{\mathrm{min,s}} = 1.0 \times 10^{-2}$ cm^{-1} for CRDS measurements at normal incidence and $\kappa_{\mathrm{min,s}} = 9.0 \times 10^{-3}$ cm^{-1} for CRDS measurements at Brewster's angle incidence. The longer pathlength at Brewster's angle incidence is responsible for the slightly improved κ_{min} compared to that determined at normal incidence, despite the slightly poorer ringdown time. These values are presented in Table 5.2.

The alternative determination of the detection limit, from the uncertainty in the x-intercept of the plots presented in Figure 5.8, yields $\kappa_{\mathrm{min,r}} = 7.4 \times 10^{-3}$ cm^{-1} for CRDS measurements at normal incidence and

Table 5.2: Sensitivity of CEAS and CRDS measurements acquired at both normal incidence and Brewster's angle incidence, using a thiolene chip, where $\kappa_{\mathrm{min,s}}$ arises from the use of Equation 5.4 or Equation 2.17 respectively, and $\kappa_{\mathrm{min,r}}$ arises from the 3σ uncertainty in the intercept of each plot shown in Figure 5.8.

Exp.	Angle	$\kappa_{\mathrm{min,s}}$ / cm^{-1}	$\kappa_{\mathrm{min,r}}$ / cm^{-1}
CRDS	Normal	1.0×10^{-2}	7.4×10^{-3}
CEAS	Normal	2.0×10^{-2}	2.0×10^{-2}
CRDS	Brewster's	9.0×10^{-3}	8.3×10^{-3}
CEAS	Brewster's	9.8×10^{-2}	1.4×10^{-2}

$\kappa_{\mathrm{min,r}} = 8.3 \times 10^{-3}$ cm^{-1} for CRDS measurements at Brewster's angle incidence. These values are close to those determined using Equation 2.17.

Given the pathlengths established through the CRDS data, we can determine the CEF at normal incidence (Figure 5.8(b)) and Brewster's angle incidence (Figure 5.8(d)). The CEF is determined from the gradient of each plot to be 83 at normal incidence and 59 at Brewster's angle incidence. The integration time was kept at 35 ms in both cases, and thus the results can be directly compared. The reduction in CEF at Brewster's angle is commensurate with the slightly increased losses arising from insertion of the chip at Brewster's angle incidence, as well as the deterioration in the chip quality with use.

The detection limit of each CEAS set-up can be established using Equation 5.4. The results are presented in Table 5.2. We find that I^0_{out} is reduced by 50.8% at Brewster's angle incidence compared to normal incidence. This decrease in light intensity was expected (Section 5.2.3). ΔI_{min} is established through the 3σ variation in I^0_{out}, which was found to be 2.1% at normal incidence and 9.1% at Brewster's angle incidence. We can calculate $\kappa_{\mathrm{min,s}}$ to be 2.0×10^{-2} cm^{-1} for CEAS measurements at normal incidence and 9.8×10^{-2} cm^{-1} for CEAS measurements at Brewster's angle incidence. Despite the longer single-pass pathlength at Brewster's angle incidence, the CEAS detection limit is poorer at Brewster's angle incidence because of the lower light intensity and the correspondingly larger error in the intensity measurement. Increasing the integration time from 35 ms to 50 ms at Brewster's angle caused ΔI_{min} to decrease from 9.1% to 5.3% owing to the increase in I^0_{out} by approximately 1.42 times, and thus at 50 ms, κ_{min} was improved to 5.7×10^{-2} cm^{-1}. Further increase in the integration time is not necessarily desirable, despite the improvement in sensitivity, as it would reduce the readout rate of the spectrometer.

The alternative determination of the detection limit for CEAS measurements, from the uncertainty in the x-intercept of the plots presented in Figure 5.8, yields $\kappa_{\mathrm{min,r}} = 2.0 \times 10^{-2}$ cm^{-1} for CEAS measurements at normal incidence and $\kappa_{\mathrm{min,r}} = 1.4 \times 10^{-2}$ cm^{-1} for CEAS measurements at Brewster's angle incidence, similar to those established using Equation 5.4.

We can draw several important conclusions from this analysis. Firstly, the sensitivity of CRDS measurements can be improved by inserting the chip at Brewster's angle incidence compared to normal incidence. In contrast, for a fixed integration time, the sensitivity of CEAS measurements is poorer when the chip is inserted at Brewster's angle compared to normal incidence. CRDS measurements are more sensitive than CEAS

measurements in both configurations, although the difference is more marked at Brewster's angle. It is worth also noting that these experiments were carried out at 570 nm, where our CEAS set-up is not limited by fluctuations in the laser intensity, but rather by noise in the detection electronics. The improvement in sensitivity of CRDS over CEAS is expected to be more significant at lower wavelengths, where the laser fluctuations dominate over the detector noise.

5.5 Single droplet analysis using CEAS

At the end of Chapter 3 (Section 3.6.3), we demonstrated the first application of CRDS to single-droplet analysis. However, we were limited in the droplet production rates we could use by the slow data transfer between the oscilloscope and computer. A demonstration of CEAS applied to single-droplet analysis was carried out in Dr. Stuart Mackenzie's laboratory, working with Simon Neil, a D.Phil. student in the Mackenzie group.

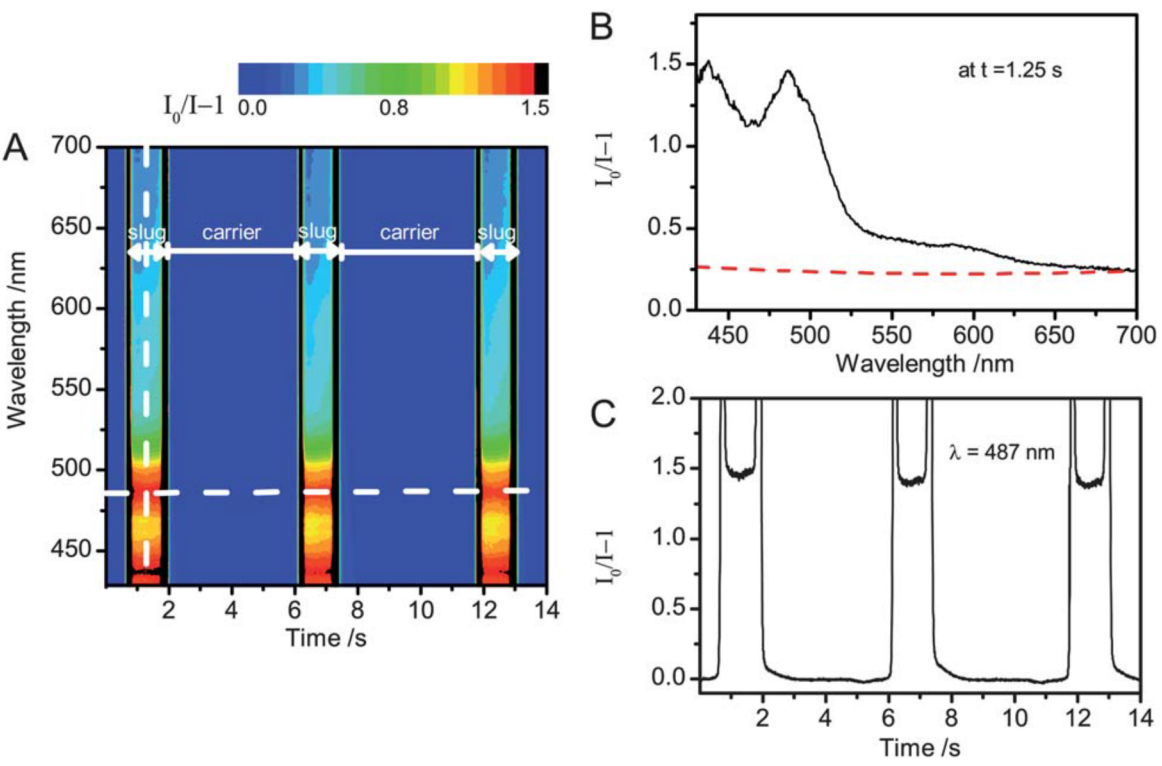


Figure 5.9: (a) Contour plot of the CEAS spectra as a function of time during a flow (0.35 mL min^{-1}) of Ir(IV) 'slugs' through the microfluidic chip. (b) Spectral cut through the contour plot at 1.25 s (red dashed line represents a baseline scattering contribution) and (c) a temporal cut through at 487 nm. Reproduced from [288].

The experimental set-up is similar to that in our laboratory, but the individual components are different and will be described briefly here. Two highly reflective mirrors (Layertec, R (400 - 800 nm) $>$ 0.9985, 1 m

radius of curvature) form a stable cavity 12 cm long. A thiolene microfluidic chip is inserted into the cavity at normal incidence. In this case, the channels had a height of 1 mm and an optical pathlength of 320 μm. The walls of the microfluidic chip consist of two 140 μm thick microscope cover slides. A commercial supercontinuum source (NKT, Koheras SuperK Power Blue) is employed [274]. Before entering the cavity, the light is spectrally filtered, yielding a bandwidth of 400 - 800 nm (300 mW visible output power). Light exiting the cavity is fibre-coupled (Thorlabs 400 μm, NA 0.39) to a grating spectrograph (Andor Technology, SR-303i), which disperses its component wavelengths onto a CCD camera (Andor Technology, Newton). Spectra are acquired with a 3.66 ms acquisition time, at a repetition rate of 273 Hz. It should be noted that the data rate is limited only by the camera acquisition settings/transfer rate. In other applications employing a different camera, it has proved possible to record full visible spectra with acquisition times of 10 μs at $>$ 600 Hz [274].

Droplets or 'slugs' of aqueous 40 μM K_2IrCl_6 solution (hereafter referred to as Ir(IV)), ca. 60 μL in volume, were monitored during their flow through a microfluidic channel in a toluene carrier phase. The flow rate was relatively rapid compared to that used in the CRDS droplet measurements described in Section 3.6.3, at 0.35 mL min^{-1}. The resulting temporally and wavelength-resolved spectra are shown in Figure 5.9(a). For these measurements, I_0 was chosen to be the signal recorded in the presence of the carrier phase only. Figure 5.9(b) highlights the excellent signal to noise achieved for an individual spectrum despite the short (3.66 ms) acquisition time. The time resolution is demonstrated by the absorbance at 487 nm shown in Figure 5.9(c). Each individual spectrum contains a spectrally flat background component which we believe arises from scatter at the interface between the slug and a thin lubricating layer of carrier phase at the walls of the chip. As the absorption spectrum of Ir(IV) is known, this scattering contribution is easily quantified and subtracted (see Figure 5.9(b)).

At both ends of the Ir(IV) slugs, lensing effects result in a large increase in the scattering, a phenomenon we also observed in the single droplet CRDS measurements. Only as the main body of the slug passes into the beam is the absorbance spectrum of Ir(IV) recovered (Figure 5.9(b)). The large scattering-induced signals at the start and end of each droplet provide convenient signals for triggering acquisition during droplet flow, and could potentially be exploited for droplet shape analysis.

These experiments demonstrate that broadband CEAS has the ability to record the complete absorption spectrum several times within each droplet passing through the laser beam. The time resolution of CEAS is better than that previously demonstrated with the best broadband FT-IR imaging techniques [72] and competitive with that demonstrated with surface-enhanced Raman scattering [83]. Using a better camera, microsecond time resolution would be possible for broadband CEAS, making this technique also competitive with the time resolution of fluorescence lifetime imaging techniques [96]. The sensitivity of CEAS can be improved significantly beyond that demonstrated within this chapter, with the use of higher

reflectivity mirrors and lower loss absorption cells. Such a technique should allow inline monitoring of many microfluidic processes.

5.6 Conclusion

In this Chapter, we have investigated the application of broadband CEAS to liquid samples contained within flow cells and microfluidic chips, acquiring the full visible spectrum in < 50 ms. The optimum angle of incidence (either normal incidence or Brewster's angle incidence) has been investigated for both CEAS and CRDS. Finally, a study of single droplet analysis was carried out. In the next Chapter, we apply CEAS to reaction analysis, and in the following Chapter, we apply both CEAS and CRDS to the detection of pH.

Chapter 6

Reaction Analysis

"I can no longer, so to speak, hold my chemical water and must tell you that I can make urea without needing a kidney, whether of man or dog; the ammonium salt of cyanic acid is urea" Friedrich Wöhler to Jöns Jakob Berzelius (1828) [29, 289].

6.1 Introduction

The discipline of organic chemistry can be traced back to Wöhler's 1828 laboratory synthesis of urea [289]. While our knowledge of organic chemistry has vastly expanded over the 180 years since, the synthetic chemist's tools have remained primarily the same, consisting of macroscopic glass components such as beakers, test tubes and round-bottomed flasks [29, 290]. Yet, the application of microfluidics to chemical synthesis has several powerful advantages over macroscale synthesis [28]. While the chemistry (reaction mechanism and kinetics) remains generally unaffected when reducing the volumes from litres or millilitres to microlitres, the physical parameters are greatly affected [291]. Indeed, when compared to the equivalent bulk reactions, "reactions performed in a micro reactor invariably generate purer products in a higher yield and in much shorter times" [292]. This meets the challenges of a large number of chemical industries [28]. The applications of microreactors span a wide range of areas, include fine chemicals [293], drug discovery and development [294, 295], green chemistry [296], combinatorial chemistry [295], nanoparticle synthesis [19] and environmental sensing [22, 24, 25, 215].

Microreactors are ideal for high purity synthesis because microfluidics offers a high level of control, in terms of flow characteristics, and heat and mass transfer [291]. Microreactors also offer advantages in terms of safety. For example, where hazardous intermediates are formed, such as azides formed in the Curtius rearrangement of isocyanates [297], or the synthesis of azo dyes via diazotisation [298], continuous flow

allows them to be both produced and consumed in the same flow section, in small volumes, eliminating the need for storage of the intermediate [291]. An additional advantage of microreactors is their flexibility: extended networks of microreactors have been demonstrated for multi-step, continuous-flow reactions and separations [297]. Finally, their appropriateness for large quantity synthesis has also been demonstrated through the process of "numbering-up", whereby rather than increasing the size of the reactors in order to increase the amount of product produced, a large number of reactors are simply run in parallel [299].

A mention should also be made of some of the challenges associated with the use of microreactors when compared with macroscale synthesis. Notably, microreactors are problematic if any solid particles are formed, because the channels will block [290]. Thus, microreactors will not be suitable for all reactions, without careful consideration of any byproducts formed.

A selection of reactions that have been carried out on-chip are shown in Table 6.1. There have been several reviews of reactions carried out in microreactors, see for example [28, 292, 295, 300, 301].

Table 6.1: Example synthetic reactions performed in continuous flow in microreactors, listed in chronological order, where detail on the type of reaction, type of chip, place of analysis (defined in Section 1.2) and analytical technique is provided.

Ref.	Reaction	Chip type	Analysis	Analytical technique
Salimi-Moosavi et al. [302]	Diazo coupling	Etched glass	On-chip	Visible absorption
Skelton et al. [39, 40]	Wittig (C=C formation)	Etched glass	Off-chip	HPLC
Lu et al. [61]	Photochemical (radical)	Etched quartz	On-chip	UV absorption
Sands et al. [42]	Enamine (C-N formation)	Etched glass	Off-chip	GC-MS
Wiles et al. [43]	Aldol (C-C formation)	Etched glass	Off-chip	GC-MS
Wiles et al. [44]	Michael addition (C-C formation)	Etched glass	Off-chip	GC-MS
Fernandez-Suarez et al. [303]	Diels-Alder (cycloaddition)	Etched glass	Off-chip	LC-MS
Wootton et al. [298]	Azo dye	Etched glass	Off-chip	IR absorption
Kawaguchi et al. [41]	Swern oxidation (C=O formation)	Stainless steel	Off-chip	GC
Leung et al. [74]	Alcohol oxidation	Etched glass	On-chip	Raman scattering
Cygan et al. [37]	Alkene bromination	Glass/thiolene	Off-chip	NMR
Benito-Lopez et al. [304]	Diels-Alder (cycloaddition)	Fused silica	Inline	UV/vis absorption
Snyder et al. [305]	Henry (nitroaldol addition)	Stainless steel	Online	FT-IR
McMullen et al. [45]	Heck (C - C coupling)	Silicon	Online	HPLC

As can be seen from Table 6.1, the bottleneck for nearly all microfluidic reaction studies is the analysis step, which is most often carried out off-chip (either offline or atline, as defined in Chapter 1) using conventional analytical techniques such as GC-MS once sufficient product has been collected. For example, Skelton and coworkers [39] demonstrated that their microreactor could be used for reaction optimisation, but were limited by the analysis of the final product yield, which was carried out using off-chip HPLC. 20 runs of 1 minute each were needed in order to generate sufficient product for off-chip analysis, increasing the optimisation time significantly for each set of reaction parameters. In a series of papers over several years, Wiles and coworkers [43, 44, 306] demonstrated optimised reactions times significantly shorter on-chip (seconds to minutes) compared to batch synthesis (up to 24 hours), but in each study the reaction had to be run for 20 minutes to ensure sufficient volume of product was generated for analysis off-chip using GC-MS. While 20 minutes for optimisation is of course a major improvement over 24 hours, there still remains considerable scope to improve the reaction time required, by at least a further order of magnitude, when the analysis is integrated on-chip. Even when the product was distinctly coloured, for example in the case of Wootton and coworkers' study of azo dye synthesis on-chip, the product was detected by visual inspection using a microscope only, and the reactors were still run for "extended periods to collect samples for analysis" off-chip [298]. To take another example, Cygan and coworkers monitored the alkene bromination reaction, which demonstrated a colour change from orange to colourless, using a camera to monitor mixing, but in order to detect the product still had to collect the eluent for 30 minutes in order to carry out NMR analysis off-chip [37].

Apart from the time and cost inherent in offline analysis, there is some debate over the integrity of reaction analysis recorded some time after the reaction mixture exits the chip. In some studies, the reaction is quenched (see, for example [305]). In other cases, dilution was assumed to either stop or delay the reaction (see, for example [303]). Such unknowns may introduce significant error into reaction analysis, errors which can be removed by carrying out rapid on-chip analysis.

As Brivio et al. stated in 2006, "The real challenge in miniaturizing organic reactions is the coupling of the microreactor to a suitable analytical instrument, which is the key for realizing the high-throughput potential of lab-on-a-chip" [307]. As has been shown, the ability to use microreactors for chemical synthesis has been demonstrated successfully over the last decade. However, the demonstration of suitable on-chip analytical techniques remains in its infancy [308].

Detection techniques for on-chip analysis were reviewed in Chapter 1. Here, we mention a few common spectroscopic techniques, which have been applied to reaction analysis. Laser-induced fluoresence (LIF) is the most common on-chip detection technique [48], and has been demonstrated down to the level of single molecule detection for a model dye [91]. However, since the majority of small molecules used in organic synthesis do not exhibit a strong fluorescence signal, LIF is not generally suitable for unlabelled reaction analysis. UV/vis spectroscopy [61, 304], IR spectroscopy [305] and Raman spectroscopy [74] have all been

used for on-chip reaction analysis. Raman spectroscopy is attractive because it does not require labelling, and can also provide structural information [73]. However, owing to the relatively low intensity of Raman scattering, long integration times are usually required, typically 1 - 60 seconds [74, 76]. This precludes measurement of rapid kinetics.

Two comparative studies have been carried out assessing near-IR, UV/vis and Raman spectroscopy for inline microreactor analysis. McGill and coworkers provided the first comparison, monitoring the acid-catalysed esterification of but-2-enoic acid with butan-2-ol [309]. For this reaction, inline UV/vis spectroscopy gave the poorest precision results, while near-IR spectroscopy provided the highest precision results. Raman spectroscopy required more time for analysis than near-IR spectroscopy. In 2007, Ferstl et al. investigated toluene nitration with two different nitrating agents, pure nitric acid and mixed acid [310]. With pure nitric acid, Raman spectroscopy was found to be the preferred method, while with mixed acid, all three methods demonstrated similar sensitivity.

In reality, the detection technique of choice depends strongly on the reaction to be studied, and its matrix, and thus no general conclusions can be drawn from these studies. For example, if an analyte is an OH-containing species in an organic solvent, near-IR spectroscopy will be preferred. If an analyte is strongly Raman active, Raman spectroscopy will be preferred. If the analyte is a strong absorber, UV/vis spectroscopy will be preferred.

We have previously demonstrated the ability of both CRDS (Chapter 3) and broadband CEAS (Chapter 5) to enhance the sensitivity of visible absorption spectroscopy in short pathlength measurements on liquids. We will now use our CEAS set-up demonstrated in Chapter 5 for reaction analysis. The set-up is appropriate because it provides us with the greatest versatility: as the set-up records absorption data from 480 - 720 nm, the excitation wavelength can be matched to an absorption maximum of any reagent or product that absorbs in the visible.

In order to determine the suitability of broadband CEAS for reaction analysis, two reactions will be investigated. The first is a well-known inorganic complexation reaction between sulphonated bathophenanthroline and iron(II), which was utilised in Chapter 4 for detecting iron. The second is a well-known organic reaction, the Diels-Alder reaction, in which one of the reagents is coloured, but the other reagent and product are both colourless. Both reactions will be discussed in more detail before describing the experimental set-up.

6.1.1 Reaction (i): Iron(II) Complexation

The complexation reaction between iron(II) and 4,7-diphenyl-1,10-phenanthroline-disulfonic acid has already been discussed in detail in Chapter 4, where it was used in the colourimetric detection of dissolved iron(II). Neither of the reagents exhibits visible absorption, but the product has a strong visible absorption

band, shown in Figure 6.1(b). The reaction ratio of iron(II) to complexing agent is expected to be 1:3 (see Figure 4.2 for the reaction scheme) [206, 207].

The iron(II) complexation reaction with 4,7-diphenyl-1,10-phenanthroline-disulfonic acid is known to be rapid [62]. The colour forms instantly on mixing the two solutions ($<$ 1 s) and does not fade over several months. In our experiments investigating the iron(II) reaction, we are probing between 30 - 60 s after the iron(II) and complex solutions are mixed. In other words, we are monitoring the product concentration of a reaction which has gone to completion. In this case, the amount of product formed simply reflects the amount of end product expected from the stoichiometric equation.

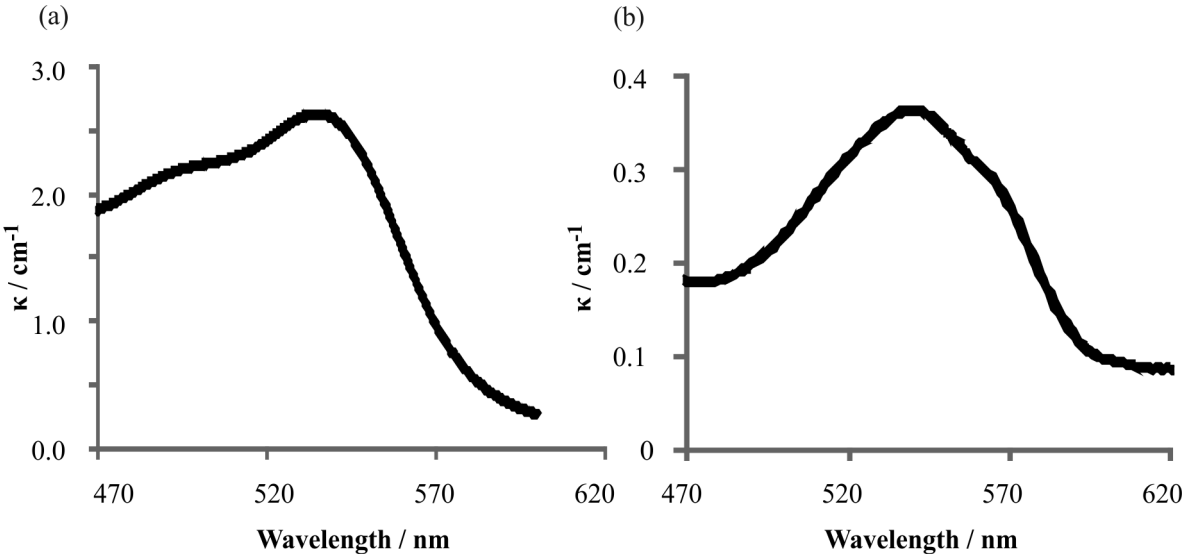


Figure 6.1: Absorption spectra of (a) iron and bathophenanthroline disulfonic acid, with iron(II) concentration = 0.05 mM; and (b) 4-phenyl-1,2,4-triazoline-3,5-dione (N-PTD), with N-PTD concentration = 1 mM.

6.1.2 Reaction (ii): Diels-Alder Reaction

In 1950, Otto Diels (1876 - 1954) and his student Kurt Alder (1902 - 1958) received the Nobel prize "for their discovery and development of the diene synthesis", which has become known as the Diels-Alder reaction [311]. Diels and Alder immediately recognised the importance of their 1928 discovery, particularly with regards to the total synthesis of natural products, and in fact attempted to claim the new field as their own: "We explicitly reserve for ourselves the application of the reaction developed by us to the solution of such problems" [312, 313]. Indeed, it was not until the 1950s that the use of the Diels-Alder reaction in total synthesis was demonstrated [314], with notable early examples including the first synthesis of morphine [315] and Woodward's synthesis of the steroids cortisone and chlolesterol [316]. The importance of the Diels-Alder reaction in synthesis lies in its ability to build complex, cyclic molecules, with regio- and stereospecific

control [314]. The mechanism of the Diels-Alder reaction is well-established to be a [4+2] cycloaddition reaction, which proceeds via a concerted single-step mechanism [314].

Several Diels-Alder reactions have previously been carried out in microreactors. Fernandez-Suarez and coworkers synthesised four different cycloadducts in an etched glass microreactor, and required 30 minutes to carry out each run in order to collect enough material for analysis using off-chip LC-MS [303]. Snyder and coworkers carried out a Diels-Alder reaction between maleic anhydride and excess 2,3-dimethylbuta-1,3-diene, with a residence time of 30 minutes in the microreactor, and analysis carried out off-chip using GC [305]. Whitesides et al. analysed the Diels-Alder reaction between 4-phenyl-1,2,4-triazoline-3,5-dione and ergosterol in a glass/PDMS chip [317], using the rapid colour change [318, 319] from bright red to yellow for visual detection of mixing on-chip, followed by off-line NMR analysis. Interestingly, no swelling of PDMS was observed during the 15 minutes the chip was exposed to the reagent mixture. Over longer times, swelling would certainly become a problem, particularly if monitoring the reaction via cavity enhanced absorbance. Benito-Lopez tracked a Diels-Alder reaction under high pressure conditions in a fused silica capillary microreactor using UV/vis absorption at 335 nm to monitor the product [304]. The most recent microreactor example of the Diels-Alder reaction was that between maleic anhydride and isoprene carried out by McMullen and Jensen in 2011 [46]. Online analysis was carried out using HPLC coupled with UV absorption detection, and scale-up by 500 times from the microreactor to a Corning flow reactor was demonstrated.

The Diels-Alder reaction that we have chosen has a coloured dienophile, 4-phenyl-1,2,4-triazoline-3,5-dione (N-PTD), which reacts with anthracene (colourless) over a period of around 5 - 10 minutes to form a colourless cycloadduct [320]. The diene was chosen for its stability, and the dienophile was chosen for its colour. Its UV/vis spectrum is shown in Figure 6.1(b). N-PTD is in fact a very important molecule in synthesis, and has even been the subject of its own review [321]. A schematic of the Diels-Alder reaction investigated in this work is shown in Figure 6.2.

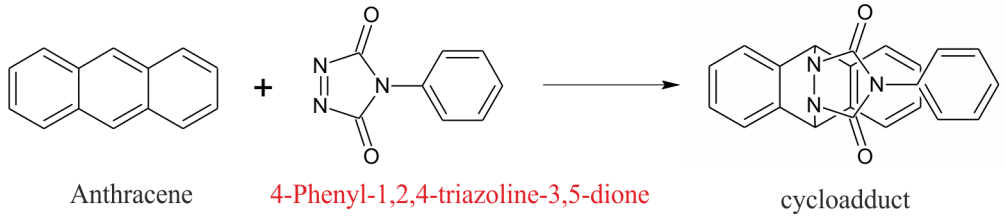


Figure 6.2: Schematic of the Diels-Alder reaction between anthracene (colourless) and 4-phenyl-1,2,4-triazoline-3,5-dione (N-PTD, red) to form a colourless cycloadduct.

In contrast to the iron complexation reaction, the Diels-Alder reaction between N-PTD and anthracene is slow. We have monitored the absorption of 2.5 mM N-PTD at 540 nm in a commercial UV/vis spectrometer, with anthracene present in a ten-fold excess (25 mM), and found that a natural logarithmic plot of absorption versus

time does not show any significant deviation from linearity over 1000 s. When anthracene is present in excess, the reaction is pseudo-first order with respect to N-PTD, with an effective rate constant $k_{\text{eff}} = 8.4 \times 10^{-4}$ s^{-1}. Given the known excess of anthracene, the second order rate constant for the Diels-Alder reaction can be calculated to be 3.3×10^{-2} dm^3 mol^{-1} s^{-1}. On-chip, the observation time (t_1) equals approximately 380 s, and although the N-PTD concentration is six times higher (15 mM), the measurements are still expected to lie within the time region where the initial rate approximation can be applied. The expected concentration of reagent remaining for a 0.015 M mixture of anthracene and N-PTD after 380 s equals approximately 0.013 M, corresponding to 16% progression through the reaction.

Given that we are observing the Diels-Alder reaction at an early time in the reaction, we can thus monitor the reaction rate by measuring the absorbance of the reagent B at t_1 and t_0 as

$$\text{rate} = -\frac{\mathrm{d[B]}}{\mathrm{dt}} = -\frac{([\mathrm{B}]_1 - [\mathrm{B}]_0)}{\mathrm{t_1 - t_0}} = \frac{[\mathrm{B}]_0 - [\mathrm{B}]_1}{\mathrm{t_1 - t_0}} \tag{6.1}$$

If the time period is constant, we can rewrite Equation 6.1 as:

$$\text{rate} \propto [\mathrm{B}]_0 - [\mathrm{B}]_1 \propto \mathrm{Abs\,(t_0)} - \mathrm{Abs\,(t_1)} \tag{6.2}$$

given that the absorbance Abs is proportional to [B]. Inserting the 1:1 reaction stoichiometry into Equation 6.2 allows the difference in absorbance (which is proportional to the rate) to be written as a function of the reagent concentrations:

$\mathrm{Abs\,(t_0)} - \mathrm{Abs\,(t_1)} \propto [\mathrm{A}][\mathrm{B}]$

At the start of the reaction ($t = 0$), $\mathrm{Abs\,(t_0)}$ is directly proportional to the percentage of B in the reaction mixture, in other words $\mathrm{Abs\,(t_0)} \propto [\mathrm{B}]_0$. This produces a linear plot of absorbance at $t = 0$ as a function of the proportion of reactant B in the mixture.

$\mathrm{Abs\,(t_1)}$ can then be determined as:

$\mathrm{Abs\,(t_1)} \propto \mathrm{Abs\,(t_0)} - \frac{[\mathrm{A}][\mathrm{B}]}{\mathrm{x}}$

where x determines how far through the reaction $t = 1$ lies, when the values are normalised.

6.2 Experimental

The set-up used is that previously described in Chapter 5. A 13.5 cm cavity length was used, and two types of absorption cell were inserted into the cavity. The 100 μm flow cell (Figure 6.3(a)) was used for analysis of the iron complexation reaction, which was fast and occurs in water. Unfortunately, the Diels-Alder reaction

could not be analysed in the 100 μm pathlength flow cell, as the reaction is slow and the toluene solvent evaporated rapidly, owing to imperfect sealing of the connectors to the flow cell. This evaporation caused the cavity losses to increase substantially owing to scatter from the resulting gas bubbles trapped in the flow cell. This scattering signal masked any expected change in absorption.

Both reactions were also analysed in a thiolene chip with 600 μm height channels (Figure 6.3(b)), composed of two 1 mm microscope slides. The fabrication of this type of chip was described in Chapter 3. The chip has two key advantages for these experiments. Firstly, the channels are sealed and thus evaporation did not occur, allowing slow flow rates to be used without increasing the scattering signal. Secondly, the reagents are mixed on chip at a well-defined time-point, which minimises dispersion, rather than mixing in the tubing, as was the case for the flow cell. However, the microfluidic chip exhibits significantly higher losses than the commercial flow cell, as has been previously noted. This means that the sensitivity of the chip analysis is lower than analysis with the 100 μm pathlength flow cell. There is a clear trade-off between optical quality and ease of fabrication.

A schematic of the experimental set-up is shown in Figure 6.3. Two syringe pumps are operated under computer control (see the following Section), and the absorbance is monitored as a function of time, which corresponds to changes in flow rate ratio. Mixing of the two reagent streams introduced by syringe pumps A and B occurs either in a T-connector in the case of the flow cell (Figure 6.3(a)) or on-chip (Figure 6.3(b)).

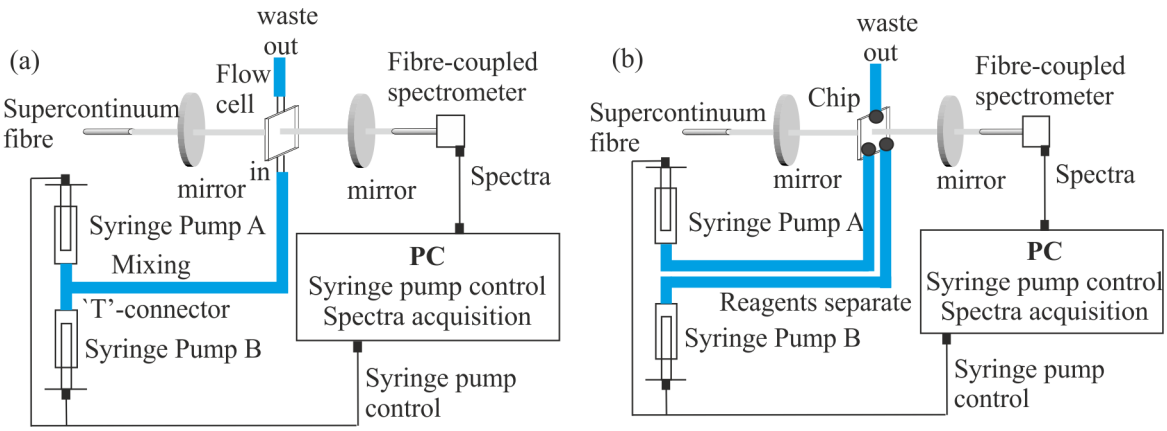


Figure 6.3: Schematic of reaction analysis using broadband CEAS. The syringe pumps are run under PC-control, as the PC simultaneously acquires spectra from the spectrometer at the cavity output. (a) Set-up when using a flow cell. Mixing occurs at a T-connector before the sample reaches the flow cell. (b) Set-up when using a microfluidic chip. Mixing occurs on-chip, and the black dots on the chip represent Nanoport inlets and outlet.

6.2.1 Syringe pump control

Reaction characterisation is carried out via variation of the flow rate ratio between the two reagent streams. In order to achieve this, a LabVIEW program was written by Jason Lee (D.Phil., Vallance group) to interface

two Chemyx syringe pumps (Fusion 400, Chemyx), allowing for control of the start and end flow rate ratio, interval size or duration between flow rate ratio changes, and total flow rate. An example table of parameters used in one run is shown in Table 6.2. The volume of reactants A and B dispensed per step is also shown. Such flow rate settings were used for reaction analysis at short reaction times, using the 100 μm flow cell. With these settings, reaction analysis across the entire range of flow rate ratios tested consumes less than 1 mL sample.

Table 6.2: Example flow rate settings. Flow rate of two syringe pumps varied from 5% - 95%, with 15% intervals, duration for each interval = 30 s, total flow rate = 0.5 mL/min. Vol.$_T$ = total volume dispensed in one run.

Step No.	% Reactant B / %	Flow rate B mL/min	Flow rate A / mL/min	Vol. B / mL	Vol. A mL
1	5	0.025	0.475	0.0125	0.2375
2	20	0.100	0.400	0.0500	0.2000
3	35	0.175	0.325	0.0875	0.1625
4	50	0.250	0.250	0.1250	0.1250
5	65	0.325	0.175	0.1625	0.0875
6	80	0.400	0.100	0.2000	0.0500
7	95	0.475	0.025	0.2375	0.0125
Vol.$_T$	-	-	-	0.8750	0.8750

The syringe pump program was run simultaneously with the data acquisition software, which was time-stamped so that the intensity versus time trace could be matched to the flow rate ratio of the syringe pumps, given the known duration of each flow rate ratio step. The resulting traces will be presented and described in detail in Sections 6.3 and 6.4. In the proof-of-concept work presented here, the entire reaction space was mapped. For relatively simple reactions with only one parameter to vary, this is possible as a proxy for reaction optimisation. With more complicated reactions and more than one variable, interfacing of the syringe pump control and data acquisition software would be beneficial, as a feedback loop could then be implemented, allowing automated optimisation of the absorbance and therefore the reaction rate. This would be a straightforward extension of the current study, which instead focused on analysis of only one variable, the flow rate ratio between two reagent streams.

6.3 Iron complexation reaction

All chemicals were purchased from Sigma-Aldrich and used without further purification. Sulphonated bathophenanthroline (Sigma-Aldrich, 11890) and iron(II) chloride (Sigma-Aldrich, 372870) solutions were prepared in MilliQ water. In order to prevent errors in reaction ratio determination arising from noticeable oxidation of iron(II) to iron(III), fresh iron(II) solutions were prepared daily. Bathophenanthroline (BPDS) was found to be stable over a period of several weeks, and the same stock solution was used for all the experiments described in this section. The visible absorption spectrum of iron/BPDS was recorded using a

commercial UV/vis spectrometer and is presented in Figure 6.1. The absorption maximum was found to lie at 533 nm, and thus this wavelength was chosen for analysis. The absorption coefficient at 533 nm was determined using 0.05 mM iron reacted with an excess of BPDS (30 mM), both dissolved in water, to be (52,600 $\pm$ 300) M^{-1} cm^{-1}. It should be emphasised that the broadband CEAS set-up records intensity at all visible wavelengths simultaneously, and single wavelength selection is only chosen to simplify the data analysis.

The iron/BPDS complexation reaction was investigated in three different ways, which will be discussed and presented below in turn.

Firstly, an iron solution of concentration 74 μM was prepared. This was reacted manually in bulk with a series of different BPDS solutions, ranging in concentration from 15 μM to 450 μM. In each case, the iron and BPDS solutions of varying strength were mixed together offline in a 1:1 ratio, and then flowed onto the 100 μm flow cell at a constant flow rate of 0.5 mL min^{-1} for 1 minute. We have already seen in Chapter 4 that rather than using water as the reference or 'blank' signal, a mixture of BPDS and water must be used. This ensures that any iron contamination in the solutions is accounted for in the 'blank' measurement. Alternating blank and sample measures were recorded in order to record alternate measurements of I_0 and I. This enabled the plot of $\frac{I_0}{I} - 1$ as a function of the the reaction ratio [BPDS]/[Fe(II)], shown in Figure 6.4, to be produced.

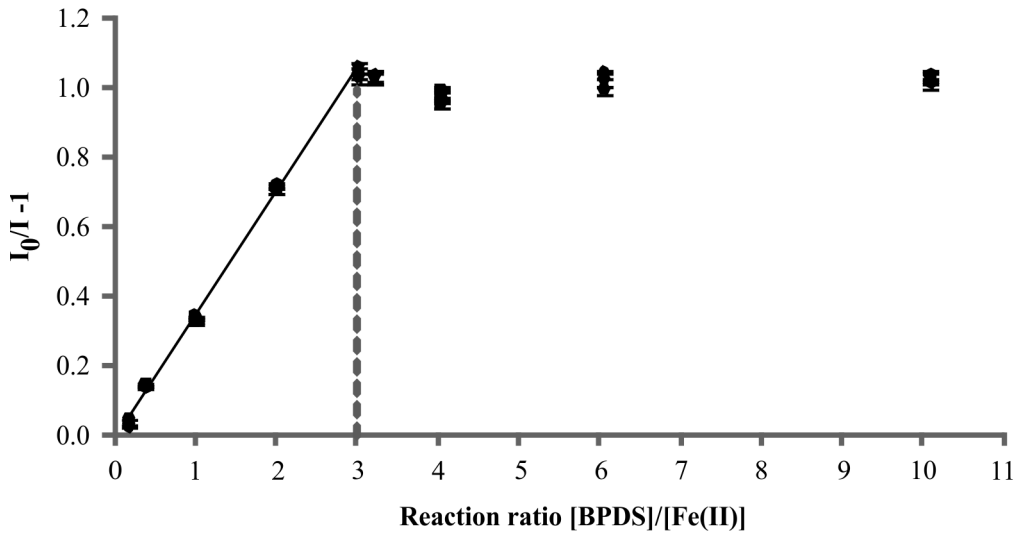


Figure 6.4: Initial iron analysis carried out in 100 μm flow cell, with offline mixing. Plot of $\frac{I_0}{I} - 1$ (which is $\propto$ Abs) plotted as a function of [BPDS]/[Fe(II)] reaction ratio. The gradient of the linear part of the graph can be used to calculate the CEF of the cell at 533 nm, when plotted against Fe(II) concentration. The CEF was found to equal 54. 1σ error bars are shown, determined by 50 repeated measurements of I_0.

It can clearly be seen in Figure 6.4 that the absorbance initially increases linearly with [BPDS]/[Fe(II)], but that once [BPDS] > [Fe(II)], increasing the concentration of BPDS further does not increase the concentration of complex formed or the absorbance. The point at which the graph levels off is clearly defined and marked

on the graph. This point corresponds to the reaction concentration ratio [BDPS]:[Fe] = 3:1, which is the reaction ratio expected from the known stoichiometry of this complexation reaction.

In the second iron complexation reaction study, solutions were mixed inline using a T-connector to join the two reagent streams, as shown in Figure 6.3(a). Concentrations of iron(II) (1×10^{-4} M) and BPDS (3×10^{-4} M) were chosen in order to demonstrate a 1:1 flow rate ratio. The analysis was carried out in the 100 μm flow cell as before.

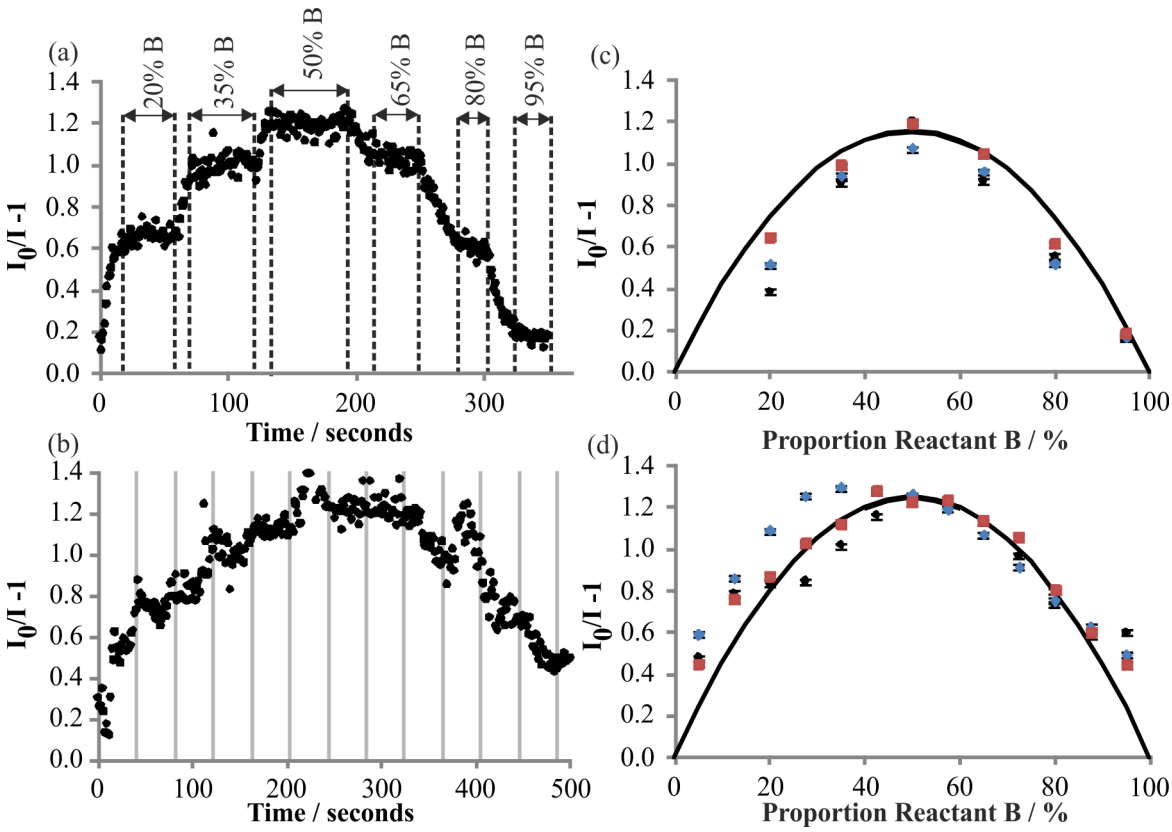


Figure 6.5: Iron analysis study carried out in 100 μm flow cell, with inline mixing. (a) Example $\frac{I_0}{I} - 1$ recorded as a function of time, which corresponds to different flow rate ratios, when optimising iron complexation between 1×10^{-4} M iron(II) and 3×10^{-4} M BPDS solutions. Flow rate ratio intervals 15% from 20% to 95%. (b) Example $\frac{I_0}{I} - 1$ recorded as a function of time, which corresponds to different flow rate ratios, when optimising iron complexation between 1×10^{-4} M iron(II) and 3×10^{-4} M BPDS solutions. Flow rate ratio intervals 7.5% from 5% to 95%. Plots (c) and (d) are the corresponding $\frac{I_0}{I} - 1$ plotted as a function of percentage of reactant B for (a) and (b) respectively. Three runs of (a) and (b) were recorded and the data points for each percentage are shown in a different type. 1σ error bars are also shown, determined by 50 repeated measurements of I_0. The black line corresponds to the expected fit for a 1:1 reaction stoichiometry.

Each data point shown in Figure 6.5(a), $\frac{I_0}{I} - 1$ versus time, is calculated from the known constant I_0, which is established before each data run, and the measured I, which is recorded every 1 s. The syringe pumps are stepped in flow rate intervals of 15% from 20% to 95%, and each flow rate interval is held constant for 30 s. This creates the stepped profile of Figure 6.5(a). When the flow rate of the syringe pumps is altered,

there is a noticeable and relatively rapid change in $\frac{I_0}{I} - 1$, if the change in flow rate ratio is relatively large, as is the case for 15% intervals used in Figure 6.5(a). This enables a plateau region to be identified, which occurs when the flow rate ratio has reached equilibrium. The average absorption within each plateau region is determined and plotted as a function of the proportion of reactant B (by volume) in Figure 6.5(c). The plateau region is identified within the dotted lines marked on Figure 6.5(a), as well as being labelled in terms of the percentage (by volume) of reactant B in the mixture. In this manner, the flow rate ratio was found to equal 1:1, which is expected as we have chosen a concentration of BDPS three times higher than iron(II) concentration. The variation in plateau length despite the fixed flow rate interval time is thought to perhaps occur because of variation in the total flow rate, which may vary as the syringe is emptied, or alternatively because the mixing time may not be well-defined in the T-connector. These variations are not particularly important for this reaction, because the product is formed instantly, but would be important for rate measurements with reaction kinetics on the same timescale as these effects.

The same iron and BPDS concentrations were used for the results displayed in Figure 6.5(b) and (d), but a smaller flow rate interval of 7.5% was used, from 5% to 95%. Consequently, the plateau regions are more poorly defined in Figure 6.5(b) compared with Figure 6.5(a), as the change in concentration occuring as the flow rate ratio is stepped is approximately halved compared with the previous measurements which used a flow rate step interval of 15%. Thus, in order to extract the data points for each flow rate ratio, a fixed interval of 27 data points was selected, which corresponds to a time interval of 40.5 s (given that the data were measured at 1.5 Hz in this case). These intervals are marked as gridlines on Figure 6.5(b). The data points within the time section between each pair of gridlines are averaged to produce the $\frac{I_0}{I} - 1$ point for each flow rate interval, which is then plotted as a function of the percentage (by volume) of reactant B in the mixture in Figure 6.5(d). It is not surprising that the variation between each run, plotted as a different colour point in each case, is higher in Figure 6.5(d), as the data points encompass the small steps in flow rate ratios, which were excluded in Figure 6.5(c). Nevertheless, a clear maximum in $\frac{I_0}{I} - 1$, which is proportional to absorbance, can be seen in the measured data, corresponding well to the black line shown on both Figures 6.5(c) and (d), which is the expected values given the known reaction stoichiometry. The maximum occurs when the volume of reactant B (BPDS) in the mixture equals 50%, in other words when the Fe(II) volume is equal to the BPDS volume. This is expected, as we have chosen the reactant concentrations of BPDS to iron to be in a 3:1 concentration ratio, corresponding to the expected reaction ratio of 3:1 for BPDS to iron.

In the measurements described above, while the reaction mixture was analysed in a flow cell with a pathlength commensurate with microfluidic dimensions, the reaction itself was performed before injection into the flow cell. Better control of the mixing process can be achieved by carrying out controlled mixing on-chip (Figure 6.3(b)). We use a chip which allows for the reactants to be kept separate before they reach the channel. The first channel section then has several bends, to create faster mixing than would otherwise occur along a straight channel. In this third set of experiments, both the reaction and the analysis are carried out on-chip

using 1×10^{-3} M iron(II) and 1×10^{-3} M BPDS solutions. Thorough mixing was achieved in the first channel of the chip. The data are similar to that acquired previously, but a 1:1 concentration ratio is used. In addition, a higher concentration of iron and BPDS is used to account for the fact that the microfluidic chip is expected to occasion more losses, and thus exhibit a lower cavity enhancement factor (CEF), compared with the measurements carried out with the 0.1 mm flow cell inserted into the cavity. The CEFs for each set-up are described in Section 6.5.

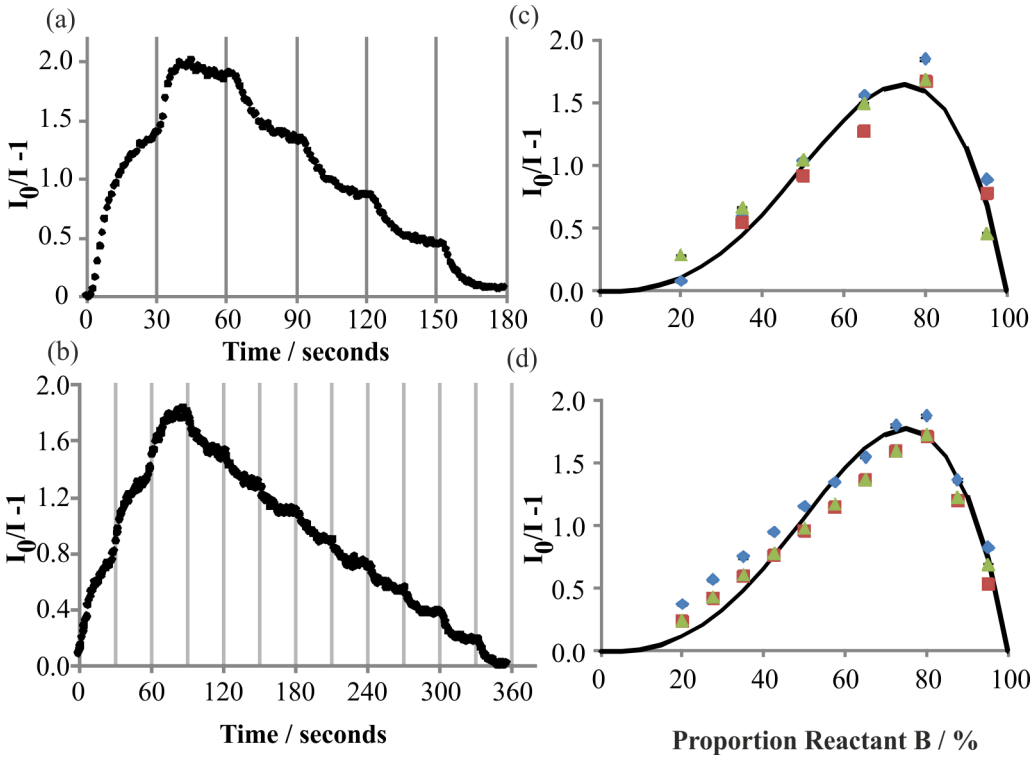


Figure 6.6: Iron analysis study carried out on-chip. (a) Example $\frac{I_0}{I} - 1$ recorded as a function of time, which corresponds to different flow rate ratios, when optimising iron complexation between 1×10^{-3} M iron(II) and 1×10^{-3} M BPDS solutions. Flow rate ratio intervals 15% from 95% to 5%. (b) Example $\frac{I_0}{I} - 1$ recorded as a function of time, which corresponds to different flow rate ratios, when optimising iron complexation between 1×10^{-3} M iron(II) and 1×10^{-3} M BPDS solutions. Flow rate ratio intervals 7.5% from 95% to 5%. (c) and (d) corresponding $\frac{I_0}{I} - 1$ as a function of the percentage of reactant B in the mixture for (a) and (b) respectively. Three runs of (a) and (b) were recorded and the data points for each percentage are shown in a different type. 1σ error bars are also shown, determined by 50 repeated measurements of I_0. The black line corresponds to the expected fit for a 1:3 reaction stoichiometry.

The plateau regions are well-defined in both Figure 6.6(a) and (b), which correspond to flow rate intervals of 15% and 7.5% respectively, indicating that the mixing is better controlled on-chip compared with the mixing that occurred in the T-connector. In addition, higher $\frac{I_0}{I} - 1$ are measured on-chip because of the three times longer pathlength and ten times higher concentration. The data were analysed in the same manner as described alongside Figure 6.5, which enables a plot of $\frac{I_0}{I} - 1$ as a function of percentage of reactant B in the mixture for Figure 6.6(a) and (b) to be plotted in Figure 6.6(c) and (d), respectively. In this case, flow rate ratio intervals were held constant for 30 s, and these gridlines are shown on each plot. Plots Figure 6.6(c) and

(d) are mirror images of plots Figure 6.6(a) and (b) because in (a) and (b), the flow rate ratio is stepped from high to low BPDS (reactant B) concentration, whereas in (c) and (d), the data are plotted from low to high BPDS (reactant B) concentration. The maximum $\frac{I_0}{I} - 1$, which is proportional to the absorbance, is found when BPDS is 80% of the mixture, if 15% flow rate ratio intervals are used. When a finer flow rate interval is used (7.5%), the maximum $\frac{I_0}{I} - 1$ is again found when BPDS is 80% of the mixture. This corresponds closely to the maximum BPDS proportion of 75% expected for this complexation reaction.

6.4 Diels-Alder reaction

All chemicals were purchased from Sigma-Aldrich and used without further purification. Anthracene (Sigma-Aldrich, 10580) and 4-Phenyl-1,2,4-triazoline-3,5-dione (Sigma-Aldrich, 280992) solutions were prepared in toluene (HPLC grade). The anthracene solutions were found to be stable over several days, whereas 4-Phenyl-1,2,4-triazoline-3,5-dione (N-PTD) solutions were prepared daily, as noticeable degradation was observed overnight. The absorption spectrum of N-PTD was recorded using a commericial UV/vis spectrometer and is presented in Figure 6.1(b). The absorption maximum was found to lie at 540 nm, with α_{540}=(363 $\pm$ 2) M^{-1} cm^{-1}, and this wavelength was chosen for analysis. Concentrations of 0.015 M for both anthracene and N-PTD were used for on-chip measurements.

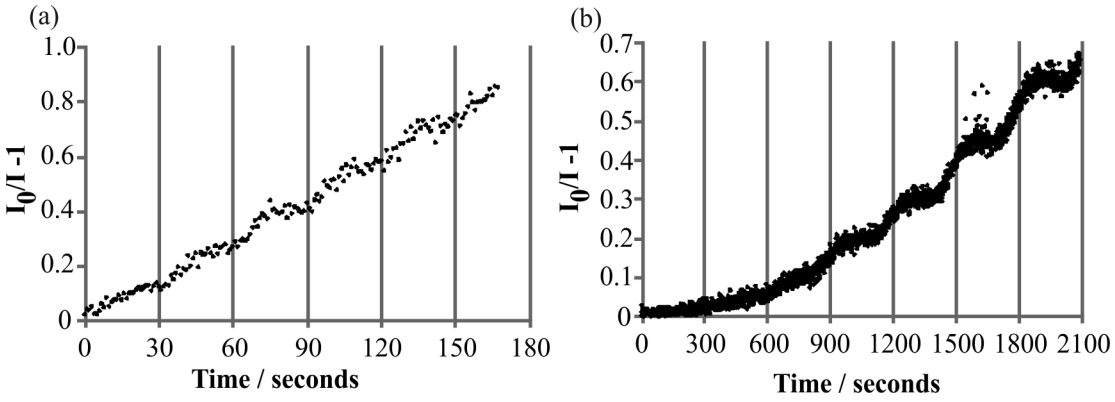


Figure 6.7: Example $\frac{I_0}{I} - 1$ recorded as a function of time when analysing the Diels-Alder reaction on 600 μm channel height chip. 15% reaction ratio intervals were used, from 5% - 95%. (a) Total flow rate 0.5 mL min^{-1}, $t \approx 48$. (b) Total flow rate 0.05 mL min^{-1}, $t \approx 380$ s.

In the case of the Diels-Alder reaction, we are monitoring a reactant concentration. Thus, if we measure the absorbance at t_0, we will be measuring the initial concentration of the reactant. The initial reactant concentration exhibits a linear relationship to the monitored absorbance. At a later time point (within the time region where the initial rate approximation holds), t_1, a reduced reactant concentration will be measured, as some of the reactant will have been converted into products, depending on the reaction rate. As discussed in

Section 6.1.2, the reaction rate can be optimised by maximising the absorbance difference between an early and a later time point, as $\text{rate} \propto \text{Abs}\,(\text{t}_0) - \text{Abs}\,(\text{t}_1)$.

Data recorded at t_0 are shown in Figure 6.7(a) and data recorded at t_1 are shown in Figure 6.7(b). A total flow rate of 0.5 ml min^{-1} was used for t_0, corresponding to a reaction time of around 48 s when the mixed solution reaches the analysis point on-chip. While this is a significant time delay from the actual $t = 0$, this is insignificant as this particular Diels-Alder reaction is so slow. We purposefully analyse the reaction close to the end of the microfluidic channel on the chip, to allow for sufficient reaction time for this very slow reaction to be probed. For faster reactions, an earlier time point in the chip could be chosen. A total flow rate of 0.05 ml min^{-1} was used for t_1, corresponding to a reaction time of around 380 s when the mixed solution reaches the analysis point on-chip. The data are analysed by breaking down the trace of $\frac{I_0}{I} - 1$ as a function of time into 30 s time sections for Figure 6.7(a) and 300 s time sections for Figure 6.7(b). Longer time sections are required in Figure 6.7(b) because of the slower flow rate in this case. Where distinct plateau regions are observed, as in later time points in Figure 6.7(b), only the plateau region is used for finding the average $\frac{I_0}{I} - 1$ value for a particular flow rate ratio. If a clear plateau region was not observed, the average $\frac{I_0}{I} - 1$ value within the defined time section shown by the gridlines in Figure 6.7 is used. The plots are shown in Figure 6.8. The average values for each individual data run are shown on the plots to indicate the variation between runs. The black line in Figure 6.8(a) is a best-fit line through the data recorded at t_0. The grey line in Figure 6.8(a) corresponds to the predicted line generated using the equations outlined in Section 6.1.2, where the reaction has progressed 26% towards completion. As expected, at short reaction times, the absorbance plot is linear with N-PTD concentration. However, when the absorbance is monitored at this later time point in the reaction, a significant change in absorbance is measured as the flow rate ratio is varied.

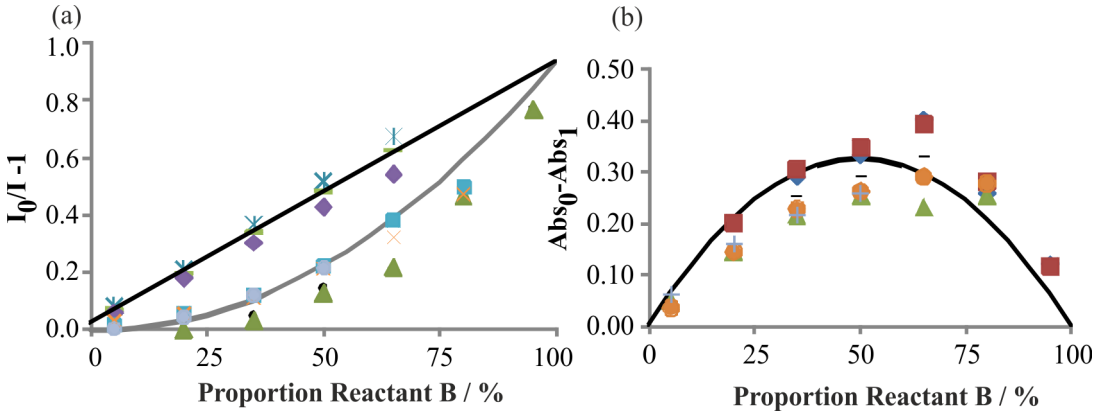


Figure 6.8: (a) Graphs of $\frac{I_0}{I} - 1$ versus [N-PTD]/[Anthracene] reaction ratio. The linear graph corresponds to the trace at t_0 and the curved graph corresponds to the trace at t_1. (b) Plot of rate $\propto -(\text{Abs}_1 - \text{Abs}_0)$ versus [N-PTD]/[Anthracene] reaction ratio, showing the maximum more clearly.

In order to visualise the difference between the absorbance plots at t_0 and t_1 more clearly, a difference plot between the initial absorbance and the final absorbance is shown in Figure 6.8(b). The maximum

absorbance difference corresponds to the proportion of N-PTD where the reaction rate is optimum. The difference is established in each repeated run and shown in a different coloured data point. The black line corresponds to the expected curve for a 1:1 reaction. The experimental maximum appears to lie above the 50% N-PTD concentration ratio expected for this 1:1 reaction stoichiometry, at around 65%, which should indicate a 2:1 reaction stoichiometry. However, given the variation between data runs around 50% and 65%, the maximum is not particularly well-defined. The relatively high uncertainty arises because of the low absorption coefficient for N-PTD, and the low number of passes recorded in this chip (see Section 6.5). This means that the absorbances are relatively low, and, indeed, significantly lower than the absorption values used in the on-chip study of the iron complexation reaction, in which the absorption coefficient is two orders of magnitude higher, and thus the maximum shown in Figure 6.6 is significantly sharper.

6.5 Determining cavity enhancement factors

The aim of this work is to demonstrate the improvement in sensitivity that can be achieved by using CEAS to analyse both the iron complexation reaction and the Diels-Alder reaction. It is worth, therefore, calculating the cavity enhancement factors (CEF) for each set-up.

The CEF for the measurements carried out with the 0.1 mm flow cell inserted into the cavity at normal incidence can be found from the gradient of the linear section of a plot of $\frac{I_0}{I} - 1$ (plotted as a function of reaction ratio in Figure 6.4) versus the concentration of the complex (not shown), given Equation 5.3. The CEF for the cavity set-up with the 0.1 mm flow cell inserted at normal incidence was found to be 54 at 533 nm.

The CEF for the measurements carried out with the microfluidic chip at 533 nm can be estimated given the known maximum absorbance $\frac{I_0}{I} - 1 \approx 1.77$ established in Figure 6.6, and the known iron-complex concentration 2.5×10^{-4} M. In this way, the CEF of the chip was found to be only 4 at 533 nm. For the chip measurements at 540 nm, the CEF is estimated from the gradient of the line in Figure 6.7(a), when plotted as a function of concentration rather than time. The concentration of N-PTD is calculated given the known flow rate ratio as a function of time and the initial concentration of N-PTD. In this manner, the CEF of the chip was found to be only 5 at 540 nm.

The CEF for the inserted chip determined at 533 nm is significantly poorer than the CEF for the inserted flow cell, and arises from imperfections inherent in the chip fabrication process. These include tilt between the two chip faces, which increases the reflections losses substantially, and also scatter at the internal channel walls. We have previously demonstrated improved CEFs on-chip, however, it is thought that the chip quality degrades with use, and this is the cause of the lower CEF found in this Chapter compared to Chapter 5.

An important point to mention about the glass/thiolene devices is that although the thiolene is much more widely compatible with organic solvents than, for example, PDMS, some swelling does occur when exposing the thiolene to toluene for even relatively short periods of time. Cygan et al. examined the swelling of thiolene in toluene over 20 hours and found that although the thiolene device still functioned well in terms of fluid flow, the toluene-filled device had lower light transmission, owing to solvent penentration into the thiolene walls of the device [37]. Such an effect is very significant in cavity-based measurements. Indeed, the solvent resistance of chips could be determined by monitoring the absorbance as a function of time, for a solvent-filled chip.

There is of course little merit in performing cavity enhanced measurements on a chip that yields such a low CEF. The optical quality of these chips needs to be improved considerably before any significant benefit over single pass measurements can be observed.

6.6 Conclusions and future work

We have demonstrated the application of CEAS to on-chip reaction analysis, which is possible when either the reagent or the product has a characteristic absorption maximum in the visible spectral region.

It should be emphasised that the visible absorption measurements employed here were chosen for demonstration only. Of greater utility would be to carry out reaction analysis either in the UV or IR spectral regions, where molecular absorptions are ubiquitous. Using the same supercontinuum light source as employed in the present work, we can already access light from 450 - 1800 nm. Reaction analysis using IR spectroscopy has already been demonstrated. For example, Snyder et al. used online FT-IR spectroscopy to monitor the Henry reaction between a nitroaldol addition reaction), via absorbance of the carbonyl stretching mode at 1702 cm^{-1} [305]:

$$H_3CNO_2 + C_6H_5COH \longrightarrow C_6H_5CHOHCH_2NO_2 \tag{6.3}$$

As the reaction proceeds, the absorbance from the carbonyl group present in the starting material benzaldehyde, but not the product 2-nitro-1-phenylethanol, decreases.

Future extensions to this first demonstration of reaction optimisation include the integration of both the syringe pump control and spectrometer data acquisition software into a feedback loop to allow for automated reaction optimisation. Variation of additional parameters, including temperature, could also be investigated. Finally, we have previously demonstrated the possibility of single droplet detection using both CRDS (at the end of Chapter 3) and CEAS (at the end of Chapter 5). Reaction analysis within a single droplet has several advantages over continuous flow systems [9] and is the next aim of this research strand.

Chapter 7

Spectrophotometric pH determination

"Spectrophotometry is ... expected to become the method of choice for the most accurate and precise measurements of seawater pH."
M. Wedborg, D. R. Turner, L. G. Anderson and D. Dyrssen, Methods of Seawater Analysis, Wiley-VCH, 2007 [184].

7.1 Introduction

The measurement of pH is an important part of environmental monitoring. Indeed, pH is often described as a 'master variable' because it plays a key role in many properties, processes and reactions of aquatic systems [184]. In seawater, pH is a key parameter because it reflects the thermodynamic state of the carbon dioxide system [322]. The significant increase in atmospheric CO_2 levels over the last century has had large effects on the oceans, including a $0.74°$C temperature rise and 17 cm increase in sea level [323]. In addition, approximately 25% of anthropogenic CO_2 currently enters the ocean [324], where dissolved CO_2 exists in equilibrium with carbonic acid H_2CO_3, which rapidly dissociates to produce HCO_3^- and H^+. The released H^+ increases ocean acidity (by 0.1 pH units over the last century [323]), and also combines with free carbonate ions CO_3^{2-}. Indeed, seawater carbonate concentrations have dropped by ca. 30 μmol kg^{-1} over the last century, limiting the formation of aragonite, the principal crystalline form of $CaCO_3$ deposited in coral skeletons [325]. In the short term, pH monitoring is important as a measure for the processes involved in biological production and respiration [322].

Historically, the predominant method for measuring pH was glass electrode potentiometry [326]. Over the last ten years, however, spectrophotometric methods of determining pH using indicators have been developed and applied to *in situ* sensing [184]. Byrne et al. provided the first at-sea comparison of the two techniques [327].

Table 7.1: Five commonly used sulfonephthalein pH indicators, listed in terms of increasing pK_a values [328], where pK_a is defined in Section 7.2, pH range is the useable pH range of the listed indicator, $\lambda_{Ind^{2-},max}$ is the wavelength of maximum absorbance by the basic form of the indicator, λ_{iso} is the wavelength of the isosbestic point, and $\lambda_{HInd^{-},max}$ is the wavelength of maximum absorbance by the acidic form of the indicator. See Figure 7.2 for an example UV/vis spectrum of bromocresol green.

Indicator	pK_a	pH range	$\lambda_{Ind^{2-},max}$ / nm	λ_{iso} / nm	$\lambda_{HInd^{-},max}$ / nm	Ref.
Bromocresol green (BCG)	4.6	3.8 - 5.2	616	510	444	[329]
Bromocresol purple (BCP)	6.3	5.2 - 6.8	589	488	432	[330]
Phenol red (PR)	7.9	6.8 - 8.4	558	480	433	[330]
m-Cresol purple (mCP)	8.6	7.4 - 9.0	578	488	434	[331]
Thymol blue (TB)	8.8	8.0 - 9.6	596	488	435	[118]

It is now generally accepted that indicator spectrophotometry is the preferred method, for several reasons. Firstly, glass electrodes are fragile and require regular *in situ* calibration in buffers, the accuracy of which greatly affects the resulting accuracy of the measured pH [184]. Secondly, glass electrodes are restricted to use above 10 ^{o}C because of their slow response time at low temperatures [184]. In contrast, indicator spectrophotometry can be calibrated in the laboratory, rather than in the field, while also responding rapidly to any sample changes.

Glass electrodes can measure pH to a precision of 0.002 pH, compared with 0.0005 pH or better with optimised spectrophotometry [184]. Byrne et al. note that ideally, spectrophotometric pH measurements should be carried out using two wavelengths (a method which will be discussed in Section 7.2), in a thermostated 10 cm pathlength absorption cell [327]. Long pathlength absorption cells are required in order to minimise the indicator concentration added to the sample. Addition of indicator to a sample is the main problem associated with spectrophotometric pH measurement. The indicator stock solution usually has a different pH from that of the sample being analysed. This causes the pH of the sample to be perturbed. It is desirable to work with low indicator concentration to minimise such pertubations, however this causes the measurable absorption change to be reduced. It is generally accepted that with optical pathlengths of at least 10 cm, indicator concentrations can be sufficiently low that pH pertubations are generally < 5 milli pH units [332].

While the sensitivity of double beam spectrophotometry is excellent [331], such systems are bulky and expensive, and may not be suitable for measuring a flowing stream of seawater on a research cruise ship [326]. In small volume systems, which can more easily be adapted for *in situ* flow sensors, optical pathlengths are much shorter, and thus precise pH measurements are more challenging. Liu et al. designed and demonstrated ship-deployment of a more robust instrument, which used specially designed, long pathlength, small volume absorption cells [332]. In the first instance, a liquid core waveguide was constructed using low refractive index Teflon AF-2400 capillary tubing (0.6 mm inner diameter), and in the second instance a 2 mm inner diameter was machined from a PEEK rod [332]. Both cells had pathlengths between 10 and 15 cm. However, the PEEK cell was found to be significantly superior to the Teflon cell in

terms of pH accuracy and precision. Results comparable to those achieved in the PEEK cell could only be achieved in the Teflon cell when an anionic surfactant was added, indicating that the hydrophobicity of the Teflon walls in the absence of an added surfactant caused the hydrophobic indicator to vary in concentration across the liquid core waveguide cross-section. Hence, Liu et al. concluded that the use of a PEEK cell was preferable, even through it did not act as a liquid core waveguide [332]. This paper raises interesting issues that may need to be considered when reducing the sample volume, and thereby increasing the cell wall surface area.

The application of spectrophotometric pH measurement to on-chip analysis has been hampered by the short absorption pathlengths common in these systems. One interesting example must be highlighted, that of Floquet et al. who applied their 80 mm absorption cell (discussed previously in Chapter 4), manufactured in tinted PMMA, to the measurement of pH using thymol blue. A multiwavelength LED with wavelengths centred on the acidic and basic absorption peaks of thymol blue (see Table 7.1) was used in combination with a photodiode. As the photodiode is not wavelength-selective, each LED die was switched on alternately to monitor the absorbance at each wavelength independently. 10 s signal averaging was used and the absorbance was measured at a fixed pH for a range of indicator concentrations. The limit of detection, in terms of absorbance, was established to be 6.3×10^{-5} cm^{-1} at 435 nm and 2.7×10^{-4} cm^{-1} at 592 nm.

Table 7.1 lists some examples of pH indicators that have been used for water sensing, along with their maximum absorption wavelengths. Generally, indicators are only useful around ± 1.5 pH units around their pK_{a} value (defined in Section 7.2) [333]. This means that meta-cresol purple [334] and thymol blue [118] have been most commonly applied to seawater pH monitoring, for which the pH is around 8.0, whereas bromocresol purple and phenol red have been used in combination for determination of freshwater pH [330], where the pH may be slightly lower. Combining two or more indicators is a well-established method to increase the usable pH range of an indicator solution [328]. Bromocresol green has a significantly lower pK_{a} value, but is used widely in determinations of the total alkalinity of seawater [327, 329], which is measured through a titration of > 50 mL of sample with hydrochloric acid. The total alkalinity is defined as the sum of the concentration of the basic species (including HCO_3^-, CO_3^{2-}, OH^-, $B(OH)_4^-$, PO_4^{3-}, HPO_4^{2-}, $SiO(OH)_3^-$), minus the sum of the concentration of the acidic species (including H^+, H_3PO_4) [322].

In this Chapter, we investigate the application of broadband cavity enhanced techniques to short optical pathlength pH detection. We begin by deriving the important equations for determination of pH using both single and dual-wavelength absorption spectroscopy, and then describe the experimental set-ups used, before presenting the results of our pH calibrations using well-characterised buffer solutions.

7.2 Theory

Table 7.1 lists five commonly used sulfonephthalein indicators. These indicators exist in three forms, $\mathrm{H_2Ind}$, $\mathrm{HInd^-}$ and $\mathrm{Ind^{2-}}$, which may be defined as follows:

$$\mathrm{H_2Ind + H_2O \rightleftharpoons HInd^- + H_3O^+} \tag{7.1}$$

$$\mathrm{HInd^- + H_2O \rightleftharpoons Ind^{2-} + H_3O^+} \tag{7.2}$$

where

$$K_{\mathrm{a},1} = \frac{[\mathrm{HInd^-}][\mathrm{H_3O^+}]}{[\mathrm{H_2Ind}][\mathrm{H_2O}]} \tag{7.3}$$

and

$$K_{\mathrm{a},2} = \frac{[\mathrm{Ind^{2-}}][\mathrm{H_3O^+}]}{[\mathrm{HInd^-}][\mathrm{H_2O}]} \tag{7.4}$$

are the equilibrium or acid dissociation constants for the $\mathrm{H_2Ind}$ and $\mathrm{HInd^-}$. K_a for each indicator transition is related to $\mathrm{p}K_\mathrm{a}$ as follows:

$$\mathrm{p}K_\mathrm{a} = -\log K_\mathrm{a} \tag{7.5}$$

Despite being polyprotic, these indicators can be treated as monoprotic as long as the experimental measurements are within ± 3 pH units of $\mathrm{p}K_{\mathrm{a},1}$ or $\mathrm{p}K_{\mathrm{a},2}$, respectively [328]. In our case, we are interested in the second transition (Equation 7.4), and thus we refer to $\mathrm{p}K_{\mathrm{a},2}$ simply as $\mathrm{p}K_\mathrm{a}$ for the remainder of this Chapter. We can combine Equations 7.4 and 7.5, given that $-\log[\mathrm{H_3O^+}] = \mathrm{pH}$, and the activity of water is unity, to produce the Henderson-Hasselbalch equation for our indicator transition of interest:

$$\mathrm{pH} = \mathrm{pK_a} + \log \frac{[\mathrm{Ind^{2-}}]}{[\mathrm{HInd^-}]} \tag{7.6}$$

If either $\mathrm{Ind^{2-}}$ or $\mathrm{HInd^-}$ displays a visible absorption spectrum, then we can monitor the pH of the solution simply by making absorption measurements at a single-wavelength, either at or close to the maximum absorption wavelength of $\mathrm{Ind^{2-}}$ or $\mathrm{HInd^-}$. If the initial (or total) indicator concentration $[\mathrm{Ind}]_\mathrm{tot}$ is known, then we can substitute $[\mathrm{Ind}]_\mathrm{tot} = [\mathrm{Ind^{2-}}] + [\mathrm{HInd^-}]$ into Equation 7.6 to produce:

$$\mathrm{pH} = \mathrm{pK_a} + \log \frac{[\mathrm{Ind}^{2-}]}{[\mathrm{Ind}]_{\mathrm{tot}} - [\mathrm{Ind}^{2-}]} \tag{7.7}$$

Therefore, if we know $\mathrm{p}K_\mathrm{a}$ and $[\mathrm{Ind}]_{\mathrm{tot}}$, we can determine pH by measuring $[\mathrm{Ind}^{2-}]$ spectroscopically, in our case either using CEAS or CRDS. This spectroscopic measurement of course also requires a knowledge of the absorption coefficient of Ind^{2-} at its maximum absorption wavelength, and the pathlength of the sample.

It is advantageous to monitor pH at two different wavelengths, because in this case the absorbance measurements become independent of both indicator concentration and pathlength [328]. This can be particularly helpful as indicators are often not particularly pure, being typically available from Sigma-Aldrich at only 90% purity, compared to analytical grade reagents which are typically available at $> 99\%$ purity.

If the absorption at two wavelengths λ_1 and λ_2 is measured, we can write the absorption per unit pathlength as a sum of the absorption arising from Ind^{2-} and HInd^{-}:

$$\frac{\mathrm{A}_\lambda}{l} = \alpha_\lambda^{\mathrm{Ind}^{2-}}[\mathrm{Ind}^{2-}] + \alpha_\lambda^{\mathrm{HInd}^{-}}[\mathrm{HInd}^{-}] \tag{7.8}$$

where A_λ is the absorption at a specific wavelength, l is the absorption cell pathlength, and α_λ is the absorption coefficient at each wavelength, for each indicator species. If the absorbances A_1 and A_2 are determined at two wavelengths λ_1 and λ_2, the absorbance ratio can be written:

$$\frac{\mathrm{A}_2}{\mathrm{A}_1} = \frac{\alpha_2^{\mathrm{Ind}^{2-}}[\mathrm{Ind}^{2-}] + \alpha_2^{\mathrm{HInd}^{-}}[\mathrm{HInd}^{-}]}{\alpha_1^{\mathrm{Ind}^{2-}}[\mathrm{Ind}^{2-}] + \alpha_1^{\mathrm{HInd}^{-}}[\mathrm{HInd}^{-}]} \tag{7.9}$$

If we rearrange Equation 7.9 and divide through by $\alpha_1^{\mathrm{HInd}^{-}}$, then we can rewrite the concentration ratio as a function of four variables:

$$\frac{[\mathrm{Ind}^{2-}]}{[\mathrm{HInd}^{-}]} = \frac{Q - e_1}{e_2 - Qe_3} \tag{7.10}$$

where $Q = \frac{\mathrm{A}_2}{\mathrm{A}_1}$, $e_1 = \frac{\alpha_2^{\mathrm{HInd}^{-}}}{\alpha_1^{\mathrm{HInd}^{-}}}$, $e_2 = \frac{\alpha_2^{\mathrm{Ind}^{2-}}}{\alpha_1^{\mathrm{HInd}^{-}}}$ and $e_3 = \frac{\alpha_1^{\mathrm{Ind}^{2-}}}{\alpha_1^{\mathrm{HInd}^{-}}}$. When choosing the two wavelengths at which to monitor, there are three commonly used options: $\lambda_{\mathrm{Ind}^{2-},\mathrm{max}}$ and λ_{iso}, the basic peak and the isosbestic point; $\lambda_{\mathrm{HInd}^{-},\mathrm{max}}$ and λ_{iso}, the acidic peak and the isosbestic point; or, $\lambda_{\mathrm{Ind}^{2-},\mathrm{max}}$ and $\lambda_{\mathrm{HInd}^{-},\mathrm{max}}$, the basic and acidic peaks. We choose to use $\lambda_{\mathrm{Ind}^{2-},\mathrm{max}}$ and λ_{iso}, which means that $e_3 = 1$, as at the isosbestic point $\alpha_1^{\mathrm{Ind}^{2-}} = \alpha_1^{\mathrm{HInd}^{-}}$. Hence, inserting Equation 7.10 into Equation 7.6 yields:

$$\mathrm{pH} = \mathrm{p}K_\mathrm{a} + \log \frac{Q - e_1}{e_2 - Q} \tag{7.11}$$

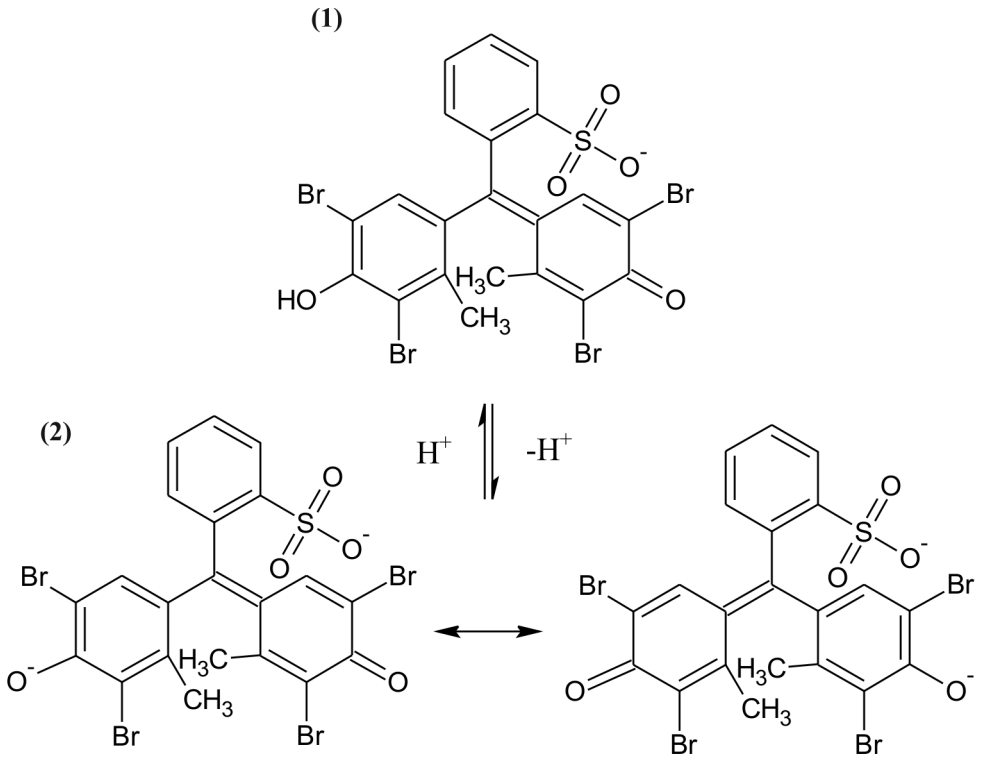


Figure 7.1: Structural forms of bromocresol green. Around pH 4.6, the indicator converts from the first structure (1) to the second resonance stabilised structure (2).

and thus the pH measurement becomes independent of both the absorption pathlength and the indicator concentration.

The absorbance ratio Q can be established either through CEAS or CRDS monitoring of the absorbance at wavelengths $\lambda_{\mathrm{Ind}^{2-},\mathrm{max}}$ and λ_{iso}. e_1 and e_2 can be established by measuring the absorption spectrum of the indicator under very acidic or very basic conditions, such that the indicator is present entirely in its Ind^{2-} or HInd^{-} forms. Our current cavity set-up, employing a supercontinuum source in combination with 99% reflective broadband mirrors and a fibre-coupled spectrometer (see Chapter 5), allows sensitive absorption measurements to be made at wavelengths above 500 nm. Among the sulfonephthalein group of indicators (Table 7.1), bromocresol green (BCG) is the only indicator with an isosbestic point above 500 nm and hence was our indicator of choice [328]. The structures of BCG are shown in Figure 7.1.

7.3 Experimental

7.3.1 Reagents

All reagents were purchased from Sigma-Aldrich and used without further purification. We use the sodium salt form of the BCG indicator (Sigma-Aldrich, 114367), which confers water solubility on the indicator solutions.

Phosphate buffers of fixed ionic strength (100 mM) were used to create the nine pH standards used in the experiments. A 0.1 M stock solution of phosphoric acid (Sigma-Aldrich, 79607) was prepared and used to make up the pH standards through addition of appropriate quantities of $\mathrm{NaH_2PO_4}$ (Sigma Aldrich, 71504), $\mathrm{Na_2HPO_4}$ (Sigma-Aldrich, 30412) and MilliQ water. The quantities of each reagent used to prepare the pH standards are listed in Table 7.3.1, with each solution being made up to 500 mL with deionised water. Fresh buffer solutions were made for each set of measurements. The pH of each buffer solution was measured using a standard pH meter (SevenEasy Mettler Toledo AG).

Table 7.2: Reagent quantities for making up pH buffer solutions with 100 mM ionic strength. * indicates that the solution is made from a 5.6 M concentration of $\mathrm{H_3PO_4}$, otherwise a 0.1 M solution was used.

Theoretical pH	$\mathrm{H_3PO_4}$ / mL	$\mathrm{NaH_2PO_4}$ / g	$\mathrm{Na_2HPO_4}$ / g	Measured pH
3.8	11.12	6.8850	0.0076	3.74
4.0	7.01	6.8762	0.0121	4.03
4.2	4.41	6.8583	0.0191	4.25
4.4	2.77	6.8309	0.0302	4.46
4.6	1.74	6.7903	0.0476	4.60
4.8	1.09	6.7300	0.0747	4.78
5.0	0.68	6.6341	0.1167	5.02
5.2	0.42	6.4844	0.1808	5.16
5.4	0.26	6.2605	0.2766	5.46
1	125.00*	6.899	0	0.95
3	1.25*	6.830	0	2.90
7	0	1.35	2.38	7.03

7.3.2 Characterising the indicator dye: determining e_1 and e_2

As can be seen from Equation 7.11, before we determine the absorption of our pH standard solutions it is necessary to determine e_1, e_2 and the $\mathrm{p}K_\mathrm{a}$ for the indicator, so that we can infer the pH of our test solution from the absorbance measurements. Initially, the indicator was added to 50 mL of five different pH buffers in the pH range 1 - 7, to give an indicator concentration of 54 μM in each solution. The absorption spectra of the resulting solutions were measured in a 1 cm cuvette, using a UV/vis spectrometer. The spectra are presented in Figure 7.2. The isosbestic point occurs at 510 nm, and the peak absorption wavelength for the

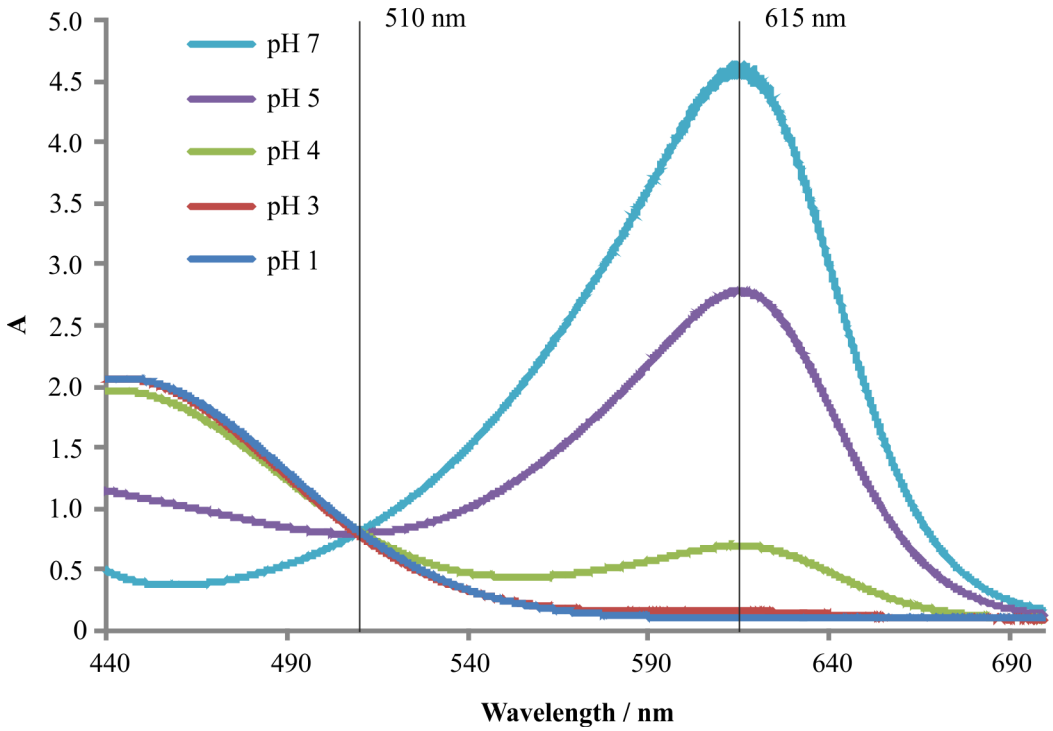


Figure 7.2: Single-pass measurement of Absorbance as a function of λ / nm, for 54 μM BCG concentration in buffer solutions from pH 1 - 7.

basic form of the indicator, Ind^{2-}, is 615 nm. Both of these values are in good agreement with the literature values presented in Table 7.1.

Having established our wavelengths of interest, we now need to determine the values of $e_1 = \frac{\alpha_{615}^{\mathrm{HInd}^-}}{\alpha_{\mathrm{iso}}}$ and $e_2 = \frac{\alpha_{615}^{\mathrm{Ind}^{2-}}}{\alpha_{\mathrm{iso}}}$. This requires knowledge of the absorption coefficients of the acidic and basic forms of the indicator.

The absorption coefficient of the basic form at 615 nm was determined by recording absorption spectra of various concentrations of BCG, in the range 2 - 54 μM, at pH 7. This experiment was carried out in a 1 cm pathlength cuvette using a UV/vis spectrometer. At pH 7, the indicator is present entirely in its basic form, and the absorbance therefore arises solely from Ind^{2-}. This allows $\alpha_{615}^{\mathrm{Ind}^{2-}}$ to be determined from the gradient of a plot of absorbance at 615 nm, $A_{615} = \alpha_{615} Cl$, as a function of concentration C. α_{iso} was determined in a similar manner from the gradient of a plot of absorbance at 510 nm as a function of concentration. The two plots are presented in Figure 7.3. From the gradient of Figure 7.3(a), we determine $\alpha_{615}^{Ind^{2-}} = (83,400 \pm 4020)$ M^{-1} cm^{-1} and $\alpha_{\mathrm{iso}} = (13,400 \pm 700)$ M^{-1} cm^{-1}, hence $e_2 = 6.22 \pm 0.63$.

To determine e_1, a similar approach to that described for the determination of e_2, above, is adopted, the only difference being that in this case the absorption measurements were carried out at pH 1. At this pH, the indicator is present only in its acidic form, HInd^-. In determining $\alpha_{615}^{\mathrm{HInd}^-}$, it was found that there was no significant absorption arising from HInd^- at 615 nm. The absorption values fluctuated around an

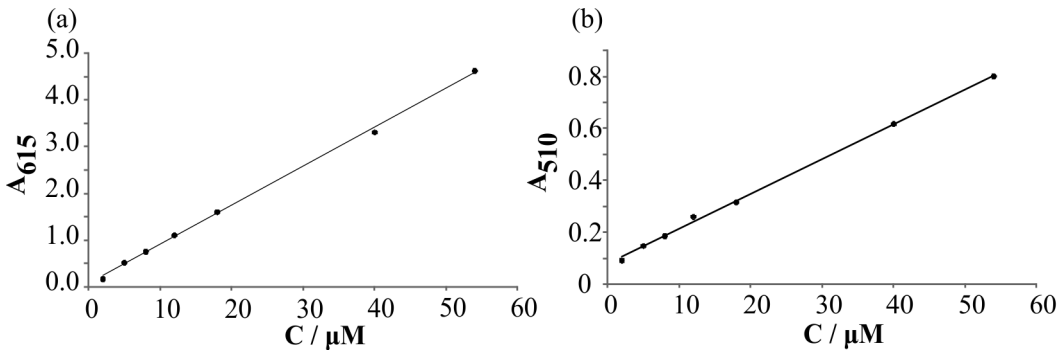


Figure 7.3: Plots of Absorbance versus indicator concentration C/μM, measured at pH 7. (a) Absorption at 615 nm. From the gradient of the plot, we can determine $\alpha_{615}^{Ind^{2-}} = (83,430 \pm 4022)$ M^{-1} cm^{-1}. (b) Absorption at 510 nm. From the gradient of the plot, we can determine $\alpha_{\mathrm{iso}} = (13,425 \pm 703)$ M^{-1} cm^{-1}.

average of 0.0808 cm^{-1}, with a 3σ standard deviation of 0.0138 cm^{-1}, very close to the detection limit of the spectrometer. Given that $\alpha_{615}^{\mathrm{HInd}^-} \approx 0$, we can determine that $e_1 = 0$.

Having established the values of e_1 and e_2, the pH of an unknown solution may be determined by measuring the absorbances A_1 and A_2, and substituting $Q = \mathrm{A}_2/\mathrm{A}_1$ into Equation 7.11.

7.3.3 Cavity set-ups

For all the pH experiments in this Chapter, we use the broadband supercontinuum light source described in Chapter 5, in combination with broadband 99% reflectivity mirrors, enabling us to monitor the absorption at both 510 nm and 615 nm simultaneously. A coloured glass bandpass filter (transmission range 315 - 710 nm) was placed in front of the cavity to prevent wavelengths not supported by the cavity from being detected by the spectrometer.

In the first set of experiments (Figure 7.4(a)), CEAS was used, collecting the entire cavity output and wavelength-resolving it using the Ocean Optics USB spectrometer. The CEAS experiments were carried out by inserting the 100 μm flow cell (used in Chapters 3 - 6) into a 13.5 cm long cavity at normal incidence. The integration time of the spectrometer was set to 6 ms in all of the experiments carried out in this Chapter. For CEAS, calibration of the cavity enhancement factor (CEF) at each wavelength was required, as it is unlikely that the number of passes (equal to the total absorption pathlength) will be equal at both wavelengths, given the varying mirror reflectivity across the visible spectrum. In order to use Equation 7.11, the pathlength must be the same at each absorption wavelength, thus we scale the absorption for the calibrated CEF before determining Q (Equation 7.11).

Problems were encountered during the intial CEAS experiments, which will be discussed in Section 7.4. It was therefore decided to modify the experiment to carry out dual-wavelength CRDS experiments. A similar set-up was used as for CEAS, with two changes. Firstly, the cavity length was increased from 13.5 cm to

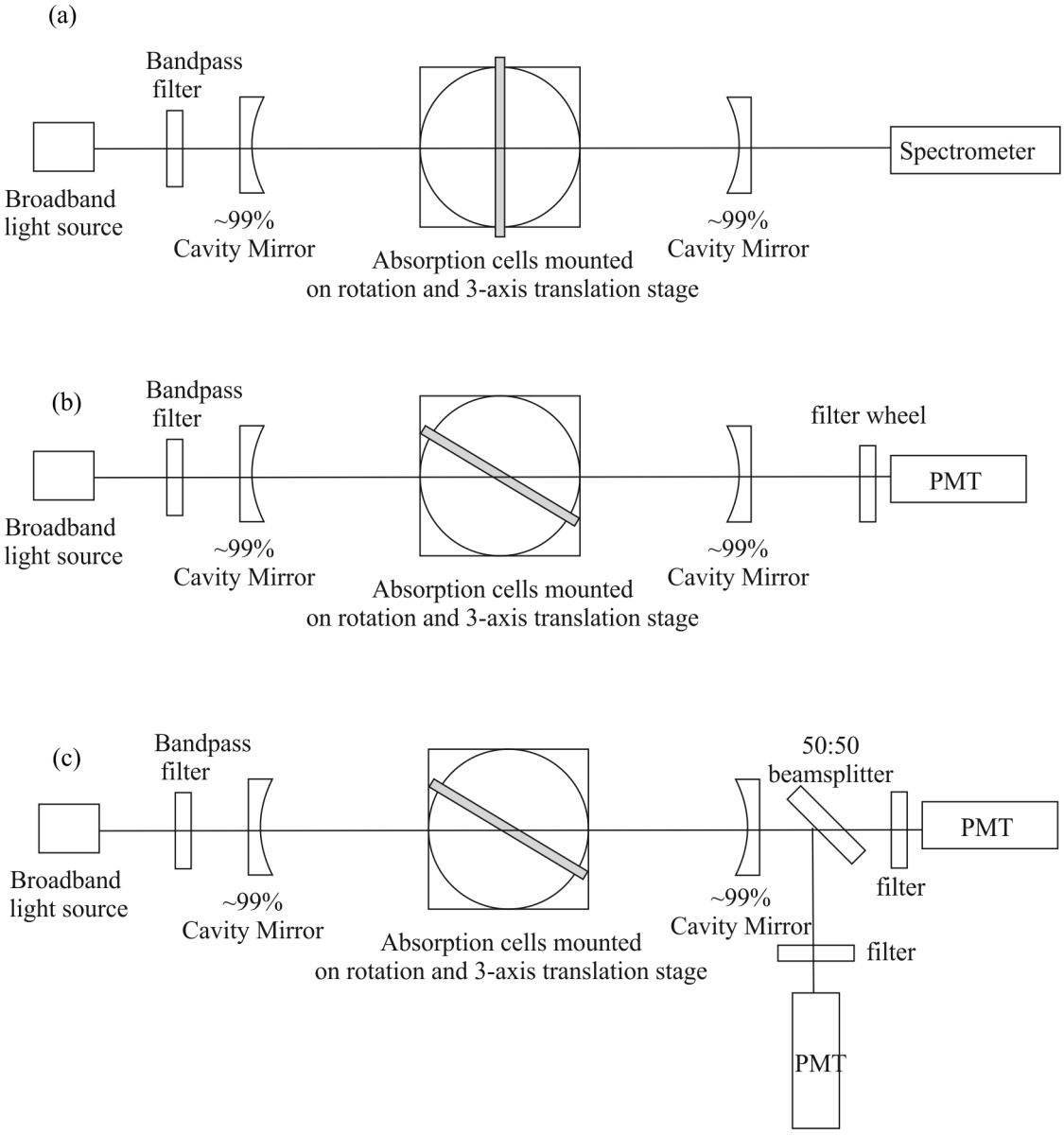


Figure 7.4: Schematic diagram of (a) Broadband CEAS experiment, with cavity length 13.5 cm, (b) alternate dual-wavelength CRDS experiment, with cavity length 49.5 cm and (c) simultaneous dual-wavelength CRDS experiment, with cavity length 49.5 cm.

49.5 cm. A longer cavity is required for ringdown measurements, which are time-resolved, compared with CEAS measurements, which are time-integrated. Secondly, taking a ringdown measurement requires selection of the appropriate wavelengths, as monitoring both wavelength and time is experimentally-challenging (for a review of broadband CRDS see [275]). As we were only interested in a maximum of two wavelengths for this pH study, we used appropriate filters to select the wavelength before detecting this wavelength only using a photomultiplier tube (PMT). In the first CRDS measurements (Figure 7.4(b)), a filter wheel was mounted behind the second cavity mirror, before the PMT. The filter wheel included two adjacent bandpass filters, with centre wavelengths of 510 nm (Thorlabs, FB510-10) and 620 nm (Thorlabs, FB620-10) respectively. In each case the filter had a 10 nm bandwidth. Samples were flowed through the flow cell (in this case, 2 mm and 100 μm cells), and ringdown times for each wavelength λ_1 and λ_2 were recorded sequentially by manually rotating the filter wheel. The two ringdown times were converted into absorbances and used to determine Q.

In the second pH measurements carried out using CRDS, a 50:50 beamsplitter (Thorlabs, EBS1) was mounted behind the second cavity mirror (Figure 7.4(c)). This split the total cavity output into two beampaths. By placing an appropriate bandpass filter in each beampath, in front of a PMT in each case, we were able to record simultaneous, dual-wavelength ringdowns. Each ringdown was visualised on a separate channel on the oscilloscope, and the LabVIEW data acquisition and analysis software was modified to allow for two channels from the oscilloscope to be simultaneously analysed. In this set-up, the 1 mm flow cell was inserted into the cavity.

It should be noted that as we in fact do know the total indicator concentration, and the pathlength through the sample, we interpret our results based on both Equation 7.6 and Equation 7.11. This allows us to compare the results from single-wavelength and dual-wavelength pH monitoring directly.

7.4 Results and Discussion

7.4.1 Finding CEF at 615 nm and 510 nm

The CEF of the 100 μm flow cell inserted at normal incidence into the cavity was established at 615 nm and 510 nm by fixing the pH of the buffer solutions at a value of 5.03, and varying the concentration of indicator. This enabled the CEF to be determined simultaneously at these two widely different wavelengths, which is often not possible for single absorbing chemical species, where the absorption range may not span across both these wavelengths. These plots are presented in Figure 7.5. The increase in scatter at 510 nm has two origins. Firstly, the absorption is four times lower at 510 nm compared to at 615 nm. Secondly, the supercontinuum source is much less stable at this lower wavelength, as discussed in Chapter 5. The high variation in light intensity at 510 nm is thought to occur partly as a result of the lower light intensity at this wavelength, owing

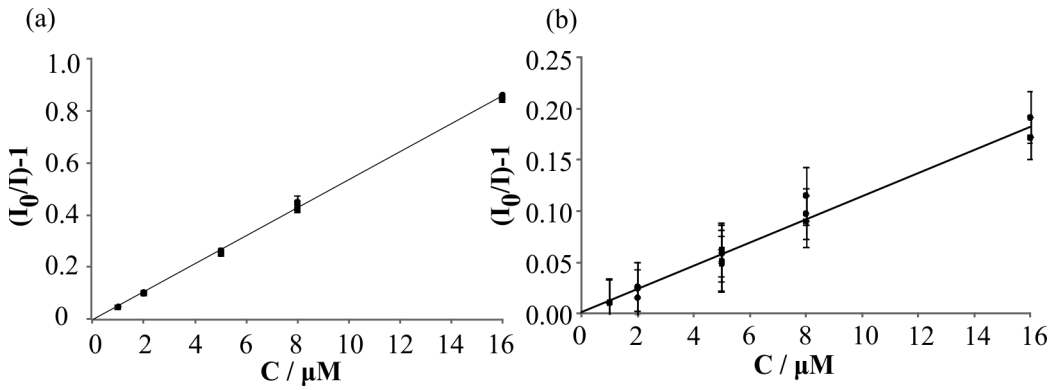


Figure 7.5: Plots of $\frac{I_0}{I} - 1$ versus indicator concentration C/μM, measured at pH 5.03 in the 0.1 mm flow cell, at (a) 615 nm and (b) 510 nm. The CEF at 615 nm is calculated from the gradient of plot (a) to be 64. The CEF at 510 nm is calculated from the gradient of plot (b) to be 84. The error bars correspond to the 1σ uncertainty determined by 50 repeated measurements of I_0.

to lower efficiency of the supercontinuum source. For measurements at 510 nm, the intensity value is only 20% of that recorded at 615 nm. At 510 nm, this intensity value has a typical 3σ variation of 7.2% (arising from high shot-to-shot noise in the supercontinuum source), compared to 2.4% (within the noise limit of the detector) at 615 nm. Unfortunately, we cannot increase the averaging time at 510 nm without saturating the signal at 615 nm, and thus signal averaging in order to reduce the noise is not possible in a simultaneous measurement.

7.4.2 CEAS determination of pK_{a}

In Section 7.2, we showed that if we know the total concentration $[\mathrm{Ind}]_{\mathrm{tot}}$ of the indicator and the concentration of $[\mathrm{Ind}^{2-}]$, via monitoring of absorbance at 615 nm only, we can determine the concentration ratio $\frac{[\mathrm{Ind}^{2-}]}{[\mathrm{HInd}^{-}]}$. Measuring this concentration ratio at a known pH allows us to determine $\mathrm{p}K_{\mathrm{a}}$ for the indicator using the Henderson-Hasselbalch equation (Equation 7.6). To obtain a more accurate value of $\mathrm{p}K_{\mathrm{a}}$, the concentration ratio was measured over a range of pH, in the 100 μm flow cell, and $\mathrm{p}K_{\mathrm{a}}$ for the indicator was then determined from the x-intercept of a plot of pH against $\log \frac{[\mathrm{Ind}^{2-}]}{[\mathrm{HInd}^{-}]}$. This plot is shown in Figure 7.6. The $\mathrm{p}K_{\mathrm{a}}$ was found to be 4.69 ± 0.04, which is close to the value of 4.66 reported in the literature [328]. In the following Sections, we use this $\mathrm{p}K_{\mathrm{a}}$ value in combination with the Henderson-Hasselbalch equation in order to determine pH from single and dual-wavelength optical measurements.

7.4.3 CEAS pH measurements

Having determined e_1, e_2 and $\mathrm{p}K_{\mathrm{a}}$ for the BCG indicator we can now calculate pH from measurements of absorbance at a single wavelength and from a ratio of absorbances at two wavelengths. BCG was added

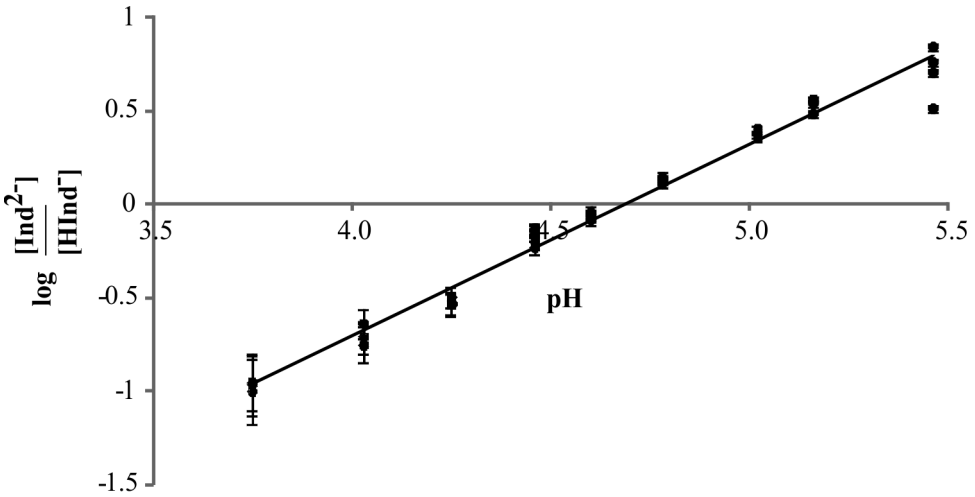


Figure 7.6: Determination of $\mathrm{p}K_\mathrm{a}$ for BCG indicator used in this Chapter. From a plot of $\log \frac{[\mathrm{Ind}^{2-}]}{[\mathrm{HInd}^{-}]}$ versus pH, for a fixed indicator concentration of 7.5 μM, with absorbance measured in 100 μm flow cell, the $\mathrm{p}K_\mathrm{a}$ for the indicator is determined from the x-intercept, yielding a value of 4.69 ± 0.04. The error bars correspond to the 1σ uncertainty determined by 50 repeated measurements of I_0 converted into $\log \frac{[\mathrm{Ind}^{2-}]}{[\mathrm{Ind}^{2-}]-[\mathrm{Ind}^{2-}]_\mathrm{min}}$ after determination of $\Delta\mathrm{A}_\mathrm{min}$ using Equation 7.13.

to 50 mL of a range of pH standards, ranging in pH from 3.8 to 5.4, such that the final concentration of indicator dye in the solutions was 7.5 μM. The resulting solution was then flowed through the 0.1 mm flow cell. The absorption was measured at 510 nm and 615 nm using CEAS. Values for the quantity $(I_0/I) - 1$ were determined and converted into absorbance values using the following Equation:

$$\mathrm{A} = \frac{(I_0/I) - 1}{\mathrm{CEF}} \tag{7.12}$$

given the previously established CEF at each wavelength (Section 7.4.1). This equation can be rewritten to enable the minimum detectable change in absorbance, ΔA_min to be established given a measured ΔI_min:

$$\Delta\mathrm{A}_\mathrm{min} = \frac{\Delta\mathrm{I}_\mathrm{min}/\mathrm{I}_0}{\mathrm{CEF}} \tag{7.13}$$

where ΔI_min, the minimum detectable change in intensity, is determined from the 3σ uncertainty within I_0. $\Delta\mathrm{A}_\mathrm{min}$ is provided as a dotted line on each plot of absorbance versus pH to give an indication of whether the measured change in absorbance is statistically significant.

For single-wavelength determinations of pH, the absorption at 615 nm (A_{615}) is used to determine $[\mathrm{Ind}^{2-}]$, and this is converted into pH using the known total indicator concentration and Equation 7.6. Figure 7.7(a) shows a plot of measured absorbance at 615 nm versus pH, with the solid curve showing the predictions of the Henderson-Hasselbalch equation. The absorbance measured using CEAS is in good agreement with this

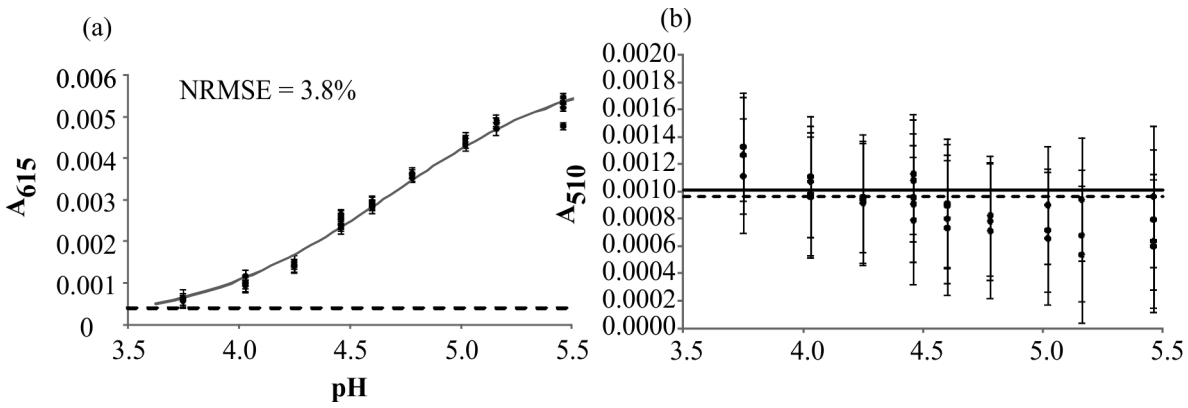


Figure 7.7: Plots of Absorbance versus pH, for a fixed indicator concentration of 7.5 μM, measured using CEAS in 0.1 mm flow cell. (a) Absorption at 615 nm. The grey curve is a plot of Equation 7.6. The dotted line corresponds to $\Delta A_{\min}$, the minimum detectable change in absorbance, which is calculated from Equation 7.13. NRMSE is the normalised root mean square error, defined in Appendix A. (b) Absorption at 510 nm. The solid line is the expected Beer-Lambert law absorbance, and the dotted line corresponds to $\Delta A_{\min}$. The error bars on both graphs represent 1σ uncertainty in 50 repeated measurements of I_0 converted into the absorbance uncertainty using Equation 7.13.

theoretical curve, indicating the validity of this approach. In addition, the measured absorbance for each pH lies significantly above $\Delta A_{\min}$.

Since the isosbestic point does not vary with changing pH, and we are working with a fixed indicator concentration, we would expect a plot of the measured absorbance at 510 nm versus pH to take the form of a flat line. Unfortunately, as Figure 7.7(b) indicates, the expected Beer-Lambert law absorbance at 510 nm lies close to, and even below, the minimum detectable change in absorbance, $\Delta A_{\min}$. As previously discussed, this is partly a consequence of α_{510} being four times smaller than α_{615}, but also arises from the significantly larger error 3σ variation in the intensity measurements at 510 nm compared to at 615 nm.

It was not possible to take the ratio of the two absorbances $Q = \frac{A_{615}}{A_{510}}$ owing to the short pathlength cell used here, and the high uncertainty in A_{510}. It was therefore decided to also carry out measurements using a similar set-up, but with dual-wavelength-resolved output rather than broadband output, as discussed in Section 7.3.3. CRDS overcomes a key problem of CEAS, in that it is relatively immune to fluctuations in light intensity.

7.4.4 Dual-wavelength pH measurements using CRDS

For all CRDS measurements, the flow cell was inserted into the cavity at Brewster's angle. Sequential ringdown times were recorded using a single PMT placed behind a filter wheel (Figure 7.4(b)). This method was used for dual-wavelength detection with a 2 mm and 0.1 mm flow cell. The 0.1 mm cell was initially tested to compare the results obtained using CRDS to the CEAS experiments, and then the 2 mm flow cell was used to see if increasing the optical pathlength improved our results further. The measured ringdown time is converted into absorbance using:

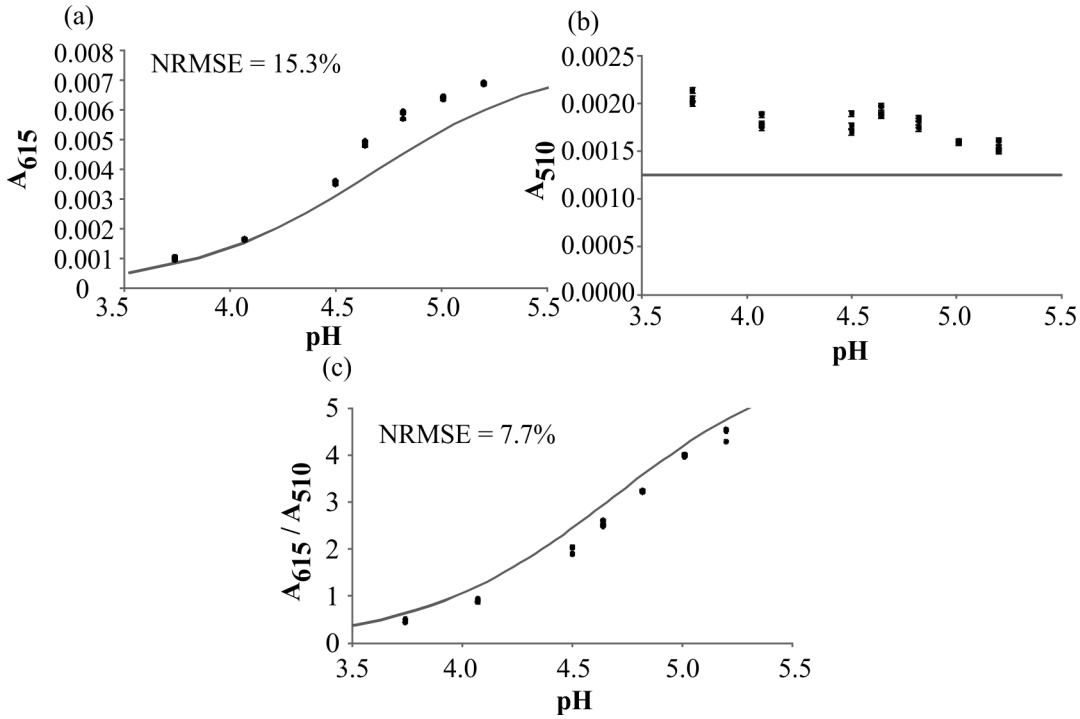


Figure 7.8: Plots of Absorbance versus pH, for a fixed indicator concentration of 8 μM, recorded in 0.1 mm flow cell using alternate wavelength CRDS. (a) Absorption at 615 nm. (b) Absorption at 510 nm. (c) Ratio of A_{615}/A_{510}. The curve shown in (a) is a plot of Equation 7.6. The line shown in (b) is the expected Beer-Lambert law absorbance. The curve shown in (c) is a plot of Equation 7.11. NRMSE is the normalised root mean square error, defined in Appendix A.

$$\mathrm{A} = \frac{d}{c}\left(\frac{1}{\tau} - \frac{1}{\tau_0}\right) \tag{7.14}$$

The absorption at each wavelength, and the ratio of the absorptions at the two wavelengths, are plotted as a function of pH in Figure 7.8 for the 0.1 mm flow cell and Figure 7.9 for the 2 mm flow cell.

The predictions of the Henderson-Hasselbalch equation are shown as solid curves on plots (a) and (c), and the predicted Beer-Lambert law absorbance is shown on plot (b). The absorption measurements at 510 nm for both flow cells are much more stable than in the CEAS experiments, showing little variation with pH, as expected. This confirms that hypothesis that instability in the supercontinuum light source near the edges of its emission spectrum was the main source of error in the CEAS measurements described earlier.

Comparing both the 0.1 mm and 2 mm flow cell data for the single-wavelength measurement at 615 nm, the 2 mm flow cell gives a much better fit to the expected Henderson-Hasselbalch curve. The poorer fit for the 0.1 mm cell is attributed to the lower absorbance and therefore larger uncertainties associated with the measurement made using the 0.1 mm flow cell. For both the plots of 510 nm absorbance, there is a systematic error between the expected Beer-Lambert law absorbance and the measured absorbance, which will be discussed in Section 7.4.5.

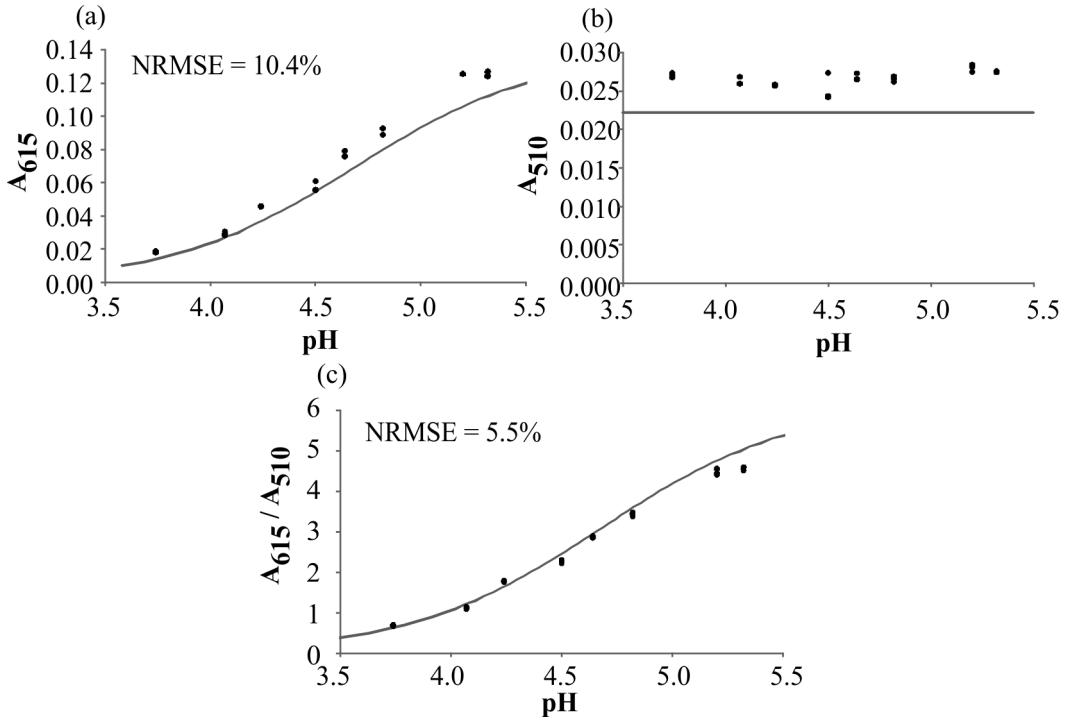


Figure 7.9: Plots of Absorbance versus pH, for a fixed indicator concentration of 8 μM, recorded in the 2 mm flow cell using alternate wavelength CRDS. (a) Absorption at 615 nm. (b) Absorption at 510 nm. (c) Ratio of A_{615}/A_{510}. The curve shown in (a) is a plot of Equation 7.6. The line shown in (b) is the expected Beer-Lambert law absorbance. The curve shown in (c) is a plot of Equation 7.11. NRMSE is the normalised root mean square error, defined in Appendix A.

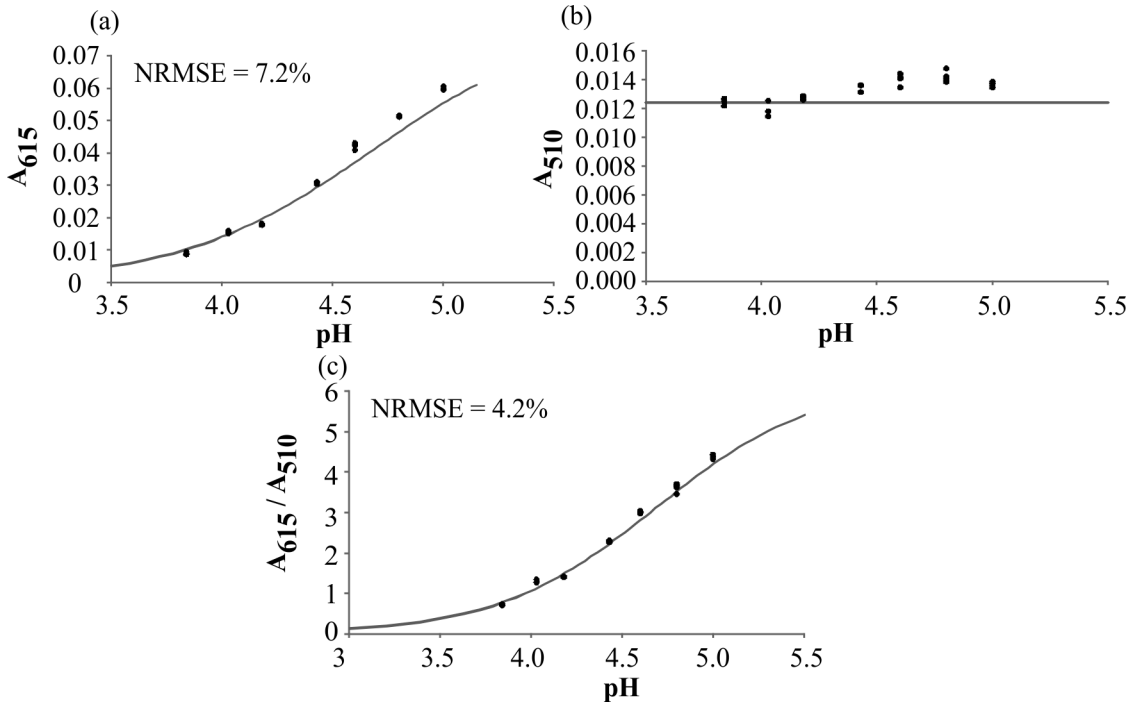


Figure 7.10: Plots of Absorbance versus pH, for a fixed indicator concentration of 8 μM, recorded in 1 mm flow cell using simultaneous dual-wavelength CRDS. (a) Absorption at 615 nm. (b) Absorption at 510 nm. (c) Ratio of A_{615}/A_{510}. The curve shown in (a) is a plot of Equation 7.6. The line shown in (b) is the expected Beer-Lambert law absorbance. The curve shown in (c) is a plot of Equation 7.11. NRMSE is the normalised root mean square error, defined in Appendix A.

This systematic error highlights the advantage of dual-wavelength pH monitoring, as the dual-wavelength data are a better fit to theory. In this case, the dual-wavelength Henderson-Hasselbalch fit for the 2 mm cell agrees better with experiment than the fit for the 0.1 mm cell. We believe this arises because of the lower absorbance and hence higher error associated with measurements employing the shorter optical pathlength.

One possible source of systematic error in these alternate ringdown measurements is that the rotation of the filter wheel may cause a slight discrepancy in the ringdown values measured, as the measured ringdown is sensitive to alignment of the cavity output beam onto the PMT. In order to combat any problems associated with making consecutive measurements of the absorbance at each wavelength, with manual rotation of the filter wheel in between each measurement, the detection system was modified to allow both wavelengths to be monitored simultaneously as described in Section 7.3.3 and shown in Figure 7.4(c). Simultaneous dual-wavelength CRDS was used in combination with the 1 mm flow cell. These results are presented in Figure 7.10 and show an appreciable improvement in fit between theory and experiment compared to the previous experiments. The fit between experiment and theory for the dual-wavelength measurements (Figure 7.4(c)) is markedly better than that for the single-wavelength measurements (Figure 7.4(a)), particularly at higher pH values, indicating that dual-wavelength monitoring can achieve greater accuracy than single-wavelength monitoring, as expected.

These experiments indicate that the best accuracy can be achieved when recording dual-wavelength ringdowns using two PMTs in combination with appropriate bandpass filters, so that no manual adjustment of the set-up is required during the experiment, and the data are decoupled from fluctuations in the light source.

7.4.5 Sensitivity

In the previous sections, we have shown that CEAS and CRDS measurements of the absorbance of an indicator added to various pH standard buffer solutions are able to reproduce the predictions of the Henderson-Hasselbalch equation for the indicator. We now determine the accuracy to which the absorbance measurements may be used to predict the pH of an unknown sample.

The pH accuracy is determined in the following manner. Firstly, the root residual squared between the experimentally measured absorbance values and the Henderson-Hasselbalch equation (either Equation 7.6 or 7.11) is determined. This provides a measure of the absorbance error, ΔA_{min}, which can be converted into the minimum detectable change in pH, $\Delta\mathrm{pH}_{\mathrm{min}}$ for either single or dual-wavelength by rearrangement of either Equation 7.6 or 7.11 as described in Appendix B. These values are presented in Table 7.3.

The accuracy of the pH measurements is affected by the systematic errors, which include uncertainties in either concentration or pathlength, as well as uncertainties in determining the intensity or the ringdown time. One point that we have not discussed in detail thus far is the difference in bandwith between each

measurement. In the UV/vis spectrometer, intensity was measured as a function of wavelength, with a bandwidth of 0.1 nm. In the CEAS measurements, the bandwidth was 0.271 ns. In the CRDS experiments, the bandwith was larger, at 10 nm. In addition, the longer wavelength filter used in the CRDS measurements was centred at 620 nm, slightly higher than the 615 nm point used in the spectrometer measurements.

We can calculate the effective absorption coefficient α_{eff} for the larger bandwidths employed for the CRDS measurements, by using the broadband single-pass data of BCG indicator solution recorded in the UV/vis spectrometer (Figure 7.2). We find that the effect of using a 10 nm bandwidth filter centred at 620 nm, compared with a 0.1 nm bandwidth at 615 nm, should be minimal: α_{eff} is calculated to be only 0.1% lower than α_{615}. This is to be expected as the base absorption peak is broad, and we are monitoring the absorbance close to its maximum, where α is relatively constant.

The situation at 510 nm is more complicated. The isosbestic point is more susceptible to the spectral bandwidth (Figure 7.2). The effective absorption coefficient, taking into account the 10 nm bandwidth employed for CRDS measurements, is 10% higher than α_{510}. This can fully account for the systematic error observed in measurements carried out using CRDS in the 1 mm flow cell at 510 nm (Figure 7.10(b)), but only partly account for the systematic error observed in Figures 7.8(b) and 7.9(b), where the measured absorbance is greater than 10% higher than predicted using α_{510}. It seems likely that any uncertainty in α is compounded in this case by the previously described uncertainty introduced by manual rotation of the filter wheel between ringdown measurements presented in Figures 7.8 and 7.9.

Table 7.3: Sensitivity analysis of each experiment, in terms of measurement accuracy. Method indicates either CEAS or CRDS measurements, Single/Dual λ indicates either single or dual-wavelength analysis, Flow cell / mm is the normal incidence pathlength through the flow cell, $\Delta\text{pH}_{\text{min}}$ is the minimum detectable change in pH determined as described in Appendix B, given to two significant figures.

Method	Single/Dual λ / nm	Flow cell / mm	$\Delta\text{pH}_{\text{min}}$
CEAS	615	0.1	0.030
CRDS	615	0.1	0.11
CRDS	Dual	0.1	0.068
CRDS	615	1.0	0.044
CRDS	Dual	1.0	0.031
CRDS	615	2.0	0.087
CRDS	Dual	2.0	0.028

Having outlined several systematic errors, we can now explain the sensitivity analysis presented in Table 7.3. Firstly, we can compare the single-wavelength CEAS and CRDS measurements, both recorded in the 0.1 mm flow cell. We find that pH measurements recorded using CEAS are more accurate than pH measurements recorded using CRDS, which can be explained by a lower systematic error for the CEAS measurements compared to the CRDS measurements. Any bias in either concentration or uncertainty in the pathlength is removed in the dual-wavelength measurements carried out in the 0.1 mm cell, where a lower $\Delta\text{pH}_{\text{min}}$ is established, although the CEAS single-wavelength measurements still achieve a greater accuracy in this case.

Secondly, we can compare the single-wavelength CRDS measurements, recorded in 0.1 mm, 1 mm and 2 mm flow cells. The pH accuracy does not follow a simple trend with increasing pathlength, which indicates that there are systematic errors dominating over the expected improvement in accuracy which should arise for measurements carried out in longer pathlength cells. Measurements carried out in the 1 mm cell have the highest accuracy among the single-wavelength CRDS measurements, at $\Delta\text{pH}_{\text{min}}$ = 0.044. This can be explained by the improvement in accuracy of the simultaneous ringdown measurements compared to the alternate ringdown measurements.

Finally, we can compare the single-wavelength to the dual-wavelength CRDS measurements, recorded within the same flow cell. The pH accuracy is always better for dual-wavelength measurements compared to single-wavelength measurements, up to a factor of three times better for the 2 mm flow cell, which has the lowest $\Delta\text{pH}_{\text{min}}$ = 0.028. Effectively, carrying out a dual-wavelength measurement removes some of the systematic errors, and thus improves the accuracy. Thus, there is a noticeable improvement in $\Delta\text{pH}_{\text{min}}$ with increasing pathlength for the dual-wavelength measurements, as we would expect for absorption measurements.

It is worth noting that the pH electrode used to calibrate the pH samples has a stipulated precision of ± 0.01 pH units, which we find in reality to be closer to ± 0.03 pH units. This limits the sensitivity analysis carried out above. It is thus not possible to demonstrate the real power of cavity enhanced absorption measurements by comparison to such a low precision pH electrode. In addition, the pH detection limits quoted in Table 7.3 represent the total errors across the entire pH range of the indicator. An alternative method to estimate the precision which cavity enhanced absorption measurements may potentially achieve is to use the 3σ variation in either I_0 or τ_0 to define the minimum detectable change in absorbance using Equations 7.13 and 2.17, and then to convert this into a minimum detectable change in pH using Equations A.4 or A.6 for either single or dual-wavelength analysis. This value represents the detection limit that the technique can achieve under optimum conditions, as it only considers the uncertainty within the measurement of I_0 or τ_0.

A_0 or Q_0 can be calculated at the pK_{a} of the indicator, via rearrangement of Equation 7.6 or Equation 7.11 respectively, where $A_0 = \frac{\alpha l \text{Ind}_{\text{T}}}{2}$ and $Q_0 = \frac{e_2}{2}$, depending on whether the measurement was carried out using single or dual-wavelength analysis. The results from this sensitivity analysis are presented in Table 7.4. $\Delta\text{pH}_{\text{min}}$ calculated in this way is of course significantly lower than $\Delta\text{pH}_{\text{min}}$ calculated from the fit to the Henderson-Hasselbalch equation.

Firstly, we can compare the single-wavelength CEAS and CRDS measurements, both recorded in the 0.1 mm flow cell. We find that pH measurements recorded using CRDS are approximately five times more precise than CEAS measurements. This is primarily due to the lower uncertainty associated with CRDS measurements compared with CEAS measurements.

Secondly, we can compare the single-wavelength CRDS measurements, recorded in 0.1 mm, 1 mm and 2 mm flow cells. The pH precision improves with increasing pathlength, from 0.0099 pH units for the 0.1 mm flow

Table 7.4: Sensitivity analysis of each experiment, in terms of measurement precision. Method indicates either CEAS or CRDS measurements, Single/Dual λ indicates either single or dual-wavelength analysis, Flow cell / mm is the normal incidence pathlength through the flow cell, I_0 / arbitrary units is the average intensity value recorded in CEAS measurements, and τ_0 / ns is the average ringdown time recorded in CRDS measurements. The 3σ uncertainty (in percentage) is then provided based on the repeated measurement of either I_0 or τ_0 which resulted in the highest error, labelled 3σ and $\Delta\text{pH}_{\text{min}}$ is then the minimum detectable change in pH given the uncertainty within one measurement, given to two significant figures.

Method	Single/Dual λ / nm	Flow cell / mm	I_0 / arb. units or τ_0 / ns	3σ / %	$\Delta\text{pH}_{\text{min}}$
CEAS	615	0.1	10,498	2.4	0.056
CEAS	510	0.1	2,113	8.1	-
CRDS	615	0.1	113	0.60	0.0099
CRDS	510	0.1	112	0.61	-
CRDS	Dual	0.1	-	-	0.034
CRDS	615	1.0	106	1.1	0.0018
CRDS	510	1.0	107	1.1	-
CRDS	Dual	1.0	-	-	0.0059
CRDS	615	2.0	84.2	0.63	0.00078
CRDS	510	2.0	84.3	0.85	-
CRDS	Dual	2.0	-	-	0.0034

cell to 0.00078 pH units for the 2 mm flow cell. This occurs despite the drop in ringdown time observed as the absorption pathlength is increased, which arises because of the increased absorption and scattering losses in the solvent.

Finally, we can compare the single-wavelength to the dual-wavelength CRDS measurements, recorded within the same flow cell. The pH precision is actually higher for single-wavelength measurements, which would be expected for this sensitivity analysis as measuring two ringdowns at two different wavelengths increases the error associated with the dual-wavelength measurement compared to the single-wavelength measurement. However, as we have seen, the dual-wavelength data fit more closely to the theoretical Henderson-Hasselbalch equation. Thus, we can conclude that the dual-wavelength measurements are more accurate, while the single-wavelength measurements are more precise.

We finish this Chapter with a brief mention of the possibilities of extending the pH range, and the challenges associated with monitoring the pH of real water samples.

7.4.6 Increasing pH range

The sensitivity of a spectrophotometric pH measurement decreases as the pH increases or decreases away from the pK_{a} of the indicator. In order to improve the sensitivity across a wider pH range, mixtures of indicators can be used to extend the pH range. For example, the combination of phenol red and bromocresol green has been shown to allow for the determination of pH over the range 3.0 - 8.2 pH units, which would allow for both seawater pH and total alkalinity to be determined simultaneously [328, 335].

7.4.7 Real water sample measurement

In this preliminary investigation into cavity-based pH measurements, we have used laboratory standards and thus have avoided many of the problems associated with measurements on real water samples. A key drawback of spectrophotometric pH measurements is the pertubation of the sample pH that arises from the added indicator stock solution [184, 322]. This is one of the reasons that low indicator concentrations must be used, hampering short pathlength measurements. In addition, pH must be corrected for ambient temperature and pressure [184, 322], so simultaneous measurements of all three parameters should be made when performing *in situ* measurements. An additional concern is the pH scale to be used. In this Chapter, we have used the standard pH scale, which is valid for solutions of zero ionic strength dominated by a single ion activity, that of the hydrogen ion. In real water samples, such as seawater samples, alternative pH scales are used, in order to account for the ionic strength of the water samples. For example, the activity of the solution can be defined with respect to hydrogen sulphate, as well as the hydrogen ion, which helps to account for the fact that at low pH, some H^+ is bound to sulphate ions [184].

7.5 Conclusion

In this Chapter, we have compared the pH sensitivity of single and dual-wavelength CEAS and CRDS and found dual-wavelength CRDS measurements carried out in the 2 mm flow cell to be most accurate. CRDS is preferable to CEAS when using a supercontinuum light source at lower wavelengths, owing to the reduced stability of the light source around 510 nm, although at 615 nm both methods have a similar accuracy. We have investigated flow cells with pathlenghs from 0.1 mm to 2 mm, and have measured pH with a sensitivity of 0.056 - 0.00078 pH units. Further improvements to the sensitivity can be achieved by the use of higher reflectivity mirrors, which would increase the total effective pathlength for each experimental set-up.

Chapter 8

Fibre-loop cavity ringdown spectroscopy: Instrumentation

"We require a coupler that has a low insertion loss, while transferring at least 0.5% of the intensity into the loop. Insertion losses due to the coupler have to remain under 20% per round trip, because high losses decrease the ringdown time of the system and therefore the sensitivity of the absorption measurement. Efficient coupling to the core of the fiber and not to the cladding is also important"
H. Waechter, K. Bescherer, C. J. Dürr, R. D. Oleschuk and H.-P. Loock, Anal. Chem., Vol. 81, 2009 [336].

8.1 Introduction

As we have seen, cavity ringdown spectroscopy (CRDS) is a highly sensitive spectroscopic technique which has been most commonly used in a two-mirror set-up for measuring weak absorptions of trace gas species [1, 152]. Indeed, the use of two-mirror cavities has reached maturity over the last few decades. However, interesting cavity innovations continue to emerge, particularly in the area of small volume liquid sample analysis [143, 159]. In particular, there has been significant interest in the development of alternative types of cavity, fabricated from optical fibres. There are two types of fibre-optic based cavities, employing linear and loop configurations, respectively (Figure 8.4). These cavities will be discussed separately below.

In our case, the use of optical fibres for microfluidic analysis is attractive because of the inherent size-matching of optical fibres (core diameters usually less than 500 μm) and microfluidic channels (dimensions of a few hundreds of micrometres). However, as we shall see, the cavities tend to have a much lower finesse than the two-mirror cavities used previously, and thus their compact and robust nature is offset

by the significantly poorer detection limits achieved in these types of cavities. In contrast, it is thought that optical fibre cavities can more easily probe the smallest sample volumes, even down to picolitre volumes. It should be noted that fibre-loop measurements are not restricted to chemical analysis [273], which will be the focus of this work. Indeed, they also find application in the measurement of physical parameters such as pressure [337], temperature [338], stress [339] and refractive index [340]. A general discussion of the fibre-loop CRDS approach, its current status and possible future developments, can be found in [86]. Waechter et al. recently provided an excellent review of chemical sensing using fibre-loop CRDS, including a description of the different types of sensor heads that can be used [273].

We begin by describing some of the key properties of optical fibres.

8.1.1 Optical fibres

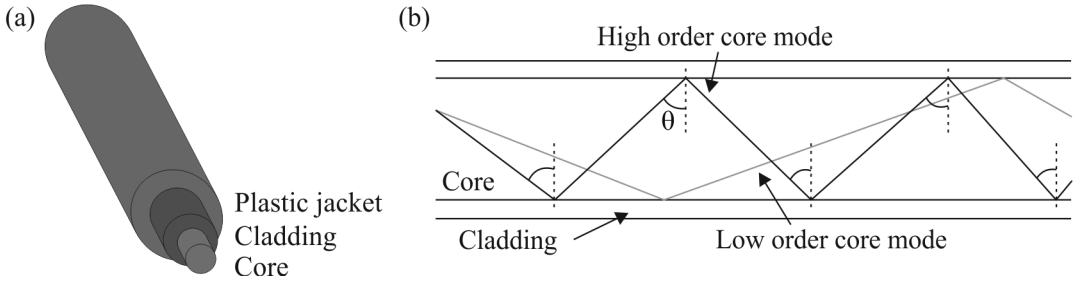


Figure 8.1: (a) Structure of an optical fibre. (b) Illustration of high and low order modes of light propagation along an optical fibre. The angles are typically small, and are exaggerated here for clarity.

A typical optical fibre consists of two layers of fused silica, the core and the cladding, with the cladding fluorine doped to give it a slightly lower refractive index than the core. A plastic outer jacket (in our case fabricated from clear acrylate) gives the otherwise fragile glass optical fibre a good degree of mechanical strength. A schematic of an optical fibre (not to scale) is shown in Figure 8.1(a). Propagating light is trapped within the fibre core by total internal reflection (TIR), which occurs when light travelling through the fibre is incident on the core/cladding boundary at an angle greater than the critical angle, θ_c from the surface normal. The critical angle for a particular interface is defined by Snell's law

$$\theta_c = \sin^{-1} \frac{n_{\text{clad}}}{n_{\text{core}}} \tag{8.1}$$

where n_{clad} and n_{core} are the refractive indices of the cladding and the core. The fused silica optical fibres employed in the work to be described in this chapter have $n_{\text{core}} = 1.461$ and $n_{\text{clad}} = 1.444$ at 532 nm, and thus the critical angle for total internal reflection to occur at the core/cladding boundary is $\theta_c = 81.25 \approx 81°$. Light will therefore be guided in the fibre core if it strikes at an angle smaller than $9°$ to the fibre axis. This angle $90 - \theta_c$ is sometimes referred to as the complementary critical angle, $\bar{\theta}_c$ [341].

In our experiments, we use step-index multimode fibres, with fibre core diameters ranging from 50 to 365 μm. Multimode fibres can support a large number of fibre modes, ranging from light propagating directly along the fibre axis (the lowest order core mode) to light reflecting at the core/cladding boundary at an angle to the surface normal equal to θ_c (the highest order core mode). Schematic illustrations of a low and high order core mode are presented in Figure 8.1(b).

Snell's law can also be used to define the acceptance cone for light entering the optical fibre, as well as light exiting the fibre end, by applying Snell's law to the refraction that occurs at the input/output face of the fibre, given $n_{\text{surr}} \sin\theta_a = n_{\text{core}} \sin\bar{\theta}_c$, where n_{surr} is the refractive index of the surroundings and θ_a is the acceptance angle (Figure 8.2). If the fibre end is in air, $n_{\text{surr}} = 1$. The right-hand side of the equation can be rearranged as follows:

$$\sin\theta_a = n_{\text{core}} \sin\bar{\theta}_c = n_{\text{core}} \sqrt{1 - \cos^2\bar{\theta}_c} = n_{\text{core}} \sqrt{1 - (n_{\text{clad}}/n_{\text{core}})^2} = \sqrt{n_{\text{clad}}^2 - n_{\text{core}}^2}.$$

Thus, the acceptance angle of the fibre core is defined as:

$$\theta_a = \sin^{-1}\text{NA} \tag{8.2}$$

where $\text{NA} = \sqrt{\text{n}_{\text{clad}}^2 - \text{n}_{\text{core}}^2}$ is the numerical aperture of the fibre [341]. The various angles referred to above are shown in Figure 8.2. Fibres with a larger NA have a larger cone of acceptance angles. This is useful for facilitating light coupling into the fibre core. However, light will also diverge more rapidly out of a fibre with a larger NA. This situation is depicted in Figure 8.2. Typical NAs for multimode optical fibres range from 0.10 to 0.48. All the optical fibres used in this Chapter have a numerical aperture of 0.22.

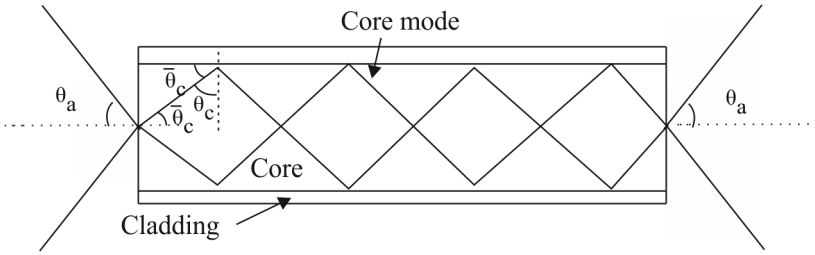


Figure 8.2: Schematic of a length of fibre, illustrating θ_c, $\bar{\theta}_c$ and θ_a. The angles are exaggerated for clarity.

One significant attraction of fibre cavities compared with two-mirror cavities is that since they rely on total internal reflection rather than dielectric mirrored surfaces to confine the light, they are capable of supporting light over a large wavelength range. While conventional high reflectivity CRDS mirrors can typically reflect light over a bandwidth of around 10% of the central optimised wavelength (for example from 495 nm - 605 nm if the central mirror reflectivity is 550 nm) fibres can transmit a much wider range of wavelengths. In this case, the cavity losses arise primarily from the inherent absorption of the fused silica fibre core, which may

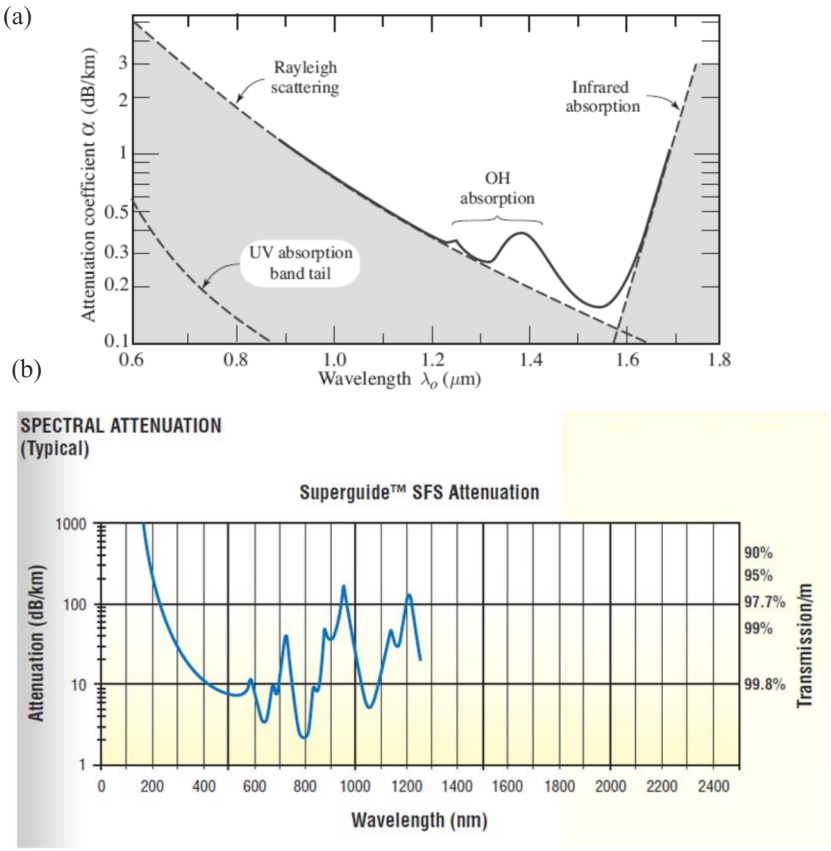


Figure 8.3: (a) Attenuation coefficient of silica glass versus wavelength. Reproduced from [341]. (b) Attentuation coefficient versus wavelength for UV/vis optimised optical fibre used in our experiments. Reproduced from Fiberguide Industries website, www.fiberguide.com.

be larger in certain wavelength regions (see Figure 8.3). Waechter et al. have previously used the broadband abilites of a fibre-loop cavity to support light at both 405 nm and 810 nm [342].

8.1.2 Linear fibre CRDS

Linear fibre CRDS measurements use a length of fibre with either mirrors [343–345] or fibre Bragg gratings [346] at either end to confine the light in the cavity, in a direct analogue to the two-mirror approach. In this case, the plastic coating is stripped from a short section of fibre core, and the fibre is tapered by heating and pulling or by etching in hydrofluoric acid, so that the evanescent field of the light travelling in the core is exposed to the surroundings (Figure 8.4(a)). By immersing the tapered region in a liquid sample, absorption measurements can be made. As far as we are aware, direct absorption measurements, carried out by introducing a gap between two fibre ends, have not been carried out in a linear fibre cavity. This is primarily because the evanescent field measurements allow a lower loss cavity to be maintained, albeit at the expense of reduced interaction of the light with the sample on each pass.

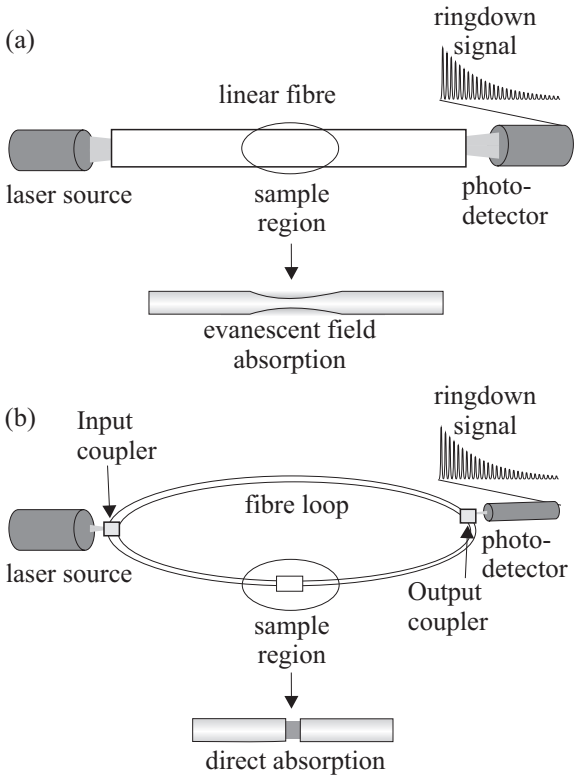


Figure 8.4: (a) Linear fibre cavity, with either mirror-coated fibre ends of fibre Bragg gratings used to confine the light in the fibre length. (b) fibre-loop cavity, with input and output coupling into the side of the optical fibre.

8.1.3 Fibre-loop CRDS

Fibre-loop CRDS has a potentially simpler experimental scheme than linear fibre CRDS: simply by taking a length of fibre and aligning the two ends together to form a loop, a cavity is created without the need for depositing high reflectivity coatings or fabricating Bragg gratings. The gap between the two fibre ends is an obvious place to introduce liquid directly to the propagating fibre core modes (Figure 8.4(b)). The challenge in this case becomes the side-coupling of light in and out of the optical fibre-loop, which will be discussed in more detail in Section 8.1.6.

The first fibre-loop CRDS experiment was reported by Stewart et al. in 2001 [347]. In their set-up, a 58 m fibre-loop was used, which incorporated a 5 cm open path micro-optical gas cell. The insertion loss of the micro-optical cell was high (around 20% loss per pass), so in order to improve the sensitivity of their measurements, Stewart et al. included a length of erbium-doped fibre which acted as an amplifier to overcome some of the unwanted round-trip losses and improve the ringdown time, and therefore the sensitivity to absorption by a gas sample introduced into the optical cell. While the ringdown time can thus be increased from around 100 ns to several tens of microseconds, the limiting factor for sensitive absorption measurements in this set-up becomes the stability of the amplifier. Improving the amplifier stability is not a trivial exercise

Table 8.1: Chronological summary of liquid-phase fibre-loop CRDS techniques. λ is the wavelength, d_{fc} is the fibre core diameter, l is the pathlength, Vol. is the volume of liquid probed, $C_{\min}$ is the minimum detectable concentration, $\kappa_{\min}$ is the minimum absorption per unit pathlength and N_τ is the number of round-trips in one ringdown time.
Where several analytes were measured, the stated detection limit corresponds to detection of the first listed analyte. Where possible, concentration detection limits have been calculated from three standard deviations (3σ) of the reported baseline noise, but limits marked with * have been estimated using other reported data.
Unmarked references represent pulsed fibre-loop CRDS. References marked $^+$ represent phase-shift fibre-loop CRDS.
**DDCI is an abbreviation of the dye 1,1'-diethyl-4,4'-dicarbocyanine iodide. Dyes AWS805DS and ADS830WS are available from American Dye Source, Inc.

Ref.	Analyte	λ / nm	d_{fc} / μm	l / μm	Vol. / nL	$C_{\min}$ / μM	$\kappa_{\min}$ / cm^{-1}	N_τ
Brown et al. [271]	DDCI**	825 450 - 900	50	3.8	0.0074	250*	100	11
Tong et al. [349]	DDCI**	810	400	47	0.70	200*	67	4
Tong et al.$^+$ [351]	DDCI**	810	400	42	5	30*	10	-
			100	31	0.24	15*	5	-
Li et al.$^+$ [352]	AWS805DS**	810	100	10	0.079	50*	18	2
				25 (Lens)	0.20	10*	4	2
Andachi et al. et al. [350]	Methylene blue	660	50	100	0.2	50*	6	2
Waechter et al.$^+$ [336]	Tartrazine	405	200	190	6	5	0.25	3
Waechter et al.$^+$ [342]	Tartrazine	405	400	800 (Lens)	100	0.9	0.046	2
	ADS830WS**	810				1	0.12	-

and tends to complicate the experimental set-up [348].

The first example of passive or non-amplified fibre-loop CRDS was published by Loock and coworkers in 2002 [271]. Round-trip losses were kept to a minimum: when the two fibre ends were joined together using a commercial fusion splicer, a ringdown time of 900 ns was measured for a 12 m fibre-loop, corresponding to a round-trip loss of 6.3%. When the fibre ends were separated by a small gap (3.8 μm), the ringdown time was reduced to around 625 ns, corresponding to a round-trip loss of 8.9%. Unfortunately, while the loss is minimised by keeping the gap small, this results in lower sensitivity measurements: in one ringdown time, a total pathlength of only 41.8 μm is sampled. In later experiments, Loock and coworkers moved to larger core optical fibre, with larger gaps and hence higher round-trip losses, leading to a low number of passes in one ringdown time (only 2 – 4), see for example [349, 350]). The output from Loock and coworkers is summarised in Table 8.1.

8.1.4 Phase-shift CRDS

A related technique, suggested by Engeln et al. in 1996 for two-mirror CRDS [353], and by Tong et al. in 2004 for fibre-loop CRDS [351] is to use an intensity-modulated continuous-wave light source rather than a

pulsed light source, which allows for reduction in experimental complexity, and also an increase in sampling rate, similar to CEAS. A phase-shift is induced between the intensity-modulated input beam and the cavity output. It can be shown that this phase-shift ϕ is proportional to the ringdown time and the angular modulation frequency ω:

$$\phi = -\arctan(\omega\tau) \tag{8.3}$$

and thus absorption measurements can be made in a similar manner to pulsed fibre-loop CRDS. Phase-shift analysis allows for the measurement of signals in high loss regimes, for which the accurate determination of the short ringdown time would be difficult. Additionally, Waechter et al. have recently demonstrated the independent intensity modulation of two different wavelengths, thus expanding the capabilities of this technique greatly [342], as well as nicely taking advantage of the broadband nature of a fibre-loop cavity. Unfortunately, it seems that moving away from pulsed fibre-loop CRDS to phase-shift fibre-loop CRDS, while lessening the need to work in lower-loss regimes for the purposes of determining the ringdown time, has disguised the fact that the number of passes recorded in one ringdown time in these systems is very low (only 2 or 3). One problem is that long fibre-loops are needed for highest sensitivity (when $\omega = 1/\tau$ [351]), and thus absorptions in the fibre core are significant. Nevertheless, if lower loss set-ups are employed, phase-shift fibre-loop CRDS could be a good alternative to pulsed fibre-loop CRDS.

8.1.5 Round-trip losses in fibre-loop CRDS

In our case, we are interested in characterising the losses associated with various fibre-loop CRDS set-ups, and thus we focus our attention on pulsed ringdown experiments, in which the loss (and number of passes) is easier to visualise in the unprocessed ringdown signal. We aim to carry out a full characterisation of the losses inherent in a fibre-loop CRDS set-up, and then to work systematically towards reducing the losses of each individual optical component, in an attempt to improve the sensitivity of this technique.

In a fibre-loop experiment, losses arise from:

- couplers used to couple light into and out of the fibre-loop;
- splices (joins) in the loop, whether fusion spliced or mechanical;
- the sample region, whether based on direct or evanescent-wave absorption;
- intrinsic absorption by the fibre core medium, which will increase as the cavity length increases, and as the wavelength gets shorter.

If we compare this to a conventional two-mirror gas-phase cavity, we can immediately see why the losses in a fibre-loop cavity are significantly higher: in a two-mirror cavity, the losses arise from the imperfect reflectivity

of the mirrors, and can be as low as 0.01% or better. In the two-mirror CRDS and CEAS measurements described in Chapters 3 - 7, we used mirrors with modest reflectivites from 99% - 99.8%, as our losses in a liquid-phase measurement also arise from the inserted absorption cell, which may have a loss of 0.2% - 1%. In contrast, every optical element inserted into a fibre-loop cavity is likely to occasion losses of a few percent. In particular, the process of side-coupling light into a looped fibre cavity is one which we feel has not been optimised to date.

The two main drawbacks of fibre-loop CRDS should be emphasised. The first is common to both fibre-loop and two-mirror CRDS experiments, namely that because of the need to retain low losses on each cavity round-trip, only a small amount of light can be coupled into or out of the cavity on each pass. This means that a high-power light source (typically a laser) and a sensitive detector (typically a photomultiplier tube) are normally required. The second drawback is more specific to fibre-loop CRDS, and involves the high loss inherent in a fibre cavity system relative to a two-mirror set-up. This is partly owing to the difficulty associated with coupling light into the side of an optical fibre without introducing high losses, as well as to the high losses associated with introduction of a sample region to the fibre-loop cavity.

8.1.6 Light coupling

In the first pulsed fibre-loop CRDS experiments [271], light from a Nd:YAG-pumped dye laser was coupled into and out of the fibre-loop by bending the optical fibre at two different positions and exploiting the resulting macrobending losses. Loss of light from an optical fibre on bending is a well known phenomenon, and has even been characterised in fibre-based CRDS measurements [343, 345, 349]. When an optical fibre is bent, some of the light travelling in the fibre core no longer strikes the core-cladding boundary at an angle greater than or equal to the critical angle θ_c required for total internal reflection to occur. When the critical angle for a fibre core mode is exceeded, this light is instead refracted through the cladding, and may be detected as output signal from a fibre-loop cavity. Conversely, if a tight bend is illuminated at a suitable angle, then light can also be coupled into the fibre core.

Bend coupling is inherently inefficient: Loock's group reported a coupling fraction of 10^{-8} when coupling light into the loop and 10^{-4} when coupling out using 3 cm bends in a loop of 50 μm core diameter optical fibre [271], and the coupling losses themselves were significantly higher, since light was lost in all directions from the bend. Coupling efficiency can be improved by using tighter bends, but at the cost of higher round-trip losses.

An alternative coupling strategy is to use commercially-available evanescent field couplers, although these are also relatively inefficient, and often occasion higher insertion losses than expected. In addition, these couplers are relatively expensive and work to specification only near a specific design wavelength. Lehmann and coworkers used two input/output couplers with a splitting ratio of 99%/1%, and found round-trip losses

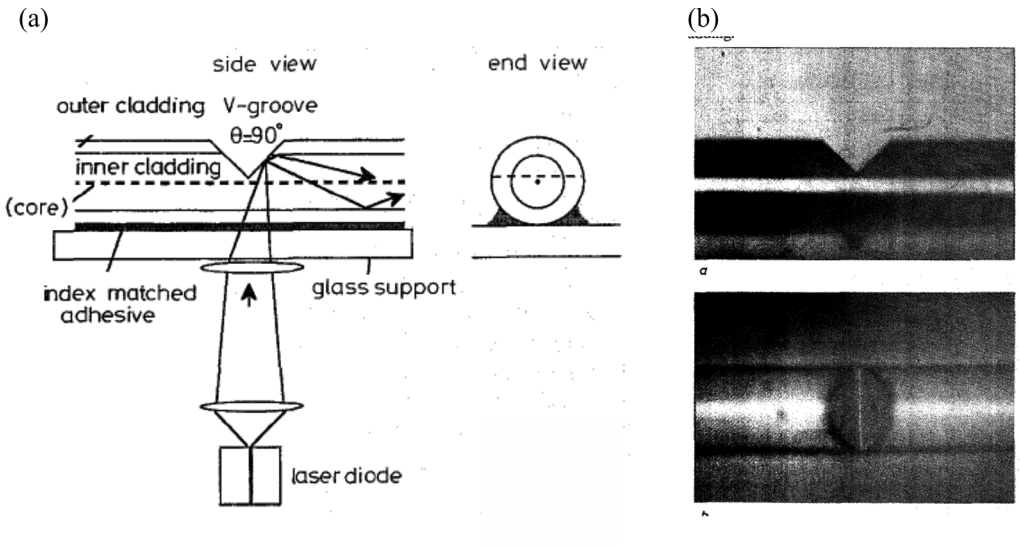


Figure 8.5: Side-coupling of light. Images reproduced from Ripin and Goldberg, Electronics Letters, Vol. 31, No. 5, 1995 [355]. (a) Fibre V-groove configuration and experimental arrangement. (b) Photographs of imbedded V-groove in 140 μm outer diameter optical fibre. Inspection of the V-groove facets revealed an optically smooth finish, and a rounding radius of less than l0 μm at the apex. Groove depth and width were 60 μm and 120 μm respectively.

of around 13%, attributed to losses from the two couplers, the four splices required to insert the couplers into the loop, and the sample region (an optical fibre taper) [354].

Waechter and coworkers recently made the fairly modest suggestion that coupling 0.5% of the initial source light into the cavity, and keeping coupling losses below 20% represent desirable design parameters [336]. To achieve this, they designed a custom interface for sending light into the fibre-loop. In their interface, a single-mode fibre-coupled laser was aligned at a shallow angle (6°), with a large (190 μm) gap in a loop of 200 μm core diameter optical fibre. Light was thus coupled into the fibre-loop through one of the fibre ends, albeit with relatively low intensity, and out-coupled at a large bend (8 cm radius). Round-trip gap losses totalling 23% were found, with an additional 10% loss from fibre absorption at 405 nm.

The telecommunications literature provides a helpful source of inspiration for improving the light-coupling methods used in fibre-loop CRDS. Side-coupling of light into an optical fibre is important for a variety of applications. It has been used most extensively in fibre lasers, where side-coupling of pump light into the inner cladding of a double clad optical fibre is advantageous for (a) increasing the maximum power that can be coupled into an optical fibre and (b) increasing the number of pump light sources that can be coupled into an optical fibre [355]. Additionally, side-coupling may be necessary because of the absence of free optical fibre ends through which to introduce light, for example in fibre ring lasers [356] and, as we have seen already, in fibre-loop cavity-based spectrometers [271]. High-efficiency side-coupling of light into and out of the cavity, while minimising the loss per pass within the cavity itself is, in these cases, a requirement.

By far the most commonly used side-coupling technique is that developed by Ripin and Goldberg, who cut a

90° V-groove, shown in Figure 8.5, into the inner cladding of a double clad fibre, and obtained a single-mode laser diode coupling efficiency of 96%, taking advantage of the total internal reflection (TIR) at the uncoated groove [355]. Such a coupler achieves excellent coupling efficiency into the fibre, and can also be designed to minimise the round-trip losses associated with this coupler, as we shall see in Section 8.3.2.

8.1.7 Chapter outline

The aim of the work described in this Chapter and in Chapter 9 has been to develop a compact, low-cost, easy-to-operate fibre-loop CRD spectrometer for applications in microfluidics and chemical sensing. Such an instrument must necessarily employ a relatively low energy laser source, and in order to optimise our signal levels, we ideally require a highly efficient means for side-coupling light into our fibre-loop. In this Chapter, we examine the various components of a fibre-loop CRD spectrometer in detail, including an improved light-coupling method. We also examine the fabrication of both direct and evanescent wave absorption set-ups. A comparison between the results obtained from each set-up is provided in Chapter 9.

8.2 Instrumentation

Optical fibres with an absorption minimum in the visible region of the spectrum ($\kappa_{\mathrm{f}} = 0.00345$ m^{-1} at 532 nm, taken from the manufacturer's specification) were chosen for this work. The cavities, fabricated from either 50 μm core diameter optical fibre (SFS50/125Y, Fiberguide Industries), 105 μm core diameter optical fibre (SFS105/125Y, Fiberguide Industries) or 365 μm core diameter optical fibre (BFH22-365, Thorlabs) will be discussed separately below.

8.2.1 Light source and detector

The light source used was a frequency-doubled Nd:YAG laser (NP-10620-100, Teem Photonics) which produces 0.9 ns, 6 μJ pulses of 532 nm light at a repetition rate of 7.4 kHz. The laser light is focused onto the fibre coupling region using a lens with a focal length of 20 cm. In the case of the small-core fibre, light from the output bend coupler is detected directly by a photomultiplier tube (PMT, H10304-06-NF, Hamamatsu), while for the large-core fibre-loop, output light from the notch coupler is directed to the PMT through a 3 mm diameter liquid lightguide (NT53-428, Edmund Optics). In a fibre-loop cavity, side-coupling injects light into both the core and cladding of the optical fibre. The short-lived cladding modes often dominate the desired core mode signal at early time delays after initial cavity excitation. Consequently, we time-gate the PMT to cut out the first part of the ringdown signal. Typically, we start data

acquisition 300 - 500 ns after the initial laser pulse has entered the cavity, when the cladding modes have decayed to negligible levels.

8.2.2 Data acquisition and analysis

The ringdown signal from the PMT signal is visualised on an oscilloscope (either TDS 2024 or TDS 3044B, Tektronix), which is interfaced to a personal computer via a GPIB-USB interface (778927-01, National Instruments). For the small-core fibre, ringdown traces were averaged 128 times on the oscilloscope, transferred to the PC and analysed after acquisition, whereas for the large-core fibre, ringdown traces (averaged 512 times on the oscilloscope) were acquired and analysed continuously using a home-written LabVIEW program (National Instruments, 2010). Data acquisition is currently limited to 4 traces per second by the relatively slow data transfer rate from the oscilloscope to the computer. The ringdown time of each recorded trace is determined separately, and the values are averaged to give a final value for τ. Typically, 30 traces are acquired from the oscilloscope for each τ measurement.

Example ringdown traces for bend-coupled fibre-loop CRDS set-ups are presented in Figure 8.6. Since the laser pulse is significantly shorter than the round-trip time of the fibre-loop cavity, the optical signal detected at the cavity output coupler consists of an exponentially decaying train of pulses. Owing to the presence of rapidly decaying cladding modes and the somewhat non-linear response of the gated PMT during the rising edge of the signal gate, the first part of the recorded ringdown trace is generally not exponential, and is therefore not fitted in the data analysis. The fitted regions of the curves are indicated in Figure 8.6. Once the user has defined the region of the trace to fit and the noise threshold, a peak finding algorithm is employed in order to determine the amplitude S of each pulse in the ringdown pulse train. The ringdown time may then be determined from the slope of a log plot of the pulse amplitudes versus time, i.e. $\ln S = \ln S_0 - \frac{t}{\tau}$. A least squares fit to the slope is carried out, and we obtain typical R^2 values over 99.8%, generally fitting to 20 - 80 data points.

8.3 Light coupling

8.3.1 Bend-coupled fibre-loop CRDS

In the first set of experiments, using 50 μm fibre and 105 μm core diameter optical fibre, bend couplers were used to couple light into and out of the loop (Figure 9.1(a)) [357]. Custom-made poly(methyl methacrylate) (PMMA) couplers were fabricated, in which the fibre is clamped between a cylinder of radius 9 mm and a prism designed to direct light into and out of the bend at the appropriate angle (shown to the right of Figure 9.1(a)). It is important to clamp the fibres very gently into the couplers to preclude losses caused

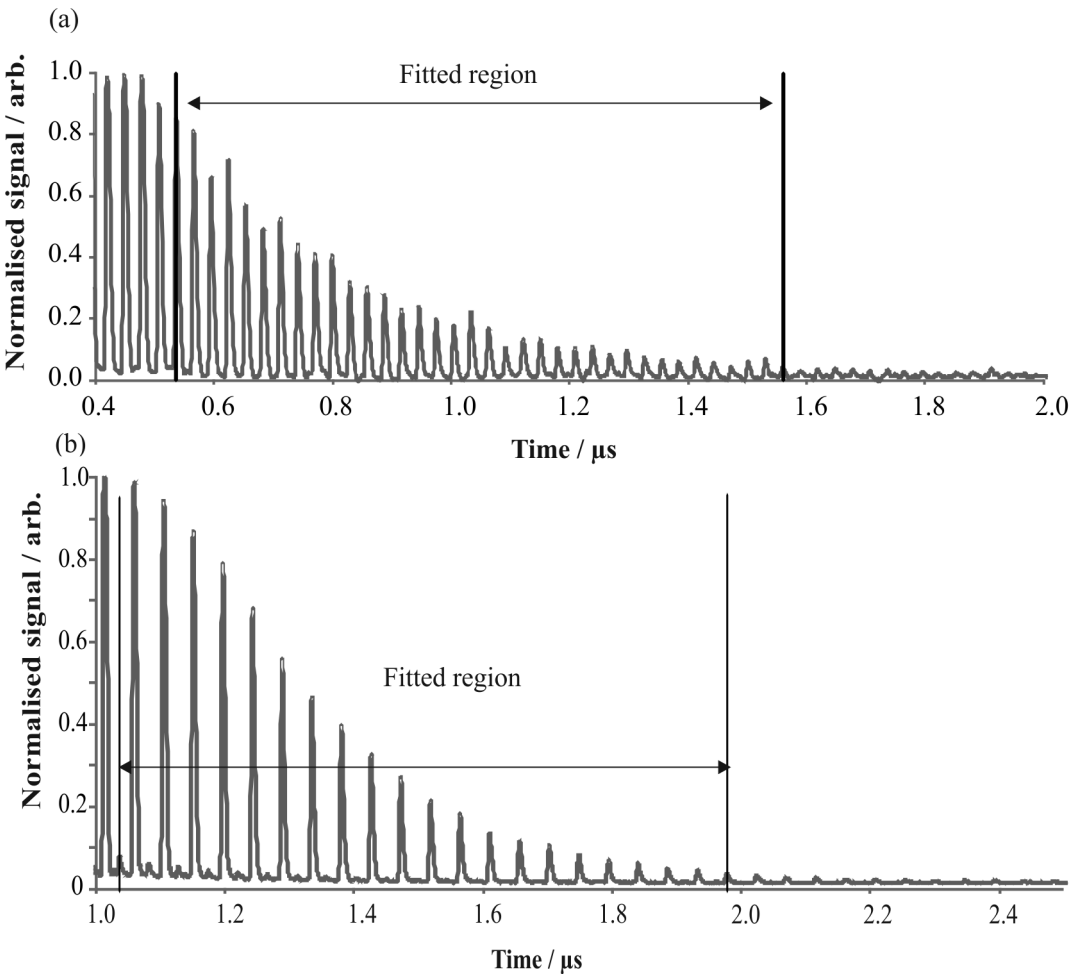


Figure 8.6: Typical ringdown signals obtained in fibre-loop CRDS, before introduction of a sample region. The non-exponentially decaying signal at short time is eliminated from the data analysis, as indicated. (a) Bend-coupled small-core fibre, fusion spliced: τ = 332 ns and d = 5.97 m. (b) Bend-coupled 105 μm core diameter fibre, fusion spliced: no end separation: τ = 225 ns and d = 9.44 m.

by the application of undue pressure at the bend regions. It should be restated that slacker bends (with lower insertion losses) have been used in the literature, but for our experiments with laser pulse power in the μJ rather than mJ range, we require tighter bends in order to couple enough light into the loop to yield a measurable signal.

The 9 mm bends used in these experiments caused a macrobending loss of about 2 - 3.5% per coupler, leading to a baseline loss of 4 - 7% per pass from the couplers alone once an input and output coupler were introduced into a fibre-loop comprising 50 μm core diameter optical fibre. Tighter bends result in higher coupling efficiency, and therefore increased signal levels, but at the cost of increased loop losses, and the bend radius chosen for these experiments was the best compromise between these two factors for the laser source and detector employed.

For a given bend radius, the increase in macrobending loss with increasing fibre core diameter is

well-known. For example, we have recorded ringdown signals for bend-coupled 105 μm core diameter optical fibre (SFS105/125Y, Fiberguide Industries) in the same way as discussed above, and found the coupling losses to be much higher than for 50 μm fibre, at around 15%. An example ringdown trace for bend-coupled 105 μm core diameter optical fibre is shown in Figure 8.6(b). We are interested in moving to even larger core diameter optical fibre because of the increased ease of handling and alignment in fibre-loop CRDS experiments, which will make the set-up more robust. However, the bend-coupling losses for 365 μm core diameter would be significantly higher than those reported for 105 μ core diameter optical fibre. These high losses mean that for our purposes, bend-coupling is not appropriate for large-core diameter fibre-loop cavities.

8.3.2 Design of a novel light-coupler

As we have already discussed in Section 8.1.6, a common side-coupling technique, which has not yet been applied in fibre-loop CRDS, is that developed by Ripin and Goldberg, who cut a 90° V-groove, shown in Figure 8.5 and Figure 8.7(a), into the inner cladding of a double clad fibre, and obtained a single-mode laser diode coupling efficiency of 96%, taking advantage of the total internal reflection (TIR) at the uncoated groove [355]. For low loss, unidirectional coupling of light (for example, in a ring fibre cavity), the fabrication of a 45°, notch as shown in Figure 8.7(b) is preferable to a V-groove. By mirroring the 45° angle surface, the notch coupler can be used as both an input and an output coupler to a fibre-loop cavity. This is represented in Figure 8.7(c). The fabrication and selective mirroring of such a notch in the side of an optical fibre is difficult, and we therefore use a slightly different approach to simplify the problem, as illustrated in Figure 8.7(d). The reflective notch is fabricated in the side of an optical fibre end, and a second, non-mirrored fibre end is aligned with the notched end to create the input/output coupler. Refractive-index matching across the gap using either a suitable liquid or adhesive effectively splices the two fibre ends together, resulting in minimal insertion losses for the device.

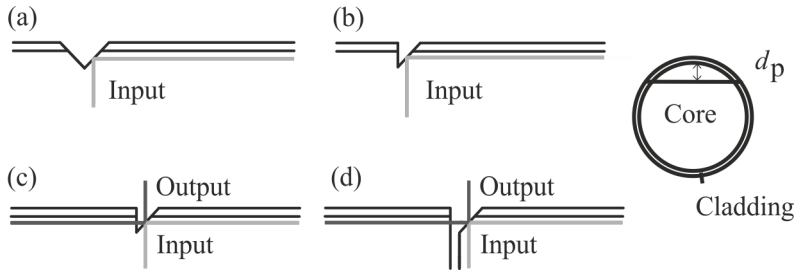


Figure 8.7: Approaches to side-coupling into optical fibres. (a) Embedded 90° V-groove. (b) Embedded 45° notch. (c) Reflective 45° notch. (d) Simple reflective 45° notch fabrication in a fibre end. Inset: end view of (d), where d_p is the penetration depth of the notch.

The new coupler extends the use of prism-based side-coupling into optical fibres from double clad fibres to single clad fibres. Crucially, for fibre-loop-based devices in particular, the reflective notch coupler can

function as a spatially separating input and output coupler. Light is coupled into the core from one side of the fibre, and a fraction of light already propagating in the core is coupled out in the opposite direction from that coupled in. The out-coupling is completely controlled simply by choosing the penetration depth of the notch to achieve the desired coupling ratio, defined using simple geometry and assuming a uniform distribution of light in the fibre core.

For a perfect notch, the output coupling efficiency, or loss at the notch L, is simply given by the fractional area of the core taken up by the notch. Defining $f = \frac{d_p}{r}$ as the fractional penetration of the notch into the fibre, with d_p the penetration depth and r the radius of the fibre core), straightforward trigonometry shows L to be:

$$L = \frac{100}{\pi}[\cos^{-1}(1-f) - (1-f)\{f(2-f)\}^{\frac{1}{2}}] \tag{8.4}$$

We have carried out simulations of the notch coupler acting as a fibre beamsplitter using the Zemax optical modelling software suite. Zemax is an optical ray-tracing program which is commonly used for optical design and tolerance analyses [358]. In the simulations, 400,000 analysis rays are launched from a fibre-coupled divergent source, whose angle of divergence (9°) matches the maximum acceptance angle of our optical fibre. This provides a fairly realistic mode picture of the fibre, so that the range of propagation angles of light escaping from the notch is modelled correctly.

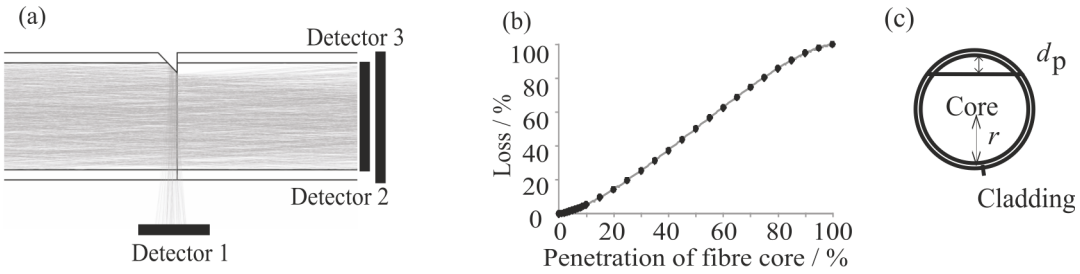


Figure 8.8: (a) ZEMAX simulations of light coupling out from notch, assuming multimode propagation of light in the core. (b) Percentage of light coupled out from the fibre core as a function of percentage penetration into the core. The x-axis is plotted as $\frac{d_p}{d}$ and thus is equal to one half of $f = \frac{d_p}{r}$ used in Equation 8.4. Solid points are the results of Zemax ray tracing simulations (Equation 8.5), and the solid line is a plot of (Equation 8.4). (c) End view of notch penetration, where d_p is the penetration depth and r is the radius of the fibre core.

The detectors labelled 1, 2 and 3 in Figure 8.8(a) are used in the software for the quantitative determination of output coupling efficiency, plotted in Figure 8.8(b) as a function of notch penetration depth. Detector 1 measures the amount of light lost at the notch, Detector 2 measures the amount of light remaining in the fibre core after the notch, and Detector 3 measures the small amount of light which travels in the cladding. The percentage of propagating light L that is coupled out of the fibre is determined from the signals D1, D2 and D3 recorded at the three detectors:

$$L = \frac{D_1}{D_1 + D_2 + D_3} \times 100 \tag{8.5}$$

As shown in Figure 8.8(b), the results of the Zemax simulations are in almost perfect agreement with the predictions of Equation 8.4.

8.3.3 Fabrication of a novel light-coupler

Initial fabrication attempts used a 45° angle steel tool fabricated in Physical and Theoretical Chemistry workshops to attempt to 'score' or mechanically cut a notch into the side of the fibre. The tool was mounted on a side-arm above a translation stage controlled by a stepper motor. A length of optical fibre was glued onto a microscope slide, and then mounted on the translation stage. The stage was then moved slowly under motor control, as the tool contacted the optical fibre. The progress of cutting was monitored using a video microscope. Using this method, it was quickly established that steel was not a hard enough material for cutting the fused silica optical fibre: rather than cutting the fibre, the steel tool was observed to be 'shaved' off as it passed over the optical fibre. This was addressed by purchasing a custom-made carbide tool (Coventry Carbide), as carbide is hard enough to be used for cutting fused silica. The carbide tool required polishing using diamond lapping film (LFG3D, Thorlabs) before use, in order to ensure that the knife edge of the tool was sufficiently sharp. A significant amount of time was spent on optimising the cutting rate and the pressure applied by the tool on the fibre, which was controlled using weights. The resulting notches successfully coupled high light intensities into the loop. However, because of the lack of vertical resolution, the notch penetrated too far through the core and therefore coupled too much light out on each pass for a fibre-loop ringdown signal to be recorded. Additionally, this fabrication method resulted in a fragile fibre, likely to break at the score-point.

The improved notch fabrication method was developed using 365 μm core diameter, 400 μm cladding diameter optical fibre (BFH22-365, Thorlabs), although our strategy can easily be extended to other fibre types and sizes. The first step is to strip the soft jacket from the optical fibre using a fibre stripping tool (T18S31, Thorlabs) and then to cleave the optical fibre using a Shortix capillary cutter (21386-U, Sigma Aldrich). The cutter has a rotating diamond blade and is designed for cutting 0.3 - 0.78 mm fused silica capillary tubing at a 90° angle to the axis. The initial cleave ensures that the fibre end is cut at a 90° angle; however the end face quality resulting from this cleave is poor, and the fibre end face must be polished to ensure optical quality. We use a home-built polishing wheel to polish our optical fibre, with the fibre clamped in a home-built perspex mount, similar to that of Figure 3 in [359], and presented in Figure 8.9.

The optical fibre is polished on 0.1 μm diamond lapping film (693118SO, Buehler). After polishing, the end face is inspected under a trinocular microscope (BMSS Trinocular zoom, Brunel Microscopes) interfaced

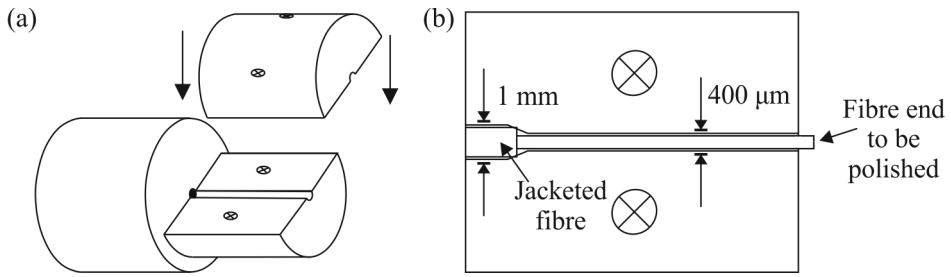


Figure 8.9: (a) Schematic of perspex mount used to clamp optical fibres during polishing processes (b) Dimensions of bare fibre clamp.

with a digital camera (P6000, Nikon), and the polishing step is repeated if necessary until the end face is flat and defect free (Figure 8.13(a)). This is the most critical stage of fibre preparation; if the fibre end is of poor quality, or not polished at $90°$ to the fibre axis, this will translate into significant losses in the finished coupler.

Once the fibre face has been prepared, the fibre is clamped in a second perspex mount at $45°$ to the polishing wheel and polished until the desired penetration depth d_p is achieved. Typically, this takes less than 30 seconds, and the fibre end is inspected frequently during this polishing step (Figure 8.13(b)). A deeper notch than required is fabricated as the penetration depth of the notch can be reduced at any point (typically the last step) simply by repolishing the fibre end face. Images of fibre polishing are shown in Figure 8.10.

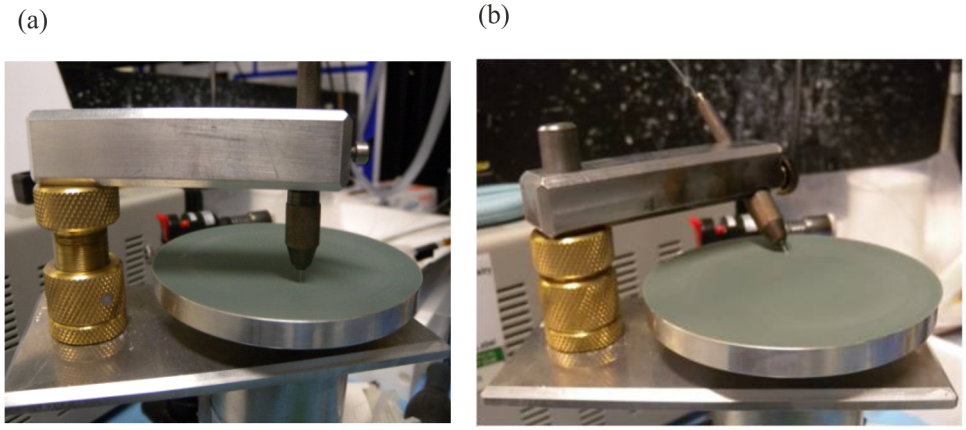


Figure 8.10: (a) Photograph of fibre being polished at 90° to the fibre axis. (b) Photograph of fibre being polished at 45° to the fibre axis. In these pictures the fibre is mounted in pin vices, but in the majority of the experimental work, fibres were actually mounted in Perspex clamps as shown in Figure 8.9.

The simple non-reflective notch that has been fabricated at this point may be used as a TIR input coupler, by directing light towards the notch at a near-normal angle to the fibre axis from the opposite side of the fibre to the notch (Figure 8.7(b)). TIR occurs above a critical angle of $43.2°$ at the glass-air boundary (the refractive indices of fused silica and air at 532 nm are 1.461 and 1.000 respectively). However, while the bare notch functions well as an input coupler, it does not perform well as an output coupler; rather than the light incident on the notch being reflected out of the fibre, the majority of the light incident on the non-reflective notch

refracts into higher order core modes or cladding modes. This may be overcome by coating the notch to form a reflective surface so that all light incident on the notch is coupled out of the fibre and detected.

The fibre end produced by the aforementioned process now has two surfaces: one angled at 45°, and the other perpendicular to the fibre axis. To produce the reflective microprism illustrated in Figure 8.13(d), we must mirror coat just the angled face, whilst leaving the perpendicular face optically transparent. Our solution is to prepare the angled surface such that an applied metal coating can form a chemical bond with the notch, but is only weakly adhesive to the untreated perpendicular surface. The metal coating can then be removed from the perpendicular face by a brief polishing step, whilst leaving the mirror surface on the angled surface intact.

Several metals were evaluated for use as a reflecting medium on the fibre surface. A high reflectivity at 532 nm is required, along with a mechanically strong bond between the metal and silica, as several polishing steps follow its application to the fibre. Gold and silver were the principal focus of this testing, as these metals show high reflectivity at the required wavelength. The wavelength-dependent reflectivities of a number of metals are shown in Figure 8.11.

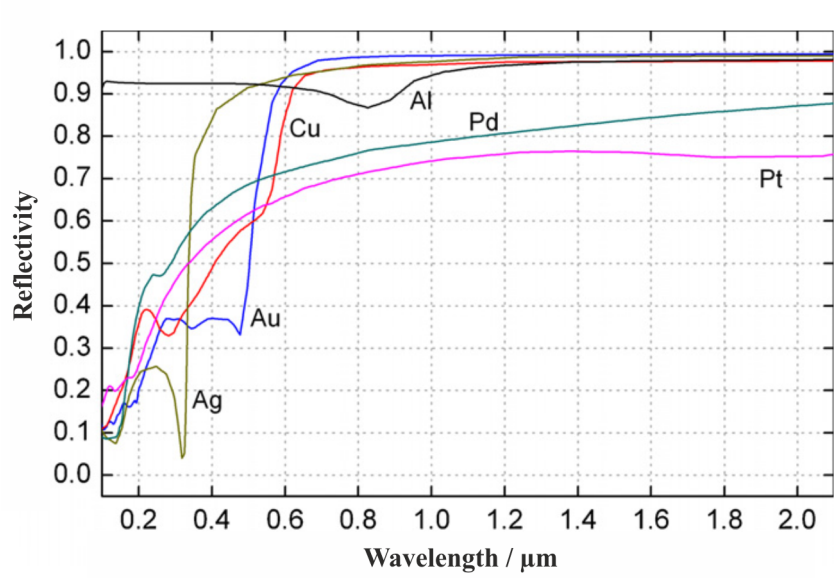


Figure 8.11: Reflectivity plotted as a function of wavelength for several metals. Image reproduced from Fabian, Lewis, Newe and Lochmann, Measurement Science and Technology, Vol. 21, No. 9, 2010 [360].

Techniques for bonding metal directly to glass are well-established [361]. Often, a chemical linking reagent is used. Such reagents typically contain a silane group at one end, which bonds to glass, and a nucleophilic group at the opposite end, which bonds to metal. In order to fabricate a reflective coating on the angled surface of our coupler, the notched fibre end was coated with two different linking groups: 3-(Mercaptopropyl)trimethoxysilane (3-MCP), a silane based reagent with a nucleophilic thiol group; and

VECTABOND (SP1800, Vector Laboratories), a proprietary silane-based reagent with a nucleophilic amine group.

To coat a fibre end with 3-MCP, it must be refluxed in a solution of 1 g 3-MCP, 1 ml deionized H_2O, and 40 ml 2-propanol for 10 minutes [361]. The fibre is then rinsed with 2-propanol, air dried, and cured in an oven at 100°C for 8 minutes. This process is then repeated twice more.

To prepare a fibre with a VECTABOND coated end, the VECTABOND is prepared according to the manufacturer's instructions. The fibre end is immersed in the resulting solution for 5 minutes, followed by rinsing with deionised water and air-drying.

After surface modification, the flat fibre end face is repolished briefly so that linking agent only remains bonded to the angled notch face, and not to the flat end face. This results in the metal coating being strongly bound to the coated notch, but only weakly adherent to the flat face.

Gold coated notches were prepared by placing the coated fibre in a gold sputter coater (Polaron SC7680), whereas silver was deposited onto the fibre end using a simple chemical redox reaction (Tollen's reagent method) to reduce silver nitrate [362]. In the Tollen's reagent method, concentrated ammonium hydroxide (255210025, Acros Organics) is added dropwise to 15 mL of 0.1 M $AgNO_3$ solution (38310, Sigma Aldrich) until the brown precipitate formed on first addition has dissolved. 7.5 mL of 0.8 M NaOH (BPE359, Fisher Scientific) is added to the solution, and additional ammonium hydroxide is added if the brown precipitate reforms. 1.5 mL of saturated glucose solution (G8270, Sigma Aldrich) is then added. The fibre end is held submerged in the solution for 3 – 5 minutes, followed by rinsing in deionised water and air-drying. Figure 8.13(c) shows an image of the silvered fibre end.

The metal coating weakly adheres to the flat fibre face, and strongly to the linking agent-coated notch. The flat face is repolished to remove the weakly bound metal coating (Figure 8.13(d)), and further polishing is carried out if required to achieve the desired penetration depth of the notch (Figure 8.13(e)).

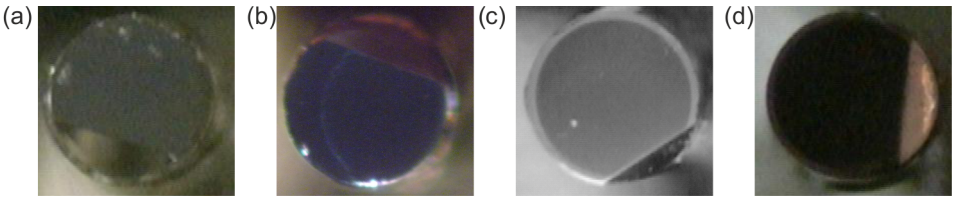


Figure 8.12: Images of coated fibre ends (a) 3-MCP with silver (b) 3-MCP with gold (c) VECTABOND with silver (d) VECTABOND with gold.

Images of each type of coated fibre end, as seen under a microscope, are presented in Figure 8.12. The thiol binding agent, 3-MCP, provides a stronger bond to the gold coating that the amide-based VECTABOND: thus a gold/3-MCP coating with high surface quality was formed, but the gold/VECTABOND coating does not remain intact during further polishing steps (see Figure 8.12(d)).

Both 3-MCP and VECTABOND formed a strong bond to silver, providing a high surface quality that is resilient to further polishing in both instances. Given an equal surface quality, the silver coating is preferable to gold, as it provides a higher reflectivity at 532 nm (see Figure 8.11), and does not require the use of an expensive sputter coater. An additional consideration is the relative complexity of the two coating methods. The repeated reflux and curing steps required for the application of 3-MCP are time-consuming, and often resulted in damage to the brittle fibre end due to the increased amount of handling required, resulting in higher cavity losses. Therefore, the silver/VECTABOND method was selected for fabricating the reflective notch.

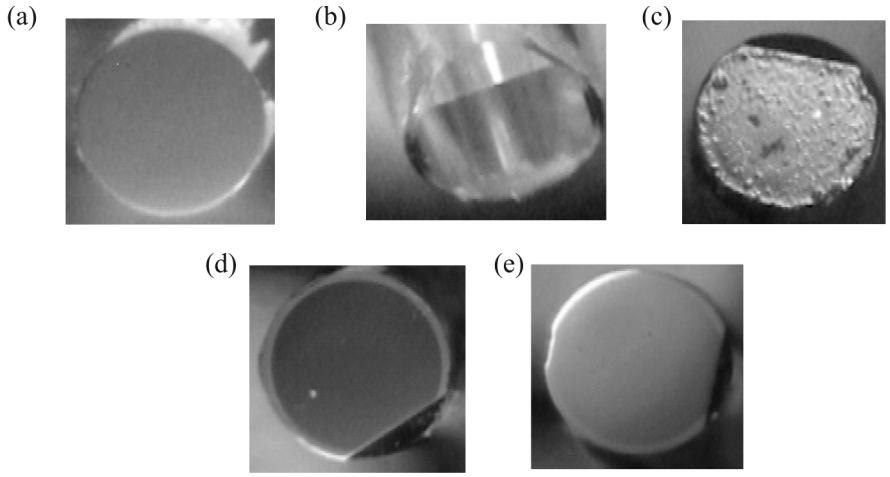


Figure 8.13: Selected reflective notch fabrication steps, shown in sequence from (a) to (e) where (a) is the polished fibre end, (b) is the polished fibre end with a 45° surface, (c) is the silver-coated fibre end, (d) is the polished fibre end with silver only remaining on the 45° surface and (e) is the polished fibre end, which has been polished further to reduce the penetration depth of the silver-coated 45° surface.

After fabrication, the notched fibre end is aligned in a fibre holder (MDE710, Elliot Scientific) fixed on a micron-precision 3-axis translation stage (MDE510, Elliot Scientific). The notched fibre end is clamped on the stationary side of the translation stage, so that the input light beam and output light collector can be aligned relative to a static fibre end. The notched fibre is rotated to the desired angle by hand and then clamped. The second fibre end is polished flat using the high-grade diamond lapping film and aligned with the notched fibre end to produce the completed coupler. In order to further reduce the insertion losses of the coupler, the air gap between the two fibre ends is minimised by bringing the fibre ends into close contact, without stressing the fibres. Fresnel reflections are reduced by refractive index matching the air gap with water or high-index oil. It is also possible to splice the fibre ends together by placing a drop of refractive index matched UV-curing optical adhesive (Norland Optical Adhesive 84, Norland) on the gap, and then rapidly curing the adhesive under a UV lamp (SB-100P/FB 110 W spot lamp, RSL NDT) while the fibre ends are well-aligned. This does not reduce the signal, although realignment of the input beam and output collector may be required after liquid has been added to the fibre ends.

Figure 8.14 presents images of the reflective notch coupler in use. Two ringdown signals recorded for a fibre-loop employing the novel notch couplers are presented in Figure 8.15. Figure 8.15(a) is a ringdown

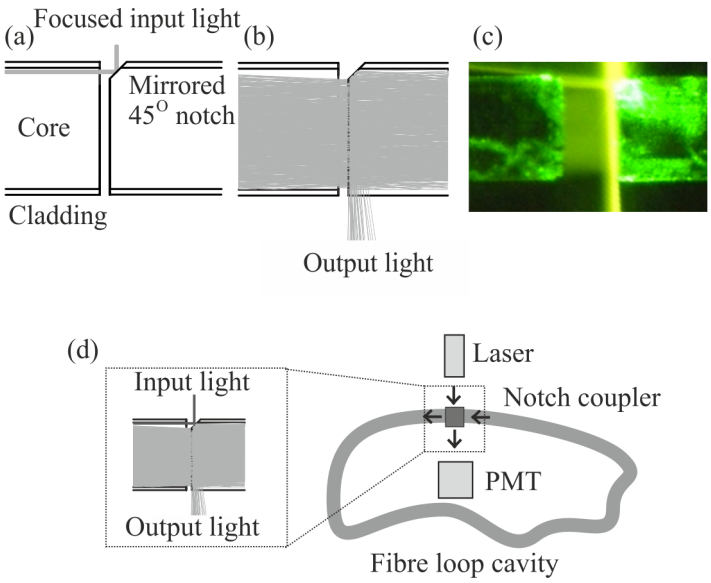


Figure 8.14: The reflective notch coupler in use. (a) shows light coupling into the fibre from the same side as the notch. (b) shows light coupling out from the opposite side as the notch, once the light has expanded to fill the entire core mode area of the fibre. (c) is a photograph of this set-up, where two fibre ends are separated by around 100 μm and the laser beam can be seen reflecting from the notch on the right-hand fibre end into the left-hand fibre face, as well as also scattering across the fibre ends, as the light is not focused entirely on the notch area. (d) is a schematic of the notch coupler used in a fibre-loop CRD spectrometer.

signal for a loop employing an uncoated notch, with the fibre ends at the notch region in air, but with no end separation. The loop length is 3.98 m and the ringdown time is 336 ns. Given the fibre absorption through 3.98 m of fibre is 1.4%, this ringdown time corresponds to a loss in the notch region of 4.3%. Figure 8.15(b) is a ringdown from an Vectabond/silver-coated notch, with the fibre ends at the notch region in water, but with no end separation. The loop length is 3.91 m and the ringdown time is 478 ns. Given the fibre absorption through 3.91 m is 1.3%, this ringdown time corresponds to a loss in the notch region of 2.5%.

8.3.4 Notch fabrication using focused ion-beam milling

While we have developed a straightforward fabrication method for our notch coupler, we were also interested to see whether the use of a more sophisticated fabrication techique such as focused ion-beam milling (FIB) would improve our results. Namely, it is advantageous to fabricate the notch coupler remote from the optical fibre ends, in order to leave the optical fibre ends free for integration with sample. FIB milling should allow us to machine a notch in the fibre without having to have a break in the fibre, unlike in our method described in Section 8.3.3. It can also potentially achieve much higher surface quality than can be achieved with polishing, which should reduce surface scattering losses. Focused-ion beam (FIB) milling is a relatively new fabrication technique, which allows for the fabrication of nanometre to micrometre scale features [363].

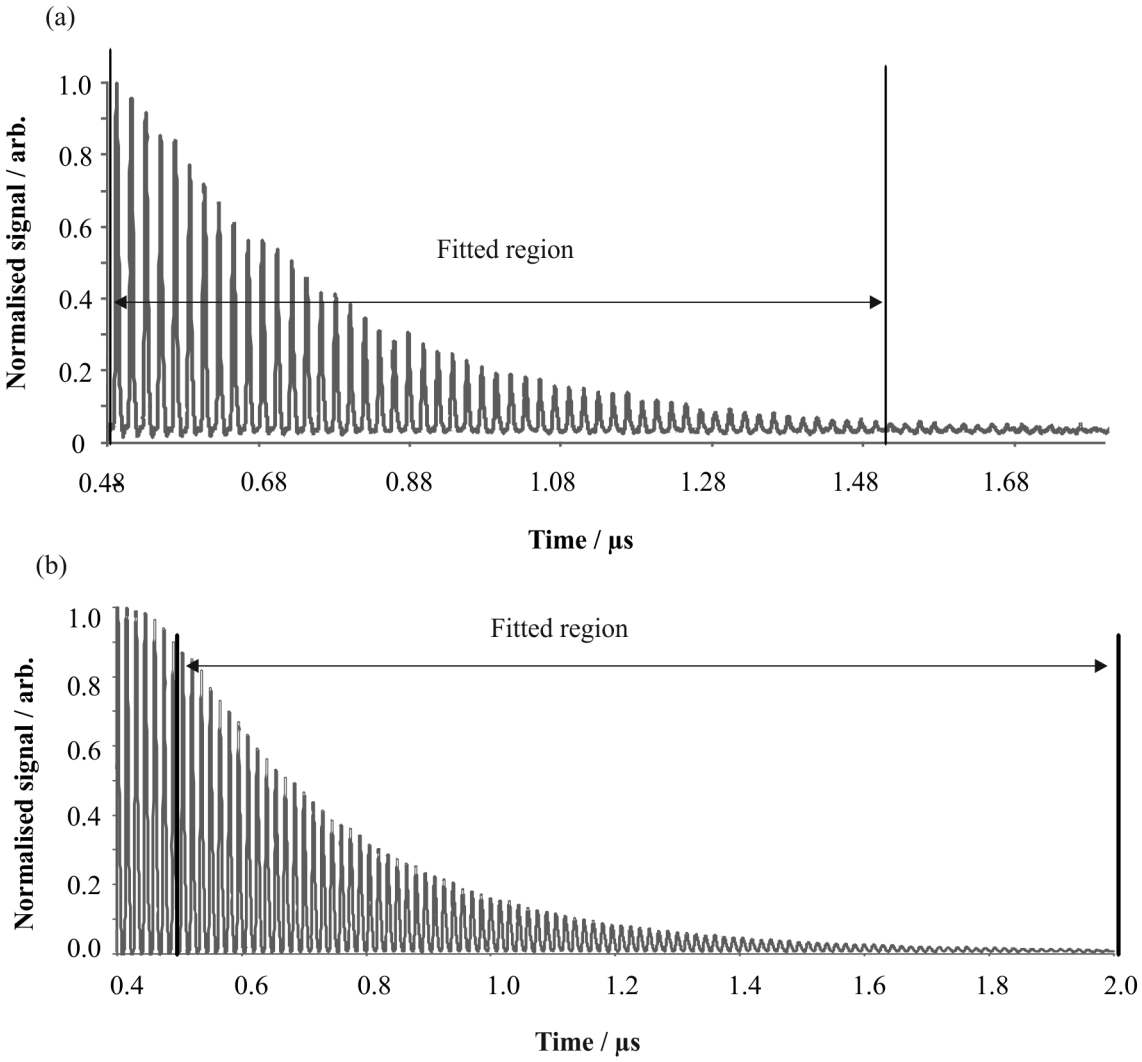


Figure 8.15: Typical ringdown signals obtained from fibre-loops employing the new notch couplers, before introduction of a sample region. The non-exponentially decaying signal at short time is eliminated from the data analysis, as indicated. (a) Uncoated notch ringdown, fibre ends with no end separation in air: τ = 336 ns and d = 3.98 m. (b) Silver-coated notch ringdown, fibre ends with no end separation in water: τ = 478 ns and d = 3.91 m.

The FIB instrument is similar to a scanning electron microscope (SEM), except that it uses an ion beam rather than an electron beam to scan over the sample. Most modern FIB instruments also include SEM, for "dual-beam" imaging, material removal and deposition [363]. Typically, the ion source is a liquid-metal ion source, such as gallium. When a finely focused beam of Ga^+ ions is directed at a sample, sputtering occurs as the ion beam hits the surface, allowing precision milling of the sample. Insulating samples such as glass must be metal-coated in order to improve their conductivity. This prevents build-up of charge on the sample, which would otherwise deflect the ion-beam and prevent high precision milling.

We first attempted to fabricate a 45° notch in the side of 105 μm core diameter optical fibre. This fibre size was chosen because it could be fusion spliced to longer lengths of fibre as required (unlike the larger core diameter optical fibre), but also the penetration depth required to reach the core was minimised. Since the cladding diameter is 125 μm for both 50 μm and 105 μm fibre core diameters, milling the core of 105 μ fibre requires machining through 10 μm of cladding, while for 50 μm, 37.5 μm of cladding must be machined before reaching the core. The removal of microns of material using focused ion-beam milling is a slow process. Initial FIB experiments were carried out over the course of two days at the EPRSC-sponsored FIB facility at University College London, with the help of Dr. Paul Warburton and Dr. Suguo Huo. It took twelve hours of milling to fabricate the resulting cuts presented in Figure 8.16, and we were not able to fabricate a useable notch in the time available. While this initial attempt demonstrates that FIB clearly has the precision required for fabrication of the notch, it shows that FIB cannot sensibly be used to remove such a large volume of material (ca. 12,700 μm^3) as required for a full 45° notch.

With this in mind, we planned our next set of FIB experiments to take advantage of the precision of the technique, and avoid the long milling times required for the fabrication of such a large notch.

8.3.5 Alternative notch design

In principle, the notch does not need to extend in a slice across the full core of the fibre, and a lower loss could be achieved by fabricating a smaller 'rectangular' notch, as shown in Figure 8.17(a). For a rectangular notch, the percentage loss *L* can be approximated as:

$$L = 100(\frac{\text{notch cross-sectional area}}{\text{core cross-sectional area}}) \approx 100(\frac{l_1 l_2}{\pi r^2}) \tag{8.6}$$

where l_1 and l_2 are the width and height of the notch cross section in the core, as defined in Figure 8.17(a). The calculated losses for a rectangular versus a semicircular notch are demonstrated in Figure 8.17(b). The rectangular notch used in the calculations has a constant width (l_1) of 10 μm, and a height (l_2) equal to the notch penetration depth of a semicircular notch. The rectangular notch has significantly lower associated losses than the semicircular notch, and would therefore make an ideal coupler for fibre-loop CRDS, if

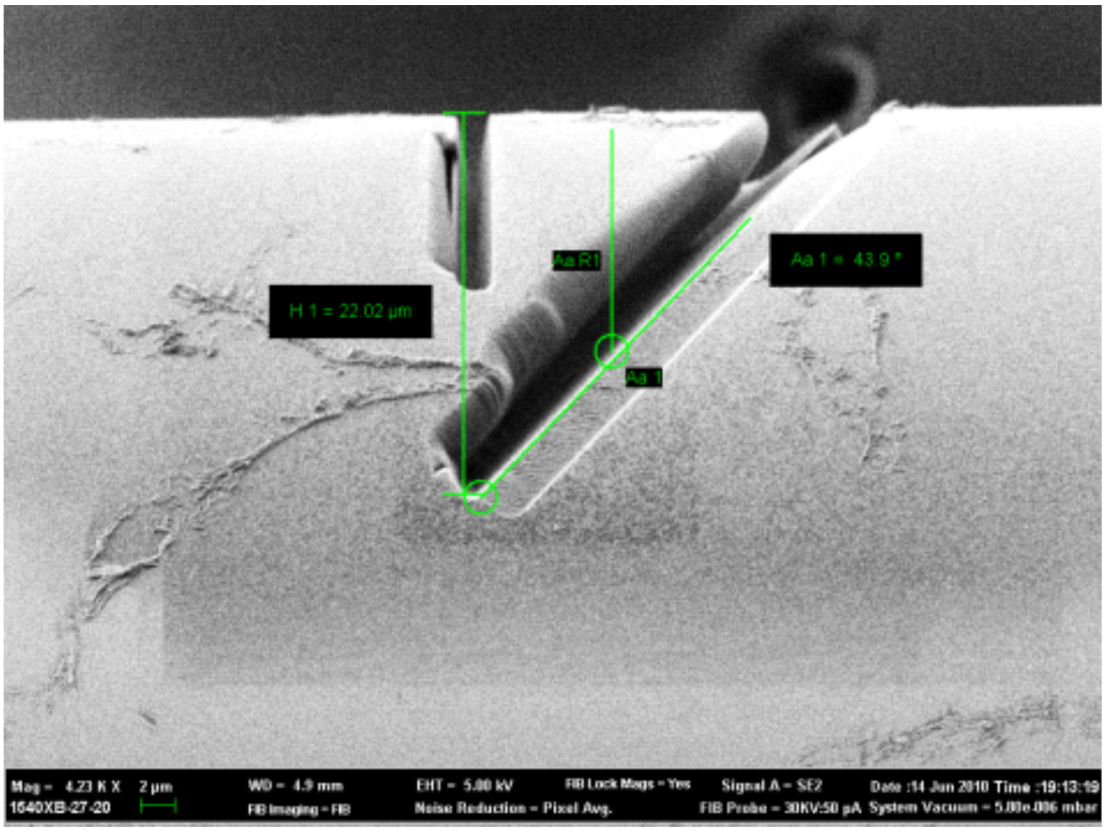


Figure 8.16: Initial FIB notch attempt.

fabrication were possible. However, the fabrication process for a rectangular notch (requiring FIB milling) is more complex than the fabrication process we developed in the previous Section, which required only polishing and chemical-coating. There is a clear trade-off between the fabrication complexity and the lowest loss achievable.

Fabrication of such notches is considerably more challenging than the structures we have considered so far. The only technique we know of that is capable of fabricating such a structure is FIB milling. While this technique yields extremely high quality structures, it is very slow, expensive and is therefore not inherently scalable, unlike our polishing technique. However, this type of notch should give us the lowest total losses, as the cross-sectional area of the notch is lowered much more than can be achieved in a semicircular notch. The benefits of the rectangular over the semicircular notch increase as the penetration depth increases. For example, a rectangular notch penetrating 10% into the fibre core has a loss of only 0.32%, around 16 times smaller than the loss of 5.2% predicted for a semicircular notch with the same penetration. If the penetration depth is increased to 20% of the fibre core, the rectangular notch has a loss 22 times smaller than the equivalent semicircular notch.

The FIB milling was carried out by Phil Dolan, a D.Phil student in Dr. Jason Smith's group in the Department of Materials at the University of Oxford. A significant amount of time was spent optimising the sample

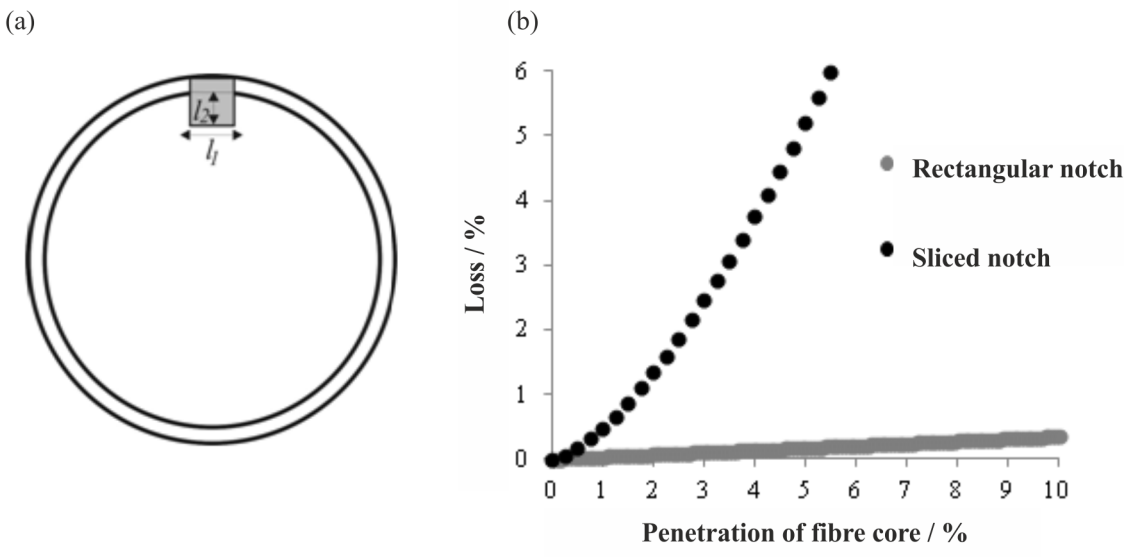


Figure 8.17: (a) Alternative lower-loss coupling design: end-view of fibre in which notch is only fabricated in the central part of the core, rather than as a slice across the top of the core. (b) Calculated losses compared for a rectangular notch, and a semicircular notch.

preparation for FIB. Pieces of fibre up to a few metres in length were coiled around a metal tube and secured, in order to keep the fibre securely out of the way of the moving parts within the FIB instrument. Longer lengths of fibre were preferred, as these could be used to form a fibre-loop without needing to splice in additional lengths of fibre. The section of fibre to be milled was glued firmly onto a small flat piece of glass, which was attached to a pin stub using a carbon sticky pad. Once glued, the top section of the fibre plastic jacket was gently removed using a razor blade, with the visual aid of a microscope. Care was taken not to damage the fibre surface. This left the cladding exposed directly to the FIB. The fibre and slide were gold coated to improve the conductivity of the sample and could then be placed in the FIB safely and securely, for milling sessions lasting up to 3 hours each. Images of some milled notches are presented in Figure 8.18.

8.3.6 Testing the FIB milled notches

Coupling of light into the FIB notches proved challenging. Firstly, the notch is so small it can be difficult to locate by visual inspection of the fibre. This is in contrast to the polished notches, where alignment was greatly facilitated by the fact that the coupler also incorporated a break in the fibre, which was very easy to locate. Secondly, once the notch has been located, it is difficult to direct the input light specifically to the notch while minimising scattering from other surface of the fibre. Light can be coupled into a fibre via a rectangular notch either via direct illumination of the notch with a free space beam, or by aligning a single mode fibre with the notch and sending the illuminating light in through the fibre. The latter directs more of the light to the notch, and minimises scattering and reflection losses from light hitting other parts of the fibre

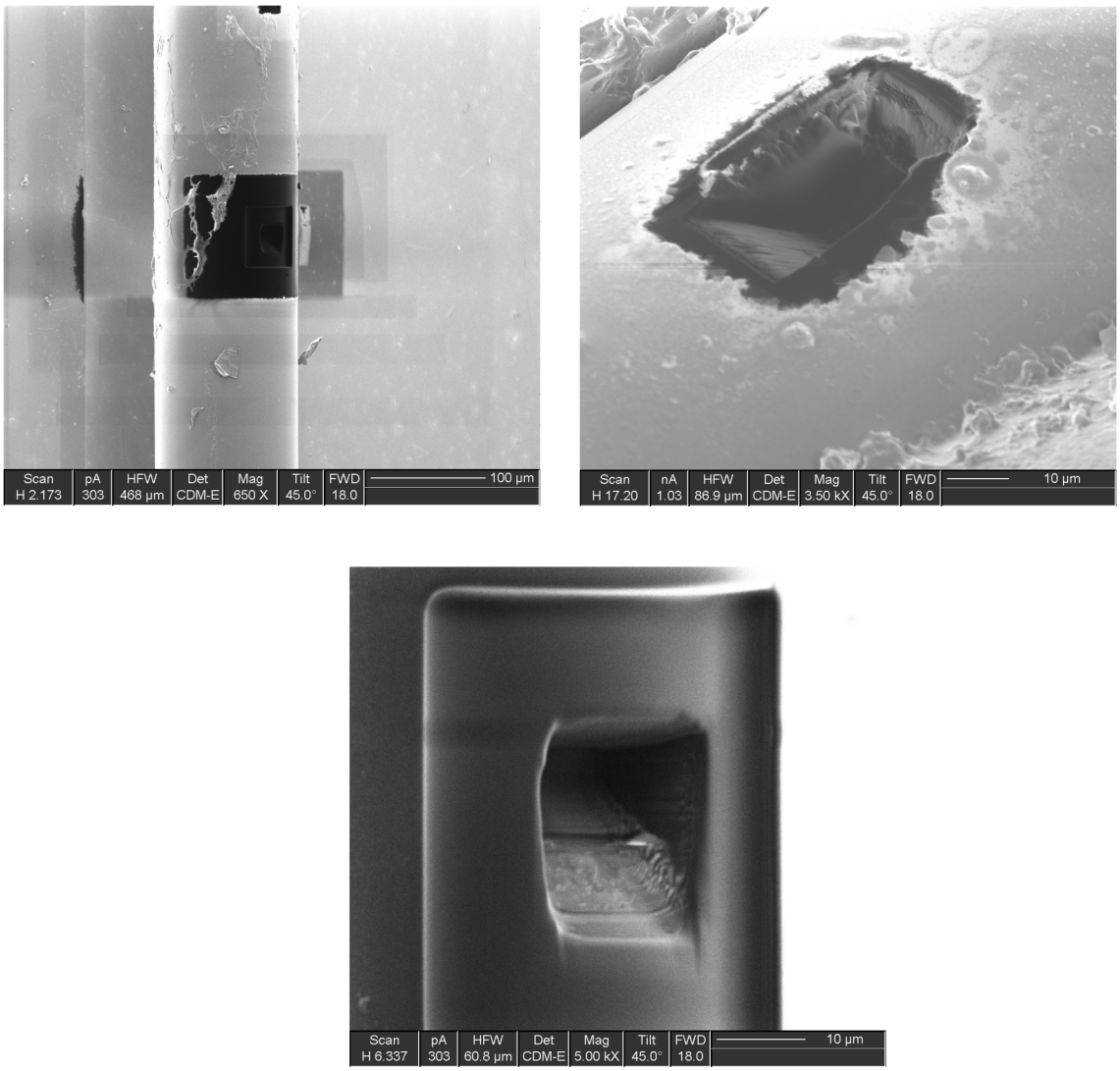


Figure 8.18: Images of rectangular FIB notches.

surface.

A webcam was used to aid alignment in these cases. Figure 8.19 shows an example image of a laser beam aligned onto the FIB milled notch on a mounted length of fibre glued to a microscope slide. In addition, the focus of the light beam onto the smaller notch was critical. Light was focused onto the FIB notches in all cases from a single-mode fibre emitting through an objective lens, mounted on a micron precision alignment stage. Three-axis alignment was carried out by translating the single-mode fibre-coupled laser beam onto the fixed fibre notch, while both fibre ends of the notched fibre length were directed to a PMT or photodiode. This allowed for the in-coupling alignment to be optimised for maximum signal on the photodetector, when light is optimally coupled into the fibre length. Once the in-coupling had been optimised, the two ends of the notched fibre length were then aligned together with the aid of a microscope, to form the looped cavity.

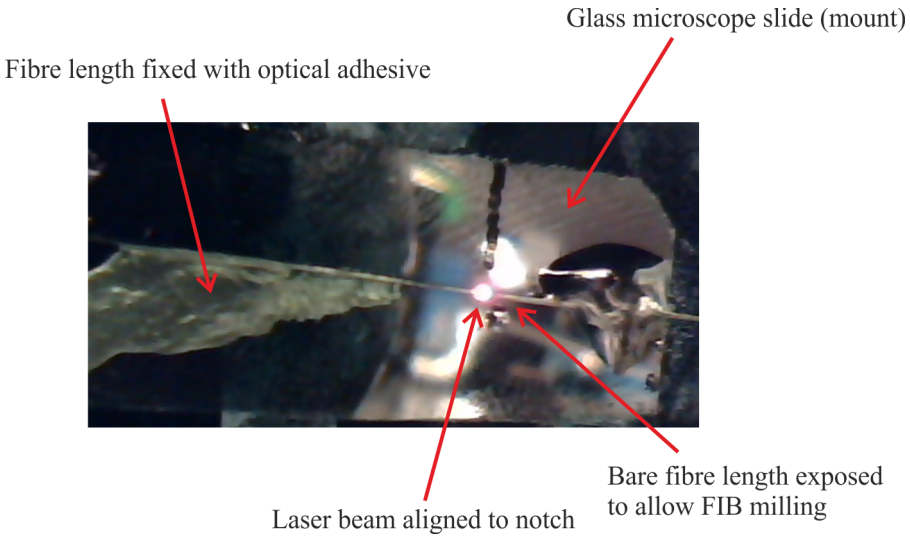


Figure 8.19: Example images taken using webcam, the light source is aligned to the fibre notch in both cases.

In initial experiments, we attempted to achieve both input and output coupling at the same rectangular notch, in the same manner as was previously achieved for the semicircular notches. However, using this strategy, we were unable to record a ringdown signal. We believe this is most likely because the ringdown time was not long enough to detect the ringdown signal, as the time-gated PMT had an inbuilt delay of 300 ns, and the loop length was shorter than those used previously (around 1 m compared to at least 3 m in the earlier experiments). There are two solutions to this problem. One is to use a longer length of fibre; an unattractive option because of the increased losses arising from the two splices required to insert the additional fibre length. The second option is to use an ungated PMT. However, an ungated PMT cannot be used with a single notch coupler, since it would be blinded by scatter from the input laser pulse. This means that the input and output must be separated, either by using a second FIB notch or a slack bend for out-coupling.

Firstly, we attempted to detect light out of a second FIB notch in the same length of optical fibre, using an ungated PMT. Unfortunately, while we could couple light into the loop with relative ease, we were not successful in detecting light out of the second notch. This can be explained by the fact that the out-coupling efficiency is expected to be much lower than previously obtained with the reflective coated notch. For example, the Fresnel reflection at a 45° air/glass boundary is predicted to be only 4.5%, compared to over 90% for a silver-coated notch (Figure 8.11). It is possible that the 45° notch could be metal-coated while in the FIB microscope, with a relatively high degree of spatial control. However, coating only the 45° face and not the 90° face remains a challenge.

Given the problems arising from out-coupling light from a FIB notch, it was decided to use one FIB notch for in-coupling, and then to use a bend for out-coupling, with a non-gated PMT placed directly next to the bend. As we have already discussed (Section 8.1.6), bends are not ideal for optimising coupling efficiency and minimising loss. However, with a highly efficient in-coupling method, achieved using notch-coupling,

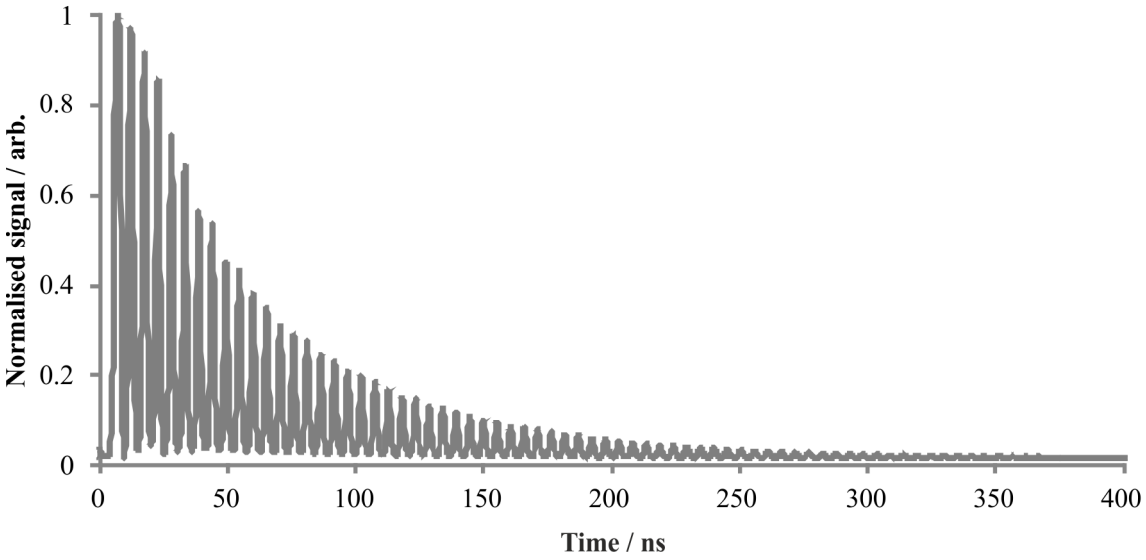


Figure 8.20: Ringdown signal using FIB notch for in-coupling, and 3 cm bend for output coupling. The ringdown time is 64 ns and the loop length is 1.10 m.

the bend can therefore be slacker, and hence lower loss. Figure 8.20 presents the ringdown signal under these conditions, where a 3 cm bend is used for output coupling, and the fibre ends are cleaved and aligned together with no end separation in water. The ringdown time is 64 ns and the loop length is 1.1 m, which corresponds to a total round-trip transmission of 92%. Given that the absorptions arising from the fibre core account for only 0.4% of the loss in this case, the combined losses arising from the FIB notch and the 3 cm bend account for a loss of nearly 8%. This is significantly higher than the 2.5% loss measured previously for a single polished notch coupler (Figure 8.15).

Despite the less advanced fabrication technique, we can conclude that notch fabrication by polishing retains advantages over FIB fabrication, in that it allows for selective mirror-coating of only one face, which therefore allows the notch coupler to function as both input and output coupler. Such a set-up has the lowest losses. However, for integration with a flow system, a second break in the fibre will generally be required, in order to keep the light-coupling remote from the sample (Figure 9.1(b)). The polished notch couplers were used in the work described in the next chapter.

8.4 Sample region

8.4.1 Direct absorption

In direct absorption measurements, the gap between the two fibre ends is exploited to introduce the absorbing sample directly to all the light circulating in the fibre-loop cavity. Unfortunately, any measures taken to

improve the sensitivity of the loop to the presence of an analyte tend to lead to an increase in the loop loss. For example, increasing the absorption pathlength between the two fibre ends is an obvious way to improve the sensitivity, but this causes the loop loss to rise. The aim is therefore to find the best compromise between maximising sensitivity to the analyte and minimising the loop loss.

The direct absorption losses are typically determined by the end separation between the two fibre ends, the numerical aperture of the fibre (described in Section 8.1.1) and the size of the fibre core diameter. Larger core diameter fibres are advantageous for direct absorption experiments as the alignment of the two fibre ends becomes less critical, allowing for greater end separation with lower losses. As a general rule of thumb, the allowable end separation between two flat fibre ends is less than the core diameter of the fibre faces. In the following Chapter we investigate the sensitivity of direct absorption measurements carried out using both bend-coupled small-core fibre-loop and a notch-coupled large-core fibre-loop.

8.4.2 Lensing

A brief mention will also be made of the opportunity for lensing one or both of the fibre ends in order to improve the gap transmission. Loock first addressed this possibility in 2006, investigating the use of a fusion splicer to apply an arc and thus melt the end of a 100 μm core diameter, 140 μm cladding diameter optical fibre into a lens [272, 352]. Typically, elliptical lens are produced, as the fusion splicer only applies the arc from two electrodes on opposite sides of the fibre. For producing a hemispherical lens, four electrodes would be preferable. Light at 810 nm was used and Loock demonstrated that the gap transmission was 60% for two straight cut fibre ends separated by 86 μm, which could be improved to 85% for a fibre lens with a radius of curvature of 76 μm [272, 352]. Unfortunately, the comparison is not a fair one, as the lensed fibre end separation was only 35 μm, compared to 86 μm for the straight cut fibre ends. Loock states that "The larger transmission for the lensed fiber end is largely due to the focusing effect, and not due to the difference in the size of the gap" [272], although as additional data is not provided, we cannot verify this fact. We note that, as will be seen in Figure 9.2, we would expect a significant difference in gap transmission to arise from such a large difference in end separation. Furthermore, Loock's losses in this case are substantially higher than typical gap transmission values we measure, which can be assumed to arise from sub-optimal alignment or fibre end preparation.

In one of their most recent publications, Loock's group used a hemispherical lens (radius of curvature 220 μm) fabricated by WT&T, Inc., on the emitting fibre end [342]. Light at both 405 nm and 810 nm was used, and the loop was composed of 400 μm core diameter, 425 μm cladding diameter optical fibre. A comparison was not made with straight cut fibre ends, but an end separation of 800 μm was used. At this end separation, the gap transmission was found to be around 57%. Such a low gap transmission, even with a lens, limits the

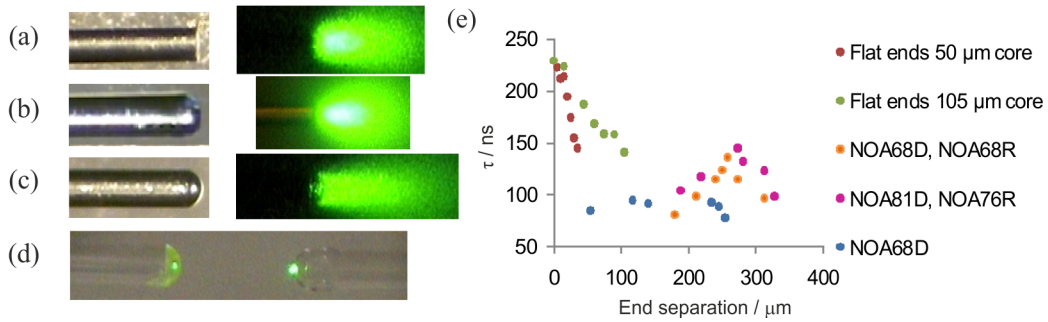


Figure 8.21: Study of 105 μm fibre, with and without lenses. Light emission is imaged in dilute milk solution. (a) Flat fibre end. (b) Arc-melted lens. (c) Lens formed from optical adhesive. (d) Achievable end separation of lensed fibre ends. (e) Comparison of ringdown time versus end separation of flat and lensed fibre ends. NOA is an abbreviation for Norland Optical Adhesive and the numbers simply represent optical adhesives with slightly different viscosities and refractive indices, which will result in lenses with different optical properties.

usefulness of the cavity. Indeed, we can calculate that only 2 round-trips may be recorded in the cavity during one ringdown time.

We have investigated two simple lensing methods. Firstly, by using the fusion splicer, as was demonstrated by Loock [272, 352], to apply an arc and thus melt the end of the optical fibre. An image of an arc-melted fibre end, along with the light beam emitted from this fibre end is shown in Figure 8.21(b). Secondly, by dipping the optical fibre end in UV-curing optical adhesive, and then allowing the surface tension to define the radius of curvature of the lens, which was then cured [364]. A variety of optical adhesives with different viscosity and refractive indices were investigated. Optical adhesives with different viscosities will create polymer lenses with different focal lengths, as the radius of curvature is defined by the amount of optical adhesive adhered to the fibre end as well as by the surface tension of the adhesive. Optical adhesives with different refractive indices will cause the light to refract differently on travelling from the polymer lens into the fibre core, which can aid light collection.

We chose 105 μm core diameter optical fibre for lens-testing because its core diameter was the largest relative to the cladding diameter, and because 105 μm fibre could be cleaved using the commercial fibre cleaver, so that lensed fibre ends could be quickly fabricated and removed. This latter requirement precluded 365 μm core diameter fibre which often requires lengthy polishing time to ensure high quality fibre ends.

Figures 8.21(c) and (d) present images of polymer lenses. Both the polymer lens and the light beam emitted from the fibre end are shown in both cases. The plot in Figure 8.21(e) demonstrates the improvement in optimum end separation which can be obtained for lensed fibre ends versus flat fibre ends. While each lens varied, some general points can be made. Firstly, it was found that lenses fabricated using UV-curing optical adhesive occasioned significantly lower losses than lenses fabricated using the fusion splicer. This can be attributed to the fact that polymer lenses are likely to be more spherical than lenses that are fabricated by arc-melting. Secondly, a clear improvement was noticed when applying a polymer lens to both fibre ends,

rather than just to the emitting fibre end (compare the pink and orange points versus the blue point in Figure 8.21(e)). Thirdly, that although an improvement in ringdown time for lensed fibre ends was marked at large end separations (around 280 μm in Figure 8.21(e)), the ringdown time was never improved to that achieveable in shorter pathlengths. This is attributed to the increased scattering losses which can be seen clearly in Figure 8.21(d). Such high scattering losses appear to be a shortcoming of the simple fabrication strategy attempted here. Given the requirement of minimising the cavity losses, we would recommend commercial fabrication of the fibre lenses, in order to produce the best surface quality, as in the previously described work of Loock et al. [342].

8.4.3 Evanescent field absorption

So far in this Chapter, we have only considered direct absorption measurements. An alternative method of sample introduction is to take advantage of the evanescent wave which is produced at the point of total internal reflection at the core/cladding boundary. If the cladding of an optical fibre is removed, either by etching [365], heating and pulling [366] or polishing [367], then total internal reflection instead occurs at the interface between the fibre core and the surrounding medium. If a sample is placed in contact with the fibre surface then light travelling in the fibre core interacts with the sample via the evanescent wave produced at the point of total internal reflection. This evanescent wave is defined by a penetration depth d_p, the distance at which the amplitude of the wave falls to 1/e of its initial value at the core-cladding boundary [279].

$$d_p = \frac{\lambda}{2\pi(n_1^2 \sin^2\theta - n_2^2)^{1/2}} \tag{8.7}$$

where θ is the angle of incidence to the interface, and n is the refractive index, as before. The penetration depth is usually on the order of half a wavelength. This makes the evanescent wave absorption approach essentially a surface-sensitive technique, and apparently unsuited to measuring absorptions for bulk liquid samples. In this context, 'bulk' refers to a complete depth of liquid sample, rather than just the sample near the fibre surface. In addition to the short penetration depth, only a small fraction of the optical power propagating in the fibre core is present in the evanescent field. These two factors taken together mean that for bulk samples we might expect direct absorption fibre-loop CRDS to be considerably more sensitive, since all of the light travelling in the fibre core interacts with the liquid sample on each pass, such that the entire sample volume within the gap between the fibre ends is sampled. However, in direct absorption the achievable pathlength per pass is limited by divergence across the gap, with the result that in some cases evanescent wave measurements can compete effectively in terms of sensitivity, even for bulk samples.

Evanescent wave fibre-loop CRDS spectroscopy is a versatile sensing technique, as the evanescent wave can respond to a variety of changes in its environment, including absorption [354, 368], scattering [369]

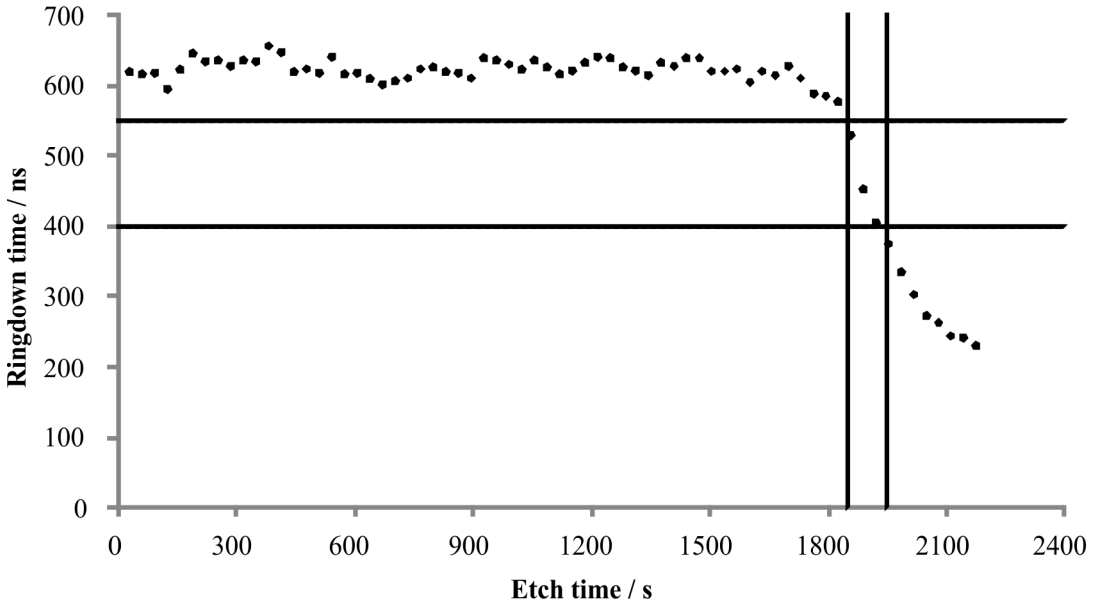


Figure 8.22: Graph of ringdown time versus etch time, for 50 μm core diameter optical fibre.

(particularly by large species such as proteins or cells) and refractive index changes [370].

It might be expected that the bend coupling method is preferable for evanescent wave absorption, compared with direct absorption, as the bend couplers couple preferentially into higher order core modes than the notch couplers. Light travelling along the fibre core therefore strikes the core-cladding boundary at larger θ and hence has a larger penetration depth d_p. Indeed, Ahmad and Hench have described the increase in evanescent wave penetration depth in a single-pass optical fibre sensor when light is launched at an angle into the end-face of the optical fibre, rather than along the optical fibre axis [371]. In Chapter 9, we investigate evanescent wave measurements using both bend-coupled 50 μm core diameter optical fibre and notch-coupled 365 μm core diameter optical fibre. We first describe the taper fabrication process in detail.

In order to produce the fibre taper, a small length (2 mm) of the fibre's plastic jacket is removed using a gas torch. This stripped length of fibre is then secured firmly onto a plastic block in preparation for etching. It is important not to exert undue pressure on the fibre at this stage, as this leads to large optical losses from the loop and degradation of the ringdown time, particularly for the small-core optical fibre. The fibre ends are either spliced together using a fusion splicer (FSM18S, Fujikura) to form a closed loop, in the case of the small core optical fibre, or used to form the notch coupler, in the case of the large core optical fibre-loop.

Tapers are produced by etching the unjacketed part of the fibre in 48% aqueous hydrofluoric acid (339261, Sigma-Aldrich) for 20 - 35 minutes for the small-core optical fibre, and 4 - 6 minutes for the large-core optical fibre. The reduction in etch time for the large-core optical fibre arises from the thinner layer of cladding surrounding the core. Within each fibre size, etching times also vary somewhat depending on the temperature,

which was not controlled during these experiments. In both cases, the etching process is controlled by monitoring the ringdown signal. At short etching times, the ringdown signal is fairly stable, as only the cladding is being eroded. However, once the cladding has been removed, the core is exposed, and the light travelling in the core decays into its surroundings. Figure 8.22 shows the dependence of the ringdown time on etching time; in this example, etching was carried out on 50 μm core diameter optical fibre until the ringdown signal disappeared completely. In order to make evanescent wave measurements, the reaction must be quenched at an appropriate point. Quenching the reaction too early (indicated on Figure 8.22 by the first vertical line) will lead to a taper with a good ringdown signal, but which is not very sensitive to its surroundings, as only a small proportion of the evanescent field will be exposed to the sample in this case. On the other hand, quenching the reaction too late (indicated on Figure 8.22 by the second vertical line) will lead to a taper which is much more sensitive to its surroundings, but has a poorer ringdown signal. A compromise between taper sensitivity and baseline ringdown signal must be chosen for maximum sensitivity.

Typically, etching is quenched 30 - 100 s after the ringdown time first starts to drop, by using saturated aqueous sodium carbonate solution to neutralise the hydrofluoric acid. After quenching the reaction, the taper is washed with deionised water and left to stabilise in 0.1 M NaOH solution for an hour, in order to ensure that no residual hydrofluoric acid remains in the sample region. After washing and drying, the taper is ready for use.

Tapers in bend-coupled small core fibre-loops and notch-coupled large-core fibre-loops will be compared in the following Chapter.

8.5 Conclusion

We have developed a reflective notch coupler which allows nearly 100% of appropriately focused light to enter the cavity, while maintaining a relatively low loss per pass of $< 4\%$. In addition, the device functions as both an input and an output coupler. Light is introduced and ejected from opposite sides of the fibre, allowing us to separate the input and output light spatially without the need for an additional beam-splitter. This is a significant improvement on previous fibre-loop cavity arrangements discussed in Section 8.1.6. We have also described the experimental set-up and two different types of sample regions that can be created in a fibre-loop cavity. In the following Chapter we examine different light couplers and sample regions in both small-core and large-core diameter optical fibres, in order to ascertain which approach has the highest sensitivity.

Chapter 9

Fibre-loop cavity ringdown spectroscopy: Characterisation

In this Chapter, we carry out a complete characterisation of the various components described in Chapter 8. We determine the loss associated with the bend-couplers used for small-core fibre-loop CRDS and the notch-coupler used for large-core fibre-loop CRDS. We then present direct absorption measurements using both set-ups, followed by evanescent wave absorption measurements. We have established the detection limit for each system through direct absorption experiments on a common laser dye, rhodamine 6G (Rh6G), which enables us to determine the highest sensitivity set-up.

9.1 Loss comparison

In order to establish the loss arising from the couplers and direct absorption sample regions, three fibre-loop CRDS set-ups are compared. Figure 9.1 presents schematic diagrams illustrating these set-ups, which consist of (a) a bend-coupled 50 μm optical fibre-loop, (b) a notch-coupled 365 μm optical fibre-loop, with sample introduced at a second gap in the loop, and (c) a notch-coupled 365 μm optical fibre-loop, with sample introduced in the notch coupling region.

In order to isolate the losses from each component of the ringdown cavity, three ringdown times were determined for each of set-ups (a), (b) and (c). Within each set-up, ringdown time τ_1 corresponds to a loop without a sample region, in which the fibre ends are joined together either by a fusion splice (in the case of 50 μm core diameter optical fibre) or a mechanical splice (in the case of 365 μm core diameter optical fibre). Ringdown time τ_2 corresponds to a loop into which, in place of a splice, a break has been introduced in

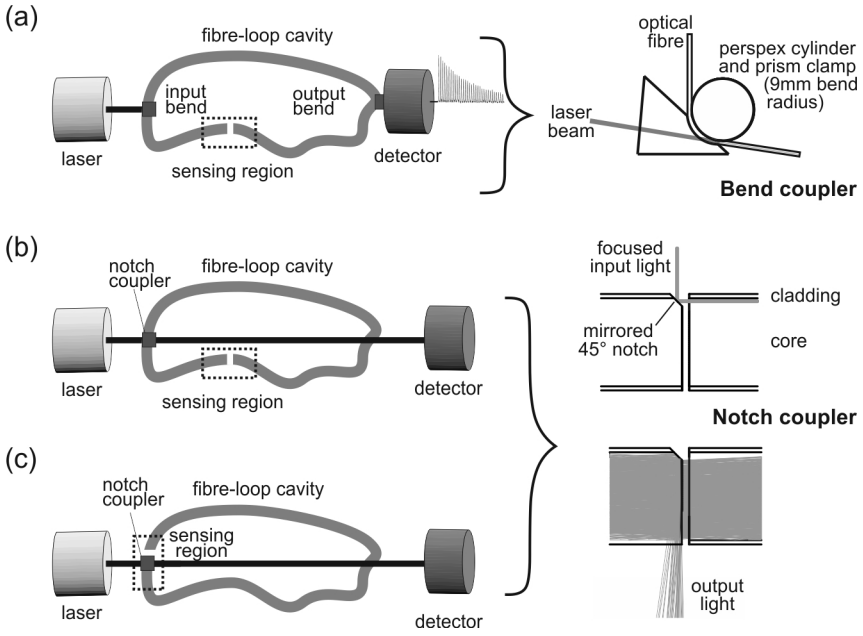


Figure 9.1: Schematic of the three fibre-loop CRDS set-ups and two coupling arrangements used in the present work: (a) bend-coupled 50 μm optical fibre-loop; (b) notch-coupled 365 μm optical fibre-loop, with sample introduced at a second gap in the loop; (c) notch-coupled 365 μm optical fibre-loop, with sample introduced in the notch coupling region. The bend and notch couplers are shown schematically to the right of the relevant fibre-loops. Zemax optical ray tracing simulations demonstrating input and output coupling at the notch coupler are superimposed on the diagrams.

order to accommodate a sample region, but the fibre ends are in contact (i.e. the sample gap is zero). Ringdown time τ_3 corresponds to the same loop as τ_2, but with the fibre ends separated by a distance *l* at the sample region. It should be noted that for cavity set-ups (a) and (c), defined in Figure 9.1, the length of the fibre-loop is the same for each τ measurement. In the case of cavity (b), however, an extra length of fibre (about 1 m) was inserted into the fibre-loop between measuring τ_1 and τ_2, in order to insert a second sample region remote from the notch coupling region. The relevant geometrical parameters for each cavity, together with the ringdown times τ_1, τ_2, and τ_3 are shown in Table 9.1. The larger *d* value noted above appears in square brackets in the Table.

In both a two-mirror cavity and a fibre-loop cavity, the ringdown time τ is dependent on the cavity length

Table 9.1: Experimental details for each cavity set-up (a) - (c), defined previously in Figure 9.1. *d* is the loop length, τ_1 is the ringdown time without a sample region, τ_2 is the ringdown time with a sample region, but with an end separation of 0 μm, and τ_3 is the ringdown time with an end separation in water of *l* μm.
*In cavity set-up (b), *d* = 3.08 before introduction of a sample region. In order to insert a second sample region, remote from the notch coupling region, an extra length of fibre (about 1 m) was inserted into the fibre-loop, so in this case *d* = 4.03. Thus, *d* = 3.08 m for τ_1 and *d* = 4.03 m for τ_2 and τ_3.

	d / m	τ_1 / ns	τ_2 / ns	*l* / μm	τ_3 / ns	Vol. probed / nL
(a)	5.97	332	201	10	170	0.020
(b)	3.08 [4.03]*	372	227	130	185	14
(c)	3.08	312	312	180	183	19

d, the refractive index of the cavity medium n_c, the speed of light in a vacuum c and the total roundtrip transmission T:

$$\tau = \frac{n_c d}{c\,(-\ln T)} \tag{9.1}$$

The refractive index of the cavity medium n_c corresponds to the refractive index of the undoped fused silica fibre core, which has a value of 1.461 at 532 nm [372].

The total round-trip transmission, T, is calculated from τ and the known loop length d in each case, by rearranging Equation 9.1:

$$T = e^{-\frac{n_c d}{\tau c}} \tag{9.2}$$

T is separated into its components using the following equations for the losses in each of the three loops described previously:

$$T_1 = T_{\text{couplers}} \times T_{\text{splice}} \times T_{\text{fibre}} \tag{9.3}$$

$$T_2 = T_{\text{couplers}} \times T_{\text{break}} \times T_{\text{fibre}} \tag{9.4}$$

$$T_3 = T_{\text{couplers}} \times T_{\text{break}} \times T_{\text{gap}} \times T_{\text{fibre}} \tag{9.5}$$

where T_{couplers} is the transmission through the couplers, T_{splice} is the transmission through the fusion splice, T_{break} is the transmission through the fibre ends at the sample gap, T_{gap} is the transmission through the sample gap itself, and T_{fibre} is the transmission through the fibre-loop. In all cases, the equivalent loss L is given by $L = 1 - T$. $T_{\text{fibre}} = e^{-\kappa_{\text{f}} d}$ and is calculated using the manufacturer's specification and the known loop length. T_{splice} was established to be 0.983 by inserting a second fusion splice into the ringdown loop, and repeating this ten times in order to determine the average fusion splice loss. The remaining terms, T_{couplers}, T_{break} and T_{gap} are established by solving Equations 9.3 to 9.5 simultaneously for each set-up. The detailed results from the analysis are presented in Table 9.2, in terms of both percentage and dB loss.

While coupling losses in two-mirror cavities are simply defined by the mirror reflectivity, and are typically less than 0.2%, coupling losses in fibre cavities are significantly higher. As noted earlier, the couplers used to couple light into and out of the cavity are often one of the major sources of loss within a fibre-loop cavity, with different types of coupler introducing characteristic losses. Figure 8.6(a) presents the ringdown

Table 9.2: Percentage losses for each cavity set-up (a) - (c), defined previously in Figure 9.1. The same losses in units of dB are given in brackets below the percentage value. Each term is defined after Equation 9.3 - Equation 9.5.
*In cavity set-up (b), d = 3.08 m before introduction of a sample region, and hence $L_{\text{fibre}} = 1.1\%$ for L_1. After insertion of a second sample gap, d = 4.03 m, and hence $L_{\text{fibre}} = 1.4\%$ for L_2 and L_3.

	L_1	L_2	L_3	L_{fibre}	L_{splice}	L_{couplers}	L_{break}	L_{gap}
Cavity (a)	8.4	13.5	15.7	2.0	1.7	4.9	7.2	2.6
	(0.381)	(0.629)	(0.743)	(0.089)	(0.074)	(0.217)	(0.323)	(0.114)
Cavity (b)	4.0	8.3	10.1	1.1 [1.4]*	-	2.9	4.2	1.9
	(0.175)	(0.376)	(0.461)	(0.046) [0.060]*		(0.129)	(0.186)	(0.085)
Cavity (c)	4.7	4.7	7.9	1.1	-	3.7	-	3.3
	(0.209)	(0.209)	(0.356)	(0.046)		(0.163)		(0.147)

time corresponding to the τ_1 measurement for cavity (a), while Figure 8.15(b) presents the ringdown time corresponding to the τ_1 measurement for cavity (b). In both cases the dominant source of loss is the couplers, with lesser contributions from absorption by the fibre and the fusion splice used to join the fibre ends into a loop in the case of the small-core fibre. Having separated the contributions from the various loss processes (see Table 9.2), as explained in the previous section, we can compare the coupling losses associated with the two experimental set-ups. For cavity (a), the total coupling loss is 4.9%, or 2.5% for each of the two 9 mm bends employed for input and output coupling. We typically find combined bend coupling and fusion splice losses to be in the region 4 - 7% for 50 μm core diameter optical fibre, with the coupler loss being dependent on the pressure exerted by the PMMA clamp on the fibre, and the splice loss being dependent on the quality of the splice. For a given bend radius, bend losses increase dramatically with the diameter of the fibre core. Increasing the bend radius reduces the losses, but at the cost of a reduction in signal intensity due to less efficient input coupling. For our applications, which employ a relatively low energy laser source, this makes bend coupling poorly suited for use with large-core fibres in our experiments.

Lower coupling losses are found for the notch-coupled large-core fibre ringdown shown in Figure 8.6(b), for which $L_{\text{couplers}} = 2.9\%$. The notch coupler reduces losses in two ways: firstly, the same coupler functions as both an input and an output coupler, so that only one coupler is needed; and, secondly, only a small fraction of the light travelling in the cavity 'sees' the coupler on each pass, so that the loss per pass can be minimised. By comparing L_{couplers} to L_{break} for cavity set-up (b), we can estimate the loss associated with the notch and the fibre ends, respectively. In this case, $L_{\text{break}} = 4.2\%$, which is in fact higher than L_{couplers}. It should be noted that the loss associated with the fibre ends is dependent on the quality of the polished fibre ends. Since these are polished on an in-house built polishing wheel, the quality (and loss) tends to vary somewhat. However, the data indicate that the majority of the loss associated with the couplers arises from the break between the fibre ends rather than from the notch itself.

9.2 Direct Absorption

As explained in Section 8.4.1, a small gap is incorporated into the fibre-loop into which a liquid sample can be introduced.

Figure 9.2 shows the normalised transmission across the gap for two cavities of configuration (a), employing 50 μm and 105 μm core fibre, respectively, and one cavity of configuration (b) employing 365 μm core fibre. The transmission is calculated from the ringdown time, which has been measured as a function of end separation for each cavity. The transmission is plotted as a function of $\frac{l}{\phi}$, where l is the end separation and ϕ is the fibre core diameter. Given that all three fibres have the same numerical aperture (0.22 in air), the three curves should in principle be identical when plotted as a function of $\frac{l}{\phi}$. The black line shows the results of a simulation based on a model by Waechter et al. [336]. The model assumes a Gaussian beam profile and a linear beam expansion coefficient dependent on the numerical aperture of the fibre, and predicts the coupling efficiency between two 'perfect' fibre ends, for which the transmission is simply a function of the fibre core size (beam waist), the refractive indices of the fibre and surrounding medium, and the end separation. In practice, the total transmission across the gap is also a function of the reflection at each fibre end (which can be calculated using the Fresnel equations), and additional scattering losses at the fibre ends themselves. We have not included this in our model line shown on the graph, because the experimental values are normalised to the transmission at zero end separation, which includes the reflection and (to some extent) scattering losses. Deviation from the model at larger end separations is caused by either a non-Gaussian beam profile, or significant scattering at the fibre ends, both of which cause the light to diverge more rapidly than predicted by the fibre numerical aperture alone.

By comparing the data for each cavity set-up, we can see that measured transmission across the gap for the notch-coupled loop is in good agreement with the model, indicating that the fibre ends are of high quality, and that the mode structure can be reasonably well-approximated as a Gaussian beam profile. In contrast, both bend-coupled fibre cavities demonstrate poorer transmission than predicted by the model, particularly when $\frac{l}{\phi} > 0.4$. In this case, both fibre ends were cleaved using a high precision cleaver, and we expect the losses at the fibre ends themselves to be minimal. We believe that the improvement in transmission for notch-coupling over bend-coupling arises from the improved core mode structure, which will be discussed in more detail in Section 9.2.2.

The sample region losses $L_{\text{break}} \times L_{\text{gap}}$ for the cavities used in the detection sensitivity measurements are presented in Table 9.2. L_{gap} is minimised by keeping the pathlength between the two optical fibre ends relatively short, although this of course comes at the expense of spectroscopic pathlength and the concentration detection limit. A greater problem in these experiments is the high loss between the two fibre ends, L_{break} which is around 4% for the large-core fibre, and 7% for the small-core fibre. As noted earlier, in order to make absorption measurements, the ends of the small-core fibre had to be mounted in ferrules in

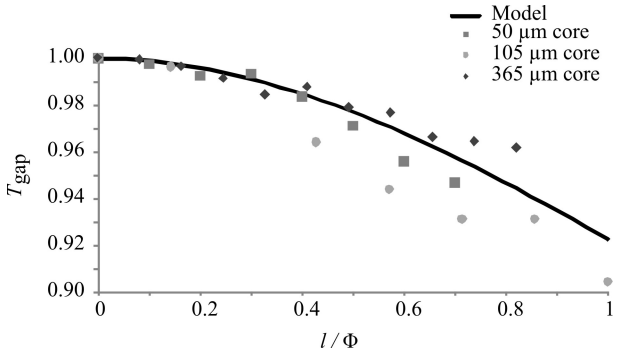


Figure 9.2: Normalised transmission across the gap, T_{gap} versus end separation in units of fibre core diameter, $\frac{l}{\phi}$, for cavity set-up (a) with 50 μm and 105 μm fibre and cavity set-up (b) with 365 μm fibre. The curve represented by diamond points corresponds to the notch-coupled fibre-loop, whereas the curves represented by square and circular points correspond to bend-coupled fibre-loops. The results of the model calculation (see text for details) are shown as the black solid line.

order to maintain alignment. The fixing and polishing procedure introduces a small amount of loss relative to the fibre ends used in Figure 9.2, in which the fibre ends were simply cleaved and aligned. The large-core fibre, in contrast, is rigid enough to be mounted as bare fibre and still maintain alignment within the sensing region.

9.2.1 Light intensity

As the notch coupler is vastly more efficient at coupling incident light into the fibre than a bend coupler, the ringdown signal intensity is improved dramatically; a maximum signal of 4 V, as read from the oscilloscope, was found for the notch-coupled loop, compared with maximum signals of around 100 mV for bend-coupled loops (note that this is after time-gating the signal, as described previously, to remove the initial intense and rapidly decaying jacket and cladding modes that persist for approximately the first 300 ns after excitation of the cavity). The dramatic increase in signal intensity when notch coupling is employed should allow the use of lower power light sources and/or detectors than the laser/PMT combination employed in the present work.

9.2.2 Cavity mode structure

In Figure 9.3, the mode structure excited by the various coupling schemes is examined, via images of the light emitted from the fibre end. In all cases, the fibre end was aligned approximately the same distance away from a CCD chip. In Figure 9.3(a), in order to avoid saturating the CCD camera, only a small proportion of the laser beam was coupled into the fibre. The intensity of this image is therefore not directly comparable with those of the remaining images. In contrast, intensities (b), (c) and (d) were measured using the same neutral density filter in front of the laser beam, with optimised light coupling, and thus can be compared directly. The desirable mode structure is that shown in Figure 9.3(a), which is an image of end-coupled 50 μm core

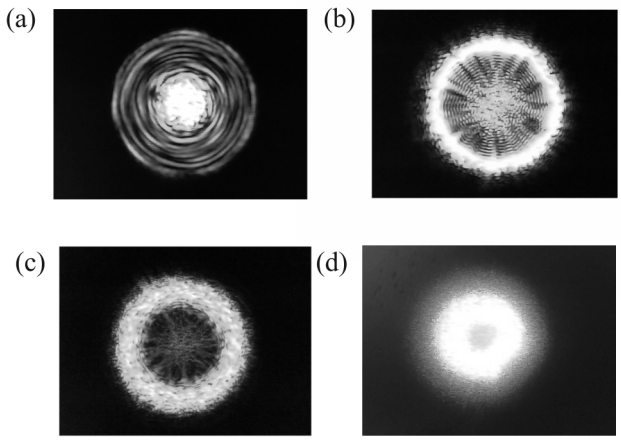


Figure 9.3: Light emission from various fibre sizes, under different coupling conditions, recorded using a CCD camera. (a) End-coupled 50 μm core diameter optical fibre. (b) Bend-coupled 50 μm core diameter optical fibre. (c) Bend-coupled 105 μm core diameter optical fibre. (d) Notch-coupled 365 μm core diameter optical fibre.

diameter optical fibre. Conventional end-coupling predominantly excites core modes over cladding modes. Images of light emitted from bend-coupled 50 μm core diameter and 105 μm core diameter fibre are shown in Figure 9.3(b) and Figure 9.3(c). A significant issue associated with bend-coupling can immediately be seen; light is coupled predominantly into cladding modes and high order core modes, whereas the light intensity in the core is low. In particular, the light emission for 105 μm core diameter optical fibre shows the poorer mode structure resulting in this case: very little light is coupled into the centre of the core, even compared with a similar coupling scheme for 50 μm core fibre. In contrast, the improvement in core mode structure when notch-coupling is employed is clear (Figure 9.3(d)). Light is coupled predominantly into the core (with light emission closer to that of end-coupled optical fibre), and the emission is much more intense than in the bend-coupled case.

Selective excitation of core modes rather than cladding modes can be achieved with the notch coupler, as the percentage coupled into either the core or the cladding is simply dependent on the alignment of the beam onto the notch. If the beam is aligned onto the core area of the notch only, then in theory 100% core excitation and 0% cladding excitation can be achieved. In practice, some cladding excitation occurs when the edge of the input beam is incident on the cladding part of the notch. However, this can be minimised during alignment, when the light intensity incident on the core is maximised. In our experiments, signal acquisition only begins at least 300 ns after the initial light pulse, which means that we do not detect the rapidly decaying cladding modes in our ringdown signal. Alternatively, Brown et al. have previously fitted the full ringdown signal to a bi-exponential composed of decaying core and cladding modes and thus extracted τ_{core} and τ_{cladding} [271].

Table 9.3: Detection limits for dilute solutions of Rh6G for each cavity set-up (a) - (c), defined previously in Figure 9.1. Limits are reported in terms of absorption per unit pathlength (κ) and concentration (C).

	κ_{min} / cm^{-1}	C_{min} / μM
(a)	5.3	43
(b)	0.20	1.7
(c)	0.11	0.93

9.2.3 Sensitivity analysis of direct absorption

The detection sensitivity achievable with each of the three fibre-loop CRDS set-ups was established using the known absorption of rhodamine 6G (Rh6G) at 532 nm. The (base e) absorption coefficient of Rh6G at 532 nm was established in single-pass measurements through a 1 cm cuvette to be $(1.22 \pm 0.06) \times 10^5$ L mol^{-1}cm^{-1}. Between each dye measurement, the ringdown time of a water blank was recorded, in order to ensure that τ had returned to its baseline value and therefore that no dye remained in the sample region.

The detection limit, or minimum detectable absorption per unit pathlength, κ_{min} (given with respect to base e), is determined from Equation 2.17 in the same manner as in Chapter 4, the only difference being that the speed of light c must be corrected for the refractive index of the fibre core n. $\Delta\tau_{\text{min}}$ (the maximum 3σ value measured for τ_0) was established to be 4.5% of the total ringdown time for the small-core fibre, and 2.5% for the large-core fibre. The improvement in the standard deviation of repeated measurements for the large-core fibre arises from the increase in signal level and from the reduction in total loss per pass, thereby increasing the number of points fitted in order to extract a ringdown time. The pathlengths for each set-up are listed in Table 9.1.

The κ_{min} values can be used to calculate the detection limit in terms of the concentration of Rh6G, where $C_{\text{min}} = \frac{\kappa_{\text{min}}}{\alpha}$, and α is known from the single-pass measurement previously recorded. The values of κ_{min} and C_{min} for each cavity set-up are presented in Table 9.3.

Ringdown measurements were made using each cavity set-up at a range of different Rh6G concentrations, in order to verify that the minimum detectable concentration was in agreement with the value of C_{min} calculated above. These measurements were also used to determine the accuracy with which the absorption coefficient α may be measured, in comparison to the single-pass measurement. Equation 2.15 can be rearranged:

$$\frac{1}{\tau} - \frac{1}{\tau_0} = \frac{\alpha l c}{n_c d} C \tag{9.6}$$

From this, we can see that a plot of $\frac{1}{\tau} - \frac{1}{\tau_0}$ versus C will be linear, with a slope m given by $m = \frac{\alpha l c}{n_c d}$. These graphs are presented in Figure 9.4 for each cavity set-up. The resulting α values were 1.57×10^5, 1.99×10^5 and 1.52×10^5 L mol^{-1} cm^{-1} for set-ups (a), (b), and (c), respectively. The dotted horizontal line on each plot marks the 3σ detection limit and agrees qualitatively with the point at which a clear linear dependence on concentration is established.

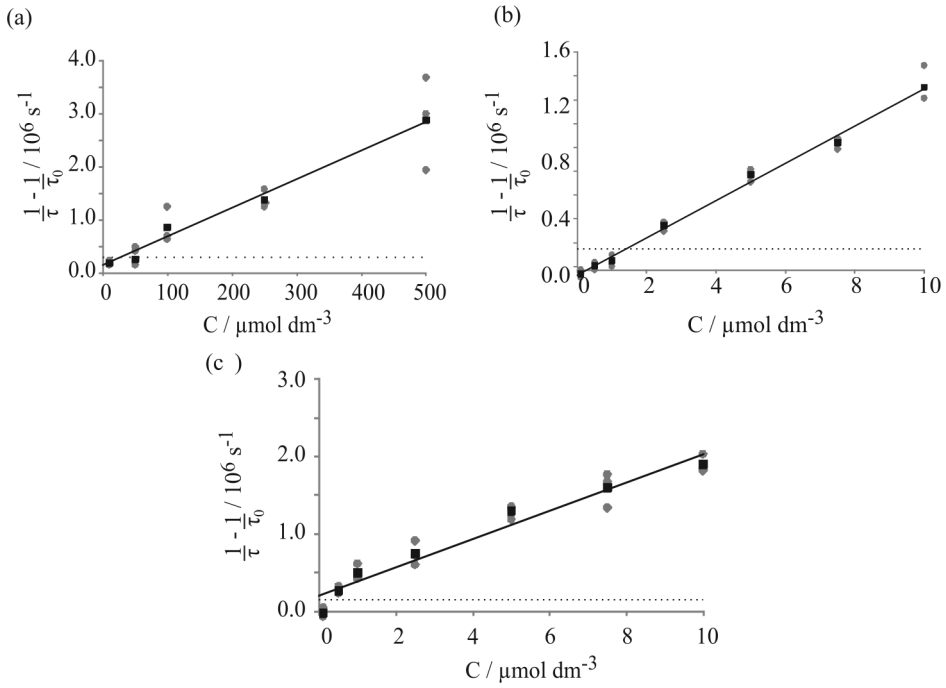


Figure 9.4: Plots of $\frac{1}{\tau} - \frac{1}{\tau_0}$ versus C, Rh6G (aq) concentration, for cavity set-ups (a) - (c), defined previously in Figure 9.1.

Notch-coupling has a dual impact on improving the detection limit: firstly, we have reduced the coupling losses (and hence maximised τ_0), and secondly, by enabling the use of larger core diameter optical fibres, we have been able to increase *l*. The measured detection limit is improved by over an order of magnitude: κ_{min} = 0.20 cm^{-1} for notch-coupled large-core fibre with a second sample gap, and κ_{min} = 0.11 cm^{-1} for notch-coupled large-core fibre with only one gap, compared to κ_{min} = 5.3 cm^{-1} for bend-coupled small-core fibre.

9.3 Evanescent wave absorption measurements

The tapers were fabricated as described in Section 8.4.3. The resulting tapers were then immersed in concentrations of rhodamine 6G and the ringdown change arising from the absorbance was monitored. By analogy with the direct absorption measurements, the absorbance can be written as $\alpha C l_{\text{eff}}$, where l_{eff} is the effective pathlength through the sample, in other words, the equivalent pathlength if all the light had passed through the sample. Measuring the absorbance therefore allows the sensitivity of the evanescent wave measurements to be compared to the direct absorption measurements, in terms of l_{eff} and loss associated with a taper with a specific l_{eff}.

In the case of the small-core optical fibre, the taper was found to be rather fragile, and thus only a single concentration of rhodamine 6G (0.1 mM) was measured and used to determine l_{eff}, from rearrangment of

Table 9.4: Evanescent wave fibre-loop CRDS results for bend-coupled small-core optical fibre. The loop length and ringdown times are provided for several different tapers, which allows the effective absorption pathlength through the sample l_{eff} to be determined for each taper.

Taper No.	Loop length / m	Pre-etch τ / ns	Post-etch τ_0 (water) / ns	τ (100 μM Rh6G) / ns	l_{eff} / μm
1	12.16	586	487	473	3
2	13.07	659	603	528	12
3	14.57	608	510	459	13
4	12.16	586	435	384	15
5	14.82	601	554	461	22

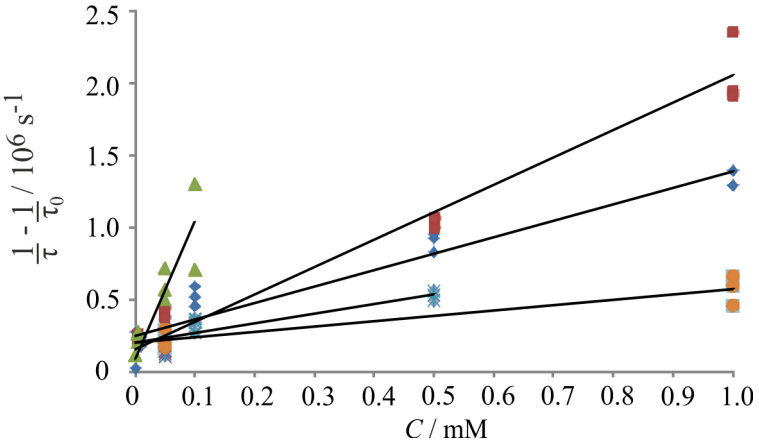


Figure 9.5: Plot of $\frac{1}{\tau} - \frac{1}{\tau_0}$ versus C, Rh6G (aq) concentration (mM), for a selection of large-core optical fibre tapers.

Equation 2.15. Improved mounting would help strengthen the taper and allow it to be used for longer time periods. Nevertheless, a range of fibre tapers were fabricated, having varying sensitivities, which are presented in Table 9.4. Using the small-core fibre, tapers with effective pathlengths ranging from only a few microns to around 20 microns could be fabricated. Given the determined pre-etch ringdown time and post-etch ringdown time and known loop length, it was determined using Equation 9.2 that the total round-trip losses before creation of the taper were around 10% and the total round-trip losses after creation of the taper were around 12%, leading to a taper loss of around 2%. This taper loss can be compared to the gap loss determined in Section 9.1, where a gap loss of 2.6% was determined for l = 10 μm for small-core optical fibre. While the evanescent wave measurements are only preliminary data, this would seem to indicate that evanescent wave absorption may be preferred over direct absorption for small-core fibre, where even short end separations occasion a relatively high gap loss.

In the case of the large-core optical fibre, the taper was much stronger, and thus several different concentrations could be analysed for each taper. These results are presented in Figure 9.5, where $\frac{1}{\tau} - \frac{1}{\tau_0}$ versus concentration is plotted for a selection of large-core optical fibre tapers. The gradient of the line for each different taper can be converted into the l_{eff} given rearrangement of Equation 2.15. In this manner, the l_{eff} for the large-core optical fibre tapers presented in Figure 9.5 was determined to range from 0.4 to 11 μm.

Given the determined pre-etch ringdown time and post-etch ringdown time and known loop length, it was determined using Equation 9.2 that the total round-trip losses before creation of the taper were around 5% and the total round-trip losses after creation of the taper were around 8%, leading to a taper loss of around 3% for the large-core optical fibre. This taper loss can be compared to the gap loss determined in Section 9.1, where a gap loss of 1.9% was determined for l = 130 μm for large-core optical fibre. This indicates that direct absorption is preferred over evanescent wave absorption for the notch-coupled large-core optical fibre, where significantly longer pathlengths can be achieved from direct absorption compared to evanescent wave absorption.

9.4 Conclusions

We have investigated the sensitivity of several fibre-loop CRDS set-ups, and have found that while typical fibre-loop approaches have a low finesse, demonstrated by the measurement of only 2 – 4 passes in one ringdown time (N_τ, Table 8.1), our reflective notch-coupled large-core fibre cavity approach has a slightly improved $N_\tau = 12$, which can be compared with $N_\tau = 6$ that we established for our bend-coupled small-core fibre cavity. Nevertheless, these enhancement values are significantly lower than that which can be achieved with a two-mirror cavity, even when a relatively low loss chip is inserted into a two-mirror cavity. It seems to be a somewhat unfortunate fact that the highest sensitivity sensing regions entail the highest insertion losses, which causes the fibre cavity set-ups designed for chemical sensing applications to tend towards single-pass experiments in reality. Given the additional complication the use of a cavity occasions through the necessity to side-couple light into the fibre core, unless the cavity enhancement can be improved further, it does not seem that fibre-loop cavities are worth pursuing further for chemical sensing.

Chapter 10

Concluding remarks

10.1 Conclusions

We have examined the potential of multi-pass absorption spectroscopy to improve sensitivity in the analysis of small volume (sub-microlitre) liquid-phase samples. We have demonstrated for the first time the coupling of both two-mirror cavity ringdown spectroscopy (Chapter 3) and cavity enhanced absorption spectroscopy (Chapter 5) with a microfluidic chip. The sensitivity of these techniques depends on the optical loss associated with the microfluidic chip, which we have found to vary both between chips and across the same chip. Nevertheless, we have demonstrated the possibility of monitoring both continuous flow and droplet flow on-chip, using both CRDS and CEAS. The CEAS results are particularly interesting as they allow for the acquisition of the full visible spectrum (430 nm $< \lambda <$ 700 nm) of each droplet passing the laser beam, in an acquisition time of 4 ms.

In Chapter 4, we demonstrated high sensitivity CRDS detection of two analytes commonly found in aquatic and marine environments, nitrite and iron. Each analyte was detected by converting it selectively into a strongly-coloured derivative compound, providing a large 'chemical-enhancement' of the absorption signal. By monitoring the optical absorption of the coloured product using CRDS, we gain additional 'cavity enhancement'. This double signal amplfication has allowed us to detect nanomolar concentrations of both nitrite and iron, when the liquid sample is contained within a high optical-quality flow cell with a pathlength of 1 mm.

We applied CEAS broadband detection in Chapter 6 to reaction analysis, including a study of a model Diels-Alder reaction which was carried out on-chip. Chapter 7 presented the utility of dual wavelength monitoring to pH detection in short optical pathlengths, achieving a measurable pH sensitivity of 0.028 pH units using a 2 mm pathlength flow cell. The determination of our detection sensitivity was limited by the accuracy of

the pH electrode used to determine the pH of the standard sample solutions. Based on a consideration of the signal-to-noise ratio of our ringdown data, we believe the technique has a potential sensitivity of 0.00078 pH units using a 2 mm pathlength flow cell.

Finally, in Chapters 8 and 9, we investigated the performance of an alternative type of cavity, based on a loop of optical fibre. Sample detection via both direct absorption and evanescent wave absorption has been examined in a loop fabricated from small-core (50 μm) multimode optical fibre. The use of large-core optical fibres in such measurements has been limited up until now by the high losses associated with available schemes for coupling light into and out of the loop. To overcome this, a novel light coupling strategy for large-core optical fibre was designed and fabricated in our laboratory. The new coupler allows for both high efficiency light coupling and low loss per pass, which is unusual for cavity-based experiments. Despite our improvements to the conventional fibre-loop CRD spectrometer, the sensitivity of this approach remains significantly lower than that which can be achieved using two-mirror cavities, even with inserted flow cells. This is due to the intrinsically much higher losses in an optical fibre-loop compared with a two-mirror cavity. For example, absorptions from the fibre will typically contribute a loss per pass of a few percent, before additional losses associated with the sample region and input and output couplers have been included. Although the cavity enhancement remains low, we have improved this by an order of magnitude over that commonly found in the literature [336].

In summary, we have demonstrated that cavity enhanced absorption spectroscopies can provide significant improvements to small volume analysis compared with single-pass absorption experiments. There are many directions in which we could take this research in the future. Below we consider a few possibilities.

10.2 Future work

The future work arising from this thesis can be separated into three key areas, which will be discussed in turn. Firstly, in Chapter 4, we demonstrated that chemically-enhanced CRDS shows considerable potential for marine sensing, but that for micronutrients such as iron, our detection sensitivity still needs to be improved by several orders of magnitude in order to be able to detect iron at ambient concentrations in all ocean environments. One promising strategy will be discussed in Section 10.2.1.

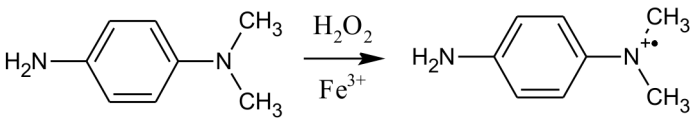
Secondly, chemically-enhanced CRDS is a general technique which allows for the quantitative detection of any analyte present at low concentration in solution, provided that a suitable colourimetric reaction for the analyte can be identified. While we have so far focused our attention on environmental sensing, there are a variety of applications in clinical chemistry which are also important. We discuss one colourimetric reaction, used for detecting acetone, in Section 10.2.2.

Finally, for many of the potential applications to be realised, our set-up needs to be miniaturized and consolidated into a stand-alone instrument, which can be packaged either into a benchtop instrument or a remote sensor. We discuss the challenges associated with miniaturization in Section 10.2.3.

10.2.1 Improving the sensitivity of iron detection

In Chapter 4, we demonstrated detection of Fe(II) down to a concentration of 4 nM. In surface seawater, iron is often present at concentrations as low as 0.02 nM [198, 322], so that quantitative detection of iron in such environments requires us to improve our detection sensitivity by a factor of 200.

One potential method to improve the absorption sensitivity is to use a technique known as catalytic spectrophotometry, which exploits the ability of iron to catalyse reactions that can be monitored spectrophotometrically. This technique was introduced briefly at the end of Chapter 4. Catalytic spectrophotometry has a number of potential benenfits over conventional end-point analysis, including a reduction in the required reaction time, and, most importantly, improved sensitivity of analysis. In the case of iron, there exists a room-temperature catalytic reation that allows for the detection of iron based on its catalytic effect on the oxidation of N,N-dimethyl-p-phenylenediamine by hydrogen peroxide in weakly acidic media [236, 239, 240]. The reaction scheme can be written as follows:



The radical cation produced by this reaction absorbs light strongly between 500 nm and 560 nm. In the absence of iron(III), the reaction proceeds very slowly. The catalytic mechanism of iron(III) occurs as follows. Iron(III) reacts quantitatively with N,N-dimethyl-p-phenylenediamine to form the radical product. The reduced iron(II) is then oxidised to iron(III) by hydrogen peroxide, which can then proceed to react with N,N-dimethyl-p-phenylenediamine again. Both iron(II) and iron(III) are therefore detected using this reaction. The absorbance was originally monitored after a reaction time of 5 minutes [236], although more recently Measures et al. reoptimised the reaction conditions to allow for detection after a reduced reaction time of 1 minute [239]. The interference of several ions was tested and only copper at concentrations above 160 nM was found to interfere [236]. Hirayama and Unohara established a detection limit for iron of 0.71 nM, determined in a 1 cm cuvette without preconcentration, and reported the molar absorption coefficient at 514 nm to be $\alpha = 3.9 \times 10^7$ M^{-1} cm^{-1} [236]. Given that this α is over 750 times that of the bathophenanthroline method we used in Chapter 4, it is expected that we will be able to achieve sufficient sensitivity using this method to measure iron even at the low concentrations (down to 0.02 nM) found in surface seawater. This will of course rely upon minimising the 'blank' levels of iron in our deionised water and reagents.

We plan to carry out this reaction in our two-mirror CRDS set-up outlined in Chapters 3 and 4, to ascertain the sensitivity of iron detection using this kinetic method compared with conventional end-point analysis. It is expected that the detection limit will improve sufficiently to allow for picomolar detection of iron to be achieved. This would be a significant achievement, particularly as no preconcentration step is required.

10.2.2 Clinical applications

While the assays used in Chapter 4 for nitrite and iron were developed with water sensing applications in mind, it is worth noting that both analytes are also important to detect in clinical diagnostics. For example, the presence of nitrite in saliva and breath is correlated with respiratory inflammation, and blood levels are known to be raised in individuals with diseases such as asthma and cystic fibrosis [373]. Whole blood nitrite levels in healthy volunteers range from 85 to 137 nM [374], while nitrite in breath condensate has a median concentration of 0.33 μM [375]. These levels lie an order of magnitude above the detection limit already established for nitrite using our optimised CRDS set-up described in Chapter 3.

The potential of CRDS for breath analysis has already been reported in the literature (see Chapter 8 of [1]). There are many analytes present in trace amounts in breath that can act as biomarkers for various diseases, and this has been the subject of several recent reviews [376,377]. In particular, the reader is directed to a thorough recent review, which describes detection in the UV, near-IR and mid-IR for a range of analytes [378]. Breath analytes are in equilibrium via capillary exchange in the lungs with dissolved volatile species in the blood, and therefore any species present in breath will also be present in higher concentrations in blood, and most probably also in other fluids such as urine or saliva. We could potentially use our chemically-enhanced CRDS technique to analyse such fluids.

Acetone is a key analyte because it is a biomarker of diabetic ketosis and is found in significantly elevated concentrations in poorly controlled diabetic patients [379]. There are several colourimetric reactions that can increase the absorption sensitivity of liquid-phase acetone detection, including reaction with vanillin [380], salicyladehyde [381] and nitroprusside [382]. We are particularly interesting in the nitroprusside reaction because the coloured product is red and can therefore be detected either using our optimised set-up described in Chapter 3 or Chapter 5. The nitroprusside reaction with acetone under basic conditions is the basis of the commercially available qualitative urine test, known as Acetest [383]. However, the solution stability is known to be poor. This is demonstrated in a Figure 10.1(a), which is a plot of κ versus wavelength measured in a commercial UV/vis spectrometer, for a final reaction mixture of 23 mM acetone, 0.8 M sodium hydroxide and 30 mM sodium nitroprusside, all dissolved in deionised water. Figure 10.1(b) presents a photograph of the reaction products for an example 'blank' and for an acetone sample. For maximum sensitivity, the reaction must be carried out by introducing the acetone to the nitroprusside before adding the base, and an absorption measurement should be made as soon as possible after thorough mixing, ideally within the first minute. The

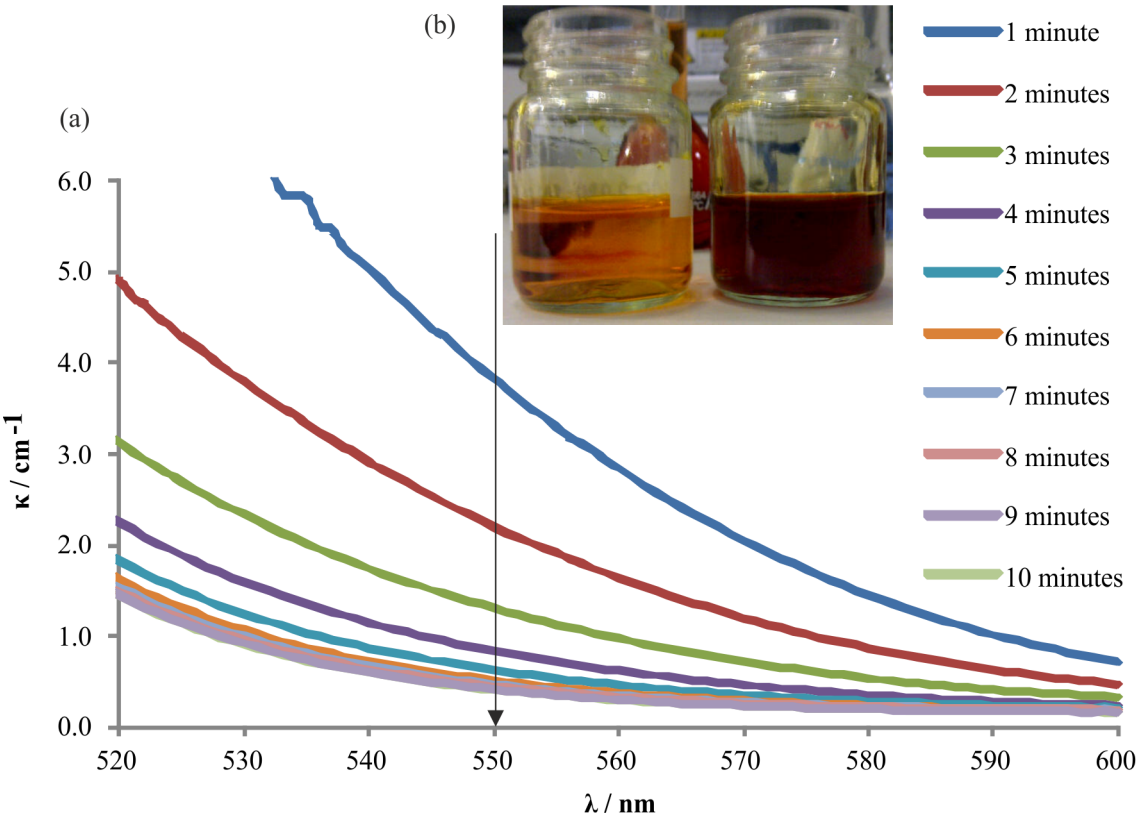


Figure 10.1: (a) Single-pass UV/vis spectrometer measurement of κ versus wavelength. A trace was recorded every 1 minute for 10 minutes, and the absorption was seen to decrease rapidly over time. (b) Photograph of 'blank' (left hand beaker) and 0.23 M acetone sample (right hand beaker).

tightly controlled reaction conditions required for this reaction make inline flow analysis an attractive choice for investigating the nitroprusside acetone test.

The detection limit established in a 1 cm cuvette for a concentration series of acetone (not shown) can be estimated to be around 1 mM acetone. Given that the first trace was acquired one minute after mixing, and the absorbance dropped rapidly over the first few minutes, a significant improvement in detection limit can be expected by probing closer to the start of the reaction, which is possible in a flow system. In addition, carrying out the reaction in a cavity will improve the sensitivity, leading to an expected detection limit around the micromolar concentration level for acetone. In contrast, the commercially available Acetest has a detection limit of around 3.4 mM [383]. These values can be compared to the typical ('normal') acetone blood and urine levels of around 14 μM [384]. The ability to accurately determine blood and urine 'normal' levels could provide a useful indicator of smaller scale variations than can currently be detected using techniques like the Acetest.

10.2.3 Set-up miniaturization

Over the course of the work described in this thesis, we have seen that inserting chips into cavities can be problematic. In addition, our current experimental set-up is very far away from being what may be termed the 'holy grail' of microfluidics, a micro-total analysis system (μTAS) [3]. As Fair notes in his excellent 2007 review, entitled 'Is a true lab-on-a-chip possible?': "The general trend in commercial devices has been to fabricate simple, disposable devices that are designed to interface with an expensive box that houses the required control electronics, reagent supply, detectors, and programming" [385]. This is essentially the approach that we have taken in this thesis. However, a better strategy towards realising a full lab-on-a-chip would be to integrate the optics and detection with the microfluidic chip itself. In essence, this would involve placing a cavity within a chip rather than a chip within a cavity. The use of a loop of optical fibre rather than a long two-mirror cavity fits within this ethos. However, as we have seen, the sensitivity of such miniaturized approaches is likely to be poorer. There are, however, some exciting possibilities that we will briefly outline below.

An interesting variant of CEAS is to integrate the mirrors into the microfluidic chip itself. This was the subject of a short paper by Billot et al. in 2008 [386]. In their work, 100 nm thick gold mirrors were deposited on the inner surfaces of two glass substrates, which were then bonded together with a 50 μm height channel fabricated in PDMS. A standard microscope halogen lamp was used as the light source, after focusing through a $\times 20$ objective. The detector was a 200 μm core diameter optical fibre-coupled spectrometer. With 100 nm thick gold mirrors, the spectrum of rhodamine B was acquired between 500 - 600 nm, and an increase in absorbance of a factor of five was found compared to an uncoated channel. This allowed a 5 μM rhodamine B solution to be detected with the 100 nm thick gold mirrors, which could not be detected in an uncoated channel. The authors note that this is a proof-of-principle experiment, and that increasing the quality factor of the cavity will continue to improve the detection limits. For example, when 150 nm gold mirrors were deposited, the sensitivity enhancement was 50 times that of an uncoated channel.

This type of cavity is attractive for two reasons: firstly, the metal mirrors have a much smoother broadband profile than most dielectric mirrors, and secondly, this system is much more capable of miniaturization and deployment in the field, because the cavity surfaces are integrated into the microfluidic chip itself. This means that mirror alignment is not required after device fabrication. However, there are also several problems: notably, the mirror surfaces come into direct contact with the solution, which means that the mirrors would probably need to be replaced on a regular basis, to avoid fouling and decrease in the cavity finesse. Additionally, matching the cavity finesses achieved with dielectric mirrors would be a challenge, as the metal mirrors are less reflective than the dielectric ones. The perfect alignment of the mirrors is also more challenging in the case of the integrated mirrors: for the most stable cavity (and hence highest sensitivity enhancement), the planar mirror surfaces must be perfectly parallel, something which may be

difficult to achieve during microfluidic chip fabrication. Nevertheless, for remotely deployable devices, this integrated mirror cavity shows great promise.

It should be noted that the development of this type of absorption device is likely to continue, as the development of microfluidic laser systems, also requiring high finesse optical cavities, develops, given that many of the fabrication techniques are the same (see, for example [387, 388]). The reader is directed to an excellent overview of the field of optofluidics, and the references therein [389]. Some interesting examples of new cavity designs based on total internal reflection to create a cavity around a microfluidic channel will be briefly highlighted. Song et al. [390] designed a cavity based on tuneable "air mirrors" fabricated in PDMS, which function in a similar way to those of Llobera et al. discussed in Chapter 1 [127]. Gersborg-Hansen built a microfluidic resonator from two isosceles triangles formed in SU8 and surrounded by air (see Figure 1 of [391]): total internal reflection maintained the light in the cavity, and to couple light out the refractive index of an adjacent channel was alternately filled with air (cavity build-up) and ethanol (cavity output) [391]. One particularly interesting example is that of Galas et al., who fabricated a laser cavity by depositing gold mirrors on two optical fibre ends inserted into a microfluidic chip with two channels in between the optical fibre ends [392]. One channel (filled with rhodamine 6G) was used for laser amplification, and one channel was filled with different absorbing solutions. The lasing output is highly sensitive to cavity loss, which is dependent on the concentration of absorbing species introduced into the cavity. In this manner, micromolar methylene blue dye solutions could be detected in an optical pathlength of 140 μm.

We are currently collaborating with Dr. Jason Smith in the Department of Materials at the University of Oxford on the application of micro-cavities to chemical sensing. The Smith research group fabricates femtolitre optical cavity arrays using focused-ion beam milling [393]. Plano-concave cavities with radius of curvature 25 μm and cavity length 4.6 μm have been fabricated in fused silica, and then custom-coated to produce mirrors with a reflectivity of 99.4% at 637 nm. The challenge in this collaboration is to integrate the micro-cavity array with fluid inlets and outlets which allow for filling and emptying the cavities.

It is expected that improvements in low-loss microfabrication of cavities will, when coupled with portable light sources (LEDs) and detectors (photodiodes), lead to great improvements in the development of a μTAS cavity enhanced absorption experiment. Improvements of several orders of magnitude in sensitivity can be expected with optimised set-ups. We believe that such a system could be particularly useful for making *in situ* measurements in aquatic and marine environments.

10.2.4 Sensor Deployment

A key research objective of the chemical oceanography community is to be able to measure dissolved chemical species in real-time in a large number of locations across the globe. This can only be achieved

using a network of remotely-deployed sensors. It is worth mentioning briefly that the networks already exist to enable miniaturized sensor deployment for oceanographic monitoring [394]. Measurements are particularly challenging because of the low concentrations of many of the ocean elements, especially in surface seawater. We are starting a collaboration with the National Oceanographic Centre at the University of Southampton, looking at the possibility of deployment of miniaturized versions of our cavity sensors. Several schemes for sensor deployment already exist, of which three will be mentioned here: (a) 'Ferrybox' or ships of oppportunity, (b) 'Gliders' and (c) Argo floats. Some graphics from the relevant websites for these networks are presented in Figure 10.2. In all three schemes, the challenges of biofouling and sensor degradation over time must be overcome.

The 'Ferrybox' scheme involves placing sensors onto commercial ships and can act as a midway point between ship-board analysis and buoy-based sensors. For example, sensors on a ferry are under controlled conditions (flow, temperature and shock), the energy consumption and mechanical dimensions are not critical, and the maintenance is cheaper and easier than offshore installations.

In contrast, schemes (b) and (c) employ autonomous underwater vehicles. Sensors placed on these probes must comply to exacting power and space requirements. 'Gliders' are autonomous underwater vehicles, which can 'fly' from the surface down to 1 km depth, while travelling around 5 km horizontally, in around 3 hours. Typically, gliders monitor pressure, temperature and conductivity. The two-way communication via satellite means that gliders can alter their sampling strategy in response to the data acquired in real-time. In addition, sensors for measuring chlorophyll-a, dissolved organic matter and dissolved oxygen concentrations are already being added to glider systems.

The Argo programme consists of a large collection of small, drifting oceanic robotic probes deployed worldwide. In a typical mission, the floats descend to a target depth of 1 km to drift and then descend again to 2 km before profiling the temperature, pressure and salinity in a series of measurements made during their ascent back up to the surface.

All three of these schemes present an exciting end-goal for deployment of a miniaturized sensor. Many biogeochemical sensors are currently not sensitive enough to probe the low concentrations of many elements found in the surface of the ocean. By implementing a cavity sensing set-up, we have the potential to improve the sensitivity sufficiently to be able to make real-time measurements of ambient concentrations.

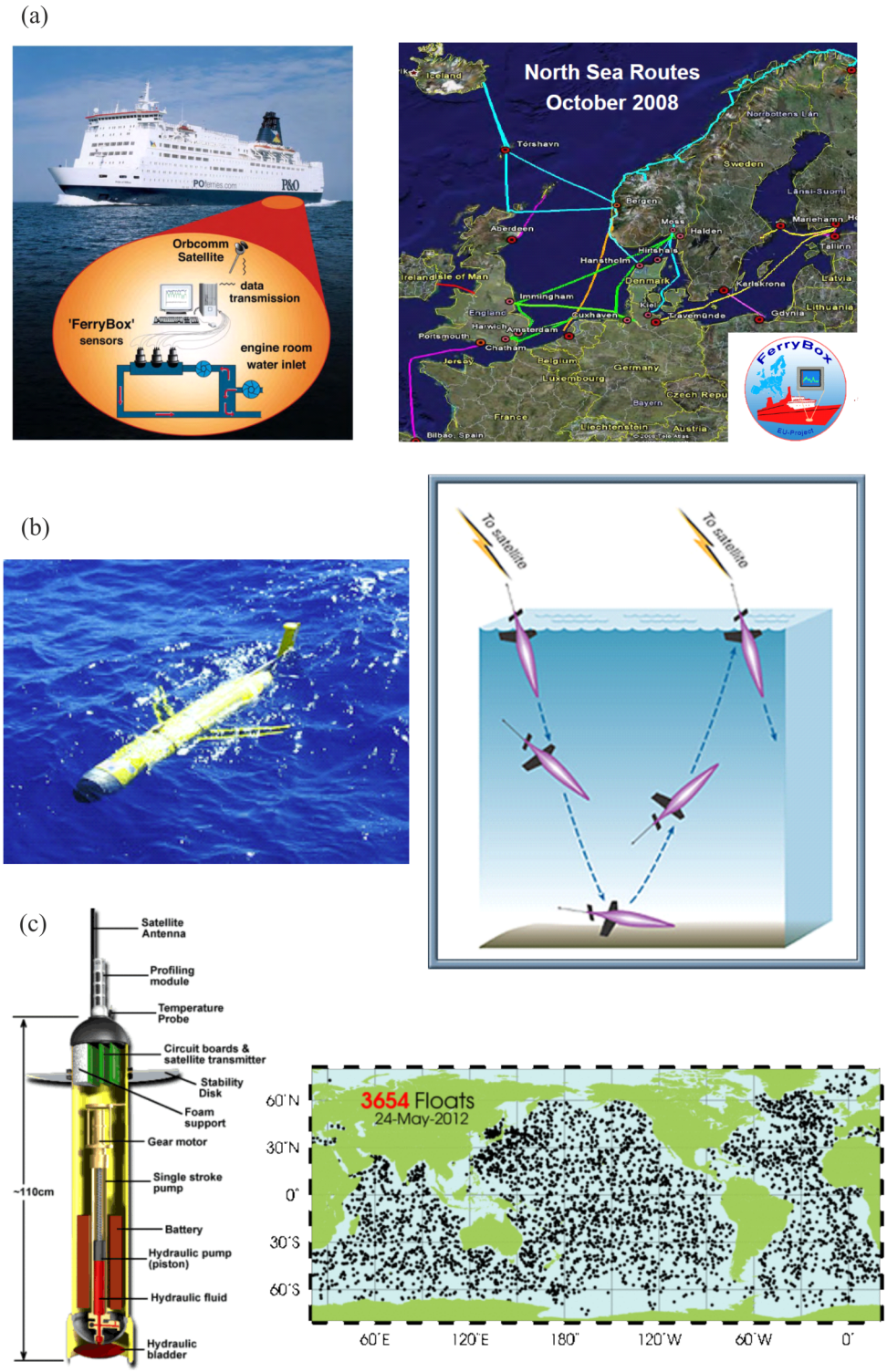


Figure 10.2: (a) 'Ferrybox' or ships of opportunity scheme. Images reproduced from www.ferrybox.org. (b) 'Gliders' scheme. Images reproduced from www.noc.soton.ac.uk/omf/projects/glider/index.php. (c) Argo floats scheme. Images reproduced from www.argo.ucsd.edu.

Appendix A

Determination of ΔpH$_{\mathrm{min}}$

The normalised root mean square error (NRMSE) is found by first determining the root mean square error:

$$\mathrm{RMSE} = \sqrt{\frac{\sum_{\mathrm{i=1}}^{\mathrm{n}} \left(\mathrm{x_{o,i}} - \mathrm{x_{t,i}}\right)}{\mathrm{n}}} \tag{A.1}$$

where x is either the single wavelength absorbance, or the ratio of the absorbance at two different wavelengths, x_o is the experimentally determined value and x_t is the predicted value, calculated using either Equation 7.6 or 7.11 for each pH measurement i, where n is the total number of measurements. The root mean square error is normalised by dividing the RMSE by the difference between the maximum and minimum experimentally determined x_o values, and converting this value into a percentage:

$$\mathrm{NRMSE} = \frac{\mathrm{RMSE}}{\mathrm{x_{0,max}} - \mathrm{x_{0,min}}} \times 100 \tag{A.2}$$

The pH accuracy is determined in the following manner. Firstly, the root residual squared between the experimentally measured absorbance values and the Henderson-Hasselbalch equation (either Equation 7.6 or 7.11) is determined. This provides a measure of the absorbance error, ΔA_{min}, which can be converted into the minimum detectable change in pH, $\Delta\mathrm{pH_{min}}$ for either single or dual-wavelength by rearrangement of either Equation 7.6 or 7.11 as described below.

$\Delta\mathrm{pH_{min}}$ can be established from single-wavelength measurements, by rewriting Equation 7.6 as the difference between two pH measurements:

$$\begin{aligned}\Delta\mathrm{pH} &= \left(\mathrm{p}K_\mathrm{a} + \log\frac{A_0/(\alpha l)}{[\mathrm{Ind}]_\mathrm{tot} - (\mathrm{A}_0/(\alpha \mathrm{l}))}\right) - \left(\mathrm{p}K_\mathrm{a} + \log\frac{(A_1)/(\alpha l)}{[\mathrm{Ind}]_\mathrm{tot} - (\mathrm{A}_1)/(\alpha \mathrm{l}))}\right) \\ &= \log\frac{A_0}{\alpha l[\mathrm{Ind}]_\mathrm{tot} - \mathrm{A}_0} - \log\frac{A_1}{\alpha l[\mathrm{Ind}]_\mathrm{tot} - \mathrm{A}_1}\end{aligned} \tag{A.3}$$

and then rearranging Equation A.3, given the approximation that $\mathrm{Ind_T}\alpha\mathrm{l} - \mathrm{A}_1 \approx \mathrm{Ind_T}\alpha\mathrm{l} - \mathrm{A}_0$ when $A_1 = A_\mathrm{min}$ to produce:

$$\Delta\mathrm{pH}_\mathrm{min} = \log\frac{\mathrm{A}_0}{\mathrm{A}_\mathrm{min}} = \log\frac{\mathrm{A}_0}{\mathrm{A}_0 - \Delta\mathrm{A}_\mathrm{min}} \tag{A.4}$$

where A_0 is the theoretical absorbance at a given pH, and A_min is the minimum detectable absorbance smaller than A_0, usually written as $A_\mathrm{min} = A_0 - \Delta A_\mathrm{min}$, where ΔA_min is the minimum detectable change in absorbance, defined as the root residual squared between experiment and theory a given measured pH. To produce a final $\Delta\mathrm{pH}_\mathrm{min}$ for each set-up, the average of Equation A.4 across all pH values measured experimentally is calculated. These values are presented in Table 7.3.

In a similar manner, $\Delta\mathrm{pH}_\mathrm{min}$ can be established from dual-wavelength measurements, by rewriting Equation 7.11 as the difference between two pH measurements:

$$\begin{aligned}\Delta\mathrm{pH} &= \left(\mathrm{p}K_\mathrm{a} + \log\frac{Q_0}{e_2 - Q_0}\right) - \left(\mathrm{p}K_\mathrm{a} + \log\frac{Q_1}{e_2 - Q_1}\right) \\ &= \log\frac{Q_0}{e_2 - Q_0} - \log\frac{Q_1}{e_2 - Q_1}\end{aligned} \tag{A.5}$$

and then rearranging Equation A.5, given the approximation that $e_2 - Q_1 \approx e_2 - Q_0$ when $Q_1 = Q_\mathrm{min}$ to produce:

$$\Delta\mathrm{pH}_\mathrm{min} = \log\frac{\mathrm{Q}_0}{\mathrm{Q}_\mathrm{min}} = \log\frac{\mathrm{Q}_0}{\mathrm{Q}_0 - \Delta\mathrm{Q}_\mathrm{min}} \tag{A.6}$$

where Q_0 is the ratio of the absorbances at two wavelengths at a given pH, and Q_min is the minimum detectable absorbance ratio smaller than Q_0, usually written as $Q_\mathrm{min} = Q_0 - \Delta Q_\mathrm{min}$, where ΔQ_min is the minimum detectable change in absorbance ratios, which is defined as the root residual squared between experiment and theory a given measured pH. To produce a final $\Delta\mathrm{pH}_\mathrm{min}$ for each set-up, the average of Equation A.6 across all pH values measured experimentally is calculated. These values are presented in Table 7.3.

Bibliography

[1] G. Berden and R. Engeln, *Cavity ring-down spectroscopy: techniques and applications*. John Wiley and Sons, Inc., 2009.

[2] G. M. Whitesides, "The origins and the future of microfluidics," *Nature*, vol. 442, pp. 368–373, 2006.

[3] A. Manz, "Miniaturized Total chemical Analysis Systems: a novel concept for chemical sensing," *Sens. Actuators, B,*, vol. 1, pp. 244–248, 1990.

[4] D. Reyes, D. Lossifidis, P. Auroux, and A. Manz, "Micro Total Analysis Systems. 1. Introduction, Theory, and Technology," *Anal. Chem.*, vol. 74, pp. 2623–2636, 2002.

[5] P. Auroux, D. lossifidis, D. Reyes, and A. Manz, "Micro Total Analysis Systems. 2. Analytical Standard Operations and Applications," *Anal. Chem.*, vol. 74, pp. 2637–2652, 2002.

[6] H. Song, J. D. Tice, and R. F. Ismagilov, "A microfluidic system for controlling reaction networks in time," *Angew. Chem. Int. Ed.*, vol. 42, no. 7, pp. 767–772, 2003.

[7] H. Song and R. F. Ismagilov, "Millisecond kinetics on a microfluidic chip using nanoliters of reagents," *J. Am. Chem. Soc.*, vol. 125, no. 47, pp. 14613–14619, 2003.

[8] H. Song, D. L. Chen, and R. F. Ismagilov, "Reactions in droplets in microfluidic channels," *Angew. Chem. Int. Ed.*, vol. 45, no. 44, pp. 7336–7356, 2006.

[9] A. Huebner, S. Sharma, M. Srisa-Art, F. Hollfelder, J. B. Edel, and A. J. deMello, "Microdroplets: A sea of applications?," *Lab Chip*, vol. 8, pp. 1244–1254, 2008.

[10] X. C. Solvas and A. J. deMello, "Droplet microfluidics: recent developments and future applications," *Chem. Comm.*, vol. 47, pp. 1936–1942, 2011.

[11] D. M. Ratner, "Microreactor-based reaction optimization in organic chemistry: glycosylation as a challenge," *Chem. Comm.*, vol. 2005, no. 5, p. 578, 2005.

[12] P. S. Dittrich and A. Manz, "Lab-on-a-chip: microfluidics in drug discovery," *Nature Reviews. Drug Discovery*, vol. 5, pp. 210–218, 2006.

[13] M. C. Mitchell, "Microchip-based synthesis and total analysis systems (μSYNTAS): chemical microprocessing for generation and analysis of compound libraries," *J. Chem. Soc. Perkin Transactions 1*, vol. 2001, no. 5, p. 514, 2001.

[14] E. Garcia-Egido, "Synthesis and analysis of combinatorial libraries performed in an automated micro reactor system," *Lab on a chip*, vol. 3, no. 2, p. 73, 2003.

[15] J. Khandurina and A. Guttman, "Bioanalysis in microfluidic devices," *J. Chromatogr. A*, vol. 943, no. 2, pp. 159–183, 2002.

[16] N. Lion, "Why the move to microfluidics for protein analysis?," *Current opinion in biotechnology*, vol. 15, no. 1, p. 31, 2004.

[17] F.-C. Huang, C.-S. Liao, and G.-B. Lee, "An integrated microfluidic chip for DNA/RNA amplification, electrophoresis separation and on-line optical detection," *Electrophoresis*, vol. 27, pp. 3297–3305, 2006.

[18] B. Zheng, L. S. Roach, and R. F. Ismagilov, "Screening of protein crystallization conditions on a microfluidic chip using nanoliter-size droplets," *J. Am. Chem. Soc.*, vol. 125, no. 37, p. 11170, 2003.

[19] I. Shestopalov, J. D. Tice, and R. F. Ismagilov, "Multi-step synthesis of nanoparticles performed on millisecond time scale in a microfluidic droplet-based system," *Lab Chip*, vol. 4, p. 316, 2004.

[20] A. Daridon, M. Sequiera, G. Pennarun-Thomas, H. Dirac, J. P. Krog, P. Gravesen, J. Lichtenberg, D. Diamond, E. Verpoorte, and N. F. de Rooij, "Chemical sensing using an integrated microfluidic system based on the Berthelot reaction," *Sens. Actuators, B*, vol. 76, pp. 235–243, 2001.

[21] S. Ramirez-Garca, M. Baeza, M. O'Toole, Y. Wu, J. Lalor, G. G. Wallace, and D. Diamond, "Towards the development of a fully integrated polymeric microfluidic platform for environmental analysis," *Talanta*, vol. 77, no. 2, pp. 463–467, 2008.

[22] J. V. Sieben, C. F. A. Floquet, I. R. G. Ogilvie, M. C. Mowlem, and H. Morgan, "Microfluidic colourimetric chemical analysis system: Application to nitrite detection," *Anal. Methods*, vol. 2, pp. 484–491, 2010.

[23] C. F. A. Floquet, V. J. Sieben, A. Milani, E. P. Joly, I. R. G. Ogilvie, H. Morgan, and M. Mowlem, "Nanomolar detection with high sensitivity microfluidic absorption cells manufactured in tinted PMMA for chemical analysis," *Talanta*, vol. 84, pp. 235–239, 2011.

[24] A. D. Beaton, V. J. Sieben, C. F. A. Floquet, E. M. Waugh, S. A. K. Bey, I. R. G. Ogilvie, M. C. Mowlem, and H. Morgan, "An automated microfluidic colourimetric sensor applied in situ to determine nitrite concentration," *Sens. Actuators, B*, vol. 156, no. 2, pp. 1009–1014, 2011.

[25] T. Fukuba, Y. Aoki, N. Fukuzawa, T. Yamamoto, M. Kyo, and T. Fujii, "A microfluidic in situ analyser for ATP quantification in ocean environments," *Lab Chip*, vol. 11, pp. 3508–3515, 2011.

[26] J. C. Jokerst, J. M. Emory, and C. S. Henry, "Advances in microfluidics for environmental analysis," *Analyst*, vol. 137, no. 1, pp. 24–34, 2012.

[27] T. M. Squires and S. R. Quake, "Microfluidics: Fluid physics at the nanoliter scale," *Rev. Mod. Phys.*, vol. 77, pp. 977–1026, 2005.

[28] A. J. deMello, "Control and detection of chemical reactions in microfluidic systems," *Nature*, vol. 442, pp. 394–402, 2006.

[29] J. P. Landers, *Handbook of Capillary and Microchip Electrophoresis and Associated Microtechniques*. CRC Press, 2007.

[30] E. M. Purcell, "Life at low Reynolds number," *American J. Phys.*, vol. 45, no. 1, pp. 3–11, 1976.

[31] N. Rott, "Note on the history of the Reynolds' number," *Ann. Rev. Fluid Dynam.*, vol. 22, pp. 1–11, 1990.

[32] J. M. Ottino and S. Wiggins, "Introduction: mixing in microfluidics," *Phil. Trans. R. Soc. Lond. A*, vol. 362, pp. 923–935, 2004.

[33] M. A. Stremler, F. R. Haselton, and H. Aref, "Designing for chaos: applications of chaotic advection at the microscale," *Phil. Trans. R. Soc. Lond. A*, vol. 362, pp. 1019–1036, 2004.

[34] L. Capretto, W. Cheng, M. Hill, and X. Zhang, "Micromixing within microfluidic devices," *Top. Curr. Chem.*, vol. 304, pp. 27–68, 2011.

[35] S. A. Pabit and S. J. Hagen, "Laminar-flow fluid mixer for fast fluorescence kinetics studies," *Biophysical J.*, vol. 83, p. 28722878, 2002.

[36] J. B. Callis, D. L. Illman, and B. R. Kowalski, "Process analytical," *Anal. Chem.*, vol. 59, no. 9, pp. 624A–637A, 1987.

[37] Z. T. Cygan, J. T. Cabral, K. L. Beers, and E. J. Amis, "Microfluidic platform for the generation of organic-phase microreactors," *Langmuir*, vol. 21, no. 8, pp. 3629–3634, 2005.

[38] S. Koster and E. Verpoorte, "A decade of microfluidic analysis coupled with electrospray mass spectrometry: An overview," *Lab Chip*, vol. 7, pp. 1394–1412, 2007.

[39] V. Skelton, G. M. Greenway, S. J. Haswell, P. Styring, D. O. Morgan, B. Warrington, and S. Y. F. Wong, "The preparation of a series of nitrostilbene ester compounds using micro reactor technology," *Analyst*, vol. 126, pp. 7–10, 2001.

[40] V. Skelton, G. M. Greenway, S. J. Haswell, P. Styring, D. O. Morgan, B. Warrington, and S. Y. F. Wong, "The generation of concentration gradients using electroosmotic flow in micro reactors allowing stereoselective chemical synthesis," *Analyst*, vol. 126, pp. 11–13, 2001.

[41] T. Kawaguchi, H. Miyata, K. Ataka, K. Mae, and J.-i. Yoshida, "Room-temperature Swern oxidations by using a microscale flow system," *Angew. Chem.*, vol. 44, no. 16, pp. 2413–2416, 2005.

[42] M. Sands, S. J. Haswell, S. M. Kelly, V. Skelton, D. O. Morgan, P. Styring, and B. Warrington, "The investigation of an equilibrium dependent reaction for the formation of enamines in a microchemical system," *Lab Chip*, vol. 1, no. 1, pp. 64–65, 2001.

[43] C. Wiles, P. Watts, S. J. Haswell, and E. Pombo-Villar, "The aldol reaction of silyl enol ethers within a micro reactor," *Lab Chip*, vol. 1, no. 2, pp. 100–101, 2001.

[44] C. Wiles, P. Watts, S. J. Haswell, and E. Pombo-Villar, "1,4-addition of enolates to α, β-unsaturated ketones within a micro reactor," *Lab Chip*, vol. 2, no. 2, pp. 62–64, 2002.

[45] J. P. McMullen, M. T. Stone, S. L. Buchwald, and K. F. Jensen, "An integrated microreactor system for self-optimization of a Heck reaction: from micro- to mesoscale flow systems," *Angew. Chem. Int. Ed.*, vol. 49, pp. 7076–7080, 2010.

[46] J. P. McMullen and K. F. Jensen, "Rapid determination of reaction kinetics with an automated microfluidic system," *Org. Proc. Res. Devel.*, vol. 15, no. 2, pp. 398–407, 2011.

[47] K. Swinney and D. J. Bornhop, "Detection in capillary electrophoresis," *Electrophoresis*, vol. 21, no. 7, pp. 1239–1250, 2000.

[48] M. A. Schwarz and P. C. Hauser, "Recent developments in detection methods for microfabricated analytical devices," *Lab Chip*, vol. 1, pp. 1–6, 2001.

[49] K. B. Mogensen, H. Klank, and J. P. Kutter, "Recent developments in detection for microfluidic systems," *Electrophoresis*, vol. 25, pp. 3498–3512, 2004.

[50] C. Yi, Q. Zhang, C.-W. Li, J. Yang, J. Zhao, and M. Yang, "Optical and electrochemical detection techniques for cell-based microfluidic systems," *Anal. Bioanal. Chem.*, vol. 384, no. 6, pp. 1259–1268, 2006.

[51] B. Kuswandi, Nuriman, J. Huskens, and W. Verboom, "Optical sensing systems for microfluidic devices: A review," *Anal. Chim. Acta*, vol. 601, pp. 141–155, 2007.

[52] H. C. Hunt and J. S. Wilkinson, "Optofluidic integration for microanalysis," *Microfluid. Nanofluid.*, vol. 4, pp. 53–79, 2008.

[53] F. B. Myers and L. P. Lee, "Innovations in optical microfluidic technologies for point-of-care diagnostics," *Lab Chip*, vol. 8, pp. 2015–2031, 2008.

[54] M. O'Toole and D. Diamond, "Absorbance based light emitting diode optical sensors and sensing devices," *Sensors*, vol. 8, pp. 2453–2479, 2008.

[55] K. B. Mogensen and J. P. Kutter, "Optical detection in microfluidic systems," *Electrophoresis*, vol. 2009, no. 30, pp. 91–100, 2009.

[56] M. Trojanowicz, "Recent developments in electrochemical flow detections–a review: Part I. flow analysis and capillary electrophoresis," *Anal. Chim. Acta*, vol. 653, pp. 36–58, 2009.

[57] M. H. Wu, H. Cai, X. Xu, J. P. G. Urban, Z.-F. Cui, and Z. Cui, "A SU-8/PDMS hybrid microfluidic device with integrated optical fibers for online monitoring of lactate," *Biomed. Devices*, vol. 7, no. 4, pp. 323–329, 2005.

[58] R. Jindal and S. M. Cramer, "On-chip electrochromatography using sol-gel immobilized stationary phase with UV absorbance detection," *J. Chromatogr. A*, vol. 1044, pp. 277–285, 2004.

[59] K. B. Mogensen, J. El-Ali, A. Wolff, and J. P. Kutter, "Integration of polymer waveguides for optical detection in microfabricated chemical analysis systems," *Appl. Opt.*, vol. 42, no. 19, pp. 4072–4079, 2003.

[60] K. B. Mogensen, F. Eriksson, O. Gustafsson, R. P. H. Nikolajsen, and J. P. Kutter, "Pure-silica optical waveguides, fiber couplers, and high-aspect ratio submicrometer channels for electrokinetic separation devices," *Electrophoresis*, vol. 25, pp. 3788–3795, 2004.

[61] H. Lu, M. A. Schmidt, and K. F. Jensen, "Photochemical reactions and on-line UV detection in microfabricated reactors," *Lab Chip*, vol. 1, no. 1, pp. 22–28, 2001.

[62] E. B. Sandell, *Colorimetric determination of traces of metals*. John Wiley & Sons Inc., 1959.

[63] D. F. Boltz and J. A. Howell, *Colorimetric Determination of Nonmetals*. John Wiley & Sons Inc., 1978.

[64] T. Pan, R. T. Kelly, M. C. Asplund, and A. T. Woolley, "Fabrication of calcium fluoride capillary electrophoresis microdevices for on-chip infrared detection," *J. Chromatogr. A*, vol. 1027, pp. 231–235, 2004.

[65] R. H. Herzig-Marx, K. T. Queeney, R. J. Jackman, M. A. Schmidt, and K. F. Jensen, "Infrared spectroscopy for chemically specific sensing in silicon-based microreactors," *Anal. Chem.*, vol. 76, pp. 6476–6483, 2004.

[66] T. M. Floyd, M. A. Schmidt, and K. F. Jensen, "Silicon micromixers with infrared detection for studies of liquid-phase reactions," *Ind. Eng. Chem. Res.*, vol. 44, pp. 2351–2358, 2005.

[67] X. Xiao, X. D. Yu, K. Wang, J. J. Xu, J. Haung, and H. Y. Chen, "Study on the separation of amino acids in modified poly(dimethylsiloxane) microchips," *Talanta*, vol. 71, pp. 2048–2055, 2007.

[68] K. F. Jensen, "Silicon-based microchemical systems: Characteristics and applications," *MRS Bulletin*, vol. 31, pp. 101–107, 2006.

[69] S. G. Kazarian, "Enhancing high-throughput technology and microfluidics with FTIR spectroscopic imaging," *Anal. Bioanal. Chem.*, vol. 388, pp. 529–532, 2007.

[70] K. L. A. Chan, S. Gulati, J. B. Edel, A. J. deMello, and S. G. Kazarian, "Chemical imaging of microfluidic flows using ATR-FTIR spectroscopy," *Lab Chip*, vol. 9, pp. 2909–2913, 2009.

[71] K. L. A. Chan, X. Niu, A. J. deMello, and S. G. Kazarian, "Rapid prototyping of microfluidic devices for integrating with FT-IR spectroscopic imaging," *Lab Chip*, vol. 10, pp. 2170–2174, 2010.

[72] K. L. A. Chan, X. Niu, A. J. deMello, and S. G. Kazarian, "Generation of chemical movies: FT-IR spectroscopic imaging of segmented flows," *Anal. Chem.*, vol. 83, pp. 3606–3609, 2011.

[73] M. Lee, "Applicability of laser-induced Raman microscopy for in situ monitoring of imine formation in a glass microfluidic chip," *J. Raman Spectr.*, vol. 34, no. 10, p. 737, 2003.

[74] S. A. Leung, R. F. Winkle, R. C. R. Wootton, and A. J. deMello, "A method for rapid reaction optimisation in continuous-flow microfluidic reactors using online Raman spectroscopic detection," *Analyst*, vol. 130, pp. 46–51, 2005.

[75] S. Mozharov, A. Nordon, J. M. Girkin, and D. Littlejohn, "Non-invasive analysis in micro-reactors using Raman spectrometry with a specially designed probe," *Lab Chip*, vol. 10, pp. 2101–2107, 2010.

[76] G. Rinke, A. Ewinger, S. Kerschbaum, and M. Rinke, "In situ Raman spectroscopy to monitor the hydrolysis of acetal in microreactors," *Microfluid. Nanofluid.*, vol. 10, no. 1, pp. 145–153, 2011.

[77] S. E. Barnes, "Raman spectroscopic monitoring of droplet polymerization in a microfluidic device," *The Analyst*, vol. 131, no. 9, p. 1027, 2006.

[78] G. Cristobal, L. Arbouet, F. Sarrazin, D. Talaga, J.-L. Bruneel, M. Joanicot, and L. Servant, "On-line laser Raman spectroscopic probing of droplets engineered in microfluidic devices," *Lab Chip*, vol. 6, pp. 1140–1146, 2006.

[79] P. A. Walker, M. D. Morris, M. A. Burns, and B. N. Johnson, "Isotachophoretic separations on a microchip. normal Raman spectroscopy detection," *Anal. Chem.*, vol. 70, pp. 3766–3769, 1998.

[80] J.-B. Salmon, A. Ajdari, P. Tabeling, L. Servant, D. Talaga, and M. Joanicot, "In situ Raman imaging of interdiffusion in a microchannel," *Appl. Phys. Lett.*, vol. 86, pp. 0941061–3, 2005.

[81] K. Kneipp, "Surface-enhanced Raman scattering and biophysics," *J. Phys.: Condensed Matter*, vol. 14, p. R597, 2002.

[82] L. Chen and J. Choo, "Recent advances in surface-enhanced Raman scattering detection technology for microfluidic chips," *Electrophoresis*, vol. 29, pp. 1815–1828, 2008.

[83] M. P. Cecchini, J. Hong, C. Lim, J. Choo, T. Albrecht, A. J. deMello, and J. B. Edel, "Ultrafast Surface Enhanced Resonance Raman Scattering detection in droplet-based microfluidic systems," *Anal. Chem.*, vol. 83, pp. 3076–3081, 2011.

[84] G. L. Liu and L. P. Lee, "Nanowell surface enhanced Raman scattering arrays fabricated by soft lithography for label-free biomolecular detections in integrated microfluidics," *Appl. Phys. Lett.*, vol. 87, pp. 0741011–3, 2005.

[85] K. R. Strehle, D. Cialla, P. Rösch, T. Henkel, M. Köhler, and J. Popp, "A reproducible Surface-Enhanced Raman Spectroscopy approach. online SERS measurements in a segmented microfluidic system," *Anal. Chem.*, vol. 79, pp. 1542–1547, 2007.

[86] C. Wang, "Fiber loop ringdown: a time-domain sensing technique for multi-function fiber optic sensor platforms: Current status and design perspectives," *Sensors*, vol. 9, pp. 7595–7621, 2009.

[87] J. R. Lakowicz, *Principles of fluorescence spectroscopy*. New York: Springer, 3rd ed., 2006.

[88] P. S. Dittrich and A. Manz, "Single-molecule fluorescence detection in microfluidic channels - the Holy Grail in μTAS?," *Anal. Bioanal. Chem.*, vol. 382, pp. 1771–1782, 2005.

[89] T. Hirschfeld, "Quantum efficiency independence of the time integrated emission from a fluorescent molecule," *Appl. Opt.*, vol. 15, no. 12, pp. 3135–3139, 1976.

[90] E. K. Hill and A. J. deMello, "Single-molecule detection using confocal fluorescence detection: Assessment of optical probe volumes," *Analyst*, vol. 125, pp. 1033–1036, 2000.

[91] D. Yin, "Single-molecule detection sensitivity using planar integrated optics on a chip," *Optics Letters*, vol. 31, no. 14, p. 2136, 2006.

[92] M. Srisa-Art, A. J. deMello, and J. B. Edel, "High-throughput DNA droplet assays using picoliter reactor volumes," *Anal. Chem.*, vol. 79, pp. 6682–6689, 2007.

[93] M. Srisa-Art, E. C. Dyson, A. J. deMello, and J. B. Edel, "Monitoring of real-time streptavidin-biotin binding kinetics using droplet microfluidics," *Anal. Chem.*, vol. 80, pp. 7063–7067, 2008.

[94] D. Sinton, "Microscale flow visualisation," *Microfluid Nanofluid*, vol. 1, pp. 2–21, 2004.

[95] M. Srisa-Art, A. J. deMello, and J. B. Edel, "Fluorescence lifetime imaging of mixing dynamics in continuous-flow microdroplet reactors," *Phys. Rev. Lett.*, vol. 101, pp. 0145021–4, 2008.

[96] X. C. Solvas, M. Srisa-Art, A. J. deMello, and J. B. Edel, "Mapping of fluidic mixing in microdroplets with 1 μs time resolution using fluorescence lifetime imaging," *Anal. Chem.*, vol. 82, no. 9, p. 39503956, 2010.

[97] T. Imasaka and N. Ishibashi, "Thermal lens spectrophotometry," *Trends Anal. Chem.*, vol. 1, no. 12, pp. 273–277, 1982.

[98] M. Tokeshi, M. Uchida, A. Hibara, T. Sawada, and T. Kitamori, "Determination of subyoctomole amounts of nonfluorescent molecules using a thermal lens microscope: subsingle-molecule determination," *Anal. Chem.*, vol. 73, no. 9, p. 2112, 2001.

[99] E. Tamaki, K. Sato, M. Tokeshi, K. Sato, M. Aihara, and T. Kitamori, "Single-cell analysis by a scanning thermal lens microscope with a microchip: Direct monitoring of cytochrome c distribution during apoptosis process," *Anal. Chem.*, vol. 74, no. 7, p. 1560, 2002.

[100] M. Tokeshi, Y. Kikutani, A. Hibara, K. Sato, H. Hisamoto, and T. Kitamori, "Chemical processing on microchips for analysis, synthesis and bioassay," *Electrophoresis*, vol. 24, pp. 3583–3594, 2003.

[101] K. Mawatari, Y. Naganuma, and K. Shimoide, "Portable thermal lens spectrometer with focusing system," *Anal. Chem.*, vol. 77, pp. 687–692, 2005.

[102] J. Wang, "Electrochemical detection for microscale analytical systems: a review," *Talanta*, vol. 56, pp. 223–231, 2002.

[103] W. R. Vandaveer, S. A. Pasas-Farmer, D. J. Fischer, C. N. Frankenfeld, and S. M. Lunte, "Recent developments in electrochemical detection for microchip capillary electrophoresis," *Electrophoresis*, vol. 25, p. 35283549, 2004.

[104] J. Wang, "Electrochemical detection for capillary electrophoresis microchips: A review," *Electroanalysis*, vol. 17, no. 13, pp. 1133–1140, 2005.

[105] F.-R. F. Fan and A. J. Bard, "Electrochemical detection of single molecules," *Science*, vol. 267, no. 5199, pp. 871–874, 1995.

[106] W. R. Vandaveer, S. A. Pasas, R. S. Martin, and S. M. Lunte, "Recent developments in amperometric detection for microchip capillary electrophoresis," *Electrophoresis*, vol. 23, p. 36673677, 2002.

[107] M. J. Moorcroft, J. Davis, and R. G. Compton, "Detection and determination of nitrate and nitrite: a review," *Talanta*, vol. 54, pp. 785–803, 2001.

[108] F. Tagliaro, G. Manetto, F. Crivellente, and F. P. Smith, "A brief introduction to capillary electrophoresis," *Forensic Sci. Int.*, vol. 92, pp. 75–88, 1998.

[109] T. de Beer, N. H. Velthorst, U. A. T. Brinkman, and C. Gooijer, "Laser-based non-fluorescence detection techniques for liquid separation systems," *J. Chromatogr. A*, vol. 971, pp. 1–35, 2002.

[110] S. E. Moring, R. T. Reel, and R. E. J. van Soest, "Optical improvements of a Z-shaped cell for high-sensitivity UV absorbance detection in capillary electrophoresis," *Anal. Chem.*, vol. 65, no. 23, pp. 3454–3459, 1993.

[111] K. W. Ro, K. Lim, B. C. Shim, and J. H. Hahn, "Integrated light collimating system for extended optical-path-length absorbance detection in microchip-based capillary electrophoresis," *Anal. Chem.*, vol. 77, no. 16, pp. 5160–5166, 2005.

[112] N. J. Petersen, K. B. Mogensen, and J. P. Kutter, "Performance of an in-plane detection cell with integrated waveguides for UV/Vis absorbance measurements on microfluidic separation devices," *Electrophoresis*, vol. 23, pp. 3528–3536, 2002.

[113] J. P. Chervet, R. E. J. van Soest, and M. Ursem, "Z-shaped flow cell for UV detection in capillary electrophoresis," *J. Chromatogr. A*, vol. 543, pp. 439–449, 1991.

[114] S. Kim, W. Kim, and J. H. Hahn, "Extended path length post-column flow cell for UV-visible absorbance detection in capillary electrophoresis," *J. Chromatogr. A*, vol. 680, pp. 109–116, 1994.

[115] Y. Xue and E. S. Yeung, "Characterization of band broadening in capillary electrophoresis due to nonuniform capillary geometries," *Anal. Chem.*, vol. 66, pp. 3575–3580, 1994.

[116] T. M. Tiggelaar, T. T. Veenstra, R. G. P. Sanders, J. G. E. Gardeniers, M. C. Elwenspoek, and A. van der Berg, "A light detection cell to be used in a micro analysis system for ammonia," *Talanta*, vol. 56, pp. 331–339, 2002.

[117] M. Grumann, I. Moser, J. Steigert, L. Riegger, A. Geipel, C. Kohn, G. Urban, R. Zengerle, and J. Ducrée, "Optical beam guidance in monolithic polymer chips for miniaturized colorimetric assays," *MEMS*, pp. 108–111, 2005.

[118] H. Zhang and R. H. Byrne, "Spectrophotometric pH measurements of surface seawater at in-situ conditions: absorbance and protonation behavior of thymol blue," *Mar. Chem.*, vol. 52, no. 1, pp. 17–25, 1996.

[119] R. Alves-Segundo, N. Ibañez Garcia, M. Baeza, M. Puyol, and J. Alonso-Chamarro, "Towards a monolithically integrated microsystem based on the green tape ceramics technology for spectrophotometric measurements. determination of chromium (VI) in water," *Microchim. Acta*, vol. 172, no. 1, pp. 225–232, 2011.

[120] J. Steigert, M. Grumann, M. Dube, W. Streule, L. Riegger, T. Brenner, P. Koltay, K. Mittmann, R. Zengerle, and J. Ducrée, "Direct hemoglobin measurement on a centrifugal microfluidic platform for point-of-care diagnostics," *Sens. Actuators, A*, vol. 130-131, pp. 228–233, 2006.

[121] M. R. Kumar and M. Adinarayana, "Oxidation of caffeine by phosphate radical anion in aqueous solution under anoxic conditions," *Proc. Indian Acad. Sci. (Chem. Sci.)*, vol. 112, no. 5, pp. 551–557, 2000.

[122] A. Mainka and M. Bächmann, "UV detection of derivatized carbonyl compounds in rain samples in capillary electrophoresis using sample stacking and a Z-shaped flow cell," *J. Chromatogr. A*, vol. 767, pp. 241–247, 1997.

[123] T. Noda, H. Takao, K. Yoshioka, N. Oku, M. Ashiki, K. Sawada, K. Matsumoto, and M. Ishida, "Performance of absorption photometry microchip for blood hemoglobin measurement integrated with processing circuits and Si(1 1 0) 45 degrees mirrors," *Sens. Actuators, B*, vol. 119, pp. 245–250, 2006.

[124] T. Wang, J. H. Aiken, C. W. Huie, and R. A. Hartwick, "Nanoliter-scale multireflection cell for absorption detection in capillary electrophoresis," *Anal. Chem.*, vol. 63, no. 14, pp. 1372–1376, 1991.

[125] E. Verpoorte, A. Manz, H. Lüdi, A. E. Bruno, F. Maystre, B. Krattiger, H. M. Widmer, B. H. van der Schoot, and N. F. De Rooij, "A silicon flow cell for optical detection in miniaturized total chemical analysis systems," *Sens. Actuators, B*, vol. 6, pp. 66–70, 1992.

[126] A. Llobera, R. Wilke, and S. Büttgenbach, "Poly (dimethylsiloxane) hollow Abbe prism with microlenses for detection based on absorption and refractive index shift," *Lab Chip*, vol. 4, pp. 24–27, 2004.

[127] A. Llobera, S. Demming, R. Wilke, and S. Büttgenbach, "Multiple internal reflection poly(dimethylsiloxane) systems for optical sensing," *Lab Chip*, vol. 7, pp. 1560–1566, 2007.

[128] M. P. Duggan, T. McCreedy, and J. W. Aylott, "A non-invasive analysis method for on-chip spectrophotometric detection using liquid-core waveguiding within a 3D architecture," *Analyst*, vol. 128, no. 11, pp. 1336–1340, 2003.

[129] H. Salimi-Moosavi, Y. Jiang, L. Lester, G. McKinnon, and D. J. Harrison, "A multireflection cell for enhanced absorbance detection in microchip-based capillary electrophoresis devices," *Electrophoresis*, vol. 21, pp. 1291–1299, 2000.

[130] P. S. Ellis, A. J. Lyddy-Meaney, P. J. Worsfold, and I. D. McKelvie, "Multi-reflection photometric flow cell for use in flow injection analysis of estuarine waters," *Anal. Chim. Acta*, vol. 499, no. 1-2, pp. 81–89, 2003.

[131] S. K. Mishra and P. K. Dasgupta, "Capillary scale light emitting diode based multi-reflection absorbance detector," *Anal. Chim. Acta*, vol. 605, pp. 166–174, 2007.

[132] A. Llobera, R. Wilke, and S. Büttgenbach, "Optimization of poly (dimethylsiloxane) hollow prisms for optical sensing," *Lab Chip*, vol. 5, pp. 506–511, 2005.

[133] M. D. Patey, M. J. A. Rijkenberg, P. J. Statham, M. C. Stinchcombe, E. P. Achterberg, and M. Mowlem, "Determination of nitrate and phosphate in seawater at nanomolar concentration," *Trends Anal. Chem.*, vol. 27, no. 2, pp. 169–182, 2008.

[134] J.-Z. Pan, B. Yao, and Q. Fang, "Hand-held photometer based on liquid-core waveguide absorption detection for nanoliter-scale samples," *Anal. Chem.*, vol. 82, no. 8, pp. 3394–3398, 2010.

[135] S. Demming, A. Llobera, R. Wilke, and S. Büttgenbach, "Single and multiple internal reflection poly (dimethylsiloxane) absorbance-based biosensors," *Sens. Actuators, B*, vol. 139, pp. 166–173, 2009.

[136] O. S. Wolfbeis, "Capillary waveguide sensors," *Trends Anal. Chem.*, vol. 15, no. 6, pp. 225–232, 1996.

[137] R. Altkorn, I. Koev, and A. Gottlieb, "Waveguide capillary cell for low-refractive-index liquids," *Appl. Spectrosc.*, vol. 51, no. 10, pp. 1554–1558, 1997.

[138] R. L. Miller, M. Belz, C. del Castillo, and R. Trzaska, "Determining CDOM absorption spectra in diverse coastal environments using a multiple pathlength, liquid core waveguide system," *Cont. Shelf Res.*, vol. 22, pp. 1301–1310, 2002.

[139] T. Dallas and P. K. Dasgupta, "Light at the end of the tunnel: recent analytical applications of liquid-core waveguides," *Trends Anal. Chem.*, vol. 23, no. 5, pp. 385–392, 2004.

[140] L. J. Gimbert and P. J. Worsfold, "Environmental applications of liquid-waveguide-capillary cells coupled with spectroscopic detection," *Trends Anal. Chem.*, vol. 26, no. 9, pp. 914–930, 2007.

[141] L. R. Adornato, E. A. Kaltenbacher, T. A. Villareal, and R. H. Byrne, "Continuous in situ determinations of nitrite at nanomolar concentrations," *Deep Sea Res. Part I*, vol. 52, no. 3, pp. 543–551, 2005.

[142] G. Chen, D. Yuan, Y. Huang, M. Zhang, and M. Bergman, "In-field determination of nanomolar nitrite in seawater using a sequential injection technique combined with solid phase enrichment and colorimetric detection," *Anal. Chim. Acta*, vol. 620, no. 1-2, pp. 82–88, 2008.

[143] L. van der Sneppen, F. Ariese, C. Gooijer, and W. Ubachs, "Liquid-phase and evanescent-wave cavity ring-down spectroscopy in analytical chemistry," *Annu. Rev. Anal. Chem.*, vol. 2, pp. 13–35, 2009.

[144] P. W. Atkins, *Physical Chemistry*. Oxford University Press, sixth ed., 1998.

[145] A. E. Siegman, *Laser*. Oxford University Press, 1986.

[146] P. Bouguer, *Essai doptique, sur la gradation de la lumière*. Claude Jombert, 1729.

[147] J. H. Lambert, *Photometria sive de mensura et gradibus luminis, colorum et umbrae*. Eberhardt Klett, 1760.

[148] A. Beer, "Bestimmung der absorption des rothen lichts in farbigen flüssigkeiten," *Ann. Phys.*, vol. 162, pp. 78–88, 1852.

[149] D. F. Shriver and P. W. Atkins, *Inorganic Chemistry*. Oxford University Press, 1999.

[150] P. F. Bernath, *Spectra of atoms and molecules*. Oxford University Press, second ed., 2005.

[151] D. Z. Anderson, J. C. Frisch, and C. S. Masser, "Mirror reflectometer based on optical cavity decay time," *Appl. Opt.*, vol. 23, no. 8, pp. 1238–1245, 1984.

[152] A. O'Keefe and D. A. G. Deacon, "Cavity ring-down optical spectrometer for absorption measurements using pulsed laser sources," *Rev. Sci. Instrum.*, vol. 59, pp. 2544–2555, 1988.

[153] A. O'Keefe, "Integrated cavity output analysis of ultra-weak absorption," *Chem. Phys. Lett.*, vol. 293, pp. 331–336, 1998.

[154] P. Zalicki and R. N. Zare, "Cavity ring-down spectroscopy for quantitative absorption measurements," *J. Chem. Phys.*, vol. 102, no. 7, pp. 2708–2717, 1995.

[155] J. J. Scherer, J. B. Paul, A. O'Keefe, and R. J. Saykally, "Cavity ringdown laser absorption spectroscopy: history, development and application to pulsed molecular beams," *Chem. Rev.*, vol. 97, pp. 25–51, 1997.

[156] M. D. Wheeler, S. M. Newman, A. J. Orr-Ewing, and M. N. R. Ashfold, "Cavity ring-down spectroscopy," *J. Chem. Soc., Faraday Trans.*, vol. 94, no. 3, pp. 337–351, 1998.

[157] M. Mazurenka, A. J. Orr-Ewing, R. Peverall, and G. A. D. Ritchie, "Cavity ring-down and cavity enhanced spectroscopy using diode lasers," *Ann. Rep. Prog. Chem., Sect. C*, vol. 101, pp. 100–142, 2005.

[158] B. A. Paldus and A. Kachanov, "An historical overview of cavity-enhanced methods," *Can. J. Phys.*, vol. 83, pp. 975–999, 2005.

[159] C. Vallance, "Innovations in cavity ringdown spectroscopy," *New J. Chem.*, vol. 29, pp. 867–874, 2005.

[160] S. E. Fiedler, A. Hese, and A. A. Ruth, "Incoherent broad-band cavity-enhanced absorption spectroscopy," *Chem. Phys. Lett.*, vol. 371, no. 3-4, p. 284, 2003.

[161] H. Kogelnik and T. Li, "Laser beams and resonators," *Proc. IEEE.*, vol. 54, no. 10, pp. 1312–1329, 1966.

[162] G. Berden, R. Peeters, and G. Meijer, "Cavity ring-down spectroscopy: Experimental schemes and applications," *Int. Rev. Phys. Chem.*, vol. 19, no. 4, pp. 565–607, 2000.

[163] A. J. Hallock, E. S. F. Berman, and R. N. Zare, "Direct monitoring of absorption in solution by cavity ring-down spectroscopy," *Anal. Chem.*, vol. 74, no. 7, pp. 1741–1743, 2002.

[164] S. E. Fiedler, A. Hese, and A. A. Ruth, "Incoherent broad-band cavity-enhanced absorption spectroscopy of liquids," *Rev. Sci. Instrum.*, vol. 76, p. 023107, 2005.

[165] S. C. Xu, G. H. Sha, and J. C. Xie, "Cavity ring-down spectroscopy in the liquid phase," *Rev. Sci. Instrum.*, vol. 73, no. 2, pp. 255–258, 2002.

[166] A. J. Alexander, "Flowing liquid-sheet jet for cavity ring-down absorption measurements," *Anal. Chem.*, vol. 78, no. 15, pp. 5597–5600, 2006.

[167] A. J. Hallock, E. S. F. Berman, and R. N. Zare, "Use of broadband, continuous-wave diode lasers in cavity ring-down spectroscopy for liquid samples," *Appl. Spectrosc.*, vol. 57, no. 5, pp. 571–573, 2003.

[168] K. L. Snyder and R. N. Zare, "Cavity ring-down spectroscopy as a detector for liquid chromatography," *Anal. Chem.*, vol. 75, no. 13, pp. 3086–3091, 2003.

[169] B. Bahnev, L. van der Sneppen, A. Wiskerke, F. Ariese, C. Gooijer, and W. Ubachs, "Miniaturized cavity ring-down detection in a liquid flow cell," *Anal. Chem.*, vol. 77, pp. 1188–1191, 2005.

[170] K. L. Bechtel, R. N. Zare, A. A. Kachanov, S. S. Sanders, and B. A. Paldus, "Moving beyond traditional UV-visible absorption detection: Cavity ring-down spectroscopy for HPLC," *Anal. Chem.*, vol. 77, no. 4, pp. 1177–1182, 2005.

[171] L. van der Sneppen, A. Wiskerke, F. Ariese, C. Gooijer, and W. Ubachs, "Improving the sensitivity of HPLC absorption detection by cavity ring-down spectroscopy in a liquid-only cavity," *Anal. Chim. Acta*, vol. 558, no. 1-2, pp. 2–6, 2006.

[172] L. van der Sneppen, A. E. Wiskerke, F. Ariese, C. Gooijer, and W. Ubachs, "Cavity ring-down spectroscopy for detection in liquid chromatography: Extension to tunable sources and ultraviolet wavelengths," *Appl. Spectrosc.*, vol. 60, no. 8, pp. 931–935, 2006.

[173] L. van der Sneppen, F. Ariese, C. Gooijer, and W. Ubachs, "Cavity ring-down spectroscopy for detection in liquid chromatography at UV wavelengths using standard cuvettes in a normal incidence geometry," *J. Chromatogr. A*, vol. 1148, no. 2, pp. 184–188, 2007.

[174] N. Seetohul, Z. Ali, and M. Islam, "Liquid-phase broadband cavity enhanced absorption spectroscopy (BBCEAS) studies in a 20 cm cell," *Analyst*, vol. 134, pp. 1887–1895, 2009.

[175] K. A. Strain, J. Hough, N. A. Robertson, and K. Skeldon, "Measurement of the absorptance of fused silica at $\lambda = 514.4$ nm," *Opt. Comm.*, vol. 117, pp. 385–388, 1995.

[176] E. S. Fry, "Visible and near-ultraviolet absorption spectrum of liquid water: comment," *Appl. Opt.*, vol. 39, no. 16, pp. 2743–2744, 2000.

[177] G. A. C. M. Spierings, "Wet chemical etching of silicate glasses in hydrofluoric acid based solutions," *J. Materials. Sci.*, vol. 28, no. 23, pp. 6261–6273, 1993.

[178] A. Del Campo and C. Greiner, "SU-8: a photoresist for high-aspect-ratio and 3D submicron lithography," *J. Micromech. Microeng.*, vol. 17, no. 6, 2007.

[179] A. Piruska, I. Nikcevic, S. H. Lee, C. Ahn, W. R. Heineman, P. A. Limbach, and C. J. Seliskar, "The autofluorescence of plastic materials and chips measured under laser irradiation," *Lab Chip*, vol. 5, no. 12, pp. 1348–1354, 2005.

[180] D. C. Duffy, J. C. McDonald, O. J. A. Schueller, and G. M. Whitesides, "Rapid prototyping of microfluidic systems in poly(dimethylsiloxane)," *Anal. Chem.*, vol. 70, no. 23, pp. 4974–4984, 1998.

[181] J. T. Cabral, "Frontal photopolymerization for microfluidic applications," *Langmuir*, vol. 20, no. 23, p. 10020, 2004.

[182] I. R. Epstein and J. A. Pojman, *An introduction to nonlinear chemical dynamics: oscillations, waves, patterns, and chaos*. Oxford University Press, 1998.

[183] B. T. Ginn, B. Steinbock, M. Kahveci, and O. Steinbock, "Microfluidic systems for the Belousov-Zhabotinsky reaction," *J. Phys. Chem. A*, vol. 108, no. 8, pp. 1325–1332, 2004.

[184] K. Grasshoff, K. Kremling, and M. Ehrhardt, *Methods of Seawater Analysis*. Wiley-VCH, third ed., 2007.

[185] F. J. Millero, *Chemical Oceanography*. CRC Press, 3rd ed., 2005.

[186] A. Tovar, C. Moreno, M. P. Mánuel-Vez, and M. García-Vargas, "A simple automated method for the speciation of dissolved inorganic nitrogen in seawater," *Anal. Chim. Acta*, vol. 469, no. 2, pp. 235–242, 2002.

[187] EEC, *A directive of the quality of freshwater needing protection or improvement in order to support fish life. 78/659/EEC*, vol. L222 of *Official J. European Union*. 1978.

[188] B. H. L. Kelso, R. Smith, R. J. Laughlin, and S. D. Lennox, "Dissimilatory nitrate reduction in anaerobic sediments leading to river nitrite accumulation," *Appl. Environ. Microbiol*, vol. 63, no. 12, pp. 4679–4685, 1997.

[189] WHO, *Guidelines for drinking-water quality*. World Health Organization, Geneva, Switzerland, fourth ed., 2011.

[190] C. S. Bruning-Fann and J. B. Kaneene, "The effects of nitrate, nitrite and n-nitroso compounds on human health: A review," *Vet. Hum. Toxicol.*, vol. 35, no. 6, pp. 521–538, 1993.

[191] J. Dutt and J. Davis, "Current strategies in nitrite detection and their application to field analysis," *J. Environ. Monit.*, vol. 4, no. 3, pp. 465–471, 2002.

[192] T. F. Rozan and G. W. Luther, "An anion chromatography/ultraviolet detection method to determine nitrite, nitrate and sulfide concentrations in saline (pore) waters," *Mar. Chem.*, vol. 77, no. 1, pp. 1–6, 2002.

[193] S. H. Lee and L. R. Field, "Postcolumn fluorescence detection of nitrite, nitrate, thiosulfate, and iodide anions in high-performance liquid chromatography," *Anal. Chem.*, vol. 56, no. 14, pp. 2647–2653, 1984.

[194] A. Büldt and U. Karst, "Determination of nitrite in waters by microplate fluorescence spectroscopy and HPLC with fluorescence detection," *Anal. Chem.*, vol. 71, no. 15, pp. 3003–3007, 1999.

[195] P. Griess, "Bemerkungen zu der Abandlung der H. N. Weselsky und Benedikt 'Uner einige Azoverbindungen'," *Ber. dt. chem. Ges.*, vol. 12, pp. 426–8, 1879.

[196] J. B. Fox Jr., "Kinetics and mechanism of the Griess reaction," *Anal. Chem.*, vol. 51, no. 9, pp. 1493–1502, 1979.

[197] J. F. Van Staden, "Automated simultaneous determination of nitrate and nitrite by pre-valve reduction of nitrate in a flow-injection system," *Anal. Chim. Acta*, vol. 138, no. 0, pp. 403–408, 1982.

[198] D. R. Turner and K. A. Hunter, *The biogeochemistry of iron in seawater*. John Wiley & Sons, 2001.

[199] E. P. Achterberg, T. W. Holland, A. R. Bowie, R. F. C. Mantoura, and P. J. Worsfold, "Review: Determination of iron in seawater," *Anal. Chim. Acta*, vol. 442, pp. 1–14, 2001.

[200] S. Pehkonen, "Determination of the oxidation states of iron in natural waters: A review," *Analyst*, vol. 120, pp. 2655–2663, 1995.

[201] J. T. Woods and M. G. Mellon, "Thiocyanate method for iron: a spectrophotometric study," *Ind. and Eng. Chem.*, vol. 13, no. 8, pp. 551–554, 1941.

[202] G. F. Smith, W. H. McCurdy, and H. Diehl, "The colorimetric determination of iron in raw and treated municipal water supplies by use of 4:7-diphenyl-1:10-phenanthroline," *Analyst*, vol. 77, pp. 418–422, 1952.

[203] L. L. Stookey, "Ferrozine - a new spectrophotometric reagent for iron," *Anal. Chem.*, vol. 42, no. 7, pp. 779–781, 1970.

[204] H. E. Bent and C. L. French, "The structure of ferric thiocyanate and its dissociation in aqueous solution," *J. Am. Chem. Soc.*, vol. 63, no. 2, pp. 568–572, 1941.

[205] W. B. Fortune and M. G. Mellon, "Determination of iron with o-phenanthroline: a spectrophotometric study," *Ind. and Eng. Chem.*, vol. 10, no. 2, pp. 60–64, 1938.

[206] P. Trinder, "The improved determination of iron in serum," *J. Clin. Pathology*, vol. 9, p. 170, 1956.

[207] D. Blair and H. Diehl, "Bathophenanthroline disulphonic acid and bathocuproinedisulphonic acid, water soluble reagents for iron and copper," *Talanta*, vol. 7, pp. 163–174, 1961.

[208] W. Yao, R. H. Byrne, and R. D. Waterbury, "Determination of nanomolar concentrations of nitrite and nitrate in natural waters using long path length absorbance spectroscopy," *Environ. Sci. Technol.*, vol. 32, no. 17, pp. 2646–2649, 1998.

[209] D. W. King, J. Lin, and D. R. Kester, "Spectrophotometric determination of iron(II) in seawater at nanomolar concentrations," *Anal. Chim. Acta*, vol. 247, pp. 125–132, 1991.

[210] P. Raimbault, G. Slawyk, B. Coste, and J. Fry, "Feasibility of using an automated colorimetric procedure for the determination of seawater nitrate in the 0 to 100 nm range: Examples from field and culture," *Mar. Biol.*, vol. 104, no. 2, pp. 347–351, 1990.

[211] E. T. Steimle, E. A. Kaltenbacher, and R. H. Byrne, "In situ nitrite measurements using a compact spectrophotometric analysis system," *Mar. Chem.*, vol. 77, pp. 255–262, 2002.

[212] R. D. Waterbury, W. Yao, and R. H. Byrne, "Long pathlength absorbance spectroscopy: trace analysis of fe(II) using a 4.5 m liquid core waveguide," *Anal. Chim. Acta*, vol. 357, no. 12, pp. 99–102, 1997.

[213] J.-Z. Zhang, C. Kelbe, and F. J. Millero, "Gas-segmented continuous flow analysis of iron in water with a long liquid waveguide capillary flow cell," *Anal. Chim. Acta*, vol. 438, pp. 49–57, 2001.

[214] J.-Z. Zhang, "Shipboard automated determination of trace concentrations of nitrite and nitrate in oligotrophic water by gas-segmented continuous flow analysis with a liquid waveguide capillary flow cell," *Deep Sea Res. Part I*, vol. 47, no. 6, pp. 1157–1171, 2000.

[215] G. M. Greenway, S. J. Haswell, and P. H. Petsul, "Characterisation of a micro-total analytical system for the determination of nitrite with spectrophotometric detection," *Anal. Chim. Acta*, vol. 387, no. 1, pp. 1–10, 1999.

[216] J. L. Manzoori and S. Soflaee, "Spectrophotometric determination of nitrite after preconcentration on an SDS coated alumun column," *Anal. Lett.*, vol. 34, no. 2, pp. 231–237, 2001.

[217] W. Hu, P. R. Haddad, K. Hasebe, K. Tanaka, P. Tong, and C. Khoo, "Direct determination of bromide, nitrate, and iodide in saline matrixes using electrostatic ion chromatography with an electrolyte as eluent," *Anal. Chem.*, vol. 71, pp. 1617–1620, 1999.

[218] M. Maruo, T. Doi, and H. Obata, "Onboard determination of submicromolar nitrate in seawater by anion-exchange chromatography with lithium chloride eluent," *Anal. Sci.*, vol. 22, pp. 1175–1178, 2006.

[219] R. J. Kieber and P. J. Seaton, "Determination of subnanomolar concentrations of nitrite in natural waters," *Anal. Chem.*, vol. 67, no. 18, pp. 3261–3264, 1995.

[220] R. T. Masserini and K. A. Fanning, "A sensor package for the simultaneous determination of nanomolar concentrations of nitrite, nitrate, and ammonia in seawater by fluorescence detection," *Mar. Chem.*, vol. 68, no. 4, pp. 323–333, 2000.

[221] X.-Q. Zhan, D.-H. Li, Z. H., and J. G. Xu, "A sensitive fluorimetric method for the determination of nitrite and nitrate in seawater by a novel red-region fluorescence dye," *Anal. Lett.*, vol. 34, no. 15, pp. 2761–2770, 2001.

[222] R. D. Cox, "Determination of nitrate and nitrite at the parts per billion level by chemiluminescence," *Anal. Chem.*, vol. 52, no. 2, pp. 332–335, 1980.

[223] C. Garside, "A chemiluminescent technique for the determination of nanomolar concentrations of nitrate and nitrite in seawater," *Mar. Chem.*, vol. 11, no. 2, pp. 159–167, 1982.

[224] T. Aoki, S. Fukuda, Y. Hosoi, and H. Mukai, "Rapid flow injection analysis method for successive determination of ammonia, nitrite, and nitrate in water by gas-phase chemiluminescence," *Anal. Chim. Acta*, vol. 349, no. 13, pp. 11–16, 1997.

[225] K. Fujiwara, H. Uchiki, F. Shimokoshi, K.-I. Tsunoda, K. Fuwa, and T. Kobayashi, "Thermal lensing colorimetry of nitrite ion with single-laser system," *Appl. Spectrosc.*, vol. 36, no. 2, pp. 157–161, 1982.

[226] S. Ferretti, S.-K. Lee, B. D. MacCraith, A. G. Oliva, D. J. Richardson, D. A. Russell, K. E. Sapsford, and M. Vidal, "Optical biosensing of nitrite ions using cytochrome nitrite reductase encapsulated in a sol-gel matrix," *Analyst*, vol. 125, no. 11, pp. 1993–1999, 2000.

[227] "www.argo.net."

[228] W. L. Miller, D. W. King, J. Lin, and D. R. Kester, "Photochemical redox cycling of iron in coastal seawater," *Mar. Chem.*, vol. 50, no. 14, pp. 63–77, 1995.

[229] K. Kuma, J. Nishioka, and K. Matsunaga, "Controls on iron(III) hydroxide solubility in seawater: The influence of pH and natural organic chelators," *Limnol. Oceanogr.*, vol. 41, no. 3, pp. 396–407, 1996.

[230] E. L. Rue and K. W. Bruland, "The role of organic complexation on ambient iron chemistry in the equatorial pacific ocean and the response of a mesoscale iron addition experiment," *Limnol. Oceanogr.*, vol. 42, no. 5, pp. 901–910, 1997.

[231] W. M. Landing and K. W. Bruland, "The contrasting biogeochemistry of iron and manganese in the pacific ocean," *Geochim. Cosmochim. Acta*, vol. 51, no. 1, pp. 29–43, 1987.

[232] J. S. Shirk, T. D. Harris, and J. W. Mitchell, "Laser intracavity spectrophotometer," *Anal. Chem.*, vol. 52, pp. 1701–1705, 1980.

[233] T. D. Harris and J. W. Mitchell, "Sub-part-per-billion iron determination by laser intracavity absorption spectrometry," *Anal. Chem.*, vol. 52, pp. 1706–1708, 1980.

[234] S. Blain and P. Tréguer, "Iron(II) and iron(III) determination in sea water at the nanomolar level with selective on-line preconcentration and spectrophotometric determination," *Anal. Chim. Acta*, vol. 308, pp. 425–432, 1995.

[235] D. W. O'Sullivan, A. K. Hanson, W. L. Miller, and D. R. Kester, "Measurement of fe(II) in surface water of the equatorial pacific," *Limnol. Oceanogr.*, vol. 36, no. 8, pp. 1727–1741, 1991.

[236] K. Hirayama and N. Unohara, "Spectrophotometric catalytic determination of an ultratrace amount of iron(III) in water based on the oxidation of N,N-dimethyl-p-phenylenediamine by hydrogen peroxide," *Anal. Chem.*, vol. 60, pp. 2573–2577, 1988.

[237] H. Obata, H. Karatani, M. Matsui, and E. Nakayama, "Fundamental studies for chemical speciation of iron in seawater with an improved analytical method," *Mar. Chem.*, vol. 56, no. 12, pp. 97–106, 1997.

[238] M. Gledhill and C. M. G. van den Berg, "Measurement of the redox speciation of iron in seawater by catalytic cathodic stripping voltammetry," *Mar. Chem.*, vol. 50, no. 14, pp. 51–61, 1995.

[239] C. I. Measures, J. Yuan, and J. A. Resing, "Determination of iron in seawater by flow injection analysis using in-line preconcentration and spectrophotometric detection," *Mar. Chem.*, vol. 50, pp. 3–12, 1995.

[240] D. A. Weeks and K. W. Bruland, "Improved method for shipboard determination of iron in seawater by flow injection analysis," *Anal. Chim. Acta*, vol. 453, pp. 21–32, 2002.

[241] P. N. Sedwick, P. R. Edwards, D. J. Mackey, F. B. Griffiths, and J. S. Parslow, "Iron and manganese in surface waters of the Australian subantarctic region," *Deep Sea Res. Part I*, vol. 44, no. 7, pp. 1239–1253, 1997.

[242] J. T. M. de Jong, J. den Das, U. Bathmann, M. H. C. Stoll, G. Kattner, R. F. Nolting, and H. J. W. de Baar, "Dissolved iron at subnanomolar levels in the Southern Ocean as determined by ship-board analysis," *Anal. Chim. Acta*, vol. 377, no. 23, pp. 113–124, 1998.

[243] Y. Sohrin, S. Iwamoto, M. Matsui, H. Obata, E. Nakayama, K. Suzuki, N. Handa, and M. Ishii, "The distribution of Fe in the Australian sector of the Southern Ocean," *Deep Sea Res. Part I*, vol. 47, no. 1, pp. 55–84, 2000.

[244] A. R. Bowie, P. N. Sedwick, and P. J. Worsfold, "Analytical intercomparison between flow injection-chemiluminescence and flow injection-spectrophotometry for the determination of picomolar concentrations of iron in seawater," *Limnol. Oceanogr.: Methods*, vol. 2, pp. 42–54, 2004.

[245] T. Imasaka, K. Miyaishi, and N. Ishibashi, "Application of the thermal lens effect for determination of iron(II) with 4,7-diphenyl-1,10-phenanthroline disulfonic acid," *Anal. Chim. Acta*, vol. 115, no. 0, pp. 407–410, 1980.

[246] V. V. Chernysh, M. Y. Kononets, M. A. Proskurnin, S. V. Pakhomova, V. V. Komissarov, and A. I. Zatsman, "Thermal lens studies of the reaction of iron(II) with 1,10-phenanthroline at the nanogram level," *Fresenius J. Anal. Chem.*, vol. 369, pp. 535–542, 2001.

[247] R. F. Nolting, L. J. A. Gerringa, M. J. W. Swagerman, K. R. Timmermans, and H. J. W. de Baar, "Fe (III) speciation in the high nutrient, low chlorophyll pacific region of the southern ocean," *Mar. Chem.*, vol. 62, no. 34, pp. 335–352, 1998.

[248] L. J. Clark, "Iron(II) determination in the presence of iron(III) using 4,7-diphenyi-1, 10-phenanthroline," *Anal. Chem.*, vol. 34, no. 3, pp. 348–352, 1962.

[249] J. Xu, P. Che, and Y. Ma, "More sensitive way to determine iron using an iron(II)-1, 10-phenanthroline complex and capillary electrophoresis," *J. Chromatogr. A*, vol. 749, no. 12, pp. 287–294, 1996.

[250] J. Metcalfe, "Methylthymol blue as a reagent for the spectrophotometric determination of magnesium," *Analyst*, vol. 90, no. 1072, pp. 409–412, 1965.

[251] B. Paull, M. Macka, and P. R. Haddad, "Determination of calcium and magnesium in water samples by high-performance liquid chromatography on a graphitic stationary phase with a mobile phase containing o-cresolphthalein complexone," *J. Chromatogr. A*, vol. 789, pp. 329–337, 1997.

[252] M. R. Hayes and J. Metcalfe, "The boron-curcumin complex in the determination of trace amounts of boron," *Analyst*, vol. 87, no. 1041, pp. 956–969, 1962.

[253] R. Greenhalgh and J. P. Riley, "The development of a reproducible spectrophotometric curcumin method for determining boron, and its application to sea water," *Analyst*, vol. 87, no. 1041, pp. 970–976, 1962.

[254] V. Y. Fain, V. G. Avakyan, B. E. Zaitsev, and M. A. Ryabov, "Metal complexes with alizarin complexone: Electronic absorption spectra and ligand structure," *Russ. J. Coord. Chem.*, vol. 30, no. 9, pp. 671–677, 2004.

[255] J. Murphy and J. P. Riley, "A modified single solution method for the determination of phosphate in natural waters," *Anal. Chim. Acta*, vol. 27, no. 0, pp. 31–36, 1962.

[256] R. Ramachandran and P. K. Gupta, "An improved spectrophotometric determination of silicate in water based on molybdenum blue," *Anal. Chim. Acta*, vol. 172, no. 0, pp. 307–311, 1985.

[257] Y. Guangyu, Y. Jiayuan, L. Mei, and X. Qiheng, "Color reaction of vanadium (V) with Diantipyryl-(p-iospropoxy)-phenyhnethane and its mechanism," *Chinese J. Anal. Chem.*, vol. 01, 1999.

[258] S. Zhao, X. Xia, X. Kong, and T. Liu, "Highly sensitive colour-reaction of nickel with a new chromogenic reagent benzothiaxolyldiazoaminoazobenzene and its application," *Talanta*, vol. 45, no. 1, pp. 13–17, 1997.

[259] A. R. Chakraborty and R. K. Mishra, "Speciation and determination of chromium in waters," *Chem. Spec. Bioavail.*, vol. 4, no. 4, pp. 131–134, 1992.

[260] Y. Jiayuan and Y. Guangyu, "Spectrophotometric determination of manganese with diantipyryl (p bromo) phenylmethane," *Chinese J. Environ. Sci.*, vol. 03, 1997.

[261] T. G. Dzherayan, V. M. Shkinev, L. K. Shpigun, P. M. Kamilova, and K. E. Geckeler, "Water-soluble polymers for spectrophotometric and flow injection determination of cobalt with nitroso-R-salt," *Talanta*, vol. 57, pp. 7–13, 2002.

[262] P. Russell, "Photonic crystal fibres," *Science*, vol. 299, pp. 358–362, 2003.

[263] N. Seetohul, Z. Ali, and M. Islam, "Broadband cavity enhanced absorption spectroscopy as a detector for HPLC," *Anal. Chem.*, vol. 81, pp. 4106–4112, 2009.

[264] S.-S. Kiwanuka, T. Laurila, and C. F. Kaminski, "Sensitive method for the kinetic measurement of trace species in liquids using cavity enhanced absorption spectroscopy with broad bandwidth supercontinuum radiation," *Anal. Chem.*, vol. 82, pp. 7498–7501, 2010.

[265] E. R. Crosson, K. N. Ricci, B. A. Richman, F. C. Chilese, T. G. Owano, R. A. Provencal, M. W. Todd, J. Glasser, A. Kachanov, B. A. Paldus, T. G. Spence, and R. N. Zare, "Stable isotope ratios using cavity ring-down spectroscopy: Determination of 13C/12C for carbon dioxide in human breath," *Anal. Chem.*, vol. 74, pp. 2003–2007, 2002.

[266] A. A. Ruth and K. T. Lynch, "Incoherent broadband cavity-enhanced total internal reflection spectroscopy of surface-adsorbed metallo-porphyrins," *Phys. Chem. Chem. Phys.*, vol. 10, no. 47, pp. 7098–7108, 2008.

[267] S. M. Ball, J. M. Langridge, and R. L. Jones, "Broadband cavity enhanced absorption spectroscopy using light emitting diodes," *Chem. Phys. Lett.*, vol. 398, pp. 68–74, 2004.

[268] J. M. Langridge, T. Laurila, R. S. Watt, R. L. Jones, C. F. Kaminski, and J. Hult, "Cavity enhanced absorption spectroscopy of multiple trace gas species using a supercontinuum radiation source," *Opt. Expr.*, vol. 16, no. 14, pp. 10178–10188, 2008.

[269] P. S. Johnston and K. K. Lehmann, "Cavity enhanced absorption spectroscopy using a broadband prism cavity and a supercontinuum source," *Opt. Expr.*, vol. 16, no. 19, pp. 15013–15023, 2008.

[270] K. K. Lehmann, P. S. Johnston, and P. Rabinowitz, "Brewster angle prism retroreflectors for cavity enhanced spectroscopy," *Appl. Opt.*, vol. 48, no. 16, pp. 2966–2978, 2009.

[271] R. S. Brown, I. Kozin, Z. Tong, R. D. Oleschuk, and H.-P. Loock, "Fiber-loop ring-down spectroscopy," *J. Chem. Phys.*, vol. 117, no. 23, pp. 10444–10447, 2002.

[272] H.-P. Loock *Trends Anal. Chem.*, vol. 25, no. 7, pp. 655–664, 2006.

[273] H. Waechter, J. Litman, A. H. Cheung, J. A. Barnes, and H. P. Loock, "Chemical sensing using fiber cavity ring-down spectroscopy," *Sensors*, vol. 10, no. 3, pp. 1716–1742, 2010.

[274] L. van der Sneppen, G. Hancock, C. Kaminski, T. Laurila, S. R. Mackenzie, S. R. T. Neil, R. Peverall, G. A. D. Ritchie, M. Schnippering, and P. R. Unwin, "Following interfacial kinetics in real time using broadband evanescent wave cavity-enhanced absorption spectroscopy: a comparison of light-emitting diodes and supercontinuum sources," *Analyst*, vol. 135, pp. 133–139, 2010.

[275] S. M. Ball and R. L. Jones, "Broad-band cavity ring-down spectroscopy," *Chem. Rev.*, vol. 103, no. 12, pp. 5239–5262, 2003.

[276] T. McGarvey, A. Conjusteau, and H. Mabuchi, "Finesse and sensitivity gain in cavity-enhanced absorption spectroscopy of biomolecules in solution," *Opt. Express*, vol. 14, no. 22, p. 10441, 2006.

[277] M. Islam, N. Seetohul, and Z. Ali, "Liquid-phase broadband cavity-enhaced absorption spectroscopy measurements in a 2 mm cuvette," *Appl. Spectrosc.*, vol. 61, no. 6, pp. 649–658, 2007.

[278] R. R. Alfano, *The supercontinuum laser source: fundamentals with updated references*. Springer Science, 2006.

[279] G. R. Fowles, *Introduction to Modern Optics*. Dover Publications Inc., New York, 2nd ed., 1975.

[280] O. Ziane, S. Zaiba, and N. Melikechi, "Continuum generation in water and carbon tetrachloride using a picosecond Nd-YAG laser pulse," *Opt. Comm.*, vol. 273, no. 1, pp. 200–206, 2007.

[281] W. J. Wadsworth, A. Ortigosa-Blanch, J. C. Knight, T. A. Birks, T. P. M. Man, and P. S. J. Russell, "Supercontinuum generation in photonic crystal fibers and optical fiber tapers: a novel light source," *J. Opt. Soc. Am. B*, vol. 19, no. 9, pp. 2148–2155, 2002.

[282] J. C. Knight, "Photonic crystal fibres," *Nature*, vol. 424, pp. 847–851, 2003.

[283] S. Coen, A. H. L. Chau, R. Leonhardt, J. D. Harvey, J. C. Knight, W. J. Wadsworth, and P. S. J. Russell, "Supercontinuum generation by stimulated Raman scattering and parametric four-wave mixing in photonic crystal fibers," *J. Opt. Soc. Am. B*, vol. 19, no. 4, pp. 753–764, 2002.

[284] M. Brouard and C. Vallance, *Tutorials in molecular reaction dynamics*. Royal Society of Chemistry, 2010.

[285] K. Okamoto, *Fundamentals of Optical waveguides*. Elsevier, 2nd ed., 2006.

[286] M. Schnippering, P. R. Unwin, J. Hult, T. Laurila, C. F. Kaminski, J. M. Langridge, R. L. Jones, M. Mazurenka, and S. R. Mackenzie, "Evanescent wave broadband cavity enhanced absorption spectroscopy using supercontinuum radiation: A new probe of electrochemical processes," *Electrochem. Comm.*, vol. 10, p. 18271830, 2008.

[287] K. Stelmaszczyk, M. Fechner, P. Rohwetter, M. Queisser, A. Czyzewski, T. Stacewicz, and L. Woste, "Towards supercontinuum cavity ring-down spectroscopy," *Appl. Phys. B*, vol. 94, no. 3, pp. 369–373, 2009.

[288] S. R. T. Neil, C. M. Rushworth, C. Vallance, and S. R. Mackenzie, "Broadband cavity-enhanced absorption spectroscopy for real time, in situ spectral analysis of microfluidic droplets," *Lab Chip*, vol. 11, pp. 3953–3955, 2011.

[289] F. Wöhler, *Grundiss der Organisch Chemie*. Berlin: Duncker und Humblot, 1848.

[290] K. Geyer, J. D. C. Code, and P. H. Seeberger, "Microreactors as tools for synthetic chemiststhe chemists' round-bottomed flask of the 21st century?," *Chemistry A European Journal*, vol. 12, no. 33, pp. 8434–8442, 2006.

[291] W. Ehrfeld, V. Hessel, and H. Löwe, *Microreactors: new technology for modern chemistry*. Wiley-VCH, 2000.

[292] P. Watts and S. J. Haswell, "Continuous flow reactors for drug discovery," *Drug Discovery Today*, vol. 8, pp. 586–593, 2003.

[293] A. de Mello and R. Wootton, "Focus but what is it good for? applications of microreactor technology for the fine chemical industry," *Lab Chip*, vol. 2, no. 1, pp. 7N–13N, 2002.

[294] L. Kang, B. G. Chung, R. Langer, and A. Khademhosseini, "Microfluidics for drug discovery and development: From target selection to product lifecycle management," *Drug Discovery Today*, vol. 13, no. 1-2, pp. 1–13, 2008.

[295] P. Watts and S. J. Haswell, "Microfluidic combinatorial chemistry," *Curr. Opin. Chem. Biol.*, vol. 7, no. 3, pp. 380–387, 2003.

[296] S. J. Haswell and P. Watts, "Green chemistry: synthesis in microreactors," *Green Chemistry*, vol. 5, pp. 240–249, 2003.

[297] H. R. Sahoo, J. G. Kralj, and K. F. Jensen, "Multistep continuous-flow microchemical synthesis involving multiple reactions and separations," *Angew. Chem.*, vol. 119, pp. 5806–5810, 2007.

[298] R. C. R. Wootton, R. Fortt, and A. J. de Mello, "On-chip generation and reaction of unstable intermediates-monolithic nanoreactors for diazonium chemistry: Azo dyes," *Lab Chip*, vol. 2, no. 1, pp. 5–7, 2002.

[299] M. Saber, J. M. Commenge, and L. Falk, "Microreactor numbering-up in multi-scale networks for industrial-scale applications: Impact of flow maldistribution on the reactor performances," *Chem. Eng. Sci.*, vol. 65, no. 1, pp. 372–379, 2010.

[300] P. D. I. Fletcher, S. J. Haswell, E. Pombo-Villar, B. H. Warrington, P. Watts, S. Y. F. Wong, and X. Zhang, "Micro reactors: principles and applications in organic synthesis," *Tetrahedron*, vol. 58, no. 24, pp. 4735–4757, 2002.

[301] P. Watts and S. J. Haswell, "The application of micro reactors for organic synthesis," *Chem. Soc. Rev.*, vol. 34, pp. 235–246, 2005.

[302] H. Salimi-Moosavi, T. Tang, and D. J. Harrison, "Electroosmotic pumping of organic solvents and reagents in microfabricated reactor chips," *J. Am. Chem. Soc.*, vol. 119, pp. 8716–8717, 1997.

[303] M. Fernandez-Suarez, S. Y. F. Wong, and B. H. Warrington, "Synthesis of a three-member array of cycloadducts in a glass microchip under pressure driven flow," *Lab Chip*, vol. 2, no. 3, pp. 170–174, 2002.

[304] F. Benito-Lopez, W. Verboom, M. Kakuta, J. G. E. Gardeniers, R. J. M. Egberink, E. R. Oosterbroek, A. van den Berg, and D. N. Reinhoudt, "Optical fiber-based on-line UV/Vis spectroscopic monitoring of chemical reaction kinetics under high pressure in a capillary microreactor," *Chem. Comm*, no. 22, pp. 2857–2859, 2005. (Han).

[305] D. Snyder, C. Noti, P. Seeberger, F. Schael, T. Bieber, G. Rimmel, and W. Ehrfeld, "Modular microreaction systems for homogeneously and heterogeneously catalyzed chemical synthesis," *Helvetica Chim. Acta*, vol. 88, no. 1, pp. 1–9, 2005.

[306] C. Wiles, P. Watts, S. J. Haswell, and E. Pombo-Villar, "Solution phase synthesis of esters within a micro reactor," *Tetrahedron*, vol. 59, p. 1017310179, 2003.

[307] M. Brivio, W. Verboom, and D. N. Reinhoudt, "Miniaturized continuous flow reaction vessels: influence on chemical reactions," *Lab Chip*, vol. 6, pp. 329–344, 2006.

[308] M. S. Congreve and C. Jamieson, "High-throughput analytical techniques for reaction optimization," *Drug Discovery Today*, vol. 7, no. 2, pp. 139–142, 2002.

[309] C. A. McGill, A. Nordon, and D. Littlejohn, "Comparison of in-line NIR, Raman and UV-visible spectrometries, and at-line NMR spectrometry for the monitoring of an esterification reaction," *Analyst*, vol. 127, no. 2, pp. 287–292, 2002.

[310] W. Ferstl, T. Klahn, W. Schweikert, G. Billeb, M. Schwarzer, and S. Loebbecke, "Inline analysis in microreaction technology: A suitable tool for process screening and optimization," *Chem. Eng. Technol.*, vol. 30, no. 3, pp. 370–378, 2007.

[311] "The nobel prize in chemistry 1950. nobelprize.org. 22 mar 2012 www.nobelprize.org/nobelprizes/chemistry/laureates/1950/."

[312] O. Diels and K. Alder *Justus Liebigs Ann. Chem.*, vol. 460, pp. 98–122, 1928.

[313] J. A. Berson, "Discoveries missed, discoveries made: creativity, influence, and fame in chemistry," *Tetrahedron*, vol. 48, no. 1, pp. 3–17, 1992.

[314] K. C. Nicolaou, S. A. Snyder, T. Montagnon, and G. Vassilikogiannakis, "The Diels-Alder reaction in total synthesis," *Angew. Chem. Int. Ed.*, vol. 41, pp. 1668–1698, 2002.

[315] M. Gates and G. Tschudi, "The synthesis of morphine," *J. Am. Chem. Soc.*, vol. 78, no. 7, pp. 1380–1393, 1956.

[316] R. B. Woodward, F. Sondheimer, D. Taub, K. Heusler, and W. M. McLamore, "The total synthesis of steroids," *J. Am. Chem. Soc.*, vol. 74, no. 17, pp. 4223–4251, 1952.

[317] J. N. Lee, C. Park, and G. M. Whitesides, "Solvent compatibility of poly(dimethylsiloxane)-based microfluidic devices," *Anal. Chem.*, vol. 75, pp. 6544–6554, 2003.

[318] S. S. H. Gilani and D. J. Triggle, "The synthesis of Nitrogen-containing steroids. I. Diels-Alder adducts of steroids and 4-phenyl-1,2,4-triazoline-3,5-dione," *J. Org. Chem.*, vol. 31, no. 7, pp. 2397–2398, 1966.

[319] D. S. Morris, D. H. Williams, and A. F. Norris, "Structure and synthesis of 25-hydroxycholecalciferol-26,23-lactone, a metabolite of vitamin D," *J. Org. Chem.*, vol. 46, no. 17, pp. 3422–3428, 1981.

[320] "www.uni-regensburg.de/fakultaeten/natfakiv/organischechemie/didaktik/keusch/p2cycloadd-e.htm."

[321] I. K. Korobitsyna, A. V. Khalikova, L. L. Rodina, and N. P. Shushina, "4-phenyl-1,2,4,-triazoline-3,5-dione," *Chem. Heterocyclic Compounds*, vol. 19, no. 2, p. 117, 1983.

[322] J. Buffle and G. Horvai, *In situ monitoring of aquatic systems*, vol. Wiley-VCH. 2001.

[323] IPCC, *The Physical Science Basis. Contribution of Working Group I to the Fourth Assessment Report of the Intergovernmental Panel on Climate Change*. Cambridge Univ. Press, 2007.

[324] J. G. Canadell, C. Le Quéré, M. R. Raupach, C. B. Field, E. T. Buitenhuis, P. Ciais, T. J. Conway, N. P. Gillett, R. A. Houghton, and G. Marland, "Contributions to accelerating atmospheric CO_2 growth from economic activity, carbon intensity, and efficiency of natural sinks," *PNAS*, vol. 104, no. 47, pp. 18866–18870, 2007.

[325] O. Hoegh-Guldberg, P. J. Mumby, A. J. Hooten, R. S. Steneck, P. Greenfield, E. Gomez, C. D. Harvell, P. F. Sale, A. J. Edwards, K. Caldeira, N. Knowlton, C. M. Eakin, R. Iglesias-Prieto, N. Muthiga, R. H. Bradbury, A. Dubi, and M. E. Hatziolos, "Coral reefs under rapid climate change and ocean acidification," *Science*, vol. 318, p. 1737, 2007.

[326] A. G. Dickson, "The measurement of sea water pH," *Mar. Chem.*, vol. 44, pp. 131–142, 1993.

[327] R. H. Byrne, G. Robert-Baldo, S. W. Thompson, and C. T. A. Chen, "Seawater pH measurements: an at-sea comparison of spectrophotometric and potentiometric methods," *Deep Sea Res. Part I*, vol. 35, no. 8, pp. 1405–1410, 1988.

[328] D. W. King and D. R. Kester, "Determination of seawater pH from 1.5 to 8.5 using colorimetric indicators," *Mar. Chem.*, vol. 26, no. 1, pp. 5–20, 1989.

[329] J. A. Breland and R. H. Byrne, "Spectrophotometric procedures for determination of sea water alkalinity using bromocresol green," *Deep Sea Res. Part I*, vol. 40, no. 3, pp. 629–641, 1993.

[330] W. Yao and R. H. Byrne, "Spectrophotometric determination of freshwater pH using bromocresol purple and phenol red," *Environ. Sci. Technol.*, vol. 35, pp. 1197–1201, 2001.

[331] T. D. Clayton and R. H. Byrne, "Spectrophotometric seawater pH measurements: total hydrogen ion concentration scale calibration of m-cresol purple and at-sea results," *Deep Sea Res. Part I*, vol. 40, no. 10, pp. 2115–2129, 1993.

[332] X. Liu, Z. A. Wang, R. H. Byrne, E. A. Kaltenbacher, and R. E. Bernstein, "Spectrophotometric measurements of pH in situ: Laboratory and field evaluations of instrumental performance," *Environ. Sci. Technol.*, vol. 40, pp. 5036–5044, 2006.

[333] L. M. Mosley, S. L. G. Husheer, and K. A. Hunter, "Spectrophotometric pH measurement in estuaries using thymol blue and m-cresol purple," *Mar. Chem.*, vol. 91, no. 14, pp. 175–186, 2004.

[334] X. Liu, M. Patsavas, and R. H. Byrne, "Purification and characterization of meta-cresol purple for spectrophotometric seawater pH measurements," *Environ. Sci. Technol.*, vol. 45, p. 4862, 2011.

[335] D. W. King and D. R. Kester, "Spectral modeling of sulfonephthalein indicators: Application to pH measurements using multiple indicators," *Appl. Spectrosc.*, vol. 44, no. 4, pp. 722–727, 1990.

[336] H. Waechter, K. Bescherer, C. J. Dürr, R. D. Oleschuk, and H.-P. Loock, "405 nm absorption detection in nanoliter volumes," *Anal. Chem.*, vol. 81, pp. 9048–9054, 2009.

[337] C. Wang and S. T. Scherrer, "Fiber loop ringdown for physical sensor development: pressure sensor," *Appl. Opt.*, vol. 43, no. 35, pp. 6458–6464, 2004.

[338] C. Wang, "Fiber ringdown temperature sensors," *Opt. Eng.*, vol. 44, p. 030503, 2005.

[339] P. B. Tarsa, D. M. Brzozowski, P. Rabinowitz, and K. K. Lehmann, "Cavity ringdown strain gauge," *Opt. Lett.*, vol. 29, pp. 1339–1341, 2004.

[340] N. Ni, C. C. Chan, L. Xia, and P. Shum, "Fiber cavity ring-down refractive index sensor," *IEEE Photo. Technol. Lett.*, vol. 20, no. 16, pp. 1351–1353, 2009.

[341] B. E. A. Saleh and M. C. Teich, *Fundamentals of Photonics*. John Wiley & Sons, 2nd ed., 2007.

[342] H. Waechter, D. Munzke, A. Jang, and H.-P. Loock, "Simultaneous and continuous multiple wavelength absorption spectroscopy on nanolitre volumes based on frequency-division multiplexing fiber-loop cavity ring-down spectroscopy," *Anal. Chem.*, vol. 83, pp. 2719–2725, 2011.

[343] T. Von Lerber and M. W. Sigrist, "Cavity-ring-down principle for fiber-optic resonators: experimental realization of bending loss and evanescent-field sensing," *Appl. Opt.*, vol. 41, no. 18, pp. 3567–3575, 2002.

[344] D. E. Vogler, M. G. Mülller, and M. W. Sigrist, "Fiber-optic cavity sensing of hydrogen diffusion," *Appl. Opt.*, vol. 42, no. 27, pp. 5413–5417, 2003.

[345] D. E. Vogler, A. Lorencak, J. M. Rey, and M. W. Sigrist, "Bending loss measurement using a fiber cavity ringdown scheme," *Opt. Laser Eng.*, vol. 43, no. 3-5, pp. 527–535, 2005.

[346] M. Gupta, H. Jiao, and A. O'Keefe, "Cavity-enhanced spectroscopy in optical fibers," *Opt. Lett.*, vol. 27, no. 21, pp. 1878–1880, 2002.

[347] G. Stewart, K. Atherton, H. Yu, and B. Culshaw, "An investigation of an optical fibre amplifier loop for intra-cavity and ring-down cavity loss measurements," *Meas. Sci. Technol.*, vol. 12, pp. 843–849, 2001.

[348] G. Stewart, K. Atherton, and B. Culshaw, "Cavity-enhanced spectroscopy in fiber cavities," *Opt. Lett.*, vol. 29, no. 5, pp. 442–444, 2004.

[349] Z. Tong, M. Jakubinek, A. Wright, A. Gillies, and H.-P. Loock, "Fiber-loop ring-down spectroscopy: A sensitive absorption technique for small liquid samples," *Rev. Sci. Instrum.*, vol. 74, no. 11, pp. 4818–4826, 2003.

[350] M. Andachi, T. Nakayama, M. Kawasaki, S. Kurokawa, and H.-P. Loock, "Fiber-optic ring-down spectroscopy using a tunable picosecond gain-switched diode laser," *Appl. Phys. B*, vol. 88, pp. 131–135, 2007.

[351] Z. Tong, A. Wright, T. McCormick, R. Li, R. D. Oleschuk, and H.-P. Loock, "Phase-shift fiber-loop ring-down spectroscopy," *Anal. Chem.*, vol. 76, no. 22, pp. 6594–6599, 2004.

[352] R. Li, H.-P. Loock, and R. D. Oleschuk, "Capillary electrophoresis absorption detection using fiber-loop ring-down spectroscopy," *Anal. Chem.*, vol. 78, no. 16, pp. 5685–5692, 2006.

[353] R. Engeln, G. von Helden, G. Berden, and G. Meijer, "Phase shift cavity ring down absorption spectroscopy," *Chem. Phys. Lett.*, vol. 262, pp. 105–109, 1996.

[354] P. B. Tarsa, P. Rabinowitz, and K. K. Lehmann, "Evanescent field absorption in a passive optical fiber resonator using continuous-wave cavity ring-down spectroscopy," *Chem. Phys. Lett.*, vol. 383, no. 3-4, pp. 297–303, 2004.

[355] D. J. Ripin and L. Goldberg, "High efficiency side-coupling of light into optical fibres using imbedded v-grooves," *Electronics Letters*, vol. 31, no. 25, pp. 2204–2205, 1995.

[356] A. Hideur, T. Chartier, C. Özkul, and F. Sanchez, "All-fiber tunable ytterbium-doped double-clad fiber ring laser," *Opt. Lett.*, vol. 26, no. 14, pp. 1054–1056, 2001.

[357] C. Rushworth and C. Vallance *Proc. SPIE*, vol. 7838, no. 1, p. 78380Y, 2010.

[358] "www.zemax.co.uk."

[359] V. Allen, T. J. H. Essex, and A. McKenzie, "A simple projector for superficial laser photodynamic therapy," *Phys. Med. Biol.*, vol. 34, no. 7, pp. 927–930, 1989.

[360] M. Fabian, E. Lewis, T. Newe, and S. Lochmann, "Optical fibre cavity for ring-down experiments with low coupling losses," *Meas. Sci. Tech.*, vol. 21, no. 9, p. 094034, 2010.

[361] C. A. Goss, D. H. Charych, and M. Majda, "Application of (3-mercaptopropyl)triethoxysilane as a molecular adhesive in the fabrication of vapour-deposited gold electrodes on glass substrates," *Anal. Chem.*, vol. 63, no. 1, pp. 85–88, 1991.

[362] S. Sandlin, T. Kinnunen, J. Ramo, and M. Sillanpaa, "A simple method for metal re-coating of optical fibre bragg gratings," *Surface & Coatings Technology*, vol. 201, pp. 3061–3065, 2006.

[363] C. A. Volkert and A. M. Minor, "Focused ion beam microscopy and micromachining," *MRS Bulletin*, vol. 32, pp. 389–395, 2007.

[364] E. H. Park, M. J. Kim, and Y. S. Kwon, "Microlens for efficient coupling between LED and optical fiber," *IEEE Photon. Technol. Lett.*, vol. 11, no. 4, pp. 439–441, 1999.

[365] J. Meng, W. G. Zhang, Q. Zhang, Y. P. Liu, and B. Liu, "Investigation on an evanescent wave fiber-optic absorption sensor based on fiber loop cavity ring-down spectroscopy," *Optics Communications*, vol. 283, no. 2, pp. 249–253, 2010.

[366] J. D. Fisk, N. W. Hayes, D. Barnett, M. Farries, K. M. Tasker, and A. M. Shaw, "Fibre optic implementation of evanescent wave cavity ring-down spectroscopy for chemical detection," *Proc. SPIE*, vol. 5990, p. 59900T, 2005.

[367] S.-M. Tseng and C.-L. Chen, "Side-polished fibers," *Appl. Opt.*, vol. 31, no. 18, pp. 3438–3447, 1992.

[368] V. Ruddy, B. D. MacCraith, and J. A. Murphy, "Evanescent wave absorption spectroscopy using multimode fibers," *J. Appl. Phys.*, vol. 67, no. 10, pp. 6070–6074, 1990.

[369] P. B. Tarsa, A. D. Wist, P. Rabinowitz, and K. K. Lehmann, "Single-cell detection by cavity ring-down spectroscopy," *Appl. Phys. Lett.*, vol. 85, no. 19, pp. 4523–4525, 2004.

[370] P. Polynkin, A. Polykin, N. Peyghambarian, and M. Mansuripur, "Evanescent field-based optical fiber sensing device for measuring the refractive index of liquids in microfluidic channels," *Opt. Lett.*, vol. 30, no. 11, pp. 1273–1275, 2005.

[371] A. Ahmad and L. L. Hench, "Effect of taper geometries and launch angle on evanescent wave penetration depth in optical fibers," *Biosensors and Bioelectronics*, vol. 20, pp. 1312–1319, 2005.

[372] E. W. Van Stryland, *Handbook of Optics Volume 4*. McGraw-Hill, 2009.

[373] M. G. Goggins, S. A. Shah, J. Goh, A. Cherukuri, D. G. Weir, D. Kelleher, and N. Mahmud, "Increased urinary nitrite, a marker of nitric oxide, in active inflammatory bowel disease," *Mediators of Inflammation*, vol. 10, pp. 69–73, 2001.

[374] E. S. Kehmeier, M. Kropp, P. Kleinbongard, T. Lauer, J. Balzer, M. W. Merx, G. Heusch, M. Kelm, W. Lepper, and T. Rassaf, "Serial measurements of whole blood nitrite in an intensive care setting," *Free Radical Biology and Medicine*, vol. 44, no. 11, pp. 1945–1950, 2008.

[375] L. P. Ho, J. A. Innes, and A. P. Greening, "Nitrite levels in breath condensate of patients with cystic fibrosis is elevated in contrast to exhaled nitric oxide," *Thorax*, vol. 53, pp. 680–684, 1998.

[376] S. A. Kharitonov and P. J. Barnes, "Biomarkers of some pulmonary diseases in exhaled breath," *Biomarkers*, vol. 7, no. 1, pp. 1–32, 2002.

[377] W. Miekisch, J. K. Schubert, and G. F. E. Noeldge-Schomburg, "Diagnostic potential of breath analysisfocus on volatile organic compounds," *Clinica Chimica Acta*, vol. 347, no. 12, pp. 25–39, 2004.

[378] C. Wang and P. Sahay, "Breath analysis using laser spectroscopic techniques: Breath biomarkers, spectral fingerprints, and detection limits," *Sensors*, vol. 9, pp. 8230–8262, 2009.

[379] C. Wang and A. B. Surampudi, "An acetone breath analyzer using cavity ringdown spectroscopy: an initial test with human subjects under various situations," *Meas. Sci. Technol.*, vol. 19, p. 105604, 2008.

[380] S. Amalathe and V. K. Gupta, "Spectrophotometric determination of acetone using vanillin," *Analyst*, vol. 115, pp. 1385–1387, 1990.

[381] J. A. Behre and S. R. Benedict, "A colorimetric method for the determination of acetone bodies in blood and urine," *J. Biol. Chem.*, vol. 70, pp. 487–494, 1926.

[382] K. W. Loach and T. A. Turney, "The acetone complex of nitroprusside ion," *J. Inorg. Nucl. Chem.*, vol. 18, pp. 179–183, 1961.

[383] L. A. Mundt and K. Shanahan, *Graff's Textbook of Urinalysis and Body Fluids*. Lippincott Williams & Wilkins, 2nd ed., 2010.

[384] G. Wang, G. Maranelli, L. Perbellini, E. Raineri, and F. Brugnone, "Blood acetone concentration in 'normal people' and in exposed workers 16 h after the end of the workshift.," *Int. Arch. Occup. Environ. Health*, vol. 65, no. 5, pp. 285–289, 1994.

[385] R. B. Fair, "Digital microfluidics: is a true lab-on-chip possible?," *Microfluid. Nanofluid.*, vol. 3, pp. 245–281, 2007.

[386] L. Billot, A. Plecis, and Y. Chen, "Multi-reflection cell based on chip label free molecules detection," *Microelectron. Eng.*, vol. 85, pp. 1269–1271, 2008.

[387] B. Helbo, A. Kristensen, and A. Menon, "Micro-cavity fluidic dye laser," *J. Micromech. Microeng.*, vol. 13, p. 307, 2003.

[388] H. Shao, D. Kumar, S. A. Feld, and K. L. Lear, "Fabrication of a Fabry-Pérot cavity in a microfluidic channel using thermocompressive gold bonding of glass substrates," *J. MEMS*, vol. 14, no. 4, p. 756, 2005.

[389] D. Psaltis, S. R. Quake, and C. Yang, "Developing optofluidic technology through the fusion of microfluidics and optics," *Nature*, vol. 442, pp. 381–386, 2006.

[390] W. Song and D. Psaltis, "Pneumatically tuneable optofluidic dye laser," *Appl. Phys. Lett.*, vol. 96, no. 8, p. 1101, 2010.

[391] M. Gersborg-Hansen, S. Balslev, N. A. Mortensen, and A. Kristensen, "A coupled cavity microfluidic dye ring laser," *Microelectron. Eng.*, vol. 78, p. 185, 2005.

[392] J. C. Galas, C. Peroz, Q. Kou, and Y. Chen, "Microfluidic dye laser intracavity absorption," *Appl. Phys. Lett.*, vol. 89, p. 224101, 2006.

[393] P. R. Dolan, G. M. Hughes, F. Grazioso, B. R. Patton, and J. M. Smith, "Femtoliter tunable optical cavity arrays," *Opt. Lett.*, vol. 35, no. 21, pp. 3556–3558, 2010.

[394] H. Claustre, D. Antoine, L. Boehme, E. Boss, F. D'Ortenzio, O. F. D'Andon, C. Guinet, N. Gruber, N. O. Handegard, M. Hood, K. Johnson, A. Körtzinger, R. Lampitt, P.-Y. LeTraon, C. Lequéré, M. Lewis, M.-J. Perry, T. Platt, D. Roemmich, S. Sathyendranath, U. Send, P. Testor, and J. Yoder, "Guidelines towards an integrated ocean observation system for ecosystems and biogeochemical cycles," *Proc. OceanObs'09*, vol. 1, 2010.